Annual Report 2002

Selected Results

Berlin 2003

Captions of cover images

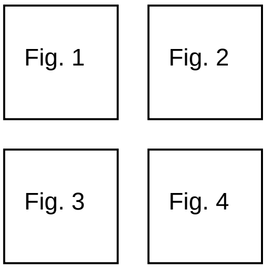

Fig. 1: “Texture modification in titanium layers with heavy ions” (HMI at BESSY / SF4). Pole figure of the irradiated area of the 3µm thick sample.

Fig. 2: “Intracellular Ca^{2+}-dynamics as a stochastic medium” (SF5). Nucleation of a calcium wave with increasing concentration in time.

Fig. 3: “Preparation of wide band gap materials by structure conformal conversion” (SE 2). Columns of Ag_2S from columnar ZnS reacted with highly diluted $AgNO_3$ solution.

Fig. 4: “Analysis of buried interfaces in $Cu(In,Ga)(S,Se)_2$ thin film solar cells by X-ray emission and photoelectron spectroscopy in the CISSY apparatus” (SE 2). CISSY endstation with attached glovebox.

1 Edition
July 2003

Annual Report 2002
Selected Results
HMI-B-593

Hahn-Meitner-Institut Berlin GmbH
Glienicker Str. 100
D-14109 Berlin (Wannsee)

Co-ordination:
Klaus Möhring
Telefon: (030) 8062 2763
Telefax: (030) 8062 2047
E-Mail: moehring@hmi.de

Table of Contents

Large Scale Facilities / User Service

ISL – Ion Beam Laboratory

HMI at BESSY

NAA-Laboratory and Irradiation Service at BER II

Scientific Departments

SF1 – Methods and Instruments

SF2 – Magnetism

SF3 – Materials

SF4 – Structure and Dynamics

SF5 – Theoretical Physics

SF6 – Trace Elements

SF7 – Nuclear Measurements

SE1 – Silicon Photovoltaics

SE2 – Heterogeneous Material Systems

SE3 – Technology

SE4 – Dynamics of Interfacial Reactions

SE5 – Solar Energetics

Foreword

With this report we present some selected results of the research and development activities in the Hahn-Meitner-Institute during the year 2002. We hope in this way to give an idea of the wide spectrum of scientific activities in HMI and of the quality of the work performed by both our own staff and the large community of external users of our facilities.

2002 also saw several evaluation procedures and, in particular, preparations for the new program-oriented funding system (POF) of the Helmholtz Association HGF.

Our Solar Energy Division successfully passed the evaluation by the Scientific Council due every four years. This was the basis for the formulation of the programmatic strategy for the period 2004 to 2008 in preparation for the first evaluation within the POF.

The first effectual funding decisions in the POF scheme affirmed the contributions to the HGF research field “Health” for the period 2003 to 2007. Here HMI participates with its R&D accompanying the tumor therapy in the Ion Beam Laboratory ISL and the research of the department SF6 studying the role of trace elements in the living body.

In summer 2002 the German Wissenschaftsrat published its evaluation of future large scale facilities in Germany.
Based on it and the subsequent decisions of the Federal Government, efforts to prepare for a European Spallation Source will be scaled down.
A final evaluation of the HMI project N40T, the installation of up to 40 Tesla magnetic fields for neutron scattering experiments, was postponed as the full scale Scientific Case and the technical Design report was available in early 2003 only.

Still, several of the results reported in this volume underline that experiments in high magnetic fields represent one of the high lights of the research possibilities at BENSC.

A new 15 Tesla magnet got operational in.2002. The erection of a second Neutron Guide Hall was one of the first priority tasks in 2002, construction work will start in summer 2003. This hall will house, among others, a new diffractometer specifically designed for experiments in extreme magnetic fields.

At BESSY, the build-up period comes towards its end. The first of the two “HMI insertion devices”, the undulator UE46 is installed and the adjacent beam line for x-.ray spectrometry and reflectometry is in operation. The installation of the very ambitious 7 Tesla Wiggler is now scheduled for early 2004.

In the responsibility of the Solar energy Division, the experimental station CISSY for in-situ studies of solar energy devices and the TGM7 experimental station for the study of semiconductor interfaces are operational, too.

Looking back on 2002, we again gratefully acknowledge the very dedicated work of our staff and of the large external community using our facilities. Going without saying this includes the engaged work of the staff outside the scientific departments – from information technology over technical units to the administration. We equally appreciate the critical and always helpful backing by our advisory boards and the trustworthy support by the federal government and the Senat of Berlin. Our thanks go to everybody for his share to preserve HMI as a place to do exciting scientific work well noticed by the national and international community.

Besides the activities directly connected to the user service at the large scale facilities BER II / BENSC, ISL and the HMI installations at BESSY, contributions in this report are arranged along the departmental organisation of the scientific divisions. (Reference to the department and the R&D-project is given in the top lines).

To this annual report, HMI publishes a separate supplement containing listed information on

- Publications
- Conference contributions
- Invited lectures
- Patents and patent applications
- Academic education
- Appointment and awards
- Participation in external scientific bodies and committees
- Organization of conferences and meetings
- Contributions to exhibitions / fairs / events
- Guests
- Co-operation partners
- External funding

Both the report and the separate supplement are available as download on the homepage of the Hahn-Meitner-Institute:

www.hmi.de/pr/druckschriften.html

or can be referred on request over the public relations office of the institute:

Hahn-Meitner-Institut Berlin
Öffentlichkeitsarbeit
Glienicker Strasse 100
D-14109 Berlin
e-mail: info@hmi.de

More detailed information on the experimental activities at BENSC and ISL are published in separate reports:

Division
SF Structural Research
(Structure and Dynamics in Condensed Matter)

The division Structural Research is formed by six departments which primarily use the three large scale facilities BER II / BENSC, ISL and BESSY. Although the study of the microscopic structure in condensed matter is the main field of research, the large scale facilities are also used for specific applications in health care and environmental protection (eye tumour therapy with proton beams, activation analysis with neutron beams).

The scientific program comprises three complementary issues: to provide a large national and international user community with top of the line research feasibilities at BENSC, ISL and BESSY, to develop new methods and instruments, and to do in-house research with instruments and methods built and developed at HMI.

Methods developed at HMI are e.g. in the fields of electron microscopy, field ion microscopy, X-ray diffraction, neutron scattering instruments, and extreme sample environment (low temperatures in the mk range, magnetic fields of up to 15 Tesla).

The division Structural Research comprises 6 scientific departments:

SF1 Methods and Instruments
SF2 Magnetism
SF3 Materials
SF4 Strukture and Dynamics
SF5 Theoretical Physics
SF6 Trance Elements
and the group
SF7 Nuclear Measurement Technique.

The three first mentioned departments form the Berlin Neutron Scattering Center BENSC, SF4 is responsible for the operation and the development of the **Ion Beam Lab** and the **Eye Tumor Therapy**, and SF6 organizes the user service for the **Neutron Activation Analysis**.

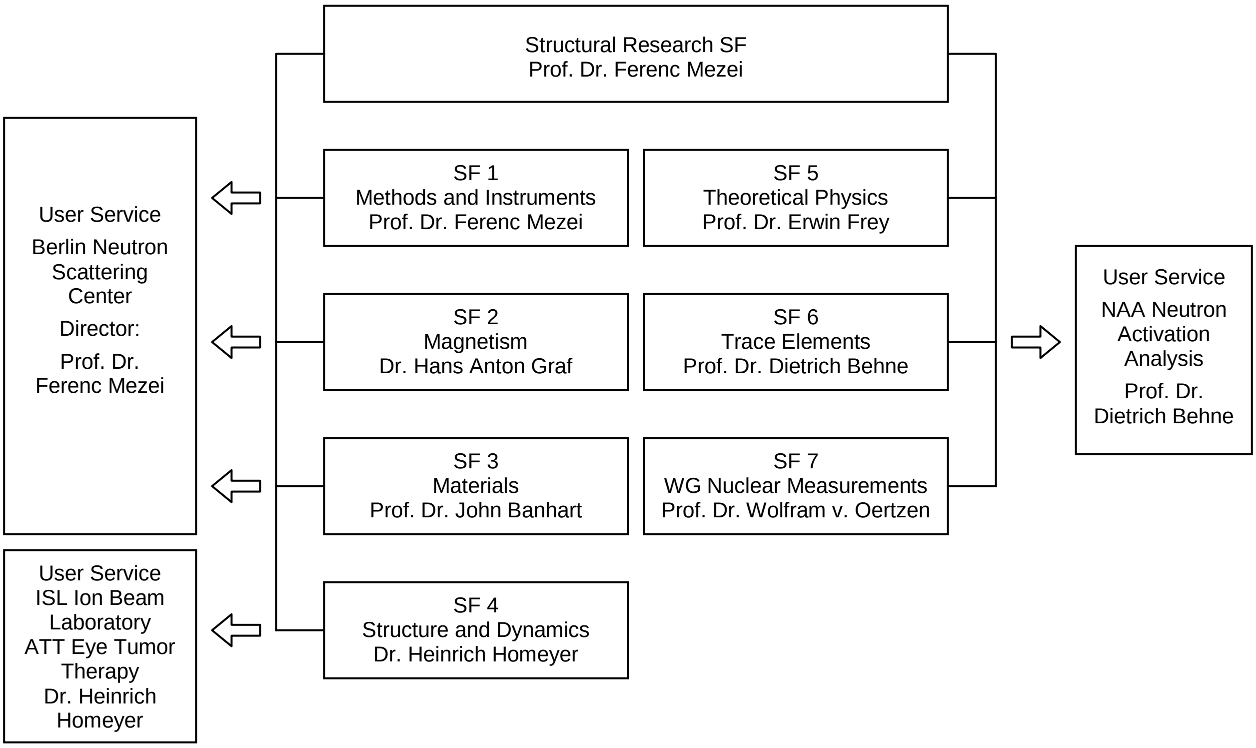

BENSC- Operation

Director: Prof. Ferenc Mezei

It is the mission of the Berlin Neutron Scattering Center *(BENSC)* to develop and operate the scientific instruments at the Berlin research reactor BER II. About 70 % of the beam time at the most important instruments is made available to external scientific user groups from all over the world.

On a **regional and national scale** BENSC performs a principal task of the Hahn-Meitner-Institute:

Service for research groups

- from German Universities
- and from other public funded research institutions.

The relevant duties assigned to BENSC cover a broad range from contributions to scientific education up to performance of high ranking scientific research. An aim of increasing importance is

- scientific and technical support for industrial applications.

This support for industry is mainly based on co-operation agreements, where the partners produce the relevant samples and in return profit from the advanced analytical methods available at BENSC and from the highly specialized know-how of the BENSC staff.

On the **international scale** BENSC plays an important role in the round of European research centers. The growing international importance of BENSC is underlined by the fact that the number of short-term guest scientists from abroad exceeds the number of German visitors (see table 1) and has been stimulated by participating in the Access to Research Infrastructures Programmes of the European Commission.

The service orientation of BENSC requires a higher degree of reliable provision, preservation and development of know-how than this applies to rather basic research oriented institutions.

Profile of BENSC

The profile of BENSC is characterized by the exceptionally wide range of the **instrumentation**, which allows experiments to be performed in many areas ranging from basic to applied research. Several advanced BENSC instruments provide neutron intensities and resolutions competitive with the best available worldwide, including those operating at high flux reactors. Most of the instruments have the option of using polarized neutrons. Examples for unique advanced instrument options are, e.g., ♦ the polarized neutron option SANSPOL, ♦ the multidetector option the time-of-flight spectrometer NEAT, and ♦ the spin-echo instrument (SPAN) with the wide-angle NSE option. ♦ the flat-cone diffractometer ♦ and especially the sample environment.

The leading role of BENSC for **sample environment at extreme conditions** is accepted worldwide: Experiments can be performed over a very large range of temperatures and/or magnetic fields. The temperature range for routine use is 15 mK to beyond 1200 K; and magnetic fields up to 17 Tesla have been made available to routine user operation. The unique Cryostat (1.5 K < T < 300 K) with a split pair superconducting magnet and a vertical field up to 17 Tesla is the world's leading magnet system in a neutron scattering facility and up-to-now available only at BENSC. A second magnet of this type has gone operational in summer 2002.

The advanced instrumentation and the unique sample environment capabilities attract renowned research groups Europe- and world-wide, and even from other powerful neutron sources. Three examples of highlight results from external user groups are included below.

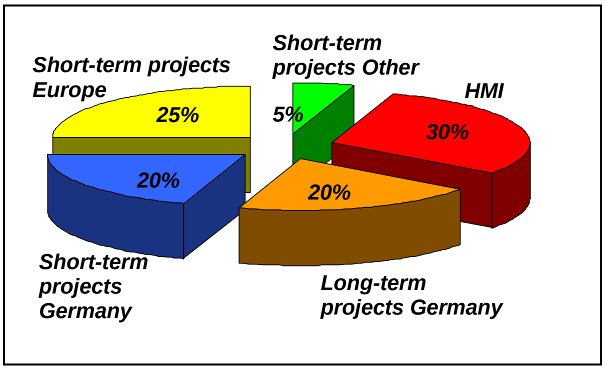

Fig. 1: *Distribution of the BENSC instrument time*

BENSC User Service

The BENSC user services provided for scientists of German universities and other national and international research institutions include

- Allocation of beam time to individual ("short-term") projects of external groups on the basis of peer reviewing by an international user committee and extensive scientific and technical support for the preparation, the experiments and the data evaluation. Logistic support and travel support for young researchers is provided.
- Long-term scientific and technical projects on the basis of co-operation agreements, which mostly include the operation of instruments for which a contingent of beam time is allocated to the group.

An amount of at least 50 % of the beam time of the 14 most important instruments operated by BENSC is reserved for individual scientific projects, up to 20% of the beam time would be made available for long-term co-operation projects.

Long-term co-operations

Long-term co-operation projects are not only in the interest of the respective co-operations partners but also increase the manpower at BENSC and broaden the capacities for scientific support to the external users. In the path breaking field of soft matter research for instance, which until recently was not a core field of HMI's own scientific program, BENSC has established close collaborative links with the Institute of Biochemistry of the Technical University Darmstadt, the Iwan-N.-Stranski Institute of the Technical University Berlin, and the Max-Planck Institute of Colloids and Interfaces in Golm/Potsdam.

The most important long-term co-operation partners from the region of Berlin-Brandenburg are

- Technische Universität Berlin,
  Iwan-N.-Stranski-Institut für Physikalische und Theoretische Chemie,
  (Prof. G.H. Findenegg)
- Max-Planck-Institut für Kolloid und Grenzflächenforschung, Golm/Potsdam
  (Prof Dr. H. Möhwald)
- Technische Universität Berlin,
  Institut für Werkzeugwissenschaften und -technologie, Metallphysik,
  (Prof. W. Reimers)
- Technische Fachhochschule Berlin,
  (Prof. W. Treimer)

Other national long-term co-operation partners in 2002 are

- Institut für Kristallographie,
  Universität Tübingen
  (Prof. W. Prandl †/Prof. Ihringer)
- Institut für Biochemie
  Technische Universität Darmstadt
  (Prof. N. Dencher)
- Institut für Physikalische Biologie
  Universität Düsseldorf
  (Prof. G. Büldt)
- FB Materialwissenschaften
  Technische Universität Darmstadt
  (Prof. H. Hahn)
- Institut für Festkörperphysik
  Technische Universität Darmstadt
  (Prof. H. Wipf)

Individual short-term research proposals of external users

It is the key issue of the BENSC user service to provide external groups with beam time and intensive scientific support for individual scientific experiments. This service is meant for both German groups and the international scientific community. The inclusion of new applications for beam time is decided by an internationally composed Scientific Selection Panel in semi-annual selection rounds on the basis of scientific merit of the proposals.

External short term proposals year 2002	Number of accepted **projects**	Allocated instrument **days**	Number of total **rejections**
D - Univ.	**44**	**260**	**9**
D - other	**28**	**180**	**5**
EU + Assoc + CH	**94**	**605**	**35**
Russia + Ukraine	**20**	**200**	**15**
USA, JAP, AUS,CAN, and other	**19**	**185**	**16**
	205	1430	80

Table 1: Allocations of BENSC instrument time for single projects in 2002 by the Scientific Panel, listed by country of home institution of principal proposer.

BENSC – A European neutron facility, Funds from the European Commission

The remarkably high number of guest scientists from member countries of the European Community have been stimulated by successfully applying for funds from the programs of the European Commission to support the transnational access to large scale research infrastructures. BENSC and users of BENSC are presently supported by 600 000 € per year. This funding under the 5th Framework Programme of the EU is effective for the support of external BENSC users until February 2004.

Human Potential Programme, Transnational Access to Research Infrastructures (IHP-ARI):

- Contract HPRI-CT 1999-00020 (2/2000-1/2003)
  (Total value: 1500 000 Euro)
- Contract HPRI-CT 2001-00138 (11/2001-2/2004)
  (Total value: 650 000 Euro)

An analysis of the distribution of the beam time allocation for EU users demonstrates that a high number of users does not only come from countries which do not have a national research neutron facility, such as Italy, Spain or Greece. Strong user contingents also come from the UK and France to take advantage of options which are not available at their national neutron facilities or at the leading European reactor neutron source, the ILL in Grenoble. The fulfilled training aspect of the EU support is proved by the age distribution of the visitors (fig. 2.)

Scientific results of the external users at BENSC

The scientific interim reports on most recent experimental results guarantee for a rapid dissemination of the results of external users of BENSC.

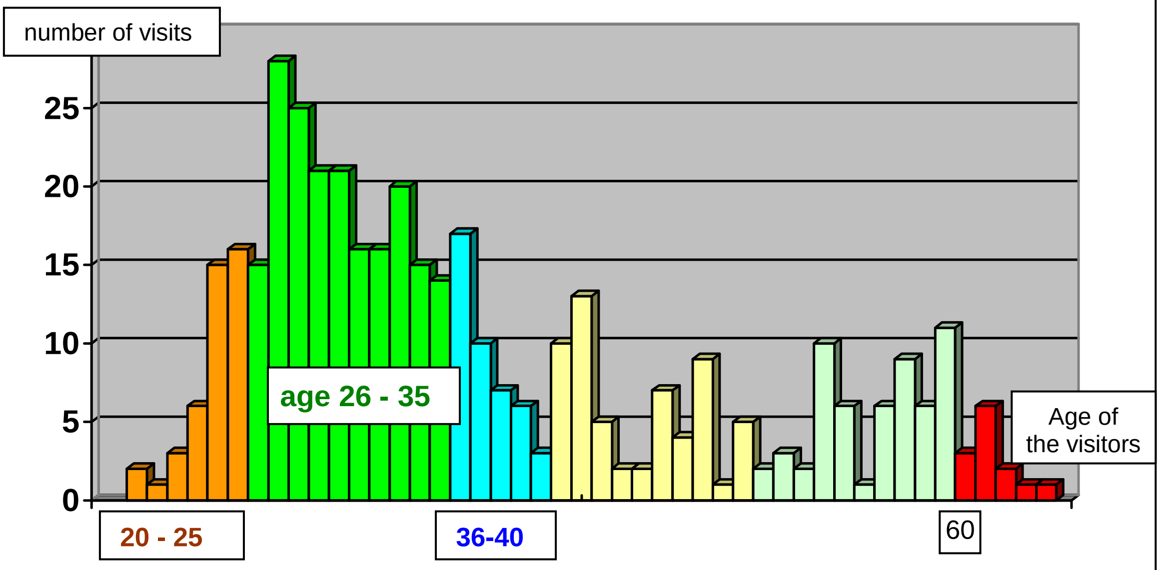

Fig. 2: *The majority of the EU grant supported external users are 24-36 years old*

These interim reports are published annually under the label of “BENSC EXPERIMENTAL REPORTS”, and the year 2002 Volume, HMI-B 590 (ISSN 0936-0891), is distributed to all users of BENSC in May 2002 as cd rom and/or in printed form. The reports for 2000 through 2002 are also available on the BENSC internet pages.

The year 2002 volume includes 250 reports of external and internal users, with 62 contributions on EU IHP-ARI supported projects. A rough split-up of the number of reports into the different fields of science is displayed in Fig.3.

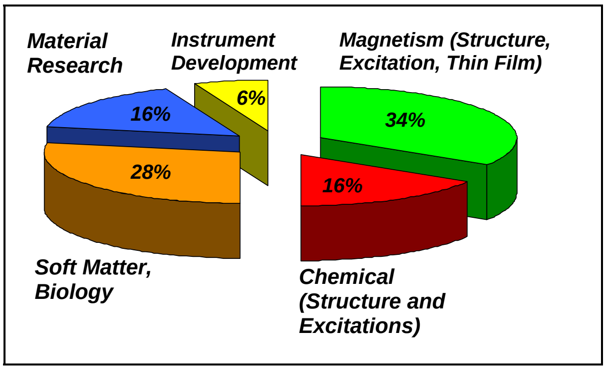

Fig.3: *Fractions of Experimental Reports in HMI-B 590 listed by field of science*

This rapid distribution of results is complemented by oral and poster contributions to national and international conferences.

Publication in internationally renowned peer reviewed journals normally follows the experiments with a delay of 1 to 2 years. Since as a rule at least one collaborating BENSC scientist is among the authors the year 2002 publications of external users are included in the publication lists of the departments SF1, SF2 or SF3. A complete compilation of the year 2002 publication lists for all BENSC users and BENSC staff members is included in the volume “BENSC EXPERIMENTAL REPORTS 2002”, HMI-B590, April 2003.

The majority of the BENSC publications has an external user as principal author, and a remarkably high fraction is published in high ranking journals:

Journal Impact Factor	total number of BENSC publications	BENSC publications @ external BENSC user is principal author
>4 - 30 e.g.: Nature, Phys. Rev. Letters, Biophys. J.,	**5**	**5**
>3 - 4 e.g.: Chem. Commun., Macromolecules, J. Phys. Chem. B, J. Chem. Phys., Phys. Rev. **B**;	**18**	**10**
>1,5 - 3 e.g.: Langmuir, Phys. Rev C, J. Appl. Cryst., Europhys. Lett	**18**	**12**
1,7 Appl. Phys. A	**89**	**62**
>0,9 - 1,5 e.g.: JMMM, Thin Solid Films, Nucl.Inst.Meth, J. Alloys Comp.,	**35**	**20**

Neutron spin echo technique for neutron reflectometry

A new method was developed to discriminate between specular and diffuse scattering in neutron reflectometry. This method, based on the neutron spin echo technique, allows the use of large beam divergence and simultaneously achieves good resolution. In addition to that large increase in intensity, the method opens up the possibility to measure the reflectivity curve of rough samples.

The essential conceptual point is that, at least for nonmagnetic samples, Larmor precession of a neutron's spin can be used to encode the difference between those components of the wave vectors of incident and reflected neutrons that are perpendicular to the reflecting sample. The fully polarized spin-echo signal is obtained only when these two components are equal, i.e. when specular reflection occurs. Neutrons that are diffusely reflected by the sample will, on average, contribute nothing to the echo polarization and hence can be distinguished from specularly reflected neutrons. The setup used on the neutron reflectometer V6 could achieve an angular resolution (i.e., the minimum angular deviation from the specular condition that can be detected) of about 1 mrad.

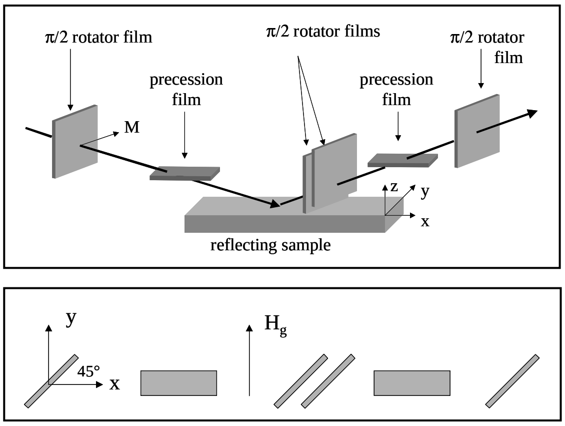

Fig. 1: Geometry of the NSE set-up. The upper part of the Figure is a three-dimensional rendering while the lower panel is a top view showing only the π/2 rotator films and the precession films. The neutron trajectory is indicated by bold lines in the upper part of the Figure. The magnetization, ***M****, in each of the π/2 rotator films is along the (1,1,0) direction. A uniform magnetic guide field of H_g ~ 20 Oe is applied in the y direction over the whole apparatus.*

The geometry of the apparatus as installed on V6 is shown in Fig. 1. The precession films as well as the π/2 rotator films are 30 µm thick permalloy films. The π/2 rotator films turn the neutron spin from the y into the x direction (or vice versa), whereas the neutrons accumulate typically about 440 radians of precession in the precession films.

With our apparatus arranged with all the films shown in Fig. 1, but without a reflecting sample, we obtained the polarization signal shown in Fig. 2 as a function of the tilt angle between the second precession film and the neutron beam.

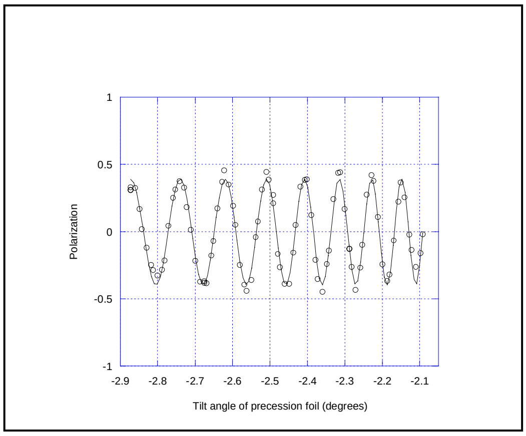

Fig. 2: *Measured polarization for the apparatus depicted in Fig.1 but without reflecting sample. the polarization is recorded as a function of the tilt angle between the second precession film and the neutron beam.*.

As can be seen from Fig. 2 the polarization is only about 0.4. That loss of echo amplitude may be due to several reasons. One origin is probably small angle scattering in the polycrystalline copper seed layer that is used during the electrochemical deposition of the permalloy films. Another origin may be the inhomogeneity of the permalloy film thickness leading to depolarization. Further experiments are planned to improve that situation.

We also performed measurements on a smooth Si wafer that led to the same results as those shown in Fig. 2 for the direct beam.

As a conclusion we have demonstrated successfully the neutron spin echo method in a reflectometry set-up. All components worked as intended and the apparatus itself is inexpensive and simple to construct. The method allows removing diffuse scattering from the measurement of specular reflectivity with an accuracy comparable to that achievable with milliradian collimation. In contrast to traditional methods of achieving this level of resolution, however, the spin echo method permits the use of relatively poorly collimated beams and hence can provide substantial gains in signal intensity.

[1] Jons, Rev. Sci. Instrum. **73**, 2948 (2002)

R. Pynn[1], M. R. Fitzsimmons[1], M. T. Rekveldt[2], J. Major[3], H. Fritzsche[4] D. Weller, E. C.[5]

1Los Alamos National Laboratory, USA, 2 Interfacultair Reactor Instituut, Delft, The Netherlands, 3 Max-Planck-Institut für Metallforschung, Stuttgart, Germany, 4 HMI, 5 Seagate Research, Pittsburgh, USA

Resolution Theory for Neutron Spin Echo Spectroscopy on Three-Axis Spectrometers

Much of the success of an inelastic neutron scattering experiment on a triple-axis spectrometer (TAS) depends on the knowledge of the resolution function. This information is also an essential prerequisite in planning and data analysis of high resolution experiments using a combination of three-axis and neutron (resonance) spin echo (N(R) SE) spectroscopy. Applying an analytical approach based on the Gaussian approximation of the triple-axis transmission function, we have derived a resolution theory for TAS + N(R)SE. The formalism is adapted to the general case of dispersive excitations with the precession field regions tilted relative to the incident and scattered beams. The results of the theory are applied in an experimental study of lifetimes of transverse acoustic phonons in Pb.

The theory allows the determination of a resolution function, i.e. the polarization as a function of spin-echo time. Intrinsic lifetimes can then be obtained by normalization of the experimental data with the calculated resolution function since a spin echo measurement is directly related to the intermediate scattering function.

When a planar dispersion and zero linewidth of the excitation are assumed, our approach includes instrumental effects resulting from the fact that without path integral corrections the Larmor phase depends on momentum variations in second order.

The approach does not take into account stray fields or field inhomogeneities as sources of signal depolarization since these quantities are difficult to describe analytically but can easily be determined experimentally in a direct beam experiment. An example of a calculated resolution function is shown in Fig.1.

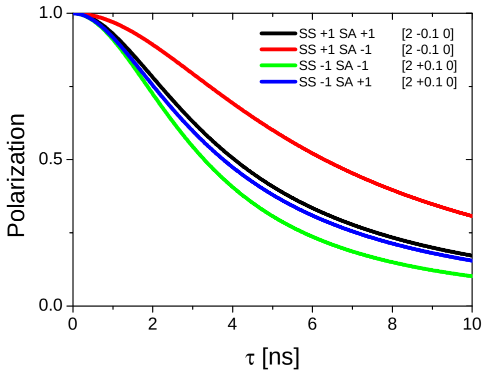

Fig.1: Instrumental resolution function for different TAS scattering senses; [2 0.1 0] TA phonon in Pb.

Parameters adopted in calculations of the TAS resolution apply to the cold TAS instrument V2 (FLEX), where measurements of Pb phonons were performed. The results of the calculations show that the depolarization is slightly dependent on the chosen TAS scattering senses, but it becomes significant only at large τ (current apparatus limits τ_{exp} < 500 ps). The purely instrumental resolution is negligible in a broad range of spin-echo times.

We have also extended the matrix formalism used to calculate TAS resolution properties to include variations in the Larmor phase. The real part of the resolution matrix is the TAS resolution matrix, while the imaginary part reflects the Larmor phase of the neutrons reaching the detector. Despite simplifications in the calculation of the resolution function, the matrix approach allows a graphical visualization of resolution volumes and phase distributions in wavevector-energy-space (see Fig.2). Furthermore, spatial effects e.g. curved monochromators, finite size of sample and beam optical elements can be included when the matrix formalism is used.

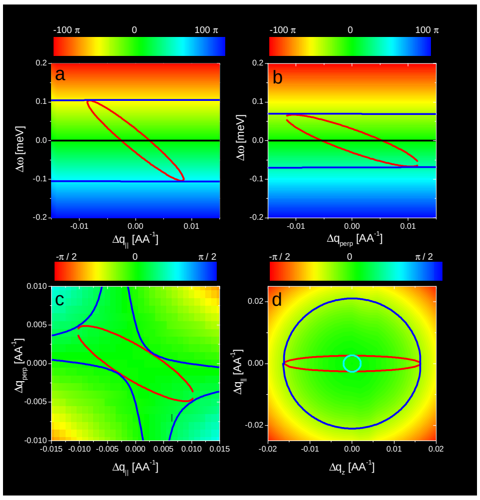

Fig. 2: Intersections of the TAS resolution ellipsoid (red lines) and surfaces of constant phase for fixed spin echo time with selected planes in (Q,ω)-space. Color indicates phase in radians.

Sample imperfections and the curvature of the dispersion surface may play important roles in lifetime measurements by leading to a signal depolarization distinct from intrinsic lifetimes. Sample mosaicity – important in transverse phonon measurements – and spread in lattice spacings – important in longitudinal phonon measurements – are included in our resolution calculations, where we assumed Gaussian distributions. Curvature of the four-dimensional dispersion surface in (Q,ω)-space is included via a second order expansion of the dispersion relation.

Furthermore, inaccuracies in the dispersion data – necessary for the setting of the tilt angles and the frequencies applied to the RF-flipper coils – may lead to instrumental misalignment and, in consequence, to an additional signal depolarization. This effect is built in explicitly in our method.

Our approach offers the opportunity to calculate resolution effects with N(R)SE-TAS instrumentation and use the results for detailed planning of experiments. Instrumental resolution can be separated from the signal. Hence, the approach can be used for data correction. This is of particular importance since in general an experimental calibration of the inelastic signal is not possible and the only clue to absolute linewidth determinations is the calculated resolution.

K. Habicht, R. Golub, T. Keller für Metallforschung Stuttgart)

Multi-spectral neutron beam extraction

Different neutron scattering experiments require different incoming neutron energies to become at all feasible or to be performed under optimal conditions. For this reason, neutron sources are equipped with so-called neutron moderators of different temperatures. Each moderator emits an approximately Maxwellian distribution of neutron energies corresponding to the temperature of the moderator. Cold moderators (or cold sources) typically consist of liquid hydrogen at about 30 K temperature and the emitted neutron spectrum peaks around 5 meV energy (or 0.4 nm neutron wavelength). Thermal moderators consisting of ambient water or Beryllium emit spectra centered around 40 meV energy (or 0.15 nm neutron wavelength). In general, neutron scattering experiments are best performed with the lowest incoming neutron energy possible. For example to observe the emission of an elementary excitation of 10 meV energy, the neutron energy has to be higher then 10 meV.

Neutron scattering instruments on reactor sources are classified by the temperature of the incoming neutron beam to hot, thermal and cold neutron machines. In many experiments part of the information to be obtained requires the use of one category and another part another one, and actually two experiments need to be made on two instruments. A new invention from HMI (in collaboration with Los Alamos National Laboratory, Patent applied for on 22.01.2002) revolutionizes the art to obtain neutron beams: it allows us to produce beams containing more than one spectrum, for example, a full intensity thermal and a full intensity cold neutron beam. It is based on the switching action of a supermirror evaporated on a neutron transparent substrate, e.g. Si wafers, which faces side-by-side neutron moderators of different temperatures (Fig. 1). At short neutron wavelength, the neutrons traverse the supermirror and the outgoing beam in the neutron guide sees the thermal moderator. At longer wavelength the supermirrors become nearly fully reflecting, and now the guide sees the cold moderator. The switching effect is well illustrated (Figure 2) by the transmission probabilities of neutrons coming one or the other moderator to emerge on the right hand side of the neutron guide in Figure 1. A particularly promising application of a neutron beam with this new multi-spectral nature is the study of magnetic samples: the determination of the atomic crystal structure requires neutrons in the 0.1 nm wavelength range, while 0.4 nm or longer wavelength neutrons offer the best or eventually only chance to detect Bragg peaks due to weak magnetic order.

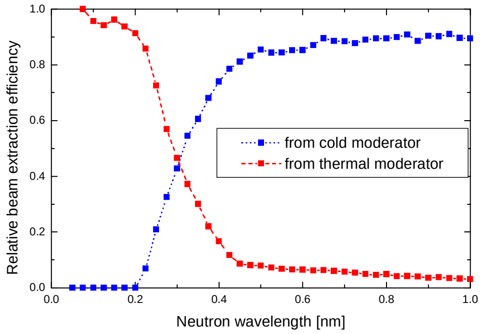

Fig. 2 *Transmission coefficient of the multi-spectral beam extraction system shown in Fig. 1 for neutrons emerging form the thermal (red) and cold (blue) moderators*

F. Mezei, M. Russina (Los Alamos National Laboratory)

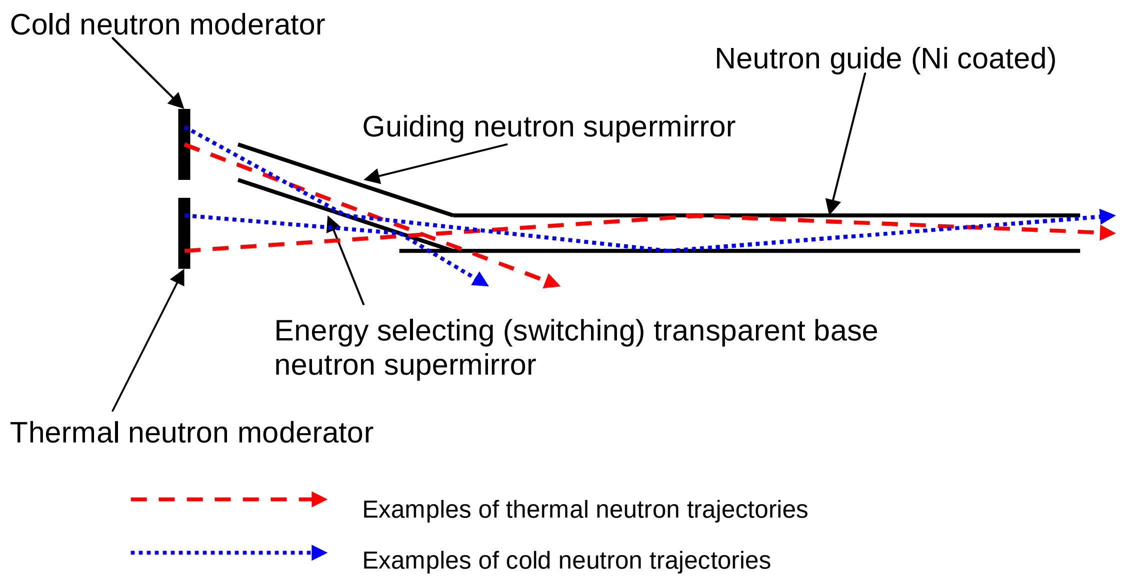

Fig.1. Example of realization of multi-spectral beam extraction

Interaction of enzymes with artificial interfaces

Whenever a protein solution is in contact with an artificial interface, e. g. the surface of a material, the interface will almost always be covered spontaneously by a layer of the protein molecules. This phenomenon is used in a wide field of applications, such as the development of biochips, the use of solid-phase immunoassays in medical diagnostics, and the separation and purification of proteins by chromatography. However, the adsorption of proteins may also have unfavourable consequences. For example, the formation of biofilms on contact lenses, mainly composed of lysozyme from the tear liquid, can cause eye infections and diseases (Fig. 1).

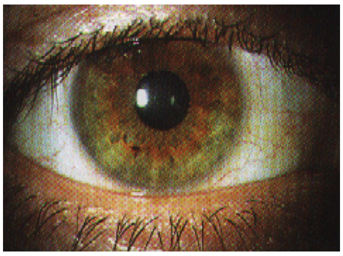

***Fig. 1** When using contact lenses, the enzyme lysozyme from the tear liquid will adsorb on the surface of the lenses and a biofilm is formed that can cause eye diseases.*

In order to control the amount of protein that is adsorbed at an interface, one has to understand the driving forces that lead to adsorption. In a thermodynamic view, these driving forces are characterized as being enthalpic or entropic. Enthalpic driving forces include attractive electrostatic interactions between the protein and the interface leading to a release of heat. On the other hand, an entropic driving force can result from conformational changes of the protein molecules to optimise surface contacts.

The enzyme staphylococcal nuclease (SNase) was used as model protein in our experiments. The biological function of SNase is the cleavage of DNA and RNA. The degree of adsorption of this protein on a negatively charged poly(styrene sulfonate) surface was studied under variation of the temperature and the pH-value of the protein solution. While a change of the pH-value will yield information about the role of electrostatic interactions, a temperature variation helps to estimate the relative weight of enthalpic and entropic contributions to the driving forces for adsorption.

Neutron reflectometry was used to analyse the structure of the poly(styrene sulfonate)/aqueous interface with adsorbed SNase molecules. Compared to other spectroscopic and reflectometric methods, this technique is most powerful to determine the structure of solid/aqueous interfaces, because neutrons can penetrate condensed matter over macroscopic distances, and their wavelength is relatively short to resolve structural details. In a neutron reflectometric experiment, a neutron beam is simply directed to the interface under different angles of incidence. The reflected beam is detected and normalised to the incident intensity.

From the analysis of the obtained neutron reflectivity curves (Fig. 2), it has been found that at pH = 7.1 the degree of SNase adsorption is increasing with increasing temperature from 2.3 mg/m^2 at 23 °C to 4.1 mg/m^2 at 43 °C. This temperature effect suggests that although strong attractive electrostatic interactions exist between the protein and the surface, the degree of adsorption is not dominated by this enthalpic driving force but by processes which increase the entropy of the system. A similar temperature effect has been found at a lower pH-value of 4.5, where the protein molecules carry a higher net positive charge. Here, the surface coverage is increasing from 1.1 mg/m^2 at 23 °C to 1.9 mg/m^2 at 43 °C. These lower amounts of adsorbed protein clearly demonstrate that the amount of adsorbed SNase on a polyelectrolyte surface is affected more strongly by repulsive electrostatic interactions between the protein molecules than by the attractive electrostatic interactions between the protein and the surface (Fig. 3). Similar observations have also been made in a neutron reflectivity study of lysozyme adsorbed at the silica/water interface [1]. Thus, it appears that attractive Coulomb interactions between a protein and an interface play a minor role for the degree of protein adsorption at interfaces.

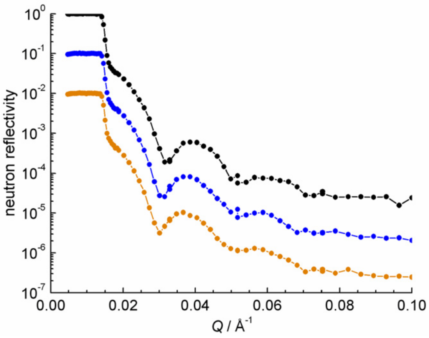

***Fig. 2** Neutron reflectivity curves of a silica/water interface that is coated with a negatively charged polyelectrolyte. The black curve refers to this interface without adsorbed protein, while the other curves have been measured when staphylococcal nuclease was adsorbed (blue: 23 °C, orange: 43 °C). The data show that the degree of protein adsorption is increasing when the temperature is raised.*

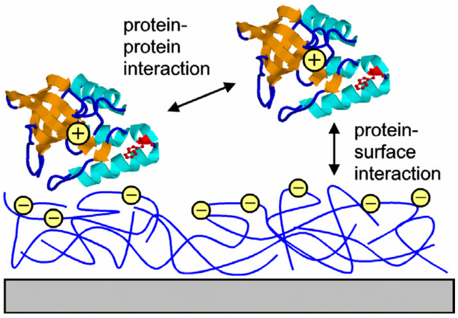

***Fig. 3** Positively charged staphylococcal nuclease was adsorbed on a negatively charged polyelectrolyte surface. The degree of adsorption largely depends on protein-protein interactions, whereas attractive electrostatic interactions between the protein and the surface play a minor role.*

[1] G. Jackler, R. Steitz, C. Czeslik, *Langmuir* **18** (2002) 6565-6570.

C. Czeslik[1], G. Jackler[1], C. Royer[2], R. Steitz[3]
1 Univ. Dortmund, 2 Univ. Montpellier (F), 3 HMI

Critical adsorption in binary liquid mixtures by neutron reflectivity: Evidence for two-phase adsorption

Although commonly believed not to mix, equal volumes of water and oil when shaken together yield equal volumes of oily water and watery oil. These liquid phases can be made to mix fully in two ways. In the simpler, adding surfactant causes the liquids to appear miscible by forming a microemulsion, a dispersion of discrete microscopic oil or water-rich regions stabilized by surfactant adsorption at the vast interface between them.

The alternative is to heat the two coexisting liquid phases, so increasing their mutual solubility, until free mixing occurs at an upper critical point (UCP), for water + hydrocarbons usually well above 200°C. UCPs are not uncommon since their energetic origin, the slight relative weakness in the energy between unlike pairs, is found in most molecules,. Accordingly, most mixtures, in the absence of freezing, would liquid-liquid phase separate at low enough temperatures.

By contrast, some pairs of partially miscible liquids mix only when *cooled* to a lower critical point (LCP). This behaviour is entropically determined under hard-to-satisfy conditions. LCPs are thus rarer than UCPs and arise chiefly in aqueous or polymer solutions. A third even rarer mixture class exhibits both an UCP and an LCP; some with the LCP at a lower temperature than the UCP and others *vice versa.*

Despite this complexity, near-critical behaviour, although unusual and, at one time, unexpected, is the same in detail for all kinds of liquid mixture and identical to that of other critical systems, that range from molecules, as here, through magnetic systems to very unusual systems involving quarks.

The details, often involving divergences in physical properties, are astonishingly independent of the nature of the interparticle forces but heavily dependent on the dimensionality of the system. Invariably, critical behaviour flows from the divergence at the critical point of the appropriate correlation length, the distance at which the constituent particles enjoy cooperative behaviour.

Criticality behaviour was first noted by Andrews in pure carbon dioxide and then partially explained by van der Waals over a century ago. The importance of the field has been recognized since by the award of several Nobel prizes, most recently to Wilson in 1982 for his *theory for critical phenomena in connection with phase transitions*.

Since criticality reflects the coexistence between phases, unsurprisingly some of the most striking phenomena are interfacial. Theory has predicted, and subsequent observation and measurement has confirmed, that in the freely mixing region near the critical point, the adsorption of one component at a noncritical interface is very strong and at the CP essentially diverges to infinity.

At a CP, the divergent adsorption of one *component* transforms into a layer of one coexisting *phase* said to *wet* one of the spectator phases – either an adjacent immiscible fluid phase or one of the container walls as illustrated below for a mixture of a primitive surfactant 2-butoxyethanol + D_2O against a silicon wall. Here successive stages reflect increasing temperature from below to above the wetting region.

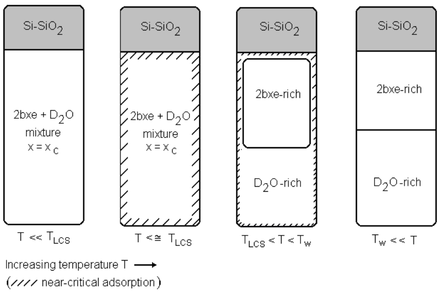

The macroscopic issues concerning wetting layers include the identities of the wetting and wetted phases and the extent of the wetting region. Deeper microscopic questions concern the structure of the layer: how thick is it, is it homogeneous, and how does the thickness fall off away from the critical point?

Neutron reflectivity offers an ideal route to resolving such matters. Recent work on the mixture above has cast light on the structure of the layers.[1] More recent work has revealed two fresh aspects of wetting.

The first is that the kinetics of formation of the wetting layer is sufficiently rapid that a wetting phase can reform spontaneously without stirring in a temperature-cycled mixture provided the sample is thin enough and the wetted area large enough thus removing a previous huge experimental uncertainty.

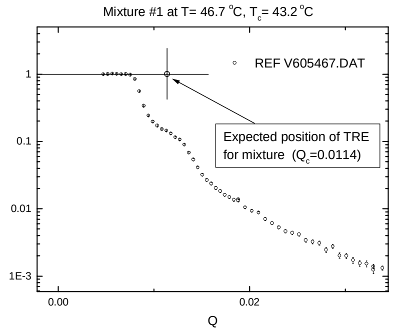

R-Q profile for CD_3OD + c-C_6H_{12} against Si/SiO_2

The second, and more theoretically challenging, finding was the repeated appearance in the reflectivity profile of *two* critical edges, suggesting strongly that surface inhomogeneities in the solid spectator phase can yield different kinds of wettable region. These may be either discrete islands of one structure embedded in a continuous sea of the other or topographically connected bicontinuous regions. These observations, if real, mirror microemulsion structural forms and call for confirming study – not least of the uniformity of chemically coupled surfaces.

J. R. Howse[1], E. Manzanares-Papayanopoulos[1], I. A. McLure[1], J. Bowers[2], R. Steitz[2, 3], and G. H. Findenegg[2]

1 University of Sheffield, UK, 2 TU Berlin, 3 HMI

Published as *J. Chem. Phys.*, **116**, 7177-7188, 2002

Field-induced condensation of magnons in an axial Haldane-gap antiferromagnet

One-dimensional (1D) integer-spin antiferromagnets (AFs) are famous for having a disordered “spin liquid” ground state and an energy gap in the excitation spectrum. Elementary excitations are a triplet of massive (gapped) long-lived “magnons". An external magnetic field modifies the magnon energies by virtue of Zeeman effect. At a certain critical field H_c the gap in one of the branches approaches zero. The result is a *condensation of magnons* and the emergence of a qualitatively new ground state. *What* this new ground state actually is, depends on the symmetry of the problem. In the *axially asymmetric* (AA) case (*e. g.*, when the field is at an angle to a magnetic anisotropy axis) the scenario is Ising-like. According to several theoretical models and to recent experimental work [1-3], the AA high-field state is characterized by true AF long-range order at low temperatures, and sports a triplet of massive breather-type excitations [3]. At elevated temperatures the system becomes a gas of quasiclassical magnetic solitons [2].

Theory predicts that the *axially symmetric* (AS) case (external field applied parallel to the anisotropy axis) is totally different. At high fields one expects a gapless “Luttinger spin liquid" state with quasi-long-range order and a diffuse continuum of particle/hole excitations (no sharp magnons). The purpose of the present experiment was to search for such unique behaviour in the Haldane-gap material NDMAP. Due to a combination of factors, NDMAP is currently the only compound in which the AS high-field state can be investigated by means of neutron scattering. The measurements were performed on the V2-FLEX 3-axis spectrometer. A horizontal field magnet was used to apply a magnetic field along the spin-chain axis *c*, which is also the axis of magnetic anisotropy. The data were collected on a fully deuterated 1.5 single crystal sample at T=30 mK and in field as high as 6 T.

Figure 1 shows typical constant-q scans taken at the 1D AF zone-center at different values of applied field. As expected, the gap in the lower mode decreases with increasing field and closes at $H=H_C\sim4$ T. A totally unexpected result is that at $H>H_c$ the gap in the lower mode *re-opens*, just as it does in the AA geometry [3]. Moreover, an analysis of several const-E scans, performed paying special attention to instrument resolution effects, reveal no evidence of excitation continuum. The scattering observed in the present AS experiment can instead be attributed to long-lived magnons with a simple relativistic dispersion, just as in the AA case.

What *is* different in the current AS setting for NDMAP is that the gap increases *sublinearly* at $H>H_c$ and seems to be close to saturation at H~6 T (see graph in the x-y plane of Fig. 1). In previous AA experiments a *linear* behavior was seen in fields as high as 11 T. Such variance suggests that the re-opening of the gap at $H>H_c$ in the two experiments represents totally different underlying physics.

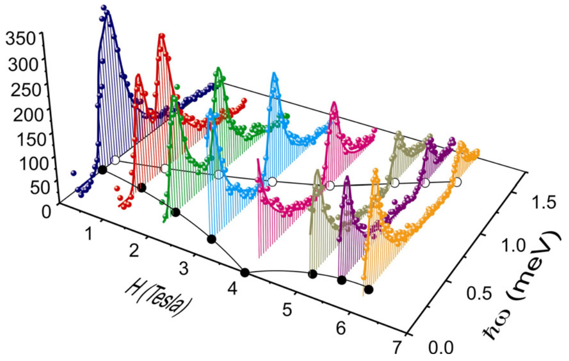

***Fig. 1**: Constant-q scans measured in NDMAP at T=30 mK for different values of magnetic field applied along the crystallographic c axis (color symbols). The data can be described by a single-mode cross section function if resolution effects are properly taken into account (color lines). The resulting field dependence of the gap energies are shown in the x-y plane.*

Several theoretical explanations are currently being considered, but the most likely one attributes the gap in the AS geometry to weak but relevant inter-chain interactions. Since isolated AS Haldane spin chains at $H>H_c$ are *critical*, inter-chain interactions should have the same effect as for critical S=1/2 chains. In particular, inter-chain coupling, no matter how weak, induces long-range order. The latter binds free spinons into sharp spin wave-like breather excitations, and induces a gap in the spectrum. A similar mechanism may be responsible for the unexpected behavior observed in NDMAP in the present study.

Work at ORNL and BNL was carried out under DOE Contracts No. DE-AC05-00OR22725 and DE-AC02-98CH10886, respectively. Work at JHU was supported by the NSF through DMR-0074571. Work at RIKEN was supported in part by a Grant-in-Aid for Scientific Research from the Japan Society for the Promotion of Science.

[1] Z. Honda, H. Asakawa, and K. Katsumata, Phys. Rev. Lett. **81**, 2566 (1998); Y. Chen, Z. Honda, A. Zheludev, C. Broholm, K. Katsumata, and S. M. Shapiro, Phys. Rev. Lett. **86**, 1618 (2001).
[2] A. Zheludev, Y. C. Z. Honda, C. Broholm, and K. Katsumata, Phys. Rev. Lett. **88**, 077206 (2002).
[3] A. Zheludev, Z. Honda, C. L. Broholm, K. Katsumata, S. M. Shapiro, A. Kolezhuk, S. Park, and Y. Qui, cond-mat/0301424.

A. Zheludev(1), S. M. Shapiro(2), Z. Honda(3), K. Katsumata(4), C. L. Broholm(5), P. Vorderwisch(6)

(1) Oak Ridge National Laboratory, USA. (2) Brookhaven National Laboratory, USA. (3) Saitama University, Japan. (4) The RIKEN Harima Institute, Japan. (5) Johns Hopkins University, USA; NIST Center for Neutron Research, USA. (6) HMI Berlin, Germany

Bose-Einstein Condensation in dimer quantum spin systems

Quantum phase transitions are radical events in solid-state physics. The ground-state of a system changes at a critical value of an external parameter like pressure, composition or external magnetic field. This happens at the lowest temperature “T= 0 K” in contrast to conventional phase transitions like for example the condensation of water vapour. The Bose-Einstein condensation is another phenomenon, which has fascinated physicists during the last decades. Gases of alkali atoms were cooled down to very low temperatures, where the particles condense, lose their individuality and behave as a single entity.

A combination of both effects could recently be observed in the magnetic insulator $TlCuCl_3$. A new type of magnetic ordering, which can be explained by Bose-Einstein condensation of magnetic quasi-particles, appears above the quantum critical point $H_c \approx 6$ T of an external magnetic field. This novel field-induced ordered phase at $H>H_c$ is identified by its excitation spectrum.

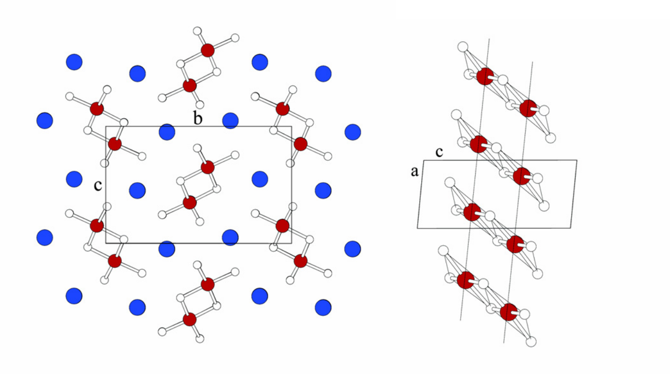

Fig. 1 *The nuclear structure of TlCuCl3 consists of characteristic pairs of copper (red) atoms, which are stacked along the a direction. The resulting “ladders” show two different orientations and are separated by the Tl atoms (blue). The magnetic exchange couplings are mediated by the Cl atoms (white).*

The characteristic features of the $TlCuCl_3$ crystal structure are the pairs of Cu^{2+} ions, which are separated by the Tl atoms (Fig. 1). A dominant antiferromagnetic exchange between the two S=1/2 spin moments inside these dimers leads to a non-magnetic singlet ground-state with total spin S=0. The excited states are threefold degenerate S=1 triplets, which can propagate along all directions due to a three-dimensional network of interdimer exchange couplings. A spin energy gap $\Delta \approx 0.7$ meV separates the ground-state from the excited triplet waves.

Inelastic neutron scattering on $TlCuCl_3$ single crystals has been used to investigate the evolution of the ground-state and the excitation spectrum as a function of the external magnetic field. The excellent possibilities at HMI to apply high magnetic field in combination with powerful neutron scattering instruments allowed collecting high-quality data in the parameter range of interest.

The triplet waves above the energy gap show *quadratic* dispersion in zero field (Fig. 2, upper panel). The application of an external magnetic field splits the excited triplet into three components with $S_z=+1$, 0, -1. The energy of the triplet $S_z=+1$ component intersects the ground-state singlet at a critical magnetic field H_c and long-range magnetic order occurs. Thus H_c is a quantum critical point separating a gapped spin-liquid state ($H<H_c$) from a field-induced magnetically ordered state ($H>H_c$). The triplet components with $S_z=+1$ can be regarded as diluted bosons, thus Bose-Einstein condensation occurs in this dimer compound at the quantum critical point H_c. However, these considerations do not stem from a diluted gas cooled below the de Broglie temperature, but from dimer states split at high magnetic fields. The magnetic excitation spectrum associated with the condensate has been theoretically predicted to be a gapless and linear Goldstone mode. The results at fixed T=1.5 K and H=14 T clearly indicated the coexistence of two higher-lying modes and such a low-lying mode (Fig. 2, lower panel). The higher-lying modes are *gapped* and retain a *quadratic* dispersion around the Bragg point, whereas the low-lying mode is *gapless* and *linear*. These experimental conclusions are in agreement with a comprehensive theoretical study of the field-induced ordered phase in $TlCuCl_3$. They do not only confirm the model description of the magnetic quantum phase transition realized in $TlCuCl_3$, but also provide a general reference for the excitation spectrum of quantum spin liquids in the field-induced ordered phase.

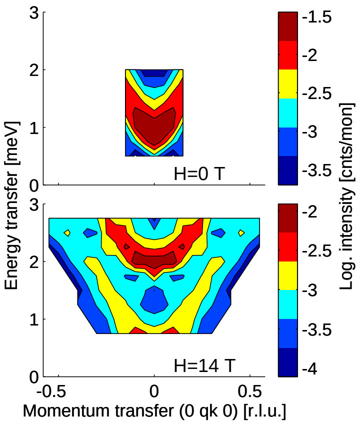

Fig. 2 *The excitation spectrum in $TlCuCl_3$ changes drastically at the quantum critical point $H_c \approx 6$ T (measured on the FLEX three-axis spectrometer, HMI Berlin). Upper panel: quadratic dispersion of the triplet excitations in zero field, H=0 T. Lower panel: gapless and linear spin wave excitations coexist with gapped and quadratic modes above the quantum critical point H=14 T>H_c. The second gapped mode at higher energy is not shown because of weak intensity.*

[1] Ch. Rüegg, N. Cavadini, A. Furrer, H.-U. Güdel, K. Krämer, H. Mutka, A. Wildes, K. Habicht, P. Vorderwisch. *Nature* **423** (2003) 62-65.

N. Cavadini(1), A. Furrer(1), H.-U. Güdel(2), K. Krämer(2), H. Mutka(3), A. Wildes(3), K. Habicht(4), P. Vorderwisch(4)
(1) ETH Zürich & Paul Scherrer Institut (CH), (2) Univ. Bern (CH), (3) Institut Laue-Langevin (F), (4) HMI

Investigation of the microstructure of ferrofluids using SANS

Ferrofluids, stable suspensions of magnetic particles dispersed in a carrier liquid, combine both fluidic and magnetic properties. Due to the possibility to change their properties, especially their viscosity by means of magnetic fields, they are a challenging subject for fundamental research as well as technical and medical application. Experiments performed with different ferrofluids indicate that a magnetic field applied to a sheared sample induces an increase in viscosity with increasing magnetic field strength (the magnetoviscous effect). The magnitude of the effect depends on the preparation methods, composition and especially upon the concentration of large particles contained in the ferrofluids. The main topic of our project is the observation of chain like agglomerates or other structures formed in ferrofluids, which are assumed to be responsible for the reversible changes of the viscosity.

For the investigations of the microstructural changes of ferrofluids under different conditions of applied magnetic field and shear rate, we use a special designed rheometer that allows SANS measurements in the same experimental conditions as used for rheological studies.

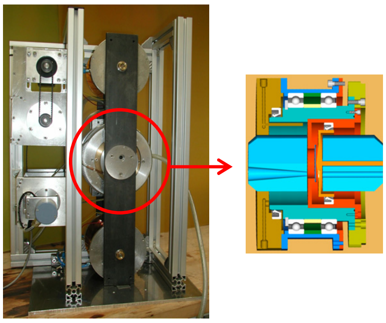

Fig.1 *Schematic sketch of the arrangement for SANS*

Two commercial ferrofluids – Ferrotec APG513A from two different production lines – and an experimental ferrofluid – TOA (UT Timisoara) – were investigated, all three containing magnetite particles. The samples have a different content of large particles and thus different magnitudes of the magnetoviscous effect.

The experiments were carried out with magnetic fields ranging from 0 - 160 kA/m, parallel to the neutron beam. As a first step for the data evaluation we have considered the high shear situation (shear rate $\dot{\gamma} = 200\ \mathrm{s}^{-1}$), i.e. the single particle situation as a reference. To eliminate the contribution of the surfactant and of the carrier liquid to the scattering, this reference scattering pattern has been subtracted from the scattering patterns obtained for different shear rates varied within the range 0 - 200 s^{-1}. The resulting scattering depends on the coupling between magnetic field strength and shear rate, which influences the lengths of the chains and their orientation (the nuclear scattering), as well as the magnetic component of the scattering pattern due to its dependency on the angle between the magnetization and the scattering vector, whereas the direction of the magnetization is determined by the shear rate (*Fig.2)*.

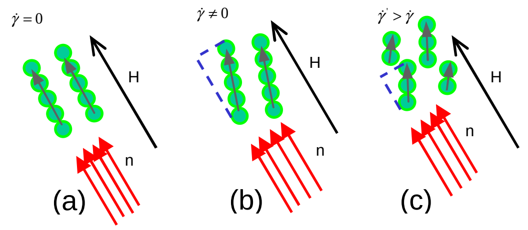

Fig.2 *Chain-like structure formation in ferrofluids: a. aligned with the magnetic field. b. An applied shear diverts the chains from the initial direction c. Breakage of the chains with increasing shear rate*

The difference patterns obtained for the fluid with high magnetoviscous effect (APG513A_1) indicate a clear dependence of the scattered intensity on the shear rate and the magnetic field strength (*Fig.3*).

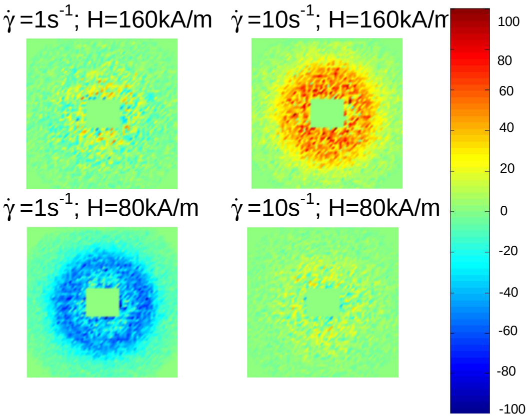

Fig.3 *Scattering patterns for APG 513A_1*

In the case of the fluids with low magnetoviscous effects (TOA, APG513A_2) only a variation with magnetic field strength can be observed (*Fig. 4*).

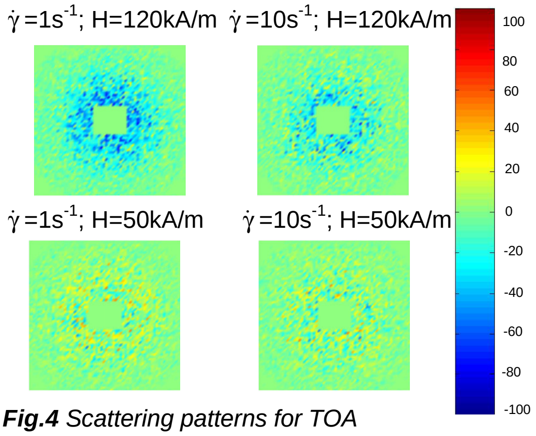

Fig.4 *Scattering patterns for TOA*

To connect the experimental results with the rheological behaviour of ferrofluids, the development of a simulation of SANS patterns, using microstructural information from numerical simulations, is planned.

For an introduction to SANS q.v. p. 39

S. Odenbach[1], J. Hilljegerdes[1], L. Pop[1], A. Wiedenmann[2], A. Hoell[2]
(1) ZARM, Uni Bremen, (2) HMI

ISL Operations and Developments

The Ion Beam Laboratory ISL offers ion beams from various accelerators and accelerator combinations with energies ranging from some tens of eV to several hundred MeV dedicated to the application of ion beam techniques. Internal and outside users study the basics of the interaction of ions with solids. They modify and analyse materials with ion beams and they perform radiotherapy of eye tumours with fast protons in a joint venture with university clinics. Users have at their disposal 15 different irradiation areas equipped with specific instrumentation.

Any user has access to the ISL via a programme advisory committee, which meets annually, and decides on the applications for beam-time solely on the basis of the proposals' scientific merit. 27 different projects involving more than 70 scientists received beam time in 2002. In total, some 50 projects are active at ISL. At its annual meeting the programme advisory committee accepted 15 proposals which were either new or addenda of running experiments. The committee acknowledged the general high scientific standards of the proposals.

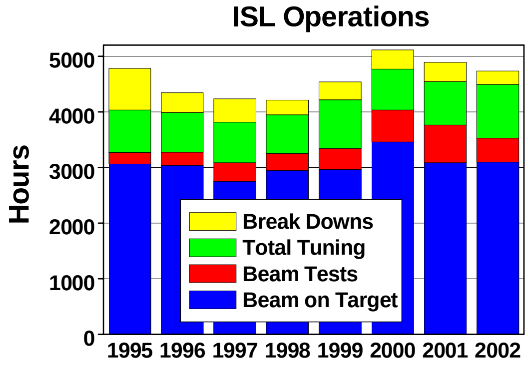

***Fig. 1**: ISL Operations up to 2002 – Again, ISL delivered the annual goal of 3000 h beam time on target. The low down time due to break-downs reflects the high reliability of the facility.*

As seen in Fig. 1 ISL confirmed its high reliability as a user facility. The annual goal of 3000 hours of beam on target had been achieved again. The total break-down time was again below 10%. With these figures, all users received their scheduled beam-time since practically all break-downs could be fixed within a short period of time. Despite our continuing efforts, the total tuning time has not been reduced. This is due to the fact that higher specifications of the beam parameters, such as ion species, beam intensities and beam stabilities have been set by the users. The statistics of the use of ISL's ion-beams (see Fig. 2) reflect very clearly the primary goals of the scientific programme. The medical part, essentially the radiotherapy of eye tumours with fast protons, stays constant with 10 therapy blocks with 5 days each per year.

In the beam time statistics the special funding which has been received for the studies of ion tracks in solids shows up in the substantial increase of the share of beam–time scheduled for ion solid interaction and materials modification. This was boosted by the offer of intense Au-ion beams (see below).

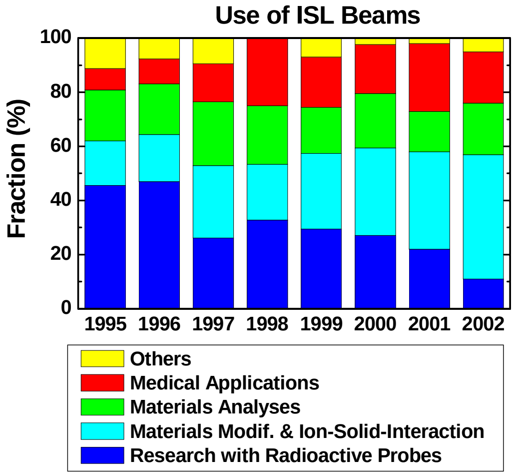

***Fig. 2**: Share of the different activities using ISL ion beams – The modification of materials with fast ions gained importance. The material analyses part is back to the year 2000 level. One has to keep in mind that in 2000 about 50% of the analytical part used low energy beams (^{15}N) compared to less than 10% in 2002.*

The share of materials analyses has come back to the year 2000 level. This means a further increase of fast ion use in materials analyses, heavy ions for ERDA and protons for high energy PIXE, since currently only a small part (<10%) of the analytical activities has been performed with low energy ions, preferentially ^{15}N, compared to about 50% in year 2000. As shown in other contributions to this report and the ISL Annual Report, most of the ERDA analyses contribute to the characterisation of thin layers of the HMI's solar energy programme.

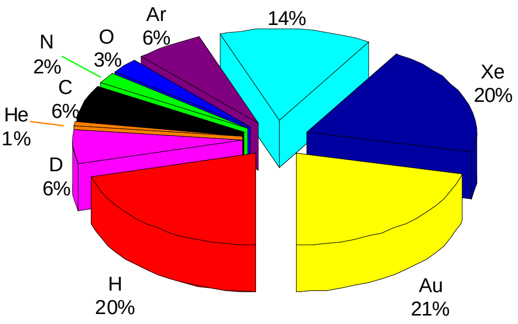

***Fig. 3:** Fast ion beams used at ISL in 2002 – The spectrum of ion beams produced at ISL reflects the main issues of the scientific programme. The lightest (protons) and the heaviest (Au) beams are the mostly used ones.*

The tendency of the scientific programme can also be observed when looking at the ion species produced. There is a clear trend towards the lightest and the heaviest ions. Au-ion beams, offered at ISL for the first time in 2001, has become the most frequently used beam in 2002 (see Fig. 3). Though tuning times are still rather long, very stable beams have been delivered over a long period of time. Further improvements can be expected.

The constitution of the user community at ISL stayed relatively constant. Nevertheless, it should be mentioned that the universities increased their share from 29% in 2001 to 34% in 2002. This increase is due to the trend in the scientific programme towards ion beam modification of materials.

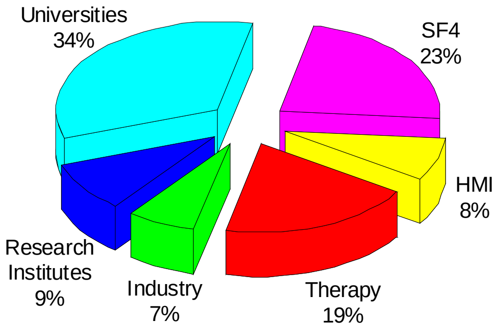

Fig. 4: *Origin of ISL Users – The universities' share underwent the biggest change compared to 2001 in rising from 29% in 2001 to 34% in 2003. This is due to their very active involvement in the materials modification scientific programme.*

Finally, as demonstrated in Fig. 5, ISL has continuously attracted a larger number of external users after its foundation in 1994. The statistics starting 1995, the first year when the nuclear physics programme practically came to an end, show that the ratio of internal to external users has practically been reversed.

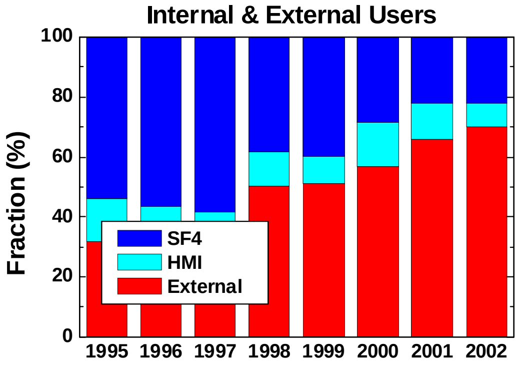

Fig. 5: *User facility ISL – Starting 1994 ISL has attracted a growing number of users. Thus, the ratio of internal to external users has been reversed within the last 8 years.*

Most developments in 2002 improved the reliability of the facility in general. The exchange of all magnet power supplies of the injection beam lines has been completed. On the high voltage terminal of the Van-de-Graaff injector the last two power supplies were switched to regulated ones. Another improvement at the ion sources was the replacement of all parts which could be hit by the beam by titanium which greatly reduced the sputtered material. Substantial progress in ion source tuning led to new beams with higher energies and higher intensities. Higher intensities have also been made possible by the installation and commissioning of the beam suppressor in front of the RFQ-injector which kicks out particles of the injected beam which appear outside the acceptance phase width of the RF-period. The continuing renovation and development of the control system, in particular the new monitoring tools, have improved the tuning and quality of the beams.

The installation of three new target stations has nearly been completed. By the middle of next year, the area equipped with the X-ray diffractometer, the one equipped with a high power laser to ionise ion beam desorbed particle and the universal irradiation area will be fully installed and operational.

Scientists: H. Homeyer, P. Arndt, W. Busse,
A. Denker, W. Pelzer, C. Rethfeldt, J. Röhrich
Operators: J. Bundesmann, R. Grünke,
G. Heidenreich, H. Lucht, E. Seidel, H. Stapel

Injector Developments at ISL

The ISL as a modern facility for the investigation of condensed matter with ion beams runs a large complex of devices for production, transport, acceleration and application of ions (see fig. 1).

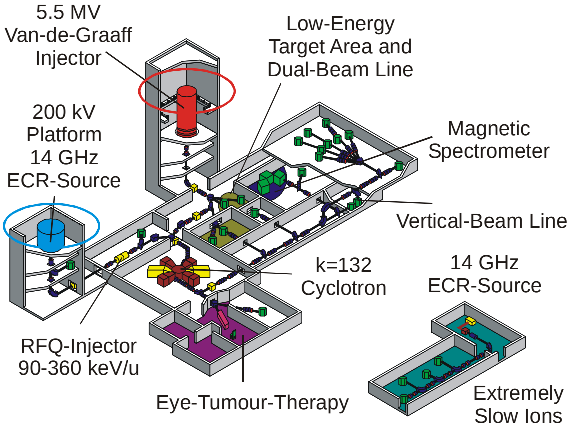

Fig. 1: *View of the ISL facility. Encircled are the areas of ion source development: the high voltage platform of the Van-de-Graaff accelerator and the 200 kV injector platform for the RFQ structure.*

In ion source development, it is always a major task to improve and to enhance the possibilities for scientific research and applications. Some milestones have been passed during the last year. They concern new ion species, ion beam stability and reliability. In particular, the production of high energetic Au beams was a great success from a scientific as well as of a technical view. Significant progress has been achieved in:

i. the reduction of wear processes at the Van-de-Graaff high voltage terminal due to mechanical and electrical refinements,

ii. oven techniques and tuning procedures for the ECRIS Supernanogan at the 200 kV high-voltage platform, allowing long term operation of highly charged Au beams and extremely stable high intensity Kr beams, and

iii. the installation of the additional 150 kV high-voltage platform for the RFQ injector.

i. Van-de-Graaff Terminal

Sputtering from stainless steel parts of the 5 GHz BECRIS extraction elements and the Wienfilter during normal operations led to various follow-up failures. The replacement of all stainless steel parts by titanium has significantly reduced the damage. The tuning, the reproducibility, and the stability of the injected beam has been improved by the switch-over from non-regulated to regulated power supplies which has been completed.

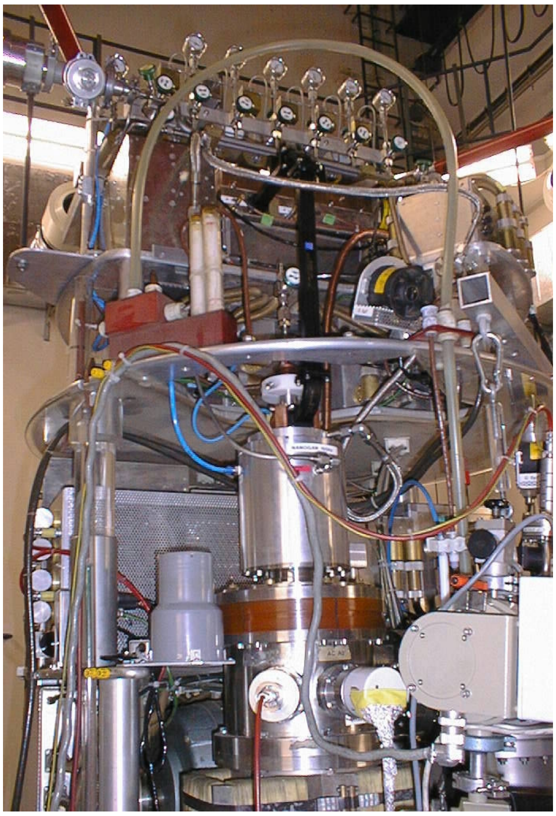

Fig. 2: *View of the Van-de-Graaff terminal with the 10 GHz Nanogan right in the middle.*

The changeover to a more powerful new source, a 10 GHz Nanogan from Pantechnik with a modified cooling system, has been promoted. This source will operate with a 50 W solid state RF-transmitter. A first test with the source installed on the terminal (see fig. 2) yielded the expected excellent results. Due to the modular design of the installation, the change from BECRIS to the Nanogan and back takes only two days. For Ar^{8+} ions 600 enA of beam current were measured after acceleration and analysis, which is a factor of 6 higher than our best results with the BECRIS. However, before the final changeover some long term stability tests of the Nanogan have to be performed in a longer shut down period.

ii. 200 kV High-Voltage Platform

The development of stable, intense and energetic Au ion beams has been continued in response to the increasing demand by various user groups. As seen in the ISL statistics of this report [1], Au ion beams have become the most frequently produced beams. Instead of the commercially available micro-oven, we use now a self-assembled and slightly revised model with higher mechanical stability and better electrical contact.

Tuning the 14.5 GHz permanent magnet ECRIS for high current and highly charged Au ions is still rather tedious and requires a lot of experience and patience. The tuning procedure has been improved by monitoring the short-term current fluctuations with an oscilloscope and a new LabVIEW™ tool (see “Beam Attenuation and Stability Monitoring” in the ISL’s annual report 2002) in addition to the total intensity. A result of careful tuning for high charge states with high RF-power of 500 W is depicted in fig. 3. About 4 μA of charge 30+ are analyzed. With this charge state, Au ion beams up to final energies of 600 MeV can be produced.

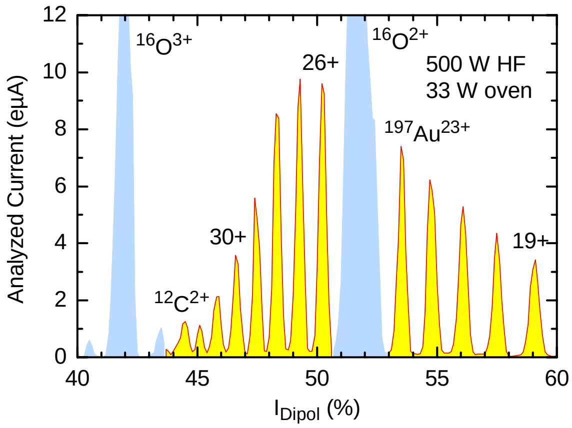

Fig. 3: *Au spectrum from the Supernanogan equipped with the standard evaporation micro oven and tuned for the charge state 30+ for a final Au energy of 600 MeV.*

With a total transmission from the source to the target between 10 and 20%, some 10 pnA for 600 MeV Au ion beams have been delivered to the target.

iii. New 150 kV High-Voltage Platform

With the tuning of the source with ions from solid material still being tedious and time consuming, an alternative injector platform should ease operations. Thus, a second platform with a Supernanogan is being installed. The design work was finished by the end of 2001. In the year 2002, most parts have been ordered. The utilities such as electricity, air conditioning, cooling, and safety doors have been installed at the foreseen site. In particular, the 1 m diameter hole for the path from the source to the existing injection beam line was sawed through a 1 m thick concrete wall (see fig. 4). Last but not least, the positioning and alignment markers for the components were prepared.

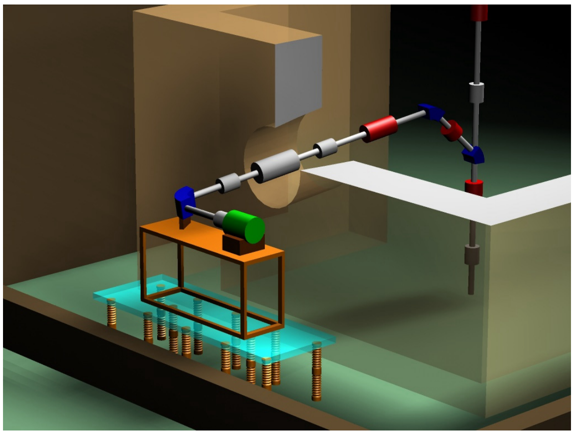

Fig. 4: *Sketch of the new HV-platform Due to our limited space, a tricky layout was designed. The new beam line will meet the vertical part of the old one (in the background right) leading to the RFQ.*

The installation work of the ion source test bench has nearly been completed. First tests will include the check of the performance of the new modified extraction system for the old Supernanogan and the development of new ion beams.

Outlook

To tap the full potential of the RFQ injector of 6 MeV/u for all masses of the periodic table, the ions need a charge to mass ratio of 1/4.7. With the existing ion sources at ISL this ratio can be produced for ions from gaseous compounds up to mass 130 (Xe) with sufficiently high currents. The necessary charge states 40+ for Au ions or 50+ for U are far beyond the current scope. Thus, ISL joins the efforts for ion source developments involving stronger confinements, higher RF-frequencies and higher RF-power. In co-operation with the ion source group of CEA Grenoble under the management of A. Girard design studies have been started. The aim of the joint venture is the layout of an appropriate source with superconducting magnets taking into account the severe boundary conditions in terms of limited space and electrical power.

[1] H. Homeyer et al., ISL operations and developments, in this report.

P. Arndt, D. Böhm, K. Effland, W. Hahn, U. Müller, J. Röhrich

Design Study for a 250 MeV-Proton Therapy Facility in Berlin

Radiotherapy is one of the most effective tools in the treatment of many tumour sites. Typically, the tumours are irradiated with high-energy photons or electrons (up to 23 MeV) produced by small hospital based medical electron accelerators. As an alternative, protons or heavy ions, particles showing more favourable physical characteristics, can be used. Their main advantage lies in the fact that they deposit most of their energy close to the end of their path in tissue. Choosing an appropriate energy makes it possible to focus most of the energy on the tumour, leaving the healthy tissue virtually unharmed. This is of particular importance in the treatment of tumours in the back of the eye, where important organs like the optic nerve often lie in close vicinity to the tumour. Eye-tumours, mostly choroidal melanoma, have been treated successfully at the ion beam laboratory (ISL) of the Hahn-Meitner-Institut for almost five years. Another important indication for particle radiotherapy are tumours close to the base of skull.

To date about 32200 tumour-patients received radiotherapy with protons, 3800 with carbon ions worldwide. Most of these patients were treated in research institutes. Based on these positive results, dedicated and/or hospital based proton and ion radiotherapy facilities have recently started operations or are currently under construction. By operating two heavy ion and four proton facilities, Japan has taken the leading position.

In Europe, however, the situation is much less advanced. A dedicated proton therapy facility, taking into account the institute's own research experience with a nuclear physics machine, is being set up at PSI in Switzerland. The excellent results of the ion therapy at GSI motivated the current construction of a dedicated heavy ion synchrotron at the German Cancer Research Center (Deutsches Krebsforschungszentrum) Heidelberg.

Starting from our experience with eye-tumour treatment and the excellent results achieved at the Hahn-Meitner-Institut, we started a design study for a dedicated medical 250 MeV proton therapy facility. This study is carried out in collaboration with the University Hospital Benjamin Franklin.

The development of the layout follows several basic ideas. Besides tumour control, the complete protection of critical structures close to the malignant tissue is of utmost importance. In many cases, this can be achieved with passive shaping of the irradiation fields that allows one to avoid complications inherently connected with sophisticated scanning devices. As far as the actual procedures during the therapy are concerned, we consider immediate access to the beam once the patient is correctly positioned to be an important asset. Finally, the option to perform independent parallel treatments in three to four rooms would decrease the costs per treatment thanks to a higher patient flow.

It has also decisive consequences for the general layout, in particular the choice of the accelerator, the necessary maximum beam intensity and the beam delivery system including radiation shielding. In the following we present a first draft of a possible conceptual design.

Proton beams with the necessary intensity can be realised only with a cyclotron. Looking at the landscape of proton facilities worldwide, we found the future facility MPRI in Bloomington, Indiana (Fig. 1) to follow similar ideas.

Their accelerator – a separated sector cyclotron – speeds up the protons to a final energy of 210 MeV. When a lower beam energy is needed, the beam has to pass through an energy degrader of variable thickness (e.g. carbon or beryllium blocks) reducing its energy. At the MPRI the beam delivery system consists of an achromatic beam line followed by a so called trunk line which ends at a beam dump. There are three beam splitting systems, each consisting of a fast ferrite kicker and a Lambertson dipole magnet making it possible to switch the 210 MeV beam from the trunk into each of the energy selection systems (ESS) of the treatment rooms. Each of the three ESSes is equipped with an energy degrader followed by an achromatic magnet design. This solution makes it possible to split the beam into slices and to treat patients at the same time in different rooms [1].

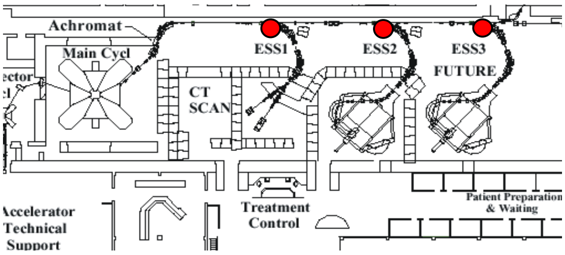

Fig. 1: *Layout of the future therapy centre MPRI in Bloomington. Each treatment room has available its own energy selection system (ESS), thereby enabling a parallel working mode for the whole facility. (Picture from V. Anferov et al., Proc. of the 2001 PAC, p. 645).*

The application of a degrader has two main disadvantages. The first one is the production of secondary particles, mainly neutrons, via nuclear reactions in the degrader material. Therefore, a proper radiation shielding of places in the facility occupied by people is required. The spatial neutron distribution produced in the degrader consists mainly of two contributions: forward peaked high-energy neutrons and an isotropic fraction of evaporation neutrons. With a large angle between the proton beam and the treatment room, the efforts required in radiation shielding (wall thickness) can be minimized.

A second disadvantage is the increase of the beam emittance due to multiple scattering of the beam in the degrader. In order to keep the beam emittance at an acceptably low level, one has to send the degraded proton beam through collimators, thus causing enormous beam losses, in particular for low energy beams. In order to compensate for the loss and to make parallel treatment possible, the considered cyclotron has to provide a proton beam intensity of up to ~10 µA.

From these sources a neutron dose arises which does not compare to other facilities so far. This is why a new concept of radiation shielding for the future facility in Berlin is developed. We decided in favour of a geometry, in which the proton beam is directed downwards in vertical direction while passing the degrader. This is different from the concept applied in Bloomington, where the kickers operate in the horizontal plane. The degrader itself is located 40 cm below ground level. This leads to larger angles between beam direction in the degrader and the treatment rooms. At the same time, the base plate will be used as a lateral shielding component. Right after the degrader an achromatic ion optic system, in which the adequate energy will be selected, transports the beam (bending it from the vertical into the horizontal direction) to the treatment room. The position of the degrader in relation to the ion optics and the ground is shown in Fig. 2. A first impression of the whole facility is shown in Fig. 3 as a 3D-simulation.

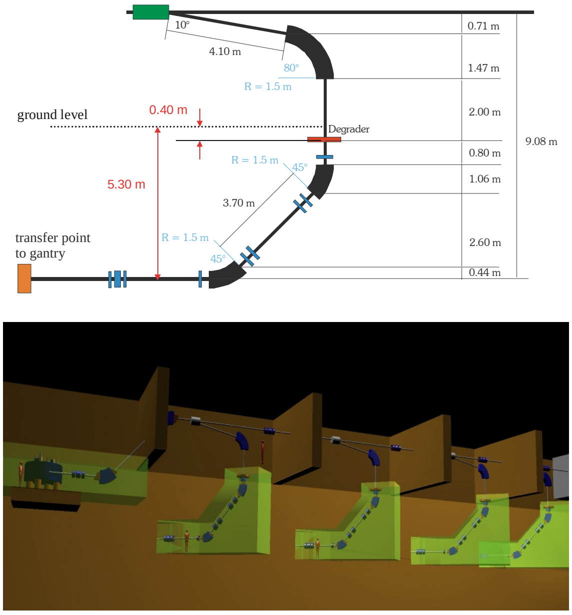

Fig. 2: Top) *A schematic drawing of the ion optics between the kicker and the transfer point to the gantry. The degrader is situated 40 cm beneath the ground.* ***Bottom)*** *3D-drawing of the cyclotron (left) the "trunk"-beam line and 4 kickers followed by the ESS to each treatment room (light green).*

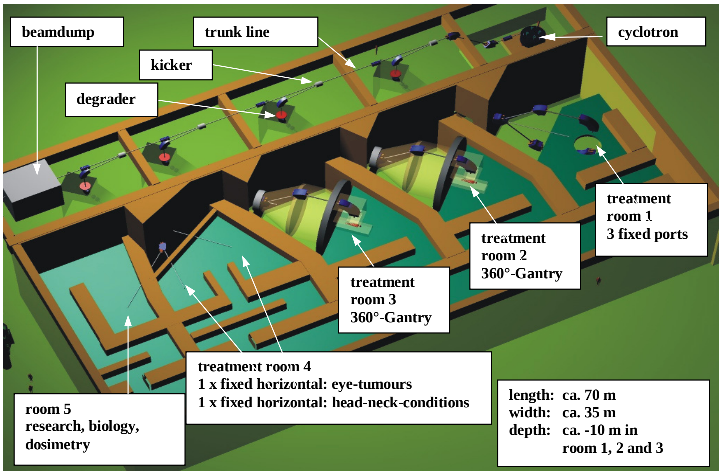

Fig. 3: *The first 3D-Overview. See the cyclotron (upper right) followed by the trunk line and 4 ion-paths to the treatment rooms. Whenever the beam is not in use, it is sent into a beam dump (shown as grey box, upper left). In treatment room no. 1 there are three fixed ports: one horizontal and two vertical ones. If needed, the fixed ports can be removed and replaced by a gantry. Rooms no. 2 and no. 3 are equipped with 360° isocentric gantries. In room 4 there are two fixed horizontal beam lines: one for eye-tumour therapy and the other for the treatment of conditions in the head-neck-area. In a fifth room scientific research in dosimetry, biology etc. can be performed.*

[1] V. Anferov et al., Proceedings of the 2001 Particle Accelerator Conference, Chicago, 645-647

A. Weber, D. Cordini, J. Heese, J. Heufelder,
H. Homeyer, H. Kluge, A. Meseck, H. Morgenstern,
W. Pelzer

Coulomb explosions of H_2O molecules in interactions with highly charged ions

Besides playing a fundamental role in the cells of living organisms, biomolecules are important for numerous applications in biotechnology. The mechanisms of their break-up in interactions with heavy ions, especially with highly charged ions (HCI), are not yet fully understood. Understanding these processes would be an important step towards a deeper insight into the interactions between radiation and biological tissues, e.g. in the case of radiation damage.

Due to the complexity of the processes that occur in the interaction of HCIs with large molecules as proteins or DNA, it is desirable to first achieve a better understanding of the interactions with smaller molecules, such as H_2O and C_2H_2. Although a gas phase target has been used in the first step, it is planed to perform measurements with solid water or proteins deposited on a crystal surface, where both ion spectroscopy and the Atomic Force Microscopy (AFM) technique can be applied.

The interaction of fast HCIs with H_2O molecules has been investigated recently by means of coincidence techniques [1,2]. These studies gave us an insight into the total kinetic energy distribution and the angular distribution of coincident fragments.

Here we report on an investigation of fragmentation of H_2O molecules in the interaction with slow, highly charged Neon and Argon ions. The energy of the fragmentation products showed a strong dependence on the incident ion charge. Additionally, we distinguish between two fragmentation mechanisms: binary collisions (high energy part of the spectrum – not shown here) and Coulomb explosions (low energy part of the spectrum). In the explanation of the low energy parts of the spectra we used a simple Coulomb explosion (CE) model. It is based on the assumption that after several electrons are removed by the incoming highly charged projectile, the molecule will become unstable and dissociate. In the first approximation, one can take that potential energy (calculated in the center of mass system) is transformed to the kinetic energy of ion fragments.

For the measurement ions from the 14.5 GHz Electron Cyclotron Resonance (ECR) ion source in the Ionenstrahllabor (ISL) at the Hahn-Meitner-Institut were used. The scattered ions and recoils were analyzed by means of an electrostatic spectrometer. A vapor target was produced from the water reservoir by means of a gas-jet under controlled conditions.

The typical spectra are presented in Fig. 1 for the case of incident 21 keV Ne^{q+} (q=3, 5, 7, 9) ions. One easily observes that when the projectile charge-state was increased, fragments with an increasing energy of up to 70 eV were detected. In the case of incident Ar^{q+} ions (q=10, 13) we found this feature to be even more pronounced.

Assuming that several electrons are removed by the incoming ion, we calculated the kinetic energy released via the Coulomb explosion mechanism. In Fig. 2, these data are compared to the Gaussian fit to experimental spectra (peaks are marked in Fig. 1). The quality of the fit is checked by the Chi-square method.

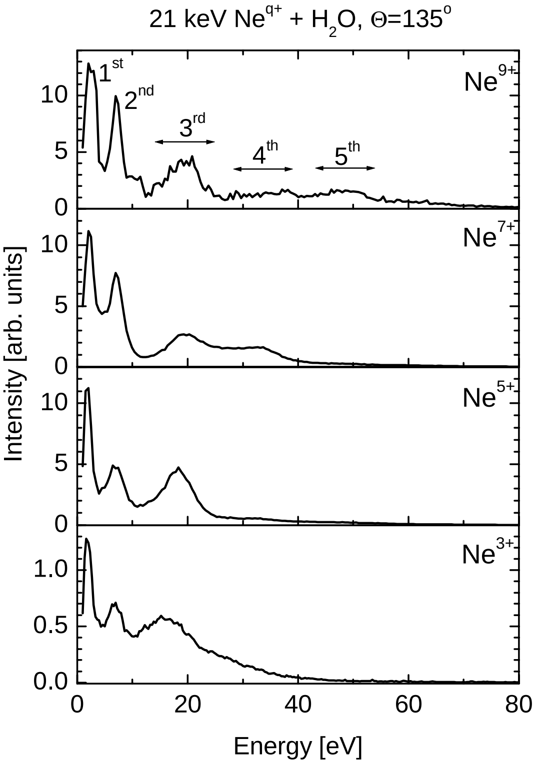

Fig. 1: *Fragments from the collision of 21 keV Ne^{q+} ions with H_2O molecules.*

The first peak in each of the spectra is attributed to slow O^{Q+} ions, while structures at energies higher than 10 eV are formed by H^+ ions from different fragmentation channels (convolution of peaks marked with numbers 3, 4 and 5). It appears that the fragmentation into two charged and one neutral particle is more probable than the fragmentation into three charged particles, i.e. the model calculation of a Coulomb explosion into $H^+ + O^{Q+} + H^0$ agrees better with the experimental results than the fragmentation into $H^+ + O^{Q+} + H^+$.

This assumption is supported by the results presented in Ref. 3, where single charged projectiles were used. Two different fragmentation channels ($H^+ + H^+ + O^0$ and $OH^+ + H^+$) might give contribution to the peak at 6 eV (labeled as 2nd peak). The angular dependence of the energy of detected ions is noticeable, slow ions are accelerated in backward directions and decelerated in forward directions.

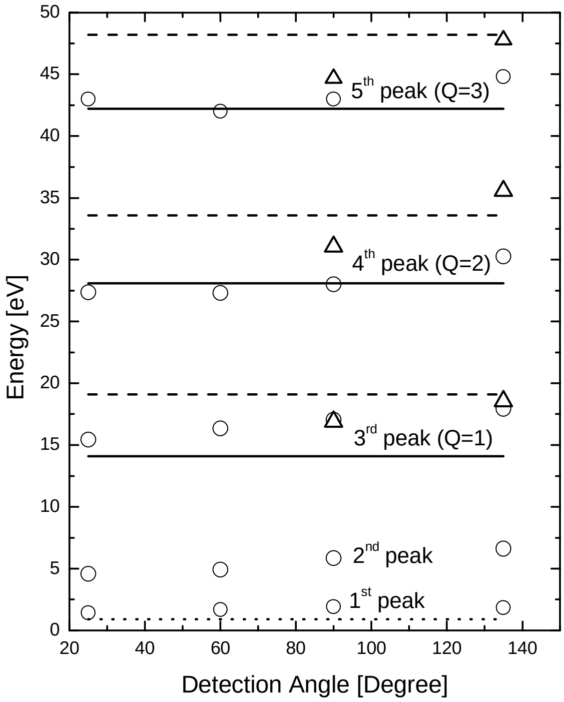

Fig. 2: *Comparison of the experimental results with the prediction of the CE model. The charge state of the oxygen ions produced in the collision is denoted by Q. The circles and triangles refer to incident Ne*$^{5+}$ *and Ne*$^{9+}$ *ions, respectively, while the calculations for the CE explosions into the* H^{+}+O^{Q+}+H^{0} *and* H^{+}+O^{Q+}+H^{+} *channels are represented by solid lines and dashed lines.*

Similar results were obtained with Ar^{q+} ions as projectiles. We were even able to resolve the H^{+}+O^{Q+}+H^{0} fragmentation with Q as high as 6, i.e. H^{+} ions with energies up to 120 eV were detected.

However, our model does not take into account a possible excitation of the molecule, which might shift the energy distribution of the fragments, especially for lower charge states of the projectiles [1,2]. Second, a calculation providing the branching ratios would lead to a better understanding of the experimental data. From the experimental point of view, it would be interesting to increase the charge state of incident ions, e.g. to use highly charged Xenon ions.

[1] B. Siegmann et al., J. Phys. B34 (2001) L587.

[2] U. Werner et al., PRL 74 (1995) 1962.

[3] U. Werner et al., NIM B98 (1995) 385.

J-Y. Chesnel (Centre Interdisciplinaire de Recherche Ions Lasers, Caen, France) in collaboration with R. Hellhammer, Z.D. Pešić, N. Stolterfoht; B. Sulik (Institute of Nuclear Research - ATOMKI, Debrecen, Hungary)

Selforganisation of NiO layers under swift heavy ion irradiation

After irradiation of thin NiO-films deposited on oxidized silicon wafers with swift heavy ions (90-260 MeV Ar, Kr, and Xe ions) at large tilt angles (above 60°) we found that the top layer had reorganized into periodic lamellae (see Fig. 1), which were oriented perpendicular to the beam direction and had a height of about 1 μm, a thickness of about 100 nm and an average distance of 1-3 μm.

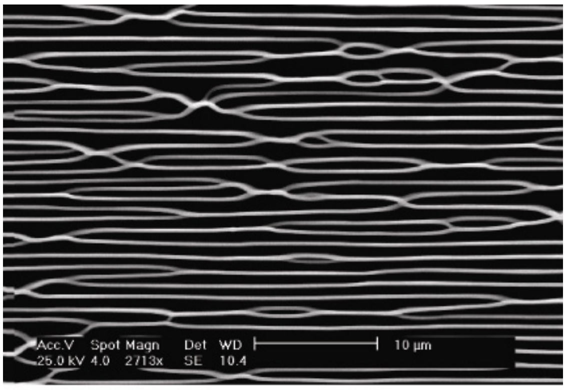

Standardprobe, 230 MeV Xe^{13+}, $\Phi = 7.6\times10^{14}/cm^2$, $\theta = 85°$

Fig. 1: *SEM top view of NiO/SiO_2 after irradiation with $7.6{\cdot}10^{13}$ Xe/cm^2 at 230 MeV.*

At low irradiation fluences, first a periodic crack system develops, which extends from the surface to the SiO_2 layer. Increasing fluence then results in shrinking of the material between the cracks along the projected beam direction and its simultaneous growth in height, until finally the initially coherent and smooth toplayer reorganizes into the lamellae structure. According to EDX and Micro-Pixe analysis the NiO from the initial layer has quantitatively been transferred into the lamellae and no NiO was found in between [1]. We could show that this phenomenon is due to the formation of molten tracks along the ion's path and the mechanical stresses induced by the twofold phase transition between the solid and the liquid phase [2]. According to Grinfeld [3] these almost uniaxial tensile stresses lead to a surface instability, which manifests itself in the formation of a periodic system of cracks, which extend from the surface to the SiO_2 layer. With increasing ion fluence the material between the cracks shrinks due to the so-called hammering effect [4,5], which finally results in the observed lamellae structure.

We have extended the experiments to 350 MeV Au-ion irradiation and we have in detail investigated the kinetics of the lamellae formation and their structure and morphology as a function of the ion fluence and the deposited energy as well as its dependence on the incidence angle of the ion beam.

The speed of lamellae formation is described by the deformation rate A^*, which is obtained by measuring the surface fraction covered by NiO as a function of the applied ion fluence ϕ. This was done by means of scanning electron microscopy (SEM) and by Rutherford Backscattering Spectrometry (RBS). Fig. 2 shows the results obtained for 140 MeV Kr at 75^0 tilt angle. At low fluences, a linear decrease of the NiO coverage occurs with slope A^*. At higher fluences a saturation is observed, the reason of which is not completely understood yet. The deformation rate as a function of the electronic stopping power S_e of the applied ion beams exhibits a threshold like behaviour

$$A^* = A_0\,(S_e - S_{ec})\,. \qquad (1)$$

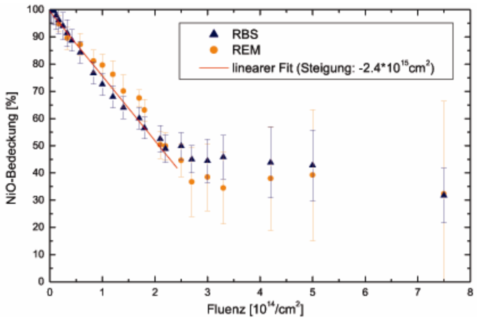

Fig. 2: *NiO coverage of the surface after 140 MeV Kr irradiation.*

The threshold value S_e=9.7(5) keV/nm compares nicely with the one found for the onset of mixing in NiO/SiO_2 and the one predicted for ion track formation and hence supports our above interpretation, that the lamellae formation is strongly related to melting of the material surrounding the ion trajectory.

The degree of order of the lamellea structure can be characterized by the number of ramifications per unit area. We found that this number increases with increasing electronic stopping S_e of the ion. The disorder increases exponentially with increasing S_e values, while it decreases for increasing tilt angle. This can be understood taking into account the homogeneity of the energy deposition and thus the homogeneity of the induced mechanical stresses, which is the better, the more ions contribute to the total effect (low stopping) and the longer is the single track within the NiO-layer (large tilt angle).

[1] A. Feyh, diploma thesis, Stuttgart University (2002) unpublished, W. Bolse, B. Schattat, A. Feyh, Appl. Phys. A (2003) in press.

[2] H. Trinkaus, J.Nucl. Mater. 223 (1995) 196.

[3] M.A. Grinfeld, Dokl. Akad. Nauk. SSSR 290 (1986) 1358.

[4] S. Klaumünzer, G. Schumacher, Phys. Rev. Lett. 51 (1983) 1987.

[5] S. Klaumünzer, A. Feyh, W. Bolse, ISL Annual Report 2002.

A Feyh[1], D. Etissa-Debissa[1], B. Schattat[1], W. Bolse[1]; S. Klaumünzer[2]; F. Schrempel[3]

(1) Institut für Strahlenphysik, Universität Stuttgart, (2) HMI, (3) Institut für Festkörperphysik, Universität Jena

Stoichiometry and density of reactively sputtered WS_x thin films

The van der Waals type layered semiconductors MX_2 (M = Mo, W; X = S, Se) are potential candidates for absorber materials in thin film solar cells [1]. The films can be deposited by various deposition techniques like sulphurisation of metal or oxide precursors with sulphur or H_2S or by reactive magnetron sputtering, the latter technique allowing film deposition at low substrate temperatures due to the ion-assistance of the film growth. For this reason, the growth of thin MoS_x and WS_x films prepared by magnetron sputtering from a metallic target in mixtures of argon and H_2S is the aim of our investigations.

From Elastic Recoil Detection (ERD) measurements the stoichiometry and the density of the films were calculated. Similar to MoS_x tungsten sulphide thin films with stoichiometries WS_x with $x \leq 2$ [2] are obtained.

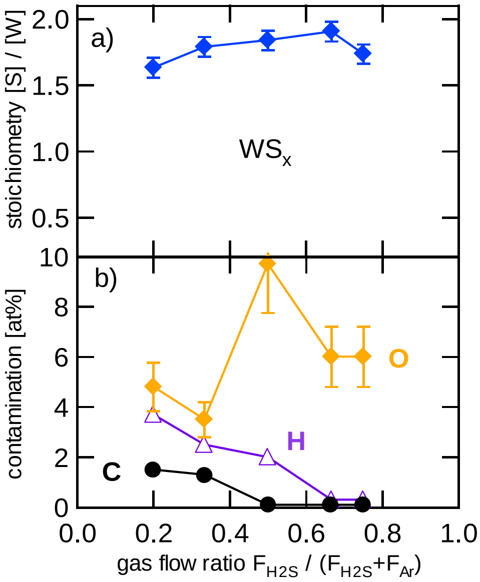

Fig. 1: *The stoichiometry [S]/[W] (a) and the concentration of the contamination H, C and O (b) of reactively sputtered* WS_x *thin films on oxidised silicon substrates in dependence on the gas flow ratio* $F_{H2S}/(F_{H2S}+F_{Ar})$*. Deposition conditions: DC sputtering power 50 W; substrate temperature 450°C; total sputtering pressure* $4{\cdot}10^{-2}$ *mbar; floating substrate potential.*

Fig. 1 shows the stoichiometry of WS_x films deposited on oxidised silicon substrates in dependence on the gas flow ratio $F_{H2S}/(F_{H2S}+F_{Ar})$. Increasing the partial pressure of H_2S leads to an increase of the sulphur content up to a maximum of $x = 1.91$. The decrease of the stoichiometry for the highest gas flow ratio $F_{H2S}/(F_{H2S}+F_{Ar}) = 0.75$ cannot be explained. With decreasing argon gas flow the concentration of the hydrogen and carbon contamination also decrease which is a hint that the argon gas supply or tubing may be the origin of this contamination. Though it is also possible that the increasing porosity (see Fig. 2) of the films in this deposition series is responsible for the increase in contamination concentrations. The enlargement of the film surface can result in higher adsorbate concentrations of water and CO_2 from air exposure after the depositions. The high oxygen concentrations in the films are difficult to assign only to the WS_x films as they were deposited on oxidised silicon. Therefore, the separation between film oxygen and substrate oxygen is only possible with a relatively large error of ± 20%. The argon concentrations in these films are below the detection limit of 0.01 at%. Even at high substrate bias potentials of -300 V no argon could be detected in the films which is unexpected.

One reason for the sulphur deficiency in WS_x films may be the intercalation of additional tungsten atoms between the S-W-S stacks which form this layer type compound. It should be noted that there are no signs for the occurrence of other phases besides the hexagonal WS_2 phase.

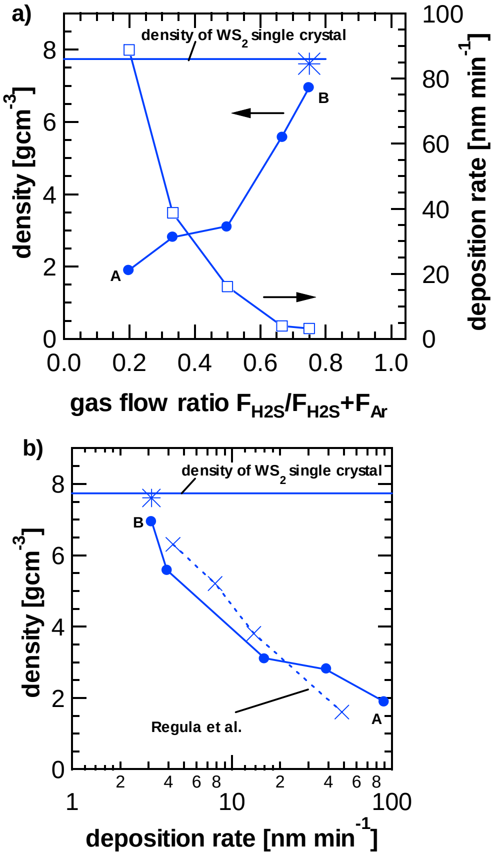

Fig. 2: *a) The density (•) and the deposition rate (□) of reactively sputtered* WS_x *thin films on oxidised silicon substrates obtained from ERD measurements in dependence on the gas flow ratio* $F_{H2S}/(F_{H2S}+F_{Ar})$*. The horizontal line marks the density of a* WS_2 *single crystal. In diagram b) the rate dependence of the film density is plotted on a semi logarithmic scale. The results from Regula et al. [3] are given for comparison (x). The star (*) marks the density of one sample measured by X-ray reflectometry. Deposition conditions: DC sputtering power 50 W; substrate temperature 450°C; total sputtering pressure* $4{\cdot}10^{-2}$ *mbar; floating substrate potential.*

From the measured atomic area densities [at cm^{-2}] film densities could be calculated for the same deposition series under variation of the gas flow ratio. They are depicted in Fig. 2 in dependence on the gas flow ratio. Low H_2S partial pressures lead to densities of only 30% of the density of a WS_2 single crystal (X-ray density), these films are very porous. At an H_2S content of 75% of the gas mixture the X-ray density is almost reached. The thin, compact film (thickness of about 50 nm) could be analysed independently by X-ray reflectometry which confirmed the value derived by ERDA. The porous morphology of WS_x films, which could be confirmed by SEM and TEM analysis, results from dentritic structures which are typical for layer type materials prepared at high deposition rates and have been reported by other groups (e.g. [3]).

The deposition rate is determined by the H_2S partial pressure, what can be seen also from Fig. 2 a, and itself influences the density of the growing films. In Fig. 2 b the dependence of the density on the deposition rate is plotted in order to compare the results with the literature data [3]. Both series fit well to each other although, the authors used a WS_2 compound target, only 1% H_2S and varied the deposition rate via the total sputtering pressure (1 - 6·10^{-2} mbar) indicating similar growth modes for both deposition procedures.

Fig. 3 shows the film stoichiometries WS_x and MoS_x in dependence on the substrate temperature. Stoichiometric MS_x can be obtained only at temperatures below 200°C. The decrease of the sulphur content in the films with increasing temperature is explained with an increased vapour pressure of sulphur, that desorbs from the substrate prior to the reaction to the sulphide [4].

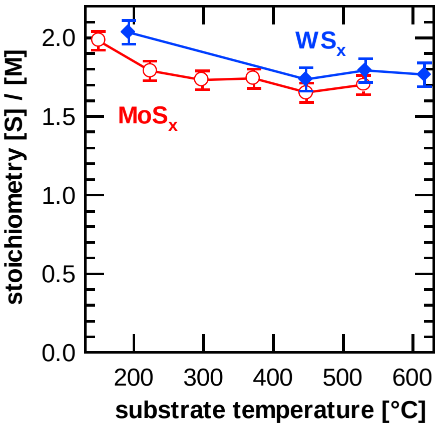

Fig. 3: *The stoichiometry [S]/[M] with M = Mo, W of reactively sputtered* WS_x *(●, ERDA) thin films on oxidised silicon substrates and of* MoS_x *(o, RBS) on glassy carbon in dependence on the substrate temperature. Deposition conditions: DC sputtering power 50 W; total sputtering pressure* $4\cdot10^{-2}$ *mbar; gas flow ratio* $F_{H2S} / (F_{H2S} + F_{Ar}) = 0.75$*; floating substrate potential.*

Further ERD experiments on the composition of reactively sputtered WS_x and MoS_x thin films are planned to find out whether the variation of the plasma excitation mode (DC and/or HF) gives rise to changes of the film composition. In situ-XRD investigations with synchrotron radiation during the sputtering process showed a remarkable effect of this deposition parameter on structural parameters especially on the texture of the films.

[1] H. Tributsch, Z. Naturforsch. 32a (1977) 972.

[2] K. Ellmer et al., J. Crystal Growth 182 (1997) 389.

[3] M. Regula et al., Thin Solid Films 280 (1996) 67.

[4] T. Ito, K. Nakajima, Phil. Mag. B 37 (1978) 773.

V. Weiß[1], K. Ellmer[1]; W. Bohne, S. Lindner, J. Röhrich, E. Strub

1 HMI, Dept SE5

The elliptical undulator UE46 of high brilliance and variable polarization for studies of magnetic nanostructures at BESSY

The 3rd generation synchrotron BESSY II offers unique possibilities for experiments with X-rays in the soft photon energy regime, which will serve as a complementary probe to magnetic neutron scattering at HMI. Therefore, three years ago, we started the strategic HMI-project to build the elliptical undulator UE46. This insertion device, which provides *polarized* soft X-rays, and the instruments at the two beamlines supplied by it, is dedicated to research on magnetism in thin films and nanostructures. The project is performed in close collaboration with BESSY and financed from the so called Helmholtz-Strategiefonds.

The undulator UE46 was designed in 2000, built in 2001, and inserted into the low beta section of the ring in February 2002. The subsequent commissioning of one of the beamlines delivered excellent results. It has a pure permanent magnet design of the Advanced Polarized Photon Light Emitter (APPLE-II) type consisting of four identical rows of high remanent NdFeB-magnets arranged in four quadrants around the axis of the electron beam (period = 46 mm).

Two rows are movable and two rows are fixed (Figs. 1, 2). The variation of gap and shift determines the energy and the state and degree of polarization of the light.

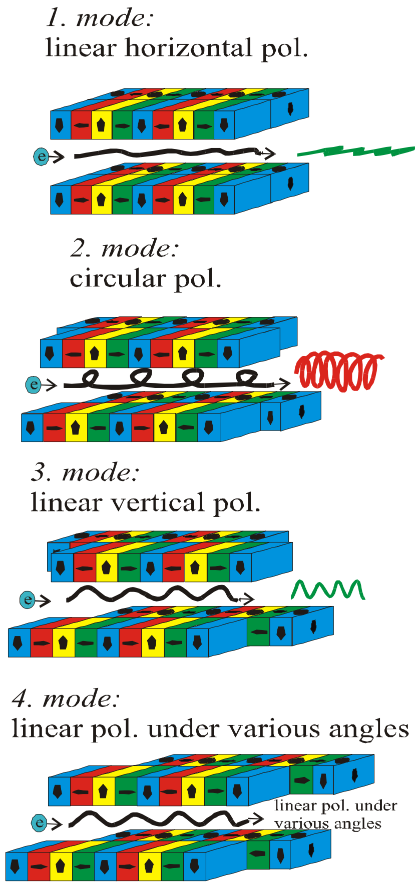

Fig. 1 (down left): Different relative positions of the magnet rows in the UE46 undulator lead to different polarization modes of the synchrotron light.

The UE46 provides polarized soft X-rays with highest brilliance over a very broad energy range from 200 to 1800 eV optimized for studies of magnetic effects in 3d transition metals and Rare Earths. The polarization is variable and allows different modes of operation: right and left circular polarization, horizontal and vertical linear polarization, and linear polarization under various angles (Fig. 1). The last option of polarization is a novel one and is achieved by an antisymmetric operation where the upper right row of magnets is moved in opposite direction to the lower left row. During this antiparallel motion additional longitudinal and transverse magnetic forces are created which forced us to improve the mechanical design. The helicity can be switched mechanically from right to left circular polarization in about 3 sec (possible thanks to an improved design). For further details see Ref.[1].

Hence, the UE46 is excellently suited for magnetic studies on nanostructures applying the polarization dependence of the absorption of X-rays in magnetic materials, an effect known as magnetic dichroism. Its brilliance is higher than that of any other undulator at BESSY. The key advantages of soft X-ray undulator experiments on magnetism in nanostructures (thin films, multilayers, laterally structured layers, magnetic clusters on surfaces, etc.) are the high brilliance and polarization of the photon beam, the tuneable energy, and the focussed beam. There is a huge enhancement of magnetic effects at the absorption edges in the soft energy regime. Furthermore, element selective studies are possible and, finally, using the magneto-optical sum rules one has experimental access to the orbital magnetic moment, which is directly linked with the magnetic anisotropy.

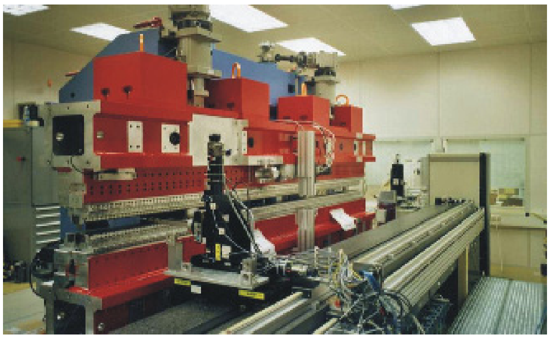

Fig. 2: Photograph of the undulator UE46 (in Aug. 2001), before it was inserted into the BESSY ring.

[1] Englisch, U., Rossner, H., Maletta, H., Brandt, J., Sasaki, S., Senf, F., Sawhney, K.J.S., Gudat, W.: Nucl. Instr. and Meth. 467-468 (2001) 541.

U. Englisch, H. Rossner, H. Maletta

A Self-Consistent Method for Multiaxial Residual Stress Analysis by Energy-Dispersive Diffraction

Compared with the well established methods of angle dispersive X-ray stress analysis, the application of energy dispersive diffraction techniques using white radiation provides several advantages. Besides the higher penetration depths which are achieved by the higher energies, the multitude of reflections recorded in one spectrum offers additional information that can be used for stress gradient evaluation in the intermediate zone between the surface and the volume of polycrystalline materials.

The diffraction analysis of residual stresses is based on the detection of lattice spacings $d_{\varphi\psi}(hkl)$ for different angle sets (φ,ψ) with respect to the sample system **P**. Information on the residual stress tensor is then obtained by means of Hooke's law. Whereas stress analysis in the near surface region up to about 10 µm is usually performed with characteristic X-rays of rather low energy, neutrons or high energy synchrotron radiation up to about 300 keV is used for the evaluation of the volume (bulk) residual stresses (Fig. 1).

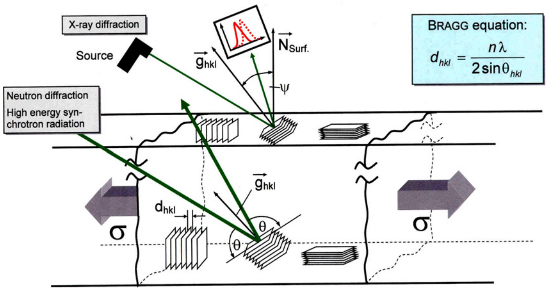

Fig. 1 Principle of residual strain/stress analysis by diffraction methods

However, there remains a gap with respect to the accessible near surface zone, which concerns a range between about 10 µm and 1 mm, where the conventional X-ray methods are no longer and the neutron methods are not yet sensitive. In order to extend the information depth to this 'intermediate' zone between the surface and the volume, use can be made of energy-dispersive (ED) diffraction in reflection geometry with photon energies up to about 100 keV. Measuring and evaluation procedures applied so far in the well-established X-ray stress analysis (XSA) by means of angle-dispersive (AD) diffraction were adapted to the ED case and further developed using the advantages provided by ED diffraction [1,2].

ED-XSA in the intermediate zone is of great theoretical as well as practical interest. On the one hand, it permits the non-destructive investigation of the transition from the biaxial surface stress state to the triaxial volume stresses in the bulk of the material. On the other hand, mechanical surface processing like grinding or shot-peening is well-known to have a deep impact on materials. Especially the latter method is used extensively in industry to generate beneficial near-surface residual stress fields in critical components, which may extend up to depths of some hundred microns into the material. Therefore, residual stress analysis in this zone is a necessary first step in order to optimize the mechanical properties of technical parts.

Fig. 2 shows a typical application for ED residual stress analysis. The investigations were performed on a normalized and subsequently shot-peened ferritic steel 42CrMo4. In this case, the scattering vector method [3], which permits a self-consistent triaxial residual stress gradient analysis, was applied for the first time to the ED case of diffraction. The multitude of reflections hkl, which are detected in each ED spectrum, are treated as additional parameter for the depth resolved analysis.

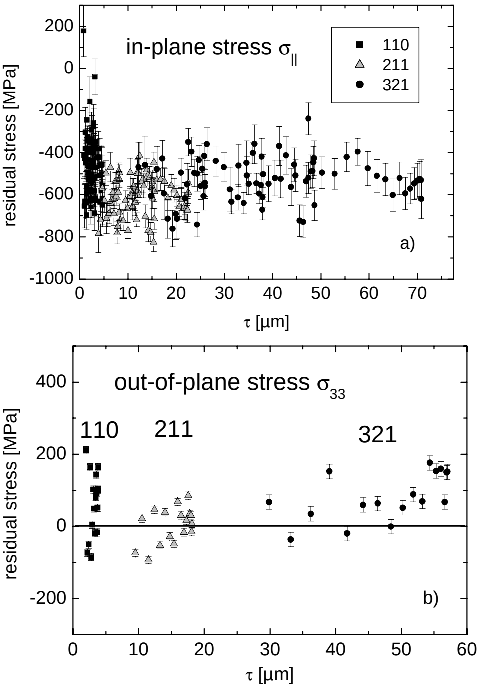

Fig. 2 Residual stress depth distribution in the shot-peened 42CrMo4 sample evaluated by means of the scattering vector method [2]. (a) In-plane stress $\sigma_{||}(\tau)$ and (b) out-of-plane stress $\sigma_{33}(\tau)$.

The results clearly show, that the residual stress state due to a homogeneous mechanical surface treatment of a single phase material remains nearly biaxial even in deeper zones below the surface.

Currently, an ED materials science synchrotron beamline up to about 100 keV is established at BESSY II in order to provide a powerful tool for advanced research activities in the field of residual stress-, texture and microstructure analysis.

[1] C. Stock, Ch. Genzel, W. Reimers, Mat. Sci. Forum **404 - 407**, 13 - 18 (2002).
[2] C. Stock, PhD Thesis, TU Berlin. 2003.
[3] Ch. Genzel, Habilitation thesis, HU Berlin, 2000.

Ch. Genzel, C. Stock, W. Reimers[1]

1 (TU Berlin)

Micro-Tomography for structural analysis of metallic foams

Computed tomography has been available for medical diagnostics since the early seventies of the last century. In 1979 the inventors G. Hounsfield and A. Cormack received the Nobel Prize for their invention. J. Radon (1917) and P. Funk (1916) contributed the mathematical foundations.

We introduced the synchrotron micro-tomography in the department SF3 (materials research) of the Hahn-Meitner-Institut in order to perform high-resolution, non-destructive, three-dimensional structural investigations and material characterizations on metallic foams. The term µ-tomography, used to describe this method, refers to a spatial resolution in the micrometer region. In Figure 1 the set-up used for the tomographic measurement is sketched schematically.

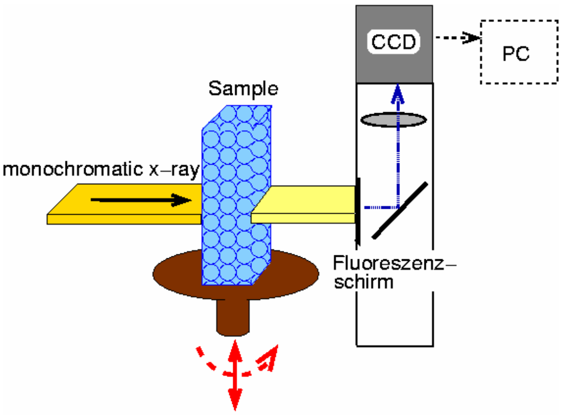

Fig. 1: Sketch of the measurement set-up for computed tomography

This tomography is based on the attenuation of monochromatic radiation by an object, e.g. by a metallic foam, for many different angular positions. Due to the different absorption coefficients of the different regions, the X-ray radiation is attenuated differently. This results in a set of about 700-900 single radiographic projections which are used for reconstructing the complete 3D-picture.

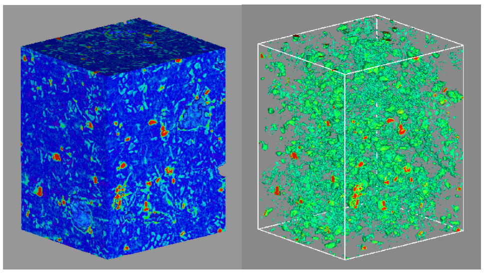

Fig. 2: Left: Tomographic image of the foam precursor containing AlSi10 Mg (blue), 10 % SiC (cyan), and 0.5 % blowing agent TiH_2 (red). Right: Distribution of the SiC-particles and the blowing agent separated from the aluminium matrix.

The measurement was carried out at BAMline, a beamline operated by the Federal Institute for Materials Research and Testing (BAM) at BESSY. The extremely parallel, highly intensive synchrotron radiation allows for a high spatial resolution and a very good signal-to-noise ratio. Moreover, by monochromizing the beam we are able to distinguish between different phases in the samples. The X-ray energy range is tuneable from 6 to 60 keV.

Figure 2 shows two tomographic images of a metallic foam precursor. The cast solid precursor consists of the aluminium alloy Al Si10 Mg (blue) and some particles of the blowing agent titanium hydride (TiH_2, red). After heating up the precursor to above the decomposition temperature of the blowing agent, the hydrogen is released and a porous structure is generated. To achieve a better stability of the metallic foam during the foaming process, 10 % (vol.) of insoluble, partially wetted, micrometer-sized silicon carbide particles (cyan) were added to the alloy. Thus, the viscosity of the melt is increased during the foaming process, and the surface tension decreases. Drainage along the walls then occurs less rapidly, and therefore the bubble collapse is slowed down. This leads to an evenly distributed pore structure. On the right hand side of Figure 2 the homogeneous distribution of the SiC-particles and the TiH_2-particles is visualized. Because silicon carbide and aluminium have nearly the same absorption coefficient, we need the monochromatic synchrotron radiation (E=25 keV, $\Delta E/E=10^{-2}$) to distinguish between them.

Fig. 3 shows a photograph and a tomographic view of the material after the foaming process.

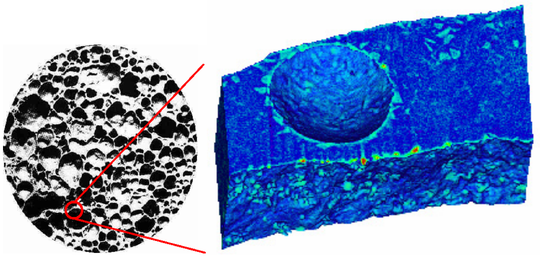

Fig. 3 Photograph of the aluminium foam (left). tomographic clip of a pore wall of the fully foamed, solid aluminium foam with a smaller pore in it (right)

Now the silicon carbide particles (cyan) are mostly arranged on the wall's surface in front and around the smaller pore. The red areas in the right picture are remnants of the blowing agent titanium hydride. Thanks to the tomographic measurements, the rearrangement mechanism can be observed three-dimensionally and the distribution of the SiC-particles can be visualized and evaluated quantitatively.

A. Haibel, A. Rack

Texture modification in titanium layers with heavy ions

Fast heavy ions interact with solid matter mainly via inelastic collisions with the target electrons. If the electronic stopping power of an ion penetrating the solid exceeds a specific critical value, a thermal spike is generated, i.e. the material "melts" in a volume of a few nanometers around the ion path. Due to the small volume, this state lasts only few picoseconds. This effect can be used to modify the material properties, e.g. its texture [1]. In the present report, the effect of the interaction of swift heavy ions on the orientation distribution of the crystals in polycrystalline hexagonal titanium is studied.

In our experiment we used two titanium samples of different thicknesses (400 nm and 3 µm) prepared by vapor deposition at 400°C on commercial (001) silicon wafers. Both titanium samples were irradiated at the Tandem accelerator of the Maier-Leibnitz-Laboratory, Garching with 200 MeV gold ions. The fluence was about 10^{15} Au/cm^2, the angle between the ion beam direction and the surface was 19° and the beam spot size on the sample only 1×2 mm^2.

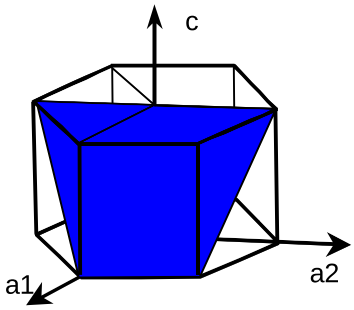

Fig. 1: *Hexagonal titanium lattice. The (101) plane is marked blue.*

The orientation distribution of the crystals, i.e. the texture of the irradiated titanium layers, was studied at the bending magnet X-ray diffraction beamline KMC2 at BESSY using a 6-circle goniometer and a 2D position sensitive detector. The wavelength was λ=0.155 nm. For each sample irradiated and unirradiated parts were examined.

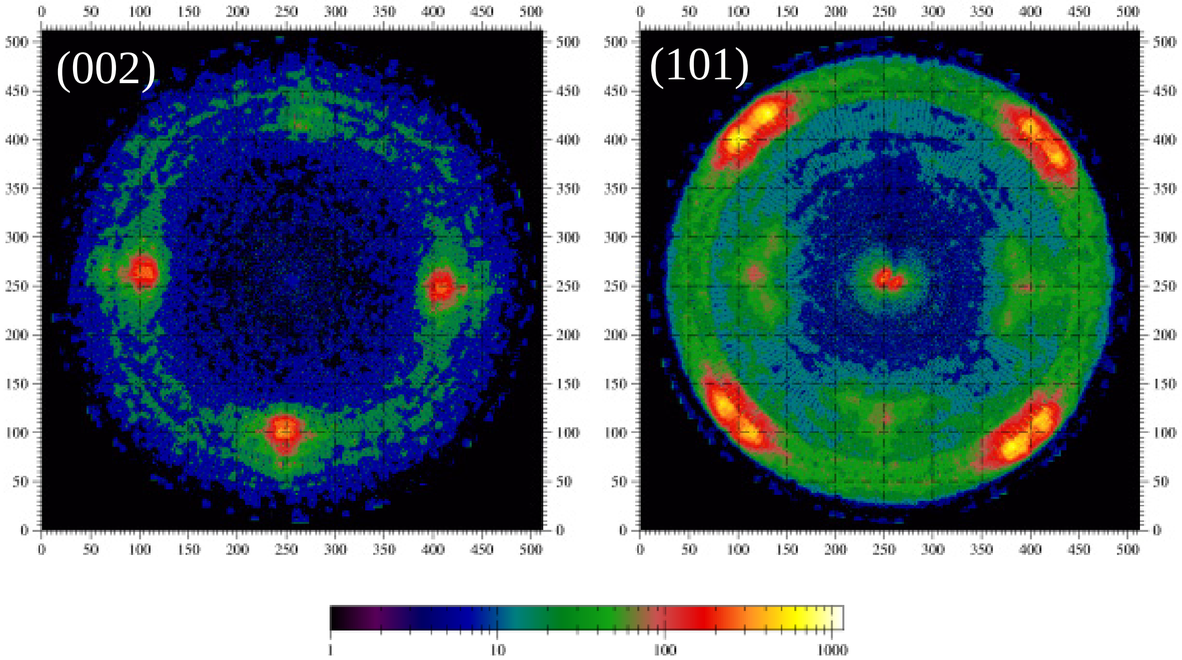

Fig. 2: *The (002) and (101) pole figure of the 400 nm thick film. The pole figures did not change despite the irradiation.*

The results of the measurements are presented as pole figure plots – the standard visualization method for the description of the crystal orientation in a material. The X-ray detector is positioned at the 2θ angle where the scattering peak is expected, and the azimuthal (φ) and polar (χ) angles of the sample are varied between 0° and 360°, and from 0° to 90° respectively. φ denotes the rotation of the sample around the surface normal and χ denotes the tilt.

In the present experiments we used a position sensitive detector (Bruker AXS) for the pole figures. This choice had some advantages when compared to a point detector.

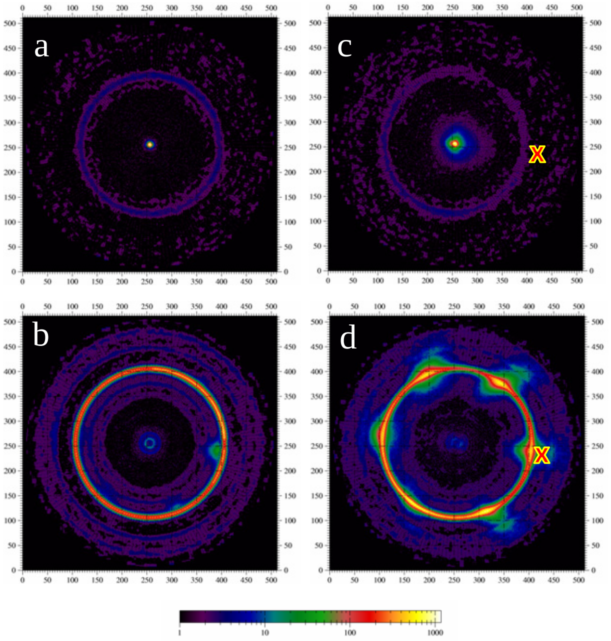

Fig. 3: *Comparison of the pole figures of the unirradiated (left) and irradiated (right) area of the 3 µm thick sample. Although the [100]-axis (a and c) does not change the direction, there is an obvious difference between the (101) pole figures (b and d). The ion beam direction is marked with a red cross on the figures c and d.*

The area detector covered a very large region in χ angle allowing for a fewer steps in the polar angle scans of the sample. The second advantage was that all Bragg angles of interest could be acquired in the same frame. In our experiment, we measured the (100), (101), and (002) Bragg reflections of titanium simultaneously (25°-45°). The step size for the measurement of the pole figures in χ direction was 15°, and in φ direction 2°. In addition, utilizing the 2D detector made a simple background correction possible. The background was estimated by averaging the intensities for 2θ values slightly larger and smaller than the Bragg reflection.

In the case of the thinner sample (400 nm), the orientation of the titanium layer was determined by the crystalline structure of the substrate (Fig. 2). The titanium lattice is oriented with its (101) plane parallel to the surface, and due to the 4-fold symmetry of the Si (001) substrate there are four different but equivalent orientations of the titanium lattice on the substrate. After irradiation the pole figure stayed unchanged.

In the case of the 3 µm thick sample the layer is thick enough in order not to be influenced by the substrate, so the [001] axis of the unirradiated sample is oriented normal to the surface. As the surface is the only symmetry-breaking element, the crystals are randomly oriented in the azimuthal direction, which can be seen on Fig. 3b as the circular intensity distribution at the polar angle 64°, corresponding to the angle between (001) and (101) plane normals in titanium. After irradiation the (101) pole figure showed changes in the azimuthal distribution. The randomness is canceled, i.e. the crystals have a preferred azimuthal direction resulting in a 6-fold symmetry (see Fig. 1). One of the (101) pole figure maxima points in the direction of the incoming ions (red cross).

One can conclude that up to some critical thickness the lattice of the deposited titanium matches to the lattice structure of the silicon (001) substrate. The next neighbor distance in (101) planes is similar to the lattice parameter of silicon in the (001) planes. This matching of the lattices can be deduced from the 4-fold symmetry of the pole figures acquired from the thinner sample. The actual processes leading to the reorientation of the crystals is not yet investigated, and has to be studied further.

As the irradiated areas are very small, it was not easy to separate the irradiated and unirradiated regions of the sample. Thus, for some measurements probably both regions contribute to the recorded signal. The distinct peak on the (101) pole figure of the unirradiated sample (Fig. 3b), as well as the ring in Fig. 3d, is attributed to this effect. Lately, the possibility to accelerate gold ions to energies of 600 MeV with fluxes larger than those available at the tandem accelerator in Garching has been introduced at the cyclotron of the ISL accelerator. It will thus be possible to irradiate larger areas of the sample, so further X-ray measurements are going to be more accurate.

To our knowledge, the recorded ordering after irradiation, which is interpreted as a recrystallization in direction of the incoming high-energy ion beam, was observed for the first time. A detailed study of the interaction process will most probably lead to a better understanding of the thermal spike model, which is still under discussion. For the future experiments are planned which will clarify the dependence of the texture on the angle of the impinging projectiles, the fluence, and the thickness of the titanium layer.

[1] K. Zhang et al., Nucl. Instrum. Methods B161-163 (2000) 1116.

I. Zizak, N. Darowski; W. Assmann[1]; J. Gerlach[2]
A. Wenzel[3]

1. Universität München, Garching, 2. Leibniz-Institut für Oberflächenmodifizierung, Leipzig, 3. Universität Augsburg

NAA-Laboratory and Neutron Activation Service at BER II

The department SF6 provides a neutron activation service at the BER II for universities, scientific institutions, hospitals and industry. Typical fields of applications are:

- Trace element determination by neutron activation analysis (NAA) for studies in various disciplines including biology, medicine, geology, environmental sciences and archeology. Certification of reference materials.
- Neutron activation experiments such as radionuclide production for medical applications, sources for Mößbauer spectroscopy and production of tracers for industrial applications.

The operation, maintenance and further development of the neutron irradiation devices at BER II and of the NAA measuring systems are a central task of the department SF6.

Irradiation devices

The BER II has been equipped with four irradiation devices which allow optimization of the irradiation conditions for the activation of short-lived, medium-lived and long-lived radionuclides.

DBVK:	rotatable irradiation device in the reactor core
DBVR:	rotatable irradiation device in the Be-reflector of the reactor core
TBR:	dry irradiation device outside the Be-reflector
SRT:	fast rabbit system

DBVK and DBVR are used for long-term activation experiments. Up to nine aluminium containers can be irradiated simultaneously.
Short-time activation experiments are carried out by means of TBR and SRT.

Device	Φ_{thermal} $[1/\text{cm}^2\text{s}]$	Φ_{fast} $[1/\text{cm}^2\text{s}]$	**Number of containers**
DBVK	1,5E+14	4,3E+13	9*
DBVR	7,5E+12	1,9E+10	9
TBR	3,4E+12	2,2E+10	1
SRT	4,4E+11	3,9E+10	1

*Temporarily restricted to 4

Status 2002

- The fast rabbit system SRT was not in use in 2002 due to insufficient man power. The control system as well as the acquisition system has to be renewed.
- The work for upgrading the in-core position DBVK is still in progress. Extensive calculations for reactivity changes were performed by IBBS.
- Installation of a new germanium detector (66% Efficiency,) with digital signal processing.
- Replacement of six control systems for the automatic sample changers

Neutron activation experiments 2002

A total of 1246 samples were irradiated in 2002. 65% of the 173 activation experiments were performed by means of the DBVK or DBVR. With these devices it is possible to irradiate up to 24 samples simultaneously in one aluminium container.

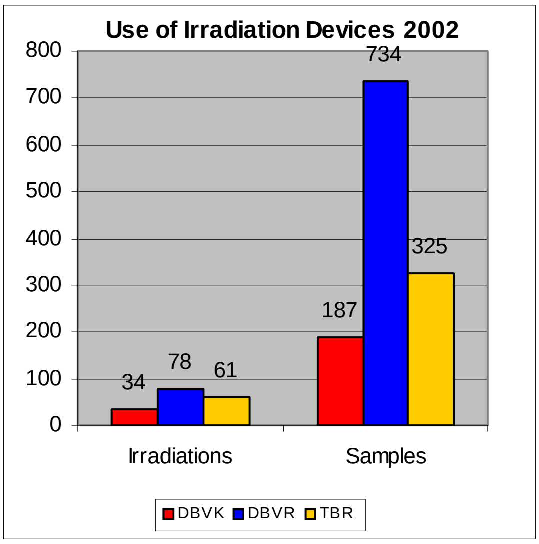

Fig. 1: Use of the irradiation devices in 2002. In 173 activation experiments carried out in the DBVK, DBVR and TBR a total of 1246 samples were irradiated and analyzed by NAA.

About 60% of the activation experiments and of the trace element analyses by NAA was carried out for external users.

Internal users

Dept. SF1
Dept. SE5

External users

Universities:
FU Berlin
HU Berlin
TU München
University München
University Mainz
University Leipzig
University Dresden
University Karlsruhe

Research Institutes:
BAM, Berlin
GSF, Neuherberg
IIF, Leipzig

Industry:
Merck KGaA
Schott Lithtec AG
TruTec Process Diagnostics
Pilkington Deutschland AG
DaimlerChrysler AG

D. Alber (SF6)

$Fe(NCS)_2(d_4\text{-pyrazine})_2$: A molecular-based system that behaves as a 2D S=1/2 Ising square lattice

The construction of molecule-based magnets through a coordination polymer approach is a particular area of contemporary materials research, which has proven quite fruitful and yielded diverse new materials. In the long run, research performed today may well enable us in the future to actually predict the topology and/or the connectivity of crystalline lattices based on the molecular structures of the small building blocks used in their assembly. This will, ideally, lead to the rational design of framework materials for specific applications. Currently, the most efficient approach to preparing such materials is via direct chemical combination of functional inorganic and organic components. Judicious choice of bridges is a crucial factor to generate fascinating structures and unusual magnetic properties. Cyano, azido, oxalato, pyrazine (pyz) and recently emerging dicyanamide (dca) ligands have been demonstrated to transmit magnetic interactions efficiently as bridges, and able to stabilize magnetic ordering temperatures up to room temperature. Of the reported coordination polymers that contain pyz, most of them possess low-dimensional structures, i.e. 1D chains or 2D sheets. Furthermore the combination of pyz and thiocyanate (NCS^-) anions leads to asymmetric lattices that may exhibit unusual magnetic magnetic properties.

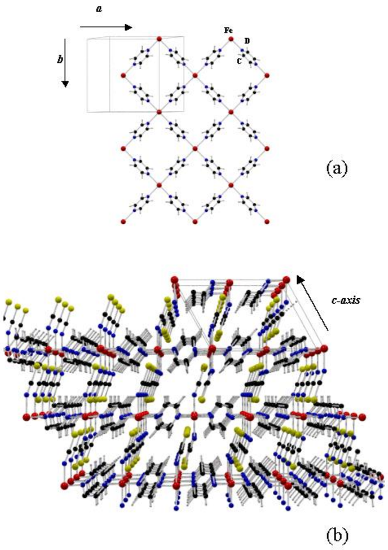

Fig. 1: Nuclear structure of $Fe(NCS)_2(d_4\text{-}pyz)_2$ perpendicular (a) and parallel (b) to the sheets. The solid line marks one unit cell space.

In this work we focus on $Fe(NCS)_2(pyz\text{-}d_4)_2$. This system crystalizes in a 2D like structure consisting of stacked Fe^{2+}-pyz sheets along the *c*-axis and shows long range antiferromagnetic order below T_N=6.6K with a sinusoidal modulation associated to a propagation vector [1,0, 1/4+χ]. Neutron powder diffraction measurements were performed using the diffractometer E6 close to T_N showing that the critical scattering resembles that of a 2D S=1/2 Ising system.

With the aim to obtain insight on the spin-wave dispersion at low temperatures and spin diffusion at high temperatures and thus better understand the 2D magnetic behaviour of $Fe(NCS)_2(pyz\text{-}d_4)_2$, inelastic neutron scattering experiments were performed using the high-resolution multi-chopper time-of-flight NEAT. Data have been collected at different temperatures, between 2 and 50 K, with incident neutron energy of 3.15 meV (λ = 5.1Å), giving a resolution of 217 μeV at the elastic peak position.

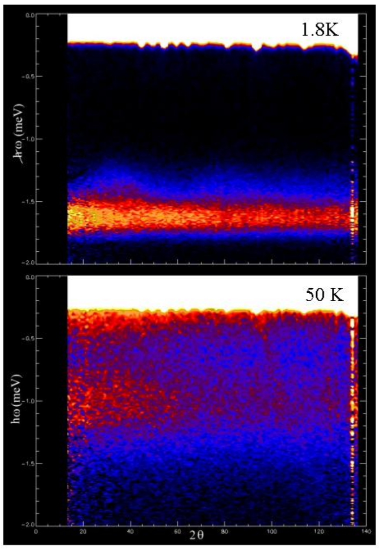

Fig. 2: Energy-momentum spectrum obtained $Fe(NCS)_2(pyz\text{-}d_4)_2$ using NEAT. Two separate features, without significant dispersion, are observed on the magnetic spectrum. Below T_N, a main inelastic response appears at 1.64 meV, which on heating seems to merge with the peak observed at higher temperatures located at 1.04 meV.

From this experiment we can unambiguously conclude that in $Fe(NCS)_2(pyz\text{-}d_4)_2$ two distinct regimes exist, which are associated to two separate features on the magnetic spectrum. Below T_N, as expected for an Ising system, a large gap is observed at 1.64 meV, equivalent to a thermal energy of about $3T_N$. Most interesting, and as also expected for an ideal Ising system, the spin wave mode presents almost no dispersion. While in the paramagnetic regime, a peak that shows a smooth form-factor-like decrease at large momentum transfer is observed at 1.04 meV. This mode can be associated with antiferromagnetic ordering which is maintained within the chains well above T_N magnetic transition temperature observed in these measurements.

L.C. Chapon[1], H.N. Bordallo[1], J.L. Manson[2], D. Ravot[3], J. Hernández-Velasco[1], W.M. Reiff[4], D.N. Argyriou[1]
(1) HMI, (2) ORNL, USA, 3 Univ. Montpellier 2, F 4 Uni Boston, USA
Work to appear in PRB.

Free quantum rotors in inclusion compounds: a study of NH_3 rotations in Hofmann-type clathrates using neutron spectroscopy

Hofmann-type clathrates $Ni(NH_3)_2Ni(CN)_4 \cdot 2G$ with guest molecules G = C_6D_6, C_6H_6 (benzene) and $C_{12}H_{10}$ (biphenyl) are among the rare examples where (almost) free rotations of molecules in the solid state have been observed: the NH_3 groups perform uniaxial quantum rotations. The rotational levels $E_J = B\,J^2$ (J = 0,1,2) are identical in these three compounds with an *effective* NH_3 rotational constant B = 0.71 meV, smaller than the gas phase value B = 0.78 meV. This difference is explained in a rotation-translation model [1] by a coupled reverse rotation of the NH_3 group and its center-of-mass.

Rotational transitions measured so far by inelastic neutron scattering (INS) are those between the rotational levels J=0,1,2. The INS spectra, taken with the time-of-flight spectrometer IN5 at ILL and with the triple-axis-spectrometer V2 at HMI, revealed a most surprising temperature dependence: line widths $\Gamma_{JJ'}$ of transitions J⇔J' broaden much faster for 0⇔2 and 1⇔2 transitions than for 0⇔1 transitions with increasing temperature.

As theoretical treatments of line widths for free rotor transitions were not available, in a joint effort with a theoretical group a new heuristic quantum dissipation algorithm has been formulated and applied to the INS data [2]. In this approach, the dephasing of the quantum mechanical state due to an interaction with the environment has been simulated, whereby thermal fluctuations are implemented through a stochastic perturbation potential. We found individual coupling strengths for the various transitions, having classical temperature dependence. A comparison of experimental and simulated line widths is shown in Fig. 1.

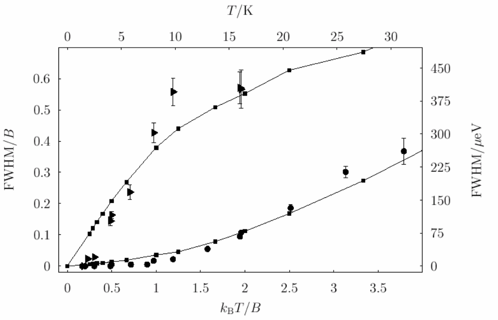

Fig. 1: Temperature dependence of transition line widths (● 0⇔1; ▶ 0⇔2) due to rotor-phonon coupling [2]

Another line broadening mechanism, based on resonant rotor-rotor coupling, has also recently been shown [3] to provide a good description of our INS data, both to the temperature dependence of the observed widths and to their relative magnitude, with only one scaling factor (Fig.2).

Thus two approaches, based on different mechanisms, describe our experimental data.

Using the time-of-flight spectrometer V3 at HMI we have, furthermore, studied transition line intensities S(Q) for different neutron momentum transfers Q.

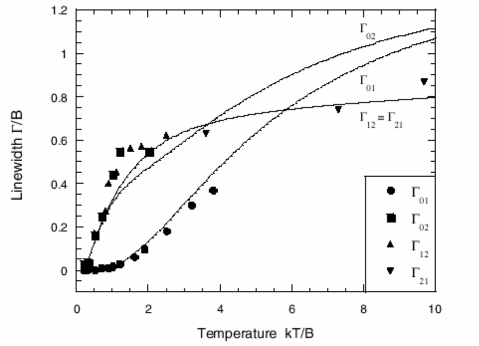

Fig. 2: Temperature dependence of transition line widths due to resonant rotor-rotor coupling [3]

This function is the Fourier transform of the proton density distribution and shows, for a free rotor [4], pronounced maxima at $Q \cdot \rho = 0.68\,\pi$ for 0⇒1 and 1⇒2 transitions and at $Q \cdot \rho = 1.22\,\pi$ for 0⇒2 transitions, where ρ is the proton distance from the rotation axis. As shown in Fig. 3, the experimental values with respect to shape and relative intensities are well described for $\rho = 0.94$ Å which is the value for free (gas phase) NH_3 with B = 0.78 meV. On the other hand, a value $\rho' = 0.99$ Å derived from the effective rotational constant (B = 0.71 meV) leads to a poorer agreement with our experimental data. This implies, in terms of the rotation-translation-coupling model [1], that (within the accuracy of the experiment) the *average* radius of the proton distribution is not essentially modified in the coupled *reverse* center-of-mass rotation.

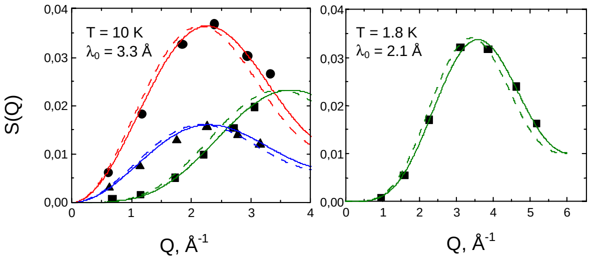

Fig. 3: Experimental transition line intensities (● 0⇒1; ■ 0⇒2; ▲ 1⇒ 2) and calculations for ρ_0=0.94 Å (solid lines) and ρ'=0.99 Å (dashed lines)

In summary, we have shown that new INS data on rotational transitions of free NH_3 rotors in inclusion compounds of Hofmann-type clathrates can be successfully described by theoretical models.

[1] M. Havighorst and M. Prager, Chem. Phys. Lett. 250 (1996) 232
[2] O. Rogalsky, P. Vorderwisch, A. Hüller and S. Hautecler, J. Chem. Phys. 116 (2002) 1063
[3] A. Würger, Phys. Rev. Lett. 88 (2002) 063002
[4] B. Asmussen, unpublished

P. Vorderwisch, O. Sobolev, A. Desmedt, in collaboration with A. Hüller and O. Rogalsky (Univ. Erlangen-Nürnberg)

New integration method for three-dimensional Bragg peaks

The correct determination of collected peak intensities, especially of low intensity peaks, is a principal problem in single crystal structure analysis. Based on an idea of Bolotovsky et al. [1] a new method has been developed for area-detector peak integration, which is based on a statistical analysis of pixel intensities. According to this so-called "seed-skewness" method, the presence of a peak in a predefined integration box is revealed by a significant skewness of the pixel intensity distribution, which is considerably larger than the skewness of the background noise. Starting from a "seed" of pixels with the highest intensities, pixels are added until the skewness outside the "seed" reaches a minimum.

In contrast to other methods, the "seed-skewness" method does not assume any a priori modelling of the reflections. The shape of the peak is determined dynamically, which allows for a clear separation of peak and background. This also avoids the risk of peak truncation, which occurs with integration methods using an integration box of a fixed size like e.g. the so-called "shoebox" method (see Fig.1)

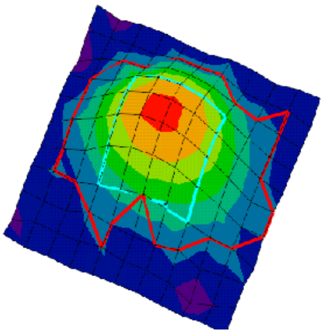

Fig. 1: Shape found by the "seed-skewness" method (red line) and by the "shoebox" method (blue line) for a Bragg peak in one time slice (pulsed neutron data) presented on a logarithmic scale.

Furthermore, it can be shown that the "seed-skewness" method optimises the standard deviations of the peak intensities, and thus increases the precision of the refined parameters determined in crystal structure refinements. As the method works for any three-dimensional reflection, we have now extended it to the integration of three-dimensional Bragg peaks obtained from neutron diffraction [2].

The superiority of the method has first been shown for data collected on the Single Crystal Diffractometer (SCD) at the Intense Pulsed Neutron Source (IPNS) in Argonne/USA, where the dimensions are the detector coordinates x, y and the time-of-flight (TOF) t. Then the program was adapted for Bragg peaks collected at two BENSC instruments (E5 and V1), where the scanning angle ω now replaces the TOF.

For single-crystal data obtained from $YTiO_3$ collected at 295 K (λ = 0.902 Å) on the instrument E5, the diffraction peaks registered were also integrated with the program RACER, which determines the three-dimensional profile by using a best fit ellipsoid [3]. It can be seen that the precision of the refined parameters is better for the data integrated with the "seed-skewness" method which results in a considerably smaller residual *R(F)* (Table 1).

Table 1: Results of the structure refinements of $YTiO_3$.

	SEED	*RACER*
x (Y)	–0.02067(13)	–0.02049(15)
y (Y)	0.07260(12)	0.07270(17)
x (O1)	0.11908(18)	0.11886(19)
y (O1)	0.45817(16)	0.45868(21)
x (O2)	–0.30893(11)	–0.30915(13)
y (O2)	0.30869(11)	0.30878(15)
z (O2)	0.05765(8)	0.05799(11)
R(F)	0.042	0.062
wR(F)	0.038	0.041
$\Sigma\sigma(F)/\Sigma F$	0.0195	0.0264
G.o.f.	5.65	4.75

Single crystals of the large membrane protein PS I have been studied by neutron diffraction on the instrument V1. For these data the program using the "seed-skewness" method has been generalised to search for Bragg reflections automatically and to determine their integrated intensity as well as their centre of gravity coordinates (x, y and ω, see Fig. 2). This now replaces a time-consuming search by hand and guarantees for objective criteria for the determination of the peak in the refinement procedure.

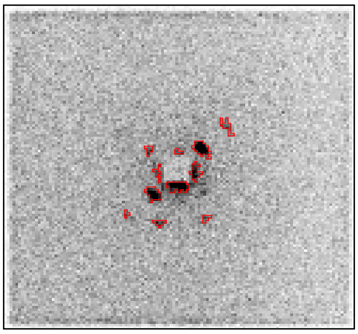

Fig.2: Diffraction pattern of a membrane protein crystal with the c-axis along the neutron beam.

[1] Bolotovsky, R.; White, M.A.; Darovsky, A.; Coppens, P., J. Appl. Cryst. 28 (1995) 86-95.
[2] J. Peters, Habilitation (2002), Université Grenoble I.
[3] Wilkinson, C.; Khamis, H.W.; Stansfield, R.F.D.; McIntyre, G.J., J. Appl. Cryst. 21 (1988) 471-478.

J. Peters, W. Jauch, M. Reehuis, Th. Hauß, Th. Gutberlet, F. Mezei

Neutron generation with GeV protons in massive target blocks

The development of new high-flux neutron sources necessitates an experimental revision of the underlying basic spallation reaction because the present reaction models and codes do not yet reach an adequate precision that would allow basing the source concept exclusively on calculations.

With this objective in mind, we have investigated the production of neutrons with proton beams of 0.4, 0.8, 1.2, 1.8 and 2.5 GeV from the COSY accelerator in FZ Jülich, thus encircling the envisaged bombarding energy for the *European Spallation Source (ESS)*, 1.33 GeV. Three target materials were probed, Pb as the standard material, Hg, the favoured material for ESS, and W because of its higher density. The target blocks, up to 35cm in length and 15cm in diameter, were inserted into the inner chamber of the Berlin Neutron Ball (BNB) as shown in Fig. 1. BNB provides two important quantities, the inelastic nuclear reaction probability P_{reac} and the neutron multiplicity distribution $P(M_n)$, both with exceptionally low detection thresholds.

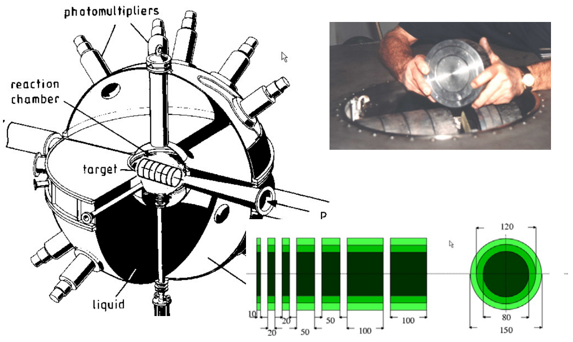

Fig. 1: The neutron detector BNB with massive and highly segmented targets placed 'by hand' in its inner chamber.

Figure 2 selects the most important results from this experiment. The left panel shows the survival probability $(1-P_{reac})$, i.e. the compliment to P_{reac}, for incident protons with E_p= 1.2 and 2.5 GeV as a function of target thickness. $(1-P_{reac})$ decreases exponentially, as expected, with slopes characteristic of each of the three materials Pb, Hg and W and independent of E_p. For 35 cm length, only 10% of the incident protons survive a nuclear reaction in Pb and only 1% in W mostly due to its higher density, while the range due to electronic interaction is as large as 170 and 97 cm for 2.5 GeV protons in Pb and W, respectively. These data allow the precise extraction of the interaction cross sections.

The right panel of Fig.2 exhibits multiplicity distributions for neutrons created by 1.2, 1.8 and 2.5 GeV protons in Pb targets of 2, 15 and 35 cm length. For thin targets, l=2 cm, these distributions originate from a single nuclear reaction. With increasing target size, however, high-energy particles from a first reaction can induce secondary reactions and thus the inter-nuclear cascade develops more and more with increasing l. As the result, the mean neutron multiplicity $\langle M_n \rangle$ nearly doubles when increasing l from 2 to 35 cm and the same is true when rising E_p from 1.2 to 2.5 GeV for fixed l=35 cm.

The various experimental results [1] can be condensed into a quantity expressing the economy of neutron production, i.e. the mean number of neutrons $\langle M_n \rangle$ produced per incident proton and per unit of beam energy. $\langle M_n \rangle/p$ increases sharply with increasing E_p or decreasing electronic energy loss of the proton in the material and culminates between 0.8 and 1.2 GeV at 22 neutrons per proton and GeV for a Pb cylinder with ℓ=35 cm and Ø= 15 cm. W gives a 10% higher yield than Pb and, hence, it would provide a brighter neutron source. HERMES simulations reproduce the measured yields reasonably good.

It appears that 1.2 GeV is the most profitable choice for E_p. A considerably higher bombarding energy would be more appropriate, however, when other aspects as, for instance, the lifetime of the window of the target station are taken into consideration. This all the more as $\langle M_n \rangle/p$ diminishes very slowly above 1.2 GeV.

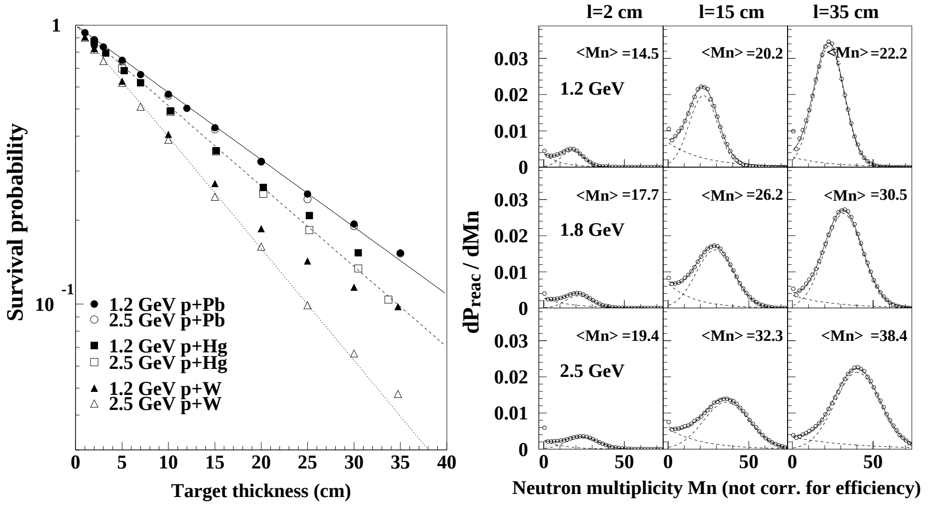

Fig. 2: Left: Survival probability of 1.2 and 2.5 GeV protons in Pb, Hg and W as a function of target length. Right: Neutron multiplicity distributions from 1.2, 1.8 and 2.5 GeV protons impinging on 2, 15 and 35 cm long Pb-targets.

[1] U. Jahnke et al., J. of Nucl. Science and Technology, Suppl.2, (2002) 1187 and refs. therein.

C.-M. Herbach, D. Hilscher, U. Jahnke for the NESSI-collaboration: HMI, FZJ, GANIL, Univ. of Warsaw

A frustrated molecular magnet

A neutron diffraction study of magnetic ordering in a triangular lattice based on a tridentate molecule

A number of organic molecules have been shown to provide pathways for magnetic interactions between transition metal ions in transition metal coordination compounds. Ligands with two binding centres ("bidentate") result in a variety of interesting structural topologies and magnetic ground states. Recently, we have investigated, e.g., $Cu(pym)(NO_3)_2(H_2O)_2$ [1], a quasi one-dimensional (1D) Heisenberg antiferromagnet with pym = pyrimidine, the magnetic ordering in the 2D rectangular network systems Co(ox)(bpy) and $Co/NiCl_2(bpy)$ with ox = oxalate ($C_2O_4^{2-}$), bpy = 4,4'-bipyridine [2,3] and the chiral 3D network $Fe(pym)_2Cl_2$ [4].

Tridentate ligands are expected to add another flavour to magnetism in molecule-based compounds, because they may give rise to triangular topologies and therefore to magnetic frustration. The tricyanomethanide anion, $C(CN)_3^-$, has three-fold symmetry (see Fig. 1, left hand side) and therefore appears to be an ideal candidate.

We have investigated manganese tricyanomethanide, $Mn[C(CN)_3]_2$, that crystallizes in an orthorhombic lattice consisting of two interpenetrating 3D rutile-like networks (see Fig. 1, centre). In each network, the $C(CN)_3^-$ anion gives rise to magnetic exchange interactions between the Mn^{2+} ions ($S = 5/2$) that can be mapped onto the "row model" for partially frustrated 2D triangular magnets. The corresponding magnetic topology is depicted in Fig. 1 (right hand side). In contrast to the ideal triangular lattice, in this model the intra- and inter-row magnetic exchange parameters, J and J', respectively, are different.

A powder sample of $Mn[C(CN)_3]_2$ was synthesised at HMI. Heat capacity data reveal a phase transition at $T_N = 1.18$ K, indicative of magnetic ordering. From magnetic-field dependent data, a saturation field $B_{sat} = 4.2$ T is estimated, at which the low-temperature magnetic ordering breaks down.

The magnetically ordered structure in zero magnetic field was determined from neutron powder diffraction data measured between 0.04 and 1.2 K on the BENSC instrument E6 using a dilution-stick cryostat. It consists of an incommensurate spiral with a temperature independent propagation vector $\mathbf{Q} = [2Q\ 0\ 0]$ with $Q = 0.311$. This corresponds to [0.311 0.311 0] in a quasi-hexagonal representation. In this structure, neighbouring magnetic moments on the Mn ions enclose an angle of $Q \times 360° = 112°$ (see Fig. 1, left). From this angle, the ratio $J'/J = 0.749$ is determined. The ordered moment $\mu = 3.3\ \mu_B$ is about 2/3 of the full Mn^{2+} moment. From the value of T_N the exchange parameters $J/k_B = 0.15$ K can be estimated. Using the latter value and the value of J'/J, theoretical calculations based on the row model give an independent estimate of the saturation field, identical with the measured value of 4.2 T.

Therefore, we conclude that $Mn[C(CN)_3]$ may serve as a "classical spin" ($S = 5/2$) model system for row-model type partial frustration.

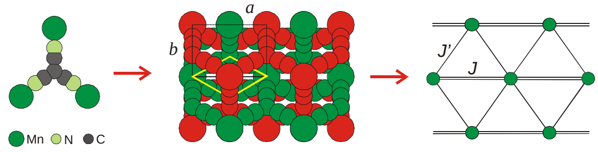

"Tridentate" molecule

Interpenetrating 3D network structure

Partially frustrated triangular topology

Fig. 1: Local geometry around the tricyanomethanide anion in $Mn[C(CN)_3]_2$ (left), the resulting 3D structure of two interpenetrating, independent networks (center), and the magnetic topology of the row model (right hand side).

For ideal triangular lattices ($J = J'$) the existence of three different field-dependent magnetic phases has been reported. A 120° spiral structure in low fields is replaced by the "up-up-down" structure with magnetization 1/3 for fields close to $B_{sat}/3$. At higher fields, the so-called 2-1 structure is realized. In our magnetic-field dependent neutron diffraction measurements, using the horizontal field magnet HM1, we did indeed observe a similar sequence of magnetic phases in $Mn[C(CN)_3]_2$, see Fig. 2.

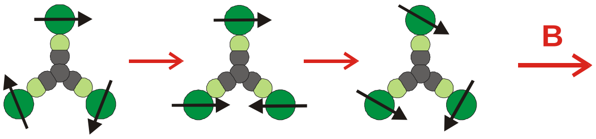

B < 1.35 T Intermed. B B > 1.60 T

Fig. 2: The three different magnetic phases observed in $Mn[C(CN)_3]_2$ when applying a magnetic field along the row direction, namely the spiral structure, the up-up-down like, and a 2-1 like phase (from left to right).

Interestingly, the corresponding propagation vector Q is magnetic-field dependent, initially increasing with increasing field. However, at the transition to the up-up-down like structure, surprisingly no lock-in transition to $Q = 1/3$ is observed, which was expected theoretically. In contrast, Q varies continuously through an intermediate field range, before the transition to the 2-1 like phase takes place. The value $Q = 1/3$ is reached only at B = 1.9 T, i.e. in the 2-1 phase, but for higher fields it decreases again. This means, the magnetic structure is incommensurate for all field values except 1.9 T. To date, there is no explanation for this highly unexpected result and more theoretical work is required. (This work was published in ref. [5]).

[1] R. Feyerherm *et al.,* J. Phys.: Condens. Matter. **39** (2000) 8495
[2] R. Feyerherm *et al.,* J. Phys. Chem. Sol. **63** (2002) 71
[3] R. Feyerherm *et al.,* Appl. Phys. A **74** [Suppl.] (2002) S778-S780
[4] R. Feyerherm *et al.,* cond-mat/0302121 (2003).
[5] R. Feyerherm, A. Loose, and J. L. Manson, J. Phys.: Condens. Matter **15** (2003) 663-673.

R. Feyerherm

Studies of U_2Pd_2In single crystal up to 17 T

Uranium intermetallics exhibit a rich variety of interesting phenomena (e.g. long-range order, superconductivity, Kondo, heavy fermion state, non-Fermi liquid state, etc.) due to several facts. First, 5f electrons, which are primarily responsible for the physical properties of these systems, have to be treated as relativistic particles (their speed is non-negligible with respect to the speed of light), they posses both spin and orbital magnetic moments with a very strong spin-orbit coupling (in contrast to the d electron systems in which the orbital part is usually quenched), and they are situated nearby the Fermi level (in contrast to 4f materials in which the 4f states are well screened by valence states). Depending on the geometry, distance, number and nature of atoms in the U-atom's neighbourhood, the 5f electrons partially or completely lose their original 5f character – they become hybridized with other states [1]. In the strong hybridization limit the system is non-magnetic, in the weak one it resembles its 4f analogue. Therefore, 5f systems are so rich in magnetic properties and at the same time sensitive to various thermodynamic parameters like temperature, magnetic field and pressure. The existence of a strong spin-orbit coupling causes a large magnetocrystalline anisotropy (magnetic moments are kept in certain crystallographic directions), which exceeds anisotropies of conventional hard magnetic materials. It is therefore of primary importance to understand this mechanism in detail.

With these issues in mind, we have conducted a study of the tetragonal antiferromagnetic (AF) U_2Pd_2In, in which magnetic moments reside only on uranium ions [2]. A complicated non-collinear ground state arrangement exists in this compound (Fig. 1a) below 38 K. In sufficiently high magnetic fields, AF interactions are broken and a field-induced metamagnetic state is formed. In the limit of very high fields, a field-forced ferromagnetic (FIF) state is established. Most of the magnetic studies are performed by means of magnetization measurements, which sense only the total magnetic response of the material and are not able to reveal the contributions of individual atoms. For that, neutron diffraction is an indispensable tool.

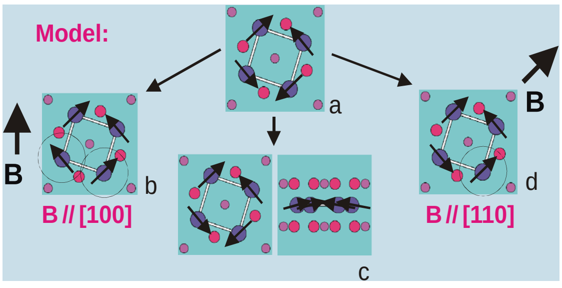

Fig. 1: The ground state antiferromagnetic structure of U_2Pd_2In (a) consists of dimerized U magnetic moments (1.7 μ_B) confined to the [110] type mirror planes. Upon application of magnetic field along the a axis (b), c axis (c) and [110] direction (d) theory predicts [3] that because of strong magnetocrystalline anisotropy only specific moments (inside circles) change their directions depending on the direction of applied field. Common feature is that all the moments stay in the [110] type mirror planes. For the field directed along the c axis no flip transition occur - U moments only tilt out of the basal plane.

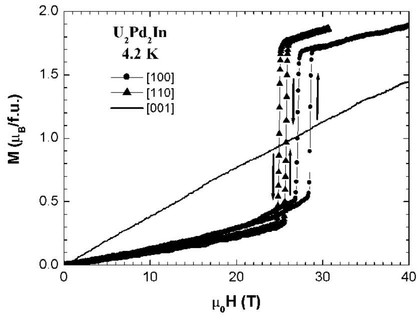

Fig. 2: High-field magnetization curves of U_2Pd_2In *measured at 4.2 K along the* c *axis ([001]), along the* a *axis ([100]) and in the [110] direction.*

Unfortunately, the critical fields at which the AF interactions are broken in U_2Pd_2In are too high. For the a axis ([100]), it amounts to 29 T and for the [110] direction to 26 T. Along the c axis ([001]), no transition is observed up to 57 T although this is the direction of the easy-magnetization axis (Fig. 2). However, it appears that above 33 K one can achieve modifications of the ground state AF structure at 17 T (maximum available steady magnetic field for neutron research). Unfortunately, the original step-like character of the field-induced transitions is lost and an S-shaped magnetization curve is observed at this temperature. Nevertheless, an analysis of all the data sets scaled together revealed field-induced noncollinear magnetic structures (Fig 1b, c, d) that agree with ab-initio theoretical calculations [3] for low temperatures. These results clearly demonstrate the importance of the hybridization-induced magnetocrystalline anisotropy in U_2Pd_2In that locks U moments in the [110] type mirror planes even at elevated temperatures. However, unlike at low temperatures, the transition is not of the spin-flip type, where the direction of the U moment changes abruptly, but the moment magnitudes of specific U ions first decrease with increasing field (e.g. for fields along the [110] direction the moment is originally antiparallel to the field), change direction and increase again. In the first approximation, moments originally perpendicular to the field are not affected.

[1] V. Sechovský and L. Havela, in *Handbook of Magnetic Materials*, Vol. 11, ed. K.H.J.Buschow, (Amsterdam: North-Holland, 1998) p. 1

[2] K. Prokeš et al., Physica B: Condensed Matter, 294-295 (2001) 288

[3] L. M. Sandratskii and J. Kübler., Physica B: Condensed Matter, 217 (1996) 167

K. Prokeš

Exposure of the EXAFS background

The X-ray absorption spectra of atoms bound in molecules or condensed matter show typical oscillations behind any of the absorption edges. This effect – known as EXAFS (Extended X-ray Absorption Fine Structure) – can be used to extract information about the structure of soft or solid materials.

In the last decades the analysis of the EXAFS data occurred in two steps: In a first one, the oscillatory part of the measured absorption data that contains the geometrical structure information, was separated from the smooth background part, which represents the embedded atom contribution. After that the oscillatory part was analyzed by a Fourier transformation technique. This analysis method neglects the error correlations between the structure parameters and the background function and makes it difficult to follow the error propagation from the measured input data to the output of the data analysis in a systematic, quantitatively reliable way.

To overcome these problems we developed a new data analysis procedure that determines the background function together with the structure parameters in one fitting process. The analysis of X-ray absorption data $\mu_{\exp}(k)$ as a function of the wave number k requires the determination of the detection efficiency $A(k)$ and the embedded atom absorption $\mu_0(k)$ (absorption without the contribution of the neighboring atoms) to obtain the EXAFS function $\chi(k)$. From the latter the radial distances R_j, Debye-Waller (DW) parameters σ^2_j, and anharmonicity parameters $C_{3,j}$ have to be inferred. Alternatively, instead of DW parameters for each scattering path j, the first few spring constants κ_s of a force-field model can be determined. We use a Bayesian approach to solve this ill-posed inversion problem. First $A(k)$ is obtained from

$$A(k) = \frac{\langle \mu(k) \rangle}{\langle \mu_0(k) \rangle}; \qquad \mu(k) = \mu_{\exp}(k) - \mu_{\mathrm{pre}}(k) ,$$

where μ_{pre} is the pre-edge background and where the brackets mean that the cross sections μ and μ_0 have been subjected to a smoothing procedure. The *a priori* embedded atom absorption $\mu_0(k)$ is obtained from calculations using the FEFF-program [1] and the smoothing procedure is performed following a proposal by Strutinsky and Ivanjuk [2].

Because of systematic errors in the oscillatory structure of $\mu_0(k)$, which are due to the approximate treatment of the many-electron problem in FEFF, the absorption function is written as

$$\mu(k) = A(k)(\mu_0(k) + \nu(k))(\chi(k) + 1)$$

with a cubic-spline correction function $\nu(k)$ for $\mu_0(k)$. The ordinates ν_p at the support points k_p of the spline are determined simultaneously with the model parameters R_j, κ_s, and $C_{3,j}$. For the direct problem FEFF is used for the electronic part and the cluster approach of Poiarkova and Rehr [3] for the lattice dynamics.

To illustrate the procedure we have used K-edge data taken at room temperature on a well-ordered Ge sample by Newville [4], where the radii are essentially given by the lattice parameter, and for the diamond type lattice of Ge we use one stretching mode (κ_1) and one bending mode (κ_3). The inverse problem is treated with our stochastic regularization method (Bayes-Turchin approach) [5]. The input of the procedure consists of an *a priori* guess of all model parameters, in particular: $\nu(k_p) = 0$, $C_{3,j} = 0$, all R_j corresponding to ideal lattice distances, all σ^2_j from the correlated Debye model with $\theta_{\mathrm{Debye}} = 360$ K or spring constants κ_1=100 N/m and κ_3=14 N/m. The results of the fit are *a posteriori* model parameters, including their errors and error correlations, *a posteriori* functions $\mu(k)$ and $\chi(k)$, and final spring constant values.

The data have been analyzed in k space between 3 Å ≤ k ≤ 20 Å. The part k = 2 – 10 Å is shown in Fig. 1. It appears that the strong oscillations in the embedded atom cross section μ_0 predicted by FEFF (dashed line) needed to be significantly damped in order to get a good description of the data.

The extension of this method to overlapping $L_{1,2,3}$ edges of 3d-transition metals in the soft x-ray regime is in progress. Instead of the expression above we now have to fit

$$\mu(k) = A(k) \sum_{s=1}^{3} D_s \left(\left(\mu_0^{(L_s)}(k) + \nu^{(L_s)}(k) \right) \left(\chi^{(L_s)}(k) + 1 \right) \right),$$

where D_s are the absolute normalization factors for each of the three cross sections, and A(k) has to be adjusted properly.

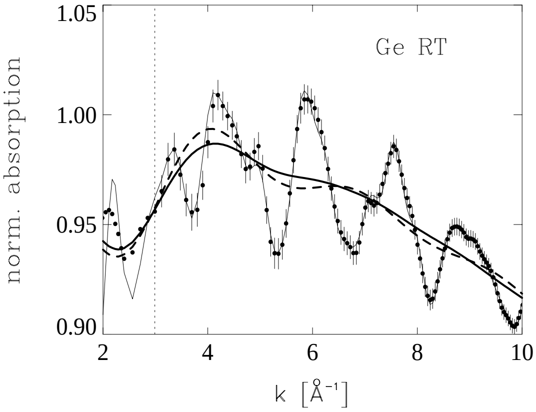

Fig.1: Wave number dependence of the measured absorption data $\mu_{exp}(k)$ divided by the detection efficiency A(k) (solid points), a posteriori $\mu(k)$ (thin solid line), a priori $\mu_0(k)$ (dashed line), and a posteriori $\mu_0(k)$ (thick solid line). The vertical dashed line marks the lowest k-value of the fit region.

[1] A.L. Ankudinov and J.J. Rehr, Phys. Rev. **B** 56, R1712 (1997)

[2] V.M. Strutinsky and F.A. Ivanjuk, Nucl. Phys. A **255**, 405 (1975)

[3] A.V. Poiarkova and J.J. Rehr, Phys. Rev. **B** 59, 948 (1999)

[4] M. Newville, Ph.D. thesis, University of Washington, 1994

[5] H.J. Krappe and H.H. Rossner, Phys. Rev. **B** 61, 6596 (2000); Phys. Rev. **B** 66, 184303 (2002)

H:J: Krappe, H.H. Rossner

Chemical gradients in superalloy Inconel 706

Inconel 706 is a wrought Ni-Fe base superalloy which is used for high temperature services [1], e.g. for gas turbine discs. It is an alloy that derives its good mechanical properties after age-hardening from a fine dispersion of ordered face centred cubic γ' and ordered tetragonal γ'' phases or γ'-γ'' co-precipitates in the solid solution γ matrix. However, the microstructural stability of Inconel 706 under service above 700°C for more than 200.000 hours is not sufficient. This is because of the growth of the hardening precipitates and their phase transformation into semicoherent η precipitates. Both lead to a strong reduction of strength. In addition, Inconel 706 tends to embrittle by stress induced grain-boundary oxidation.

Usually, in order to improve the creep rupture life of the Inconel 706, one applies a stabilization heat treatment (ST) between the solution treatment and the double-aging treatment. By this treatment, Ni_3Ti based η precipitates are produced [2-4] that do not appear after direct ageing. They form either at the grain boundaries or inside the grains. Optimum creep rupture properties were achieved by a further slight modification of the ST heat treatment cycles as proposed by [5].

Up to now, the morphology of the precipitates, which cause the improved properties and their inner arrangement, is not exactly known. In the present study the microstructure of the two differently heat treated materials was investigated by means of high resolution methods such as transmission electron microscopy (HRTEM) and three-dimensional atom probe (3DAP).Both direct aged (DA) and modified standard (MST) heat treated IN 706 samples were analyzed by 3D atom probing. Fig. 1 displays reconstructed positions of Ti (pink) Al (blue) and Nb (yellow) atoms in a volume of 7.8 x 7.8 x 23.1 nm^3 of the alloy after MST heat treatment. The reconstructed volume contains regions enriched or depleted in Ti, Nb and Al atoms. Since these elements are usually the major constituents of the various precipitate phases, the Ti, Nb and Al rich regions are either γ' or γ'' precipitates, or γ'-γ'' co- precipitates.

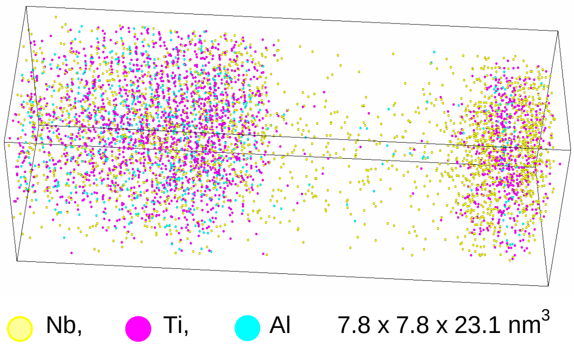

Fig. 1 Three-dimensional reconstruction of Nb, Ti and Al atoms of MST heat-treated Inconel 706 alloy

The region depleted of Ti, Nb and Al is generally the continuous γ matrix. The Ti, Nb and Al lattice planes in the γ' phase (left precipitate) are clearly visualized by the stripy pattern. The precipitate on the right hand side is a sandwich γ''-γ'-γ'' co-precipitate which is shown from a different angle in Fig. 2a. The lattice planes inside the precipitate are rich in Al and Ti, i.e. this region is γ'.

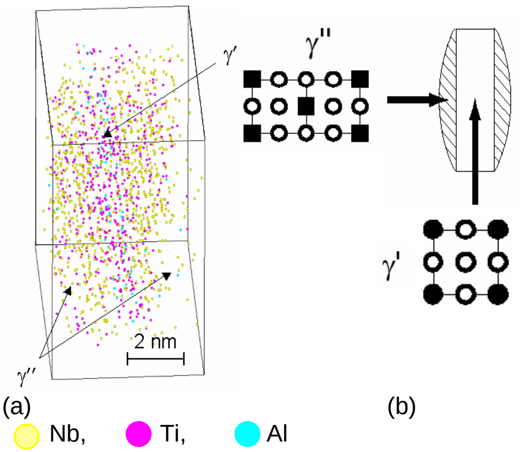

Fig. 2 (a) Three-dimensional reconstruction of Nb, Ti and Al atoms of a sandwich γ''-γ'-γ'' co-precipitate after MST heat treatment (b) schematic image of γ' and γ'' phases.

The regions right and left of this γ' phase are rich in Nb and Ti while practically no Al has been measured there, i.e. they correspond to the composition of the γ''-phase. The γ' phase is coherent to the γ'' in the (001) plane. The morphology of the γ'/γ'' co-precipitate is shown in Fig. 2b. The schematic sketch in Fig. 2b shows the arrangement of both phases in the precipitate.

From the concentration depth distribution of the components Al, Nb and Ti through a γ'/γ'' co-precipitate, the width of the interface between γ' and γ'' of about 0.2 nm can be deduced.

[1] E.E. Brown and D.R. Muzyka, “Nickel-Iron Alloys”, Superalloys II, ed. C.T. Sims, N.S. Stoloff and W. Hagel (New York, John Willey & Sons, 1987), 165-188

[2] H.L. Eiselstein, “Properties of a Fabricable, High Strength Superalloy”, Metals Engineering Quarterly, November (1971), 20-25

[3] J.H. Moll, G.N. Maniar and D.R. Muzyka, “Heat Treatment of 706 Alloy for Optimum 1200 F Stress Rupture Properties”, Metallurgical Transactions, 2 (1971) 2153-2160

[4] L. Remy, J. Laniesse and H. Aubert, Materials Science and Engineering, 38 (1979) 227-239

[5] J. Rösler, and S. Müller, D. Del Genovese, M. Götting, "Design of Inconel 706 for Improved Creep Crack Growth Resistance", in Superalloys 718, 625, 706 and Various Derivatives, E.A. Loria (eds.), TMS, pp. 523 -534 (2001).

N. Wanderka, V. Kindratchuk

Structure investigations in nanomaterials using SANS

Small Angle Neutron Scattering (SANS) is used as a non-destructive technique for the analysis of nano-structures in modern materials. This nano-analytical technique allows composition, density and magnetisation fluctuations to be identified on a length scale between 0.5 and 300 nm. Macroscopic averages of the nano-structural parameters are obtained and correlated with basic material properties in magnetic liquids, magnetic and ceramic nanomaterials, in amorphous and partly crystallised materials. The quantity actually measured in SANS is the intensity of the neutron flux as a function of the Q-value – the momentum transfer in the probe.

Core-shell nanostructures in Magnetic Liquids: Solvent dependent arrangement of surfactants.

Ferrofluids are liquids with magnetic properties. They consist of small particles with diameters of several nanometres floating in a carrier liquid (water, organic solvents). The particles themselves are built of a core contributing the magnetic properties (Cobalt, Magnetit, Ba-Hexaferrite) and a nonmagnetic shell consisting of organic macromolecules. The shells separate the particles from each other and prevent them from sticking together and forming larger structures. This way they create a colloidal suspension that can remain stable for long periods of time.

The work presented here focused on a comprehensive study of nanoscaled structures in ferrofluids by a systematic variation of the magnetic core materials, shell-forming surfactants (mono- and bi-layers) and of the carrier liquids. This research was performed within the DFG Priority Program 1104.

Currently great effort is undertaken to prepare new bio-compatible magnetic liquids for potential bio-medical applications. Magnetically supported drug targeting and delivering are mainly determined by the properties of the shell: Immunoassays and antibodies have to be attached selectively by chemical bonding to the shell via functional groups. In this context, two identical magnetite-ferrofluids with oleoylsarcosine as surfactant have been prepared. They were stabilized in different solutions in water or in toluene. Combining contrast variation using polarized neutrons (SANSPOL) with H/D isotope variation of solvents allows different magnetic and non-magnetic structural units of ferrofluids to be identified by Small Angle Neutron Scattering. A new approach of data analysis has been developed which uses in a first step the least-square fit of the nuclear magnetic cross-term as obtained from the difference of the scattering intensities of the two neutron polarisation states $I^{(-)}(\boldsymbol{Q}\perp\boldsymbol{H}) - I^{(+)}(\boldsymbol{Q}\perp\boldsymbol{H})$ = const * $F_N\,F_M$ (Fig. 1). Here $I^{(-)}$ and $I^{(+)}$ refer to the intensities for polarized neutrons with negative and positive spin, respectively. F_N is the polarization independent nuclear contribution, F_M the magnetic one. Thanks to this method, only magnetic particles are separated out allowing a precise determination of size, composition and magnetization of the particles.

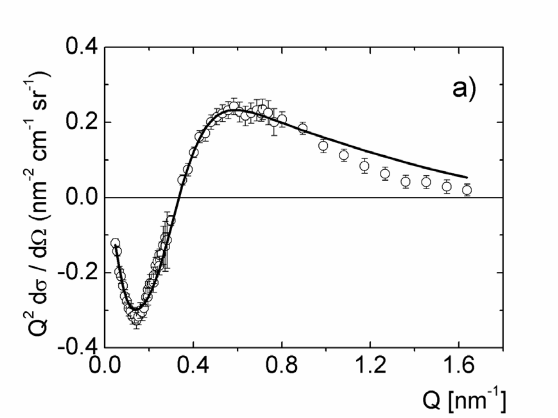

Fig.1: *The fit of the difference (solid line) of the SANSPOL intensities $I^{(+)}(\boldsymbol{Q}\perp\boldsymbol{H}) - I^{(-)}(\boldsymbol{Q}\perp\boldsymbol{H})$ corresponds to the magnetic-nuclear cross term of magnetic core-shell particles and magnetic aggregates.*

It turned out that two magnetic units are present in this ferrofluid. Besides the main component of magnetic core-shell particles, a definite amount of larger aggregates was identified. These aggregates

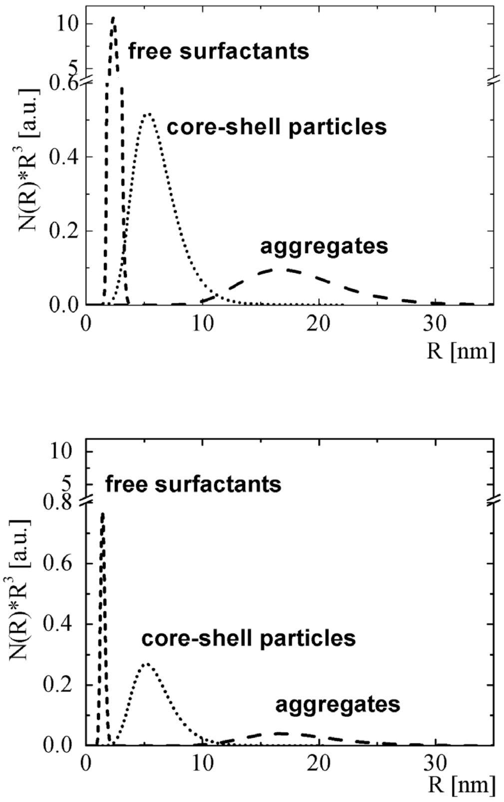

Fig.2: *Volume weighted size distributions of the structural parts in water (top) and toluene (bottom) based ferrofluids*

consist of a mixture of magnetic cores and a higher amount of surfactants with a broader size distribution. Using this result derived from the cross term, the reconstruction of the curves for the two polarization directions revealed large discrepancies with respect to the measured curves at larger Q-values. This is the direct evidence that the sample must contain additional non-magnetic nano-structures of similar sizes. In a second step, three structural parts are analysed by a simultaneous least-square fit of all curves using constraints between various parameters. Beside the previous magnetic contributions, a non-magnetic surfactant structure was identified in both the water and toluene based ferrofluids. The final fits correspond to the volume size distributions of Fig. 2. The averaged core radii <R> of 5 nm were found to be identical in both solvents.

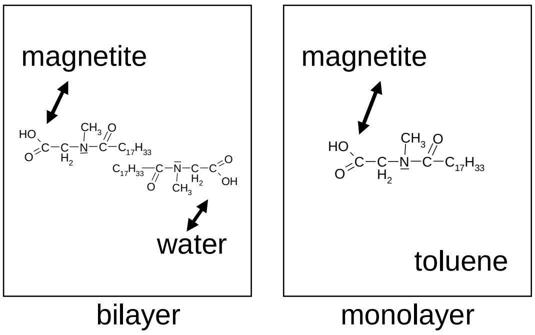

bilayer monolayer

Fig.3: This sketch shows the bonding of oleoylsarcosine on the magnetite surface via the hydrophilic acid group. A bilayer is necessary for the solubility in water whereas a monolayer can stabilize the cores in toluene.

As main result the shell thickness of the surfactant, oleoylsarcosine, is found to be clearly different in ferrofluids based on water (2.3 nm ± 0.1 nm) and on toluene (1.9 nm ± 0.1 nm). Therefore, we conclude that the surfactant must form a bi-layer in water and a monolayer in toluene (Fig.3). This indicates that bonding of the surfactants to the magnetic core must be mediated via the hydrophilic acid group and not via the nitrogen atom. This is an important information in view of potential use of such types of ferrofluids for drug targeting.

[1] A. Wiedenmann, Lecture Notes in Physics (2002) S. 33-61
[2] A. Heinemann, A. Wiedenmann J. Appl. Cryst. 2003, accepted for publication

---

A.Wiedenmann, M.Kammel, A. Hoell, A. Heinemann

Microstructures in Semi Solid Metal Alloys under Shear Stress: SANS and Rheological Characterization

Metal alloys in the semi-solid state show special thixotropic flow behaviour. In this semi-solid state the alloys consist of a fluid phase and a globolitic solid phase. Modern casting processes, the so-called "Thixoforming"-processes take advantage of these special characteristics. In a common project of the German Research Foundation (Wi 1151/1-1) with the Institut für Verfahrenstechnik of RWTH Aachen, Germany, we investigate the structure evolution during solidification when shear fields are applied. SANS measurements are performed in-situ simultaneously with rheological characterization. A specially designed rotation rheometer and a heatable shear cell was in stalled at the SANS instrument of the HMI (V4).

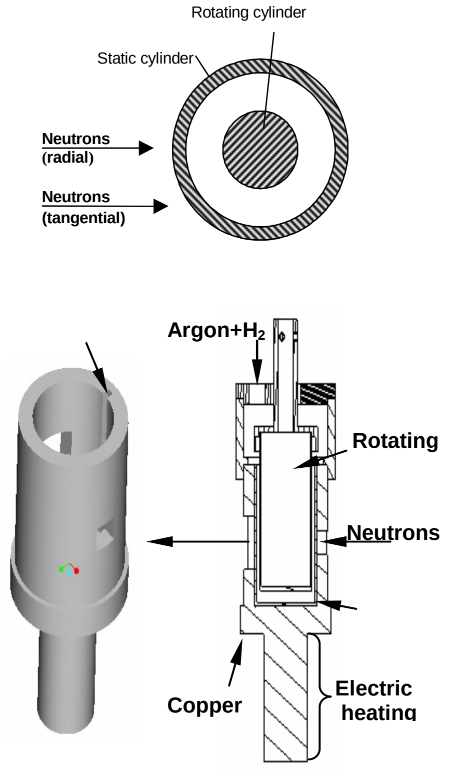

***Fig. 4:** Sketch of the heatable shear cell*

The inner cylinder is rotating to impress a certain shear stress while the outer one is fixed. Both cylinders are composed of synthetic quartz. Measurements are possible in radial and tangential geometries.

The set-up was tested using a synthetic polymer suspension generated at the RWTH Aachen with a mean particle diameter of 80 nm and a solid fraction of ~40%. The rheological measurements showed that the viscosity changed with every change of the shear rate, whereas the SANS just observed an alteration in microstructure at certain points. Fig.5 shows the SANS pattern corresponding to a lamellar hexagonal arrangement of particles induced by the shear stress. At low shear rates, the planes are stacked parallel to the flow direction while at high shear rates the planes are arranged perpendicular to it.

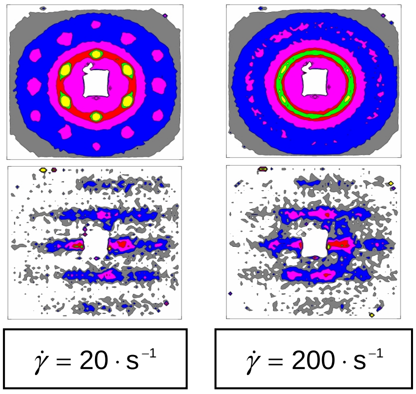

$\dot{\gamma} = 20 \cdot s^{-1}$ $\dot{\gamma} = 200 \cdot s^{-1}$

Fig. 5: SANS of polymer suspensions at different shear-rates in radial (upper part) and tangential scattering geometry (lower part)

For the investigations of a Sn-15%Pb metal alloy the cell had to be optimized concerning heating and oxidizing conditions. The alloy was cooled from 225°C to the solid state at 197°C and reheated again: at first without a shear strain, then with a shear rate of $100s^{-1}$. As expected, the intensity increased after reaching the semi solid state and reached the highest value in the solid state. This effect is reversible. When the results with and without shear rate are compared, it can be stated that a mechanical load during cooling leads to smaller particles and a more isotropic structure (Fig. 6).

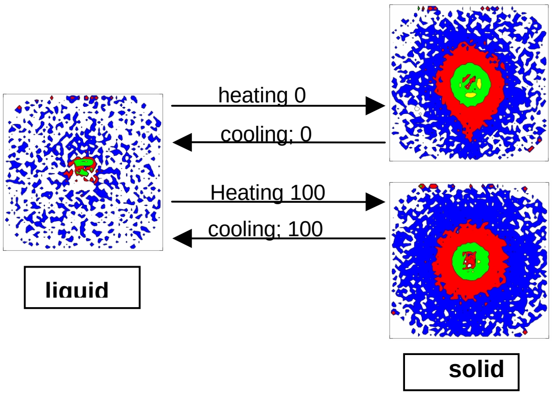

Fig. 6: *SANS patterns of Sn-15%Pb alloy during solidification without and with shear stress*

Afterwards the alloy was cooled down to the semi solid state applying different shear rates ($100s^{-1}$, $200s^{-1}$). The integral intensity increased after achieving the semi solid state, but was not completely reversible as a result of a small rate of oxidization. Nevertheless, a change in structure occurs when the alloy is sheared while cooling and this structure disappears after heating up (Fig. 7, $100s^{-1}$).

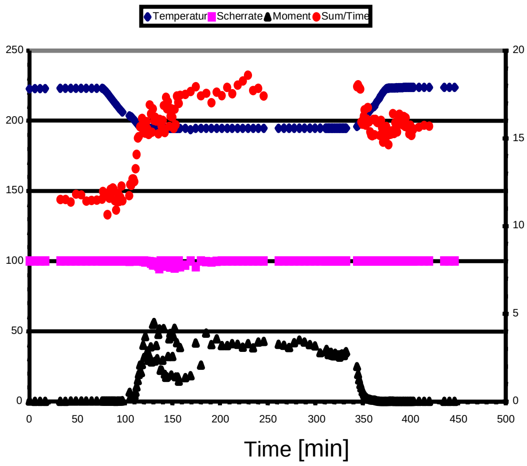

Fig. 7*: Correlation between temperature, viscosity and total SANS intensity during cooling and reheating of a Sn-15%Pb alloy*

A. Wiedenmann, J. Pape, M.Modigell

Guided transmission of 3 keV Ne7+ ions through nanocapillaries in PET polymers: dependence on the capillary diameter

The outstanding progress in nanotechnology is accompanied by a continuous miniaturization of interfaces used in microelectronics and related fields. Particular attention has been paid to linear structures of mesoscopic dimensions, such as pores or capillaries. Advantageous tools for producing capillaries with great precision are ion tracks created by energetic projectiles in the solid [1].

Recently, we started experiments in which PET (Mylar) polymer foils of 10 µm thickness were irradiated by 400 MeV xenon-ions. Capillaries with a diameter of a few hundreds nm in foil were obtained etching ion tracks using NaOH [2].

To study the capillary interior, we measured the transmission of 3 keV Ne^{7+} ions through the capillaries. The final charge state of the transmitted ions was analyzed including neutrals by means of an electrostatic deflector. Angular distributions of the transmitted Ne^{7+} ions obtained with insulating PET material were compared to results with capillaries covered by a thin Ag metal film. Transmission measurements were made with a foil tilted with respect to the incident beam direction. Particular emphasis was given to the comparison of results achieved with capillary diameters of 100 and 200 nm.

The angular distributions of the transmitted Ne^{7+} ions for PET are found to be essentially different from those obtained with metals. In the latter case, the Ne^{7+} angular distribution is rather narrow (FWHM of 1°) and ion transmission vanishes when the foil is tilted (Fig. 1). In contrast, for the 5° tilted PET foil, the angular distribution of the Ne^{7+} is found to be relatively broad (FWHM of 4°-6°) and the maximum is shifted by 5°. Similar effects were found for tilt angles as large as 25°. The latter observation suggests a “guidance” of the Ne^{7+} ion within the capillary, i.e. scattering events alter the main propagation direction of the Ne^{7+} ions along the capillary axis. This observation is surprising, since scattering events are expected to change the charge state of the projectile, i.e., highly charged ions scattered from the surface by, e.g., 5° are neutralized [3].

The present finding of ion guidance provides evidence that the inner walls of the capillaries become charged and close collisions with the surface are suppressed.

The charge deposition occurs by means of a self-organizing process, which allows charge up until a certain maximum value where the electric field becomes so high that the ions are deflected and further charge deposition is inhibited.

From Fig. 1 it is seen that the transmissions of the ions depend both on the tilt angle and the capillary diameter. Specifically, for 0° tilt angle the transmissions are about equal for the two capillary diameters, whereas for 15° tilt angle the transmission through 100 nm capillaries is about an order of magnitude larger than the corresponding transmission through 200 nm capillaries. This finding supports the picture of ion guiding in the capillary. The higher the aspect ratio of the capillary the higher the capability to bend the ions along the axis of the capillary and transport them to its exit.

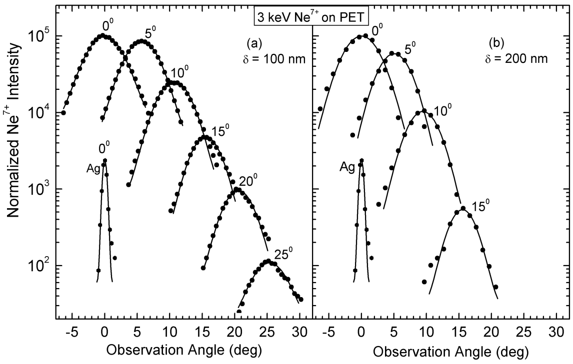

Fig. 1: Angular distributions of Ne^{7+} ions transmitted through capillaries in PET. The tilt angle is indicated. Also plotted are data for capillaries in Ag. In (a) and (b) results for capillary diameters of 100 and 200 nm are compared.

As the present effects are associated with charge deposition, we expect a time dependence of the capillary guiding. When the beam is turned on we observe the capillary charging with a time constant of τ_c. We obtained 2.5 min and 0.75 min for 100 nm and 200 nm capillaries, respectively. These values are plausible, since within the linear model $\tau_c = Q_\infty / J_{in}$ where Q_∞ is the final charge deposition in the capillary [2], and the incident beam J_{in} increases by a factor of 4 when the capillary diameter increases from 100 nm to 200 nm. After 10 min the beam is turned off to verify the capillary discharging which was found to take place with an initial time constant of τ_d^0=40 min. This is done by probing the transmission by short beam pulses whose contributions to the capillary charging can be neglected. It is noted, however, that due to the non-linear behaviour of the charge depletion, observable charges remain in the capillary even after weeks.

[1] R. Spohr, in Ion Tracks and Microtechnology, edited by K. Bethge, Vieweg, Braunschweig (1990).
[2] N. Stolterfoht, J.H. Bremer, V. Hoffmann, R. Hellhammer, S. Petrov, D. Fink, and B. Sulik, Phys. Rev. Lett. 88 (2002) 133201.
[3] Z. Pešić, H. Lebius, R. Schuch, Gy. Víkor, V. Hoffmann, D. Niemann, and N. Stolterfoht Nucl. Instrum. Methods Phys. Res. Sect. B164 (2000) 511-516.
[4] N. Stolterfoht, V. Hoffmann, R. Hellhammer, D. Fink, A. Petrov, Z.D. Pešić, and B. Sulik, Nucl. Instrum. Methods (2003) in print.

N. Stolterfoht, R. Hellhammer, Z. D. Pešić,
V. Hoffmann, A. Petrov, D. Fink, B. Sulik

Ion-track based microstructures for electronic applications

Irradiating a thin polymer foil with fast ions and subsequent etching leads to the creation of a dense array of straight pores – ion tracks – with diameters of several hundred nanometers. In the present report we discuss a novel application of membranes created this way: the production of miniature electronic components, like magnets or transformers. Fig 1 shows a sketch of these devices. The wires crossing the foil were created by deposition of evaporated metal in selected ion tracks. We did not include ferromagnetic cores in these prototypes, as they become obsolete at the high frequencies where the devices are thought to be used.

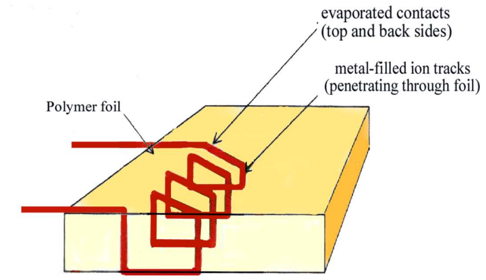

ion track magnet

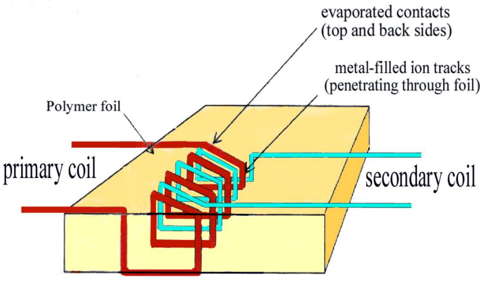

ion track transformer

Fig. 1: *Ion track based micro-magnets and micro-transformers, principle sketch.*

Similarly, first ion-track based microcondensor structures have been realised (see Fig. 2).

For a first feasibility test of micro-magnets and micro-transformers, we started with relatively large devices with areas of a few mm^2 in 20 µm thick kapton foils and with only a few windings. The conducting connections were made of copper, silver, and/or gold. Though these devices still show a poor inductance and operate reliably only up to the GHz range, they already allow reasonable signal transformation and have non-negligible quality factors.

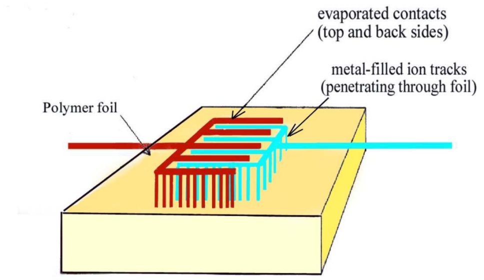

ion track condensor

Fig. 2: *First ion track-based microcondensor structures.*

In Fig. 3 (top), the individual etched tracks of the PI microporous foil can be clearly recognized in the transmission optical microscope image as small black spots. This Figure indicates that a further reduction in size by one more order of magnitude is still possible, which will make the devices interesting for technical applications, e.g. in anticollision radar systems.

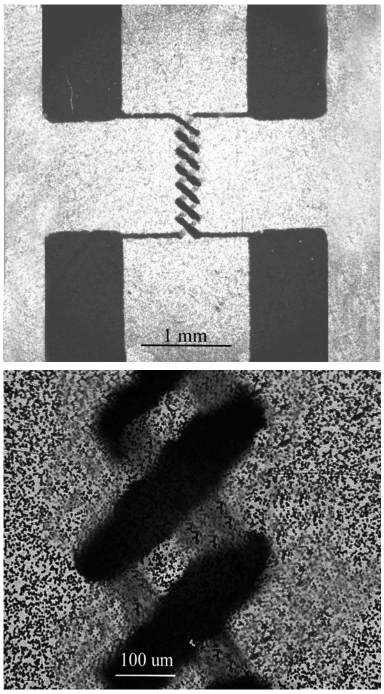

Fig. 3: *First miniaturized ion-track based transformer. Top) overall view, Bottom) detail. Grey: microporous PI (polyimide) foil, dark: evaporated Au wires.*

A. Petrov, D. Fink, P. Szimkowiak; G. Richter[1],
P. Alegaonkar[2]; A. Berdinsky[3]

1. HMI, Dept. I/DH, 2. Pune University, India, 3. Novosibirsk State Technical University, Russia

Thermal-spike-induced crystal growth in nanocrystalline nickel

In nanocrystalline materials many physical properties are altered compared to their coarser-grained counterparts because 30% of the atoms belong to or are affected by the presence of interfaces. Due to their distorted structure these interfaces are expected to affect also the behaviour of radiation-induced defects [1,2] and the time evolution of thermal spikes – regions along the track of the ion with a very high temperature of the electron gas. It is argued that a small grain size leads to a reduced thermal conductivity and, consequently, to an enhancement of the spike lifetime. The work presented here aims at an exploration of the latter possibility.

Commercially available nanocrystalline Ni foils of 100 and 50 µm thickness were irradiated with 230 MeV Xe or 350 MeV Au ions at room temperature. Prior to and after irradiation, we examined the samples using X-ray diffractometry. For the evaluation of the X-ray diffraction data the (111) and (200) peaks have been used. Both a small average size of the crystallites and the presence of microstrains in a nanocrystalline sample lead to broadening of X-ray diffraction peaks, and we had to use a special mathematical technique in order to separate them. The Lorentzian line width w_L (FWHM) is linked to the mean grain size D by the Debye-Scherrer formula:

$$D = \frac{2}{\pi} \frac{K\lambda}{(w_L - w_I)\cos\theta}, \qquad (1)$$

where $K \approx 1.15$ is a crystallite form factor [3] and w_I is the instrumental resolution. D is about 12 nm for the unirradiated specimens. Fig. 1 displays w_L as a function of ion fluence for irradiation with Au ions. It can be seen that w_L decreases rapidly below 1×10^{14} ions/cm^2 followed by small changes at higher fluences. Obviously, in the beginning ion bombardment induces a rapid crystal growth accompanied by a rapid decrease of microstrains. This process ends on a fluence scale of a few 10^{13} ions/cm^2 and is followed by a comparatively slow process. Tentatively, the two processes are described by

$$w_L = w_{L0} e^{-\sigma\Phi t} - a\Phi t + b, \qquad (2)$$

where w_{L0} denotes the total line width change due to the fast process occurring with a cross-section σ. The slow process is empirically approximated as a straight line; the physical meaning of its parameters a and b is not clarified yet. For both, the (111) and (200) peaks the cross-section σ is $(9\pm3)\times10^{-13}$ cm^2. This cross-section is 3000 times larger than the total displacement cross-section for direct elastic collisions between the projectiles and the target atoms. Therefore, the fast process is definitively caused by the electronic excitation of the nickel atoms. From the values for w_{L0} we deduce an increase of the mean diameter of the nanocrystals by (1±0.1) nm. If we assume that crystal growth proceeds isotropically this finding implies that about 25% of the specimen atoms are involved in the fast process. Probably, a thermal spike released by the electronic excitations in a radius of about 2 nm around a projectile's path induces a rearrangement of all atoms to a "final" position in the grain boundaries. Further thermal spikes by later ion impacts do not change these positions. It is the slow process, which is probably very different in nature, which leads to further crystal growth.

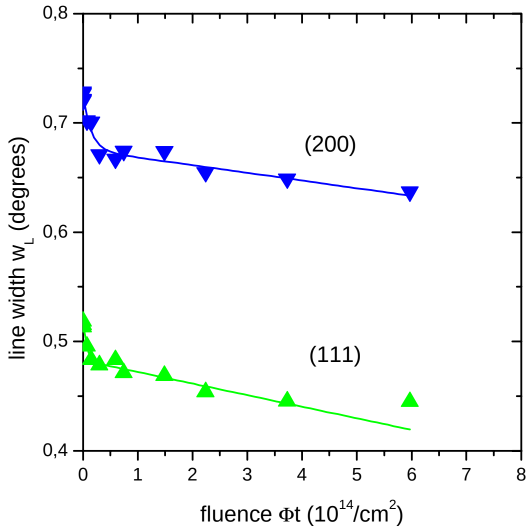

Fig. 1: *Lorentzian line width of the (200) and (111) reflections as a function of the applied 350 MeV Au-fluence.*

[1] W. Voegeli, K. Albe, H. Hahn, Nucl. Inst. Meth. Phys. Res. B (2002) in press.

[2] K. Sugio, Y. Shimomura, T.D. de al Rubia, J. Phys. Soc. Jpn. 67 (1998) 882.

[3] H. Kluge, L.E. Alexander, Wiley&Sons, New York 1974.

Th. Zumkley, G. Schumacher, S. Klaumünzer

ASPIC*: Dominance of coordination-number dependence in a zero-dimensional magnetic system

In our recent experimental study [1], magnetic hyperfine fields (B_{hf}'s) at a nonmagnetic probe atom – cadmium (Cd) - positioned at different sites on nickel surfaces were measured with unsurpassed atomic resolution. A simple relationship between the B_{hf} values and the coordination number (NN), i. e. the number of nearest nickel neighbours, was found essentially confirming earlier predictions [2].

Basically, nonmagnetic (or magnetic) atoms on a ferromagnetic surface constitute a two-dimensional magnetic system. The results of our measurements [1], however, rather correspond to the predicted and measured properties of 0D systems: The coordination number seems to rule the magnetic properties. Thus, the introduction of an impurity on a ferromagnetic surface may be considered as a means of creating magnetic 0D systems embedded in 2D systems. In the present experiment, we wanted to find out to what extent the magnetic properties of the cadmium atom are only governed by the number of its nearest neighbours and not the symmetry of their arrangement.

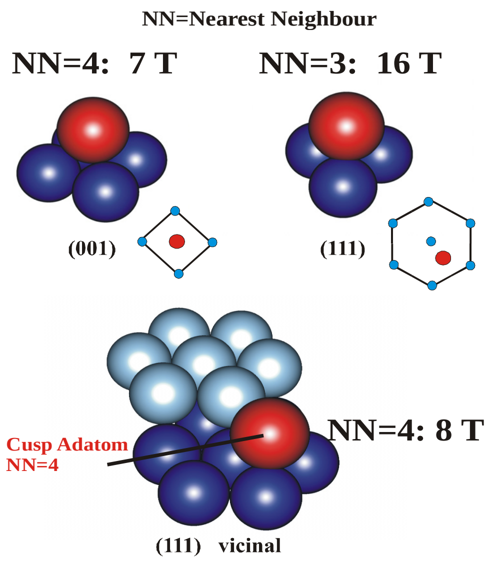

Fig. 1: *Adatom configurations of Cd impurities on Ni(001), Ni(111) and vicinal Ni(111).*

The results of these investigations – presented in Ref [1] – show that the experimentally obtained values for B_{hf} did not depend on the orientation of the surface but were equal as long as the coordination number remained unchanged. This observation was made for NN=7, where the differences in geometry are not very pronounced. For smaller coordination number the differences in symmetry between nickel surfaces with (001) and (111) orientations become stronger. The extreme case of symmetry difference is given for NN=4 by the comparison of the adatom on the fourfold hollow site on Ni(001), and the threefold hollow site on Ni(111), where the probe atom is additionally in contact with *only one atom* at a step of the next atomic monolayer. The comparison of B_{hf} for NN=4 on Ni(001) and on Ni(111) allows for a decisive judgment on the role of local symmetry. In the present experiment we have measured the magnetic hyperfine field for ^{111}Cd on Ni(111) with NN=4.

This surface site is created on a Ni(111) crystal with zigzag shaped steps (cf. Fig. 2). On such a crystal, the cadmium atom can be located on three different sites: the adatom site with NN=3, the free step site (NN=5) and the cusp adatom site with NN=4. The fields at all three sites are measured simultaneously in a PAC measurement.

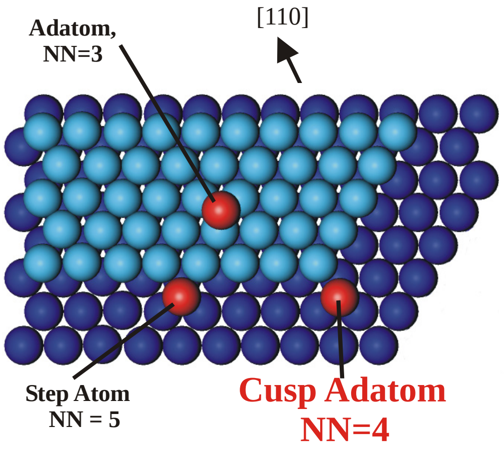

Fig. 2: *Zig-zag shaped steps on vicinal Ni(111) with possible impurity sites.*

The properties of the first two sites are known. Therefore, the evaluation of the data could be focused on the small third fraction with the result of $|B_{hf}|$=8 T. This coincides remarkably well with the adatom value on Ni(001), $|B_{hf}|$=7.3(3) T [3] and thus supports our initial assumption that the coordination number rules the magnetic behaviour of the Cd impurity irrespective of the local symmetry.

* **A**pparatus for **S**urface **P**hysics and **I**nterfaces at **C**ERN

[1] K. Potzger, A. Weber, H.H. Bertschat, W.-D. Zeitz, and M. Dietrich, Phys. Rev. Lett. 88 (2002) 247201.
[2] Ph. Mavropoulos, N. Stefanou, B. Nonas, R. Zeller, and P.H. Dederichs, Phys. Rev. Lett. 81 (1998) 1505.
[3] J. Voigt, Ph.D. thesis, Uni. Konstanz, 1990.

M.J. Prandolini, Y. Manzhur, A. Weber, K. Potzger, and H.H. Bertschat; M. Dietrich and ISOLDE Collaboration [EP Division, CERN, Geneva]

Anomalous emission of secondary positive ions from BeO films irradiated by swift Au Ions

In contrast to the nuclear sputtering which is directly energized by projectile-atom screened nuclear collisions, the electronic sputtering is mediated by the electronic excitation of the target along the path of swift heavy ions. Only in a second step the electronic energy is coupled into atomic modes of motion and the emission of secondary ions as well as neutral particles can occur. The electron-phonon coupling is usually assumed as the energy transfer mechanism leading to the thermodynamical equilibrium within the ion tracks and consequently to the thermal-like emission of secondary particles.

In this report we show that the electronic sputtering from BeO films irradiated by swift heavy ions deviates significantly from the generally assumed model. It seems that the primary electronic excitation strongly influences the following sputtering process.

The BeO films of about 10 nm thickness produced by 500 eV oxygen implantation [1] were irradiated by 350 MeV Au^{41+} ions delivered by the ISL cyclotron and by 2.5 keV Argon ions from the sputter gun placed at the target chamber. The secondary ions Be^+, O^+, O^-, BeO^- and BeO_2^- were detected by a mass spectrometer working under UHV conditions in the energy dispersive mode. Since the mass spectrometer was mounted at the target chamber at the fixed backward angle of 135° with respect to the ion beam direction, the angular distributions of emitted particles were investigated by means of target rotation.

The experimental results obtained for Be^+ and O^- ions are displayed in Fig. 1. The measured angular distributions are presented as a function of the emission angle β which is directly connected to the incident angle α by the relation $\alpha+\beta=45°$ (both angles are defined with respect to the target normal). As the sputtering yield depends on both angles, we have to make some assumptions to discuss the experimental results.

Due to a larger energy deposition in the target for oblique impact of the projectiles, the experimentally observed yield behaves typically as cos α. On the other hand the thermal emission of secondary particles should show the cos β dependence because of refraction at the surface binding potential. Applying both corrections we can define a corrected sputtering yield

$$Y_{corr}(\alpha,\beta) = Y_{\exp}(\alpha,\beta)\cos(\alpha)/\cos(\beta) \quad (1)$$

which should be constant for the thermal emission. As shown in Fig. 1 the angular distribution of O^- ions agrees with this assumption quite well, whereas the emission of Be^+ ions increases strongly for negative emission angles corresponding to the incident half space. The results obtained for other ions imply that the discussed differences in angular distributions occur generally for positive and negative ions.

Similarity between emission of positive and negative ions observed for the nuclear sputtering suggests that the resonance electron exchange at the target surface [3] as a reason for large differences observed in the electronic sputtering can be excluded. Thus, it seems that the negative and positive ions induced by the swift heavy-ion irradiation of BeO films obey different sputtering mechanisms. The negative ions could be emitted at a later stage of the ion track evolution when the thermodynamical equilibrium has already been reached. In contrast, the positive ions should predominantly be created at an earlier time scale before the memory about the incident direction would be lost. The latter coincides with our conclusions concerning the mechanism of the energy transfer to the atomic system by a fast lattice relaxation [1] based on the analysis of Auger electrons emitted from BeO films. According to this model, the quickly arising plasma could expand along the ion track leading to the jet-like emission of positive ions. However, further detailed experimental and theoretical investigations of above phenomena are necessary.

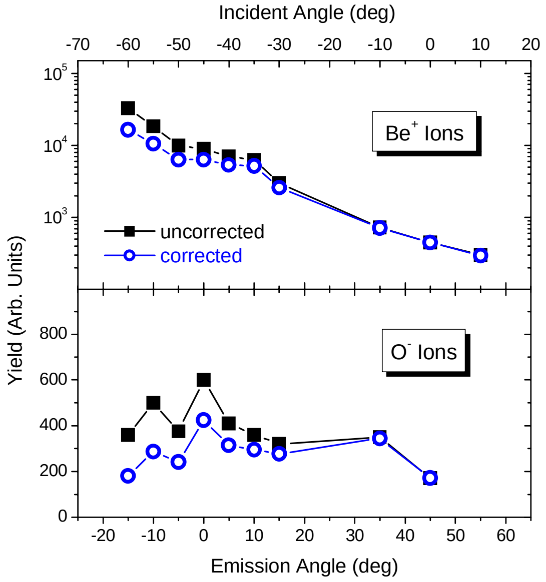

Fig. 1: *Angular distribution of secondary ions induced by irradiation with 350 MeV* Au^{41+} *ion*

[1] K. Czerski, F. Staufenbiel, M. Roth, G. Schiwietz, P.L. Grande, ISL Annual Report 2002

[2] H.E. Roosendaal, J.B. Sanders, Rad. Eff. 52 (1980) 137.

[3] M.L. Yu, N.D. Lang, Nucl. Instr. Meth. B14 (1986) 403.

K. Czerski, G. Schiwietz, M. Roth, F. Staufenbiel; P.L. Grande[1] ; S. Bhattacharyya[2]

1. UFRG, Porto Alegre, Brazil, 2. SINP, Kolkata, India

Giant Barkas effect observed for light ions channelling in Si

The energy loss of ions slowing down in matter has been investigated for many years because of its relevance for ion beam analysis, materials modification and nuclear physics. Moreover, there exist fundamental issues concerning the underlying physical processes of the energy loss at low and intermediate projectile energies. In particular, important points related to energy loss in the polarization field are still unclear. Here [1] we have studied the Barkas effect, an energy-loss enhancement proportional to the third power of the projectile charge at high energies.

In this work [1] we report on measurements of a strong Barkas effect under channeling conditions for He and Li ions impinging along the Si main axial directions. Such a channeling investigation has many advantages compared to previous measurements performed in amorphous targets or at a random direction.

a) The main contribution to the channelling stopping-power stems from the valence electrons and exactly these electrons are sensitive to the polarization field.

b) Disturbing effects such as shell corrections (originating from finite target-electron velocities), electron capture, or other inner-shell effects that usually overshadow the Barkas term are strongly reduced.

c) Channelling conditions provide the best scenario for the applicability of electron-gas models.

We have used the Rutherford backscattering technique with SIMOX targets, a method that allows for energy loss measurements at low analyzing energies. In connection with the recently developed unitary convolution approximation UCA, we were able to extract the Barkas contribution to the energy loss with high precision. This effect is clearly separated from other processes and contributes with about 50% to the energy loss for Li ions channeling along the Si <110> direction [1]. This is the largest Barkas effect observed so far for non-exotic incident particles.

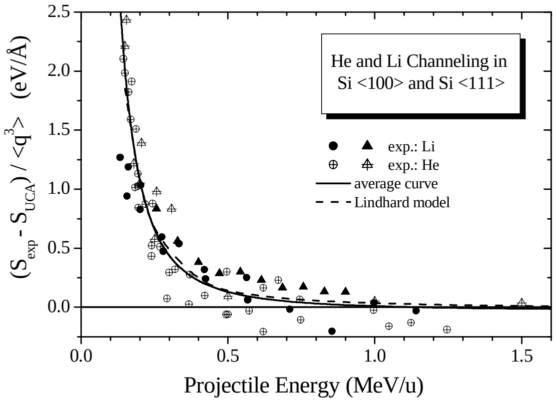

Fig. 1: *Presentation of all experimental channelling data after subtraction of the Bethe-Bloch term (through the UCA method) and division by the mean third power of the projectile charge-state as a function of the projectile velocity. An inspection of this figure shows that the data are well grouped around an average curve (determined by a best fit), independent of the channelling direction and projectile specie. This gives a rather strong support to the interpretation of the Barkas term. In addition, the average curve agrees rather well with the Lindhard model.*

P.L. Grande[1], G. de M. Azevedo[1], M. Behar[1],
J.F. Dias[1] G. Schiwietz

1. [Instituto de Física da Universidade Federal do Rio Grande do Sul Porto Alegre, Brazil];

Plasticity in current driven vortex lattices

A theoretical analysis of recent experiments on current-driven vortex dynamics in the Corbino disk geometry

The physics of vortex matter in type-II superconductors has been a very active field of research since the discovery of high-temperature superconductivity. An external magnetic field typically penetrates the sample in the form of an array of flux lines (vortex tubes). Depending on the magnetic field, the temperature, and the sample preparation that controls quenched disorder, the flux line array can form crystalline (Abrikosov lattice), liquid, or glassy phases. Of particular interest is the dynamics of the vortex array in the various phases and in the proximity of phase transitions. Transport experiments are often performed in a strip geometry where current is injected at one end and is removed at the opposite end. The current-voltage relation provides information about the dynamics of the vortex array because moving vortices induce an electric field perpendicular to their velocity. Edge effects complicate transport experiments in the strip geometry and can be avoided using the Corbino disk geometry shown in Fig. 1. This geometry provides another advantage too: the controlled spatial inhomogeneity of the driving Lorentz force which is inversely proportional to the distance from the center of the disk yields an inhomogeneous shear stress and allows one the probe the shear rigidity of the vortex array.

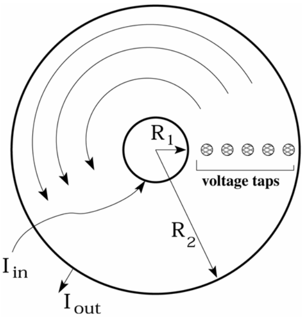

Fig. 1: The Corbino disk geometry. The external magnetic field is out of the page. The electric current flows radially from the inner circumference to the outer rim of the disk. The radial current density causes the vortices to move in circular orbits around the disk, without crossing the edges of the sample.

In the experiments done by the Argonne group a series of voltage taps placed in the radial direction probes the velocity profile of the moving vortex array as a function of the radius. If the vortices are in the liquid phase, their local velocity is inversely proportional to the radius (proportional to the driving Lorentz force density). If they are in the crystalline lattice phase, they move as an elastically deformed rigid body with a fixed angular velocity, provided that the shear stresses due to the local force gradients are not too strong. This kind of motion gives a velocity profile proportional to the radius. Above a certain value of the applied current, the local shear stress becomes strong enough to break the lattice bonds and cause a plastic response with the lattice breaking into two or more concentric annular sections rotating at different angular velocities and slipping past each other. In the experiments, it is possible for elastic, liquid and plastic response to coexist at a given value of the applied current. The shear stress associated with the spatial dependence of the Lorentz force is proportional to the current and inversely proportional to the square of the radius. Near the outer rim of the disk, the shear stress is very small and the vortex array rotates as a rigid body. Near the inner circumference, the shear stress is very large and the vortex array flows like a liquid. In the middle, the response is plastic.

In our theoretical analysis [1] of these experiments, the onset of plasticity is described as a nonlinear effect due to the stress-induced proliferation of free dislocations in the vortex lattice which in turn contributes to the relaxation of the shear. The result is a nonlinear voltage-current scaling. Two mechanisms can cause unbinding of dislocations from tightly bound pairs: thermal fluctuations and an externally applied shear stress. The latter is dominant at low temperatures and thick samples. In the absence of an external stress a pair of dislocations with opposite Burgers vectors is held bound in an infinitely high potential well. A shear stress changes the well to a finite barrier and allows the dislocations to unbind. When the position of the barrier becomes of the order of the intervortex spacing, free dislocations proliferate. This criterion for the onset of plasticity is in very good qualitative agreement with the experiments. Our analysis of finite temperature effects involves the generalization of standard methods of stochastic dislocation dynamics to spatially inhomogeneous external stress. In accord with the experiments, we obtain a “critical” current for the onset of plasticity at a certain radius which decreases with increasing temperature. The resulting phase diagram is shown in Fig. 2.

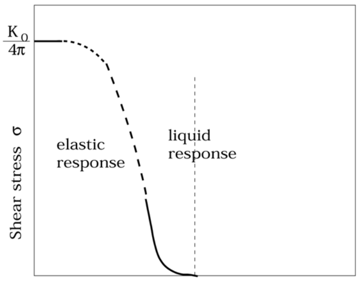

Fig. 2: A schematic phase diagram in the shear stress - temperature plane. The dashed vertical line is the location of the Kosterlitz-Thouless melting transition where thermal unbinding of neutral dislocation pairs occurs in the absence of external shear.

[1] (G. W. Crabtree et al. Physica C, 341-348, 996 (2000)),

[2] P. Benetatos and M. C. Marchetti, Phys. Rev. B, 65, 134517 (2002).

P. Benetatos

Dipolar tracer studies in F-Actin fluctuations

Theoretical studies on contour fluctuations of single semiflexible polymers. Comparison of experimental data with theoretical predictions for actin filaments at different length and time scales.

Actin filaments have been the subject of intensive biophysical in vitro studies over the past years. Besides the motivation to mimic cellular mechanics with reconstituted purified systems, actin, one of the few available semiflexible polymers, became a model case to study the effect of rigidity on polymer dynamics.

Loic Legoff from the Curie Institute in Paris found a beautiful noninvasive method to observe contour fluctuations of single actin filaments using video microscopy [1]. He mixed sparsely fluorescently labeled filaments with densely labeled ones, yielding in typical “copolymer” filaments as shown in Fig. 1. The size of the brighter segments was reduced to below optical resolution by gentle sonication. Their position and orientation was then easily determined by image analysis, and thereby they acted as end tags for the darker filament. With this method he could measure the time dependent end-to-end distance R(t) for filaments with lengths ranging between 6 µm and 26 µm in a time window of 10^{-2} s to seconds.

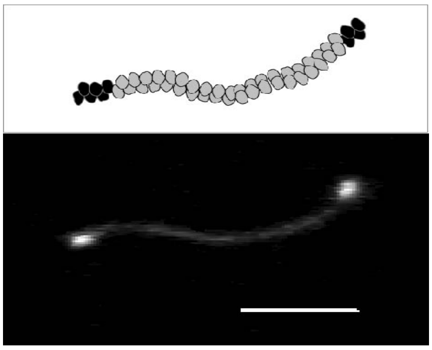

Fig. 1: Fluorescence microscopy image of an actin filament. As shown on the sketch, it is made of one long filament that is annealed by the ends with two bright fragments, The scale bar is 5 µm.

We analyzed the experimental results relying on the simple model of a *wormlike chain,* which considers the polymer to be locally inextensible and to have a bending stiffness, so that the contour of lowest elastic energy is the straight one. However a polymer in solution is permanently fluctuating because it is subject to thermal kicks of the surrounding solvent molecules. A *semiflexible* polymer like actin has a large bending rigidity compared to the energy of a thermal kick, so that it only weakly fluctuates around the straight contour. The ratio between bending stiffness κ and thermal energy $k_B T$ is the so-called persistence length ι_p . It is the length scale over which the wormlike chain appears straight. A polymer is *semiflexible*, if the contour length is much smaller than the persistence length.

Figure 2 shows a typical probability distribution G(R) for the end-to-end distance R of an actin filament sampled over 6200 configurations. The theoretical prediction for a wormlike chain [2] could be brought into excellent agreement with the data by adjusting the persistence and contour length of the filament. In this way the persistence length of actin could be extracted to a very high accuracy (l_p=16.1±0.2µm).

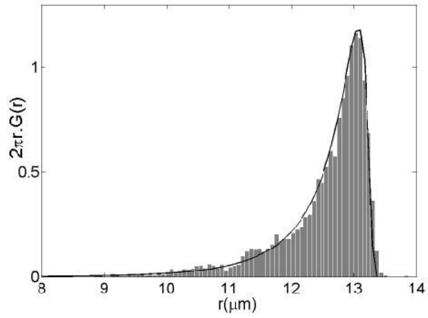

Fig. 2: Measured radial distribution function (bars), and theoretical expression for the 2D RDF (line) for a filament of 13.40 µm contour length.

As an important observable for characterizing the dynamics of semiflexible polymers we analyzed the time-dependent mean-square difference (MSD) of the end-to-end distance,

$$\delta R^2(t) \equiv \left\langle \left[R(t_0+t)-R(t_0)\right]^2 \right\rangle_{t_0} \cdot$$

In Figure 3 the data is shown on a double logarithmic scale. On short times it obeys a simple power law, which is a straight line in a log-log plot and on large times it saturates at an equilibrium value. Both, the dynamical exponent and the equilibrium value agree very well with theoretical prediction (thick line) over several orders of magnitude.

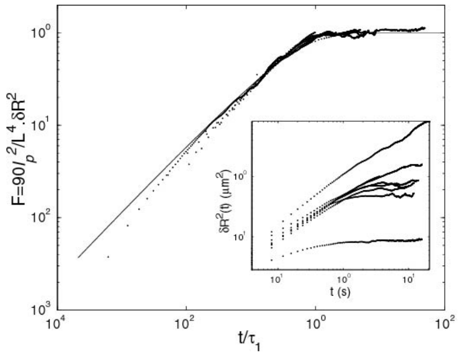

Fig. 3: Inset: Measured MSD for filaments with lengths ranging from 5.9 µm (bottom) to 25.6 µm (top). Upon rescaling all data come close to one line (large figure), which is predicted by the wormlike chain model very well (solid line).

[1] L. Le Goff, O. Hallatschek, E. Frey and F. Amblard, Phys. Rev. Lett. **89**, 258101 (2002).
[2] J. Wilhelm and E. Frey, Phys. Rev. Lett. **77**, 2581 (1996).

O. Hallatschek

Light scattering and structural relaxation

Theoretical predictions of light scattering by longitudinal acoustic modes in molecular supercooled liquids

Light scattering has become an important tool to investigate the structural relaxation in supercooled liquids. The sensitivity of these systems to slight lowering in temperature manifests itself most prominently in the drastic increase in viscosity. However, also other transport coefficients like the bulk viscosity or the single-particle diffusivity and more general dynamic susceptibilities exhibit this phenomenon. Recent developments in extending the dynamic window of polarized and depolarized light scattering opened the possibility to study the whole dynamic evolution of structural relaxation in the frequency range of 1 GHz to 1 THz as a function of temperature. The increase of the structural relaxation time can therefore be directly observed as the supercooled system changes from liquid-like to solid-like behavior.

As was already predicted by Brillouin in 1922 the scattering of light by excitation of longitudinal acoustic modes leads to a narrow inelastic doublet in the polarized light scattering spectrum (see Figure 1). Its first observation was reported in 1930 by Gross, who noticed that the spectrum consisted of the Brillouin doublet superimposed on a central Rayleigh line. An explanation of this Rayleigh-Brillouin triplet, based on the equations of macroscopic hydrodynamics, was suggested by Landau and Placzek in 1934.

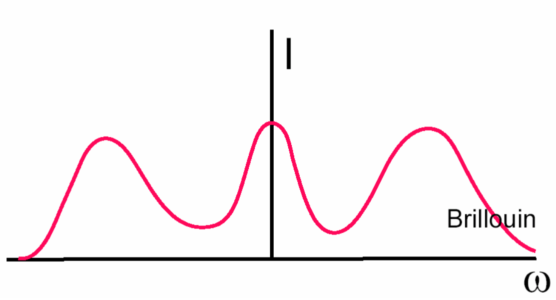

Fig. 1: A schematic drawing of the intensity measured in a light scattering experiment as a function of frequency. The spectrum consists of a central Raleigh line and a Brillouin doublet at finite frequencies. The Brillouin doublet results from the excitation of longitudinal acoustic phonon modes.

Yet, for supercooled systems one expects that the hydrodynamic description breaks down once the frequency of the sound waves becomes comparable to the inverse structural relaxation time. Then the spectral shape of the resonances is dependent on the details of the line shape of the longitudinal viscosity. Differently speaking, a study of the polarized light scattering spectrum reveals the dynamical processes that underly the slow structural relaxation. In order to give a direct correspondence of the different effects involved, we have derived expressions for the intensity of the Brillouin polarized spectrum of a molecular liquid formed of axially symmetric molecules. These expressions take into account both the molecular dielectric anisotropy and the modulation of the local polarizability by density fluctuations. They also incorporate all the retardation effects which occur in such liquids. We have shown that the spectrum splits into a wavenumber-independent rotational contribution and wavenumber-dependent term, which reflects the propagation of longitudinal phonons. In the latter, the two light scattering mechanisms enter on an equal footing and generate three scattering channels. The influence of the two new channels has been studied, and we have shown that they may substantially modify the Brillouin line-shape when the relaxation time of the supercooled liquid and the phonon period are of the same order of magnitude.

[1] R.M. Pick, T. Franosch, A. Latz, C. Dreyfus, Eur. Phys. J. B 31, 217 (2003)
[2] T. Franosch, A. Latz, R.M Pick, Eur. Phys. J. B 31, 229 (2003)

T. Franosch

A new Thermodynamics – from nuclei to stars

In the past years we developed a new **geometrical** formulation of thermo-statistics. Whereas traditional (canonical) statistics applies to homogeneous systems in the thermodynamic limit, our new thermo-statistics addresses also inhomogeneous systems as nuclei, clusters, soft-matter and even stars and star-systems [1 ,2].

By using the microcanonical ensemble and Boltzmann's principle $S=\ln[W(E)]$, the thermodynamic limit is not invoked. Here $W(E)$ is the geometric size of the manifold of points in the $6N$-dim. phase space with the prescribed energy. One of the most important differences to the conventional theory is the appearance of a **negative heat capacity** which can be seen by a **back-bending caloric curve** $T(E)$. A negative heat capacity is strictly forbidden in any canonical theory. This implies a *violation* of Clausius' old formulation *of the Second Law of Thermodynamics*: "Heat can only flow from hot to cold". Nevertheless, in the form of "The entropy rises or remains constant during the approach to equilibrium" it is valid also for small systems [2].

In paper [3] we discussed the microcanonical properties of a system of N classical particles interacting via Newtonian gravity as a function of the total energy E and, for the first time, of the total angular momentum L. At low E and small L we obtained a single star phase and for larger L a double star phase. At intermediate angular-momenta we even find rotating homogeneous rings and also multi-star systems. These are all *equilibrium* configurations in the new statistics. The results of our theoretical calculations, depicted in figure 1, correspond to the structures of well known astronomical objects. In predicting them, our geometric theory proves to be superior to any canonical or other statistics based on the canonical ensemble.

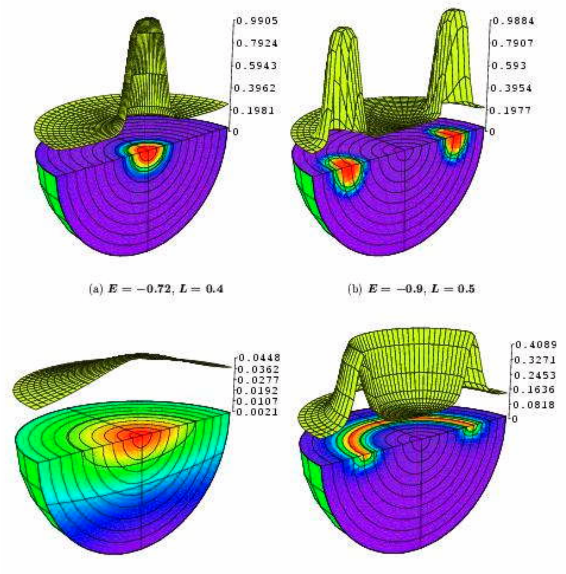

(a) $E = -0.72$, $L = 0.4$ (b) $E = -0.9$, $L = 0.5$

(c) $E = -0.06$, $L = 0.4$ (d) $E = -0.42$, $L = 0.5$

Fig.1 *Inhomogeneous equilibrium distributions of rotating, self-gravitating systems*

Negative heat capacities are well known here. These are impossible in conventional canonical statistics but ubiquitous in real nature. These systems are much larger than any "thermodynamic limit" allows but nevertheless must be treated microcanonically.

The next example confirming our theory is the experimental finding of a *negative heat capacity* (back-bending caloric curve $T(E)$) in the decay of an excited Na_{147}^{+} cluster. The experiment was performed at the University of Freiburg [4].

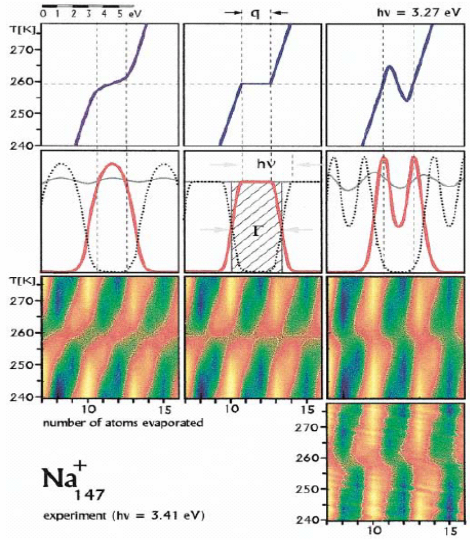

Fig. 2 (from Ref.[4]): Photo-fragmentation of Na_{147}^{+} *clusters. The three caloric curves in the upper line correspond to different models of the thermodynamics of a cluster. They agree in their latent heat q, and melting temperature* T_m, *but show a different behaviour near* T_m. *The corresponding energy distributions are shown in the second line (red), the fragmentation patterns in the third line. The lower figure shows the experimental data. Only the pattern of a back-bending caloric curve is reconcilable with the experiment.*

[1] D.H.E. Gross et al. HMI-Annual Report 2001, p. 69

[2] D.H.E. Gross. *Microcanonical thermodynamics: Phase transitions in "Small" systems*, volume 66 of *Lecture Notes in Physics*. World Scientific, 2001.

[3] E.V. Votyakov, H. Hidmi, A. De Martino, and D.H.E. Gross. Phys. Rev. Lett., 89, cover story, July 2002.

[4] M. Schmidt et.al. Phys. Rev. Lett. 86, 1191, 2001.

D.H.E. Gross

Domain wall roughening in disordered dipolar films

In this work, we have mathematically characterized the shape of a magnetic domain wall in a thin ferromagnetic film which is part of a superconductor/-ferromagnetic-film/superconductor hetero-structure.

In this work, we have studied the scaling properties of a domain wall in a thin ferromagnetic film, which is part of a hetero-structure composed of layers of thin magnetic films which alternate with bulk superconductors. This domain wall can be viewed as an open line which stretches across the two-dimensional magnetic layer. As we have shown in [1], in this case the dipolar interaction between the underlying spins of the magnetic film is modified by the presence of the superconductors, which expel the magnetic field generated by the film from their interior, due to the Meissner effect. Since the elastic energy of the domain wall contains a contribution coming from the dipolar energy of the magnetic spins, such energy modifies the properties of the domain wall, even at large distances.

There are essentially three main contributions to the elastic energy of a domain wall. The first contribution arises from the Heisenberg short-range exchange interaction between the spins, which is of electrostatic nature. A second contribution arises from the long-range magnetic dipolar interaction referred above, whose form is dependent on the (magnetic) environment where the spins are placed. Finally, the third contribution is due to the presence of magnetic impurities, which generate a fixed (i.e. quenched) random magnetic field. A fourth type of interaction, namely on-site anisotropy, is also present in the microscopic Hamiltonian describing the system [2] and is necessary to stabilize the domain wall, but does not contribute to its elastic energy.

We have used a well known mapping which permits to interpret the line-domain as the world line of a quantum particle in a one-dimensional space where the y coordinate of the magnetic layer plays the role of a fictitious, imaginary time. In a pure system and at zero temperature, the line domain is straight, i.e. the quantum particle is not moving: it simply forms a line extending along the *y*-axis. But due to impurities (always present in real systems) and due to thermal fluctuations, the line will deviate from this straight configuration, i.e. the particle will start to move. Such a mapping is quite useful, as it allows one to apply a series of well-known approximations to a problem which would otherwise be intractable.

In particular, the original domain-wall problem was reduced to the one of a quantum particle in a random potential (generated by the random-field) with a self-interaction which is non-local in ‘time’ and whose nature is determined by the form of the underlying dipolar interaction between the spins. The fact that such an interaction is non-local is simply a consequence of the long-range character of the dipolar field generated by the magnetic spins. Such model systems were first studied by Feynman in the context of the so-called polaron problem [3], i.e. the problem of a single electron which interacts with a cloud of lattice vibrations, i.e. phonons. Due to the presence of the phonon cloud, the electron also acquires a retarded self-interaction, as we have found in our case.

An additional difficulty, which is characteristic of problems involving the presence of quenched impurities, is that these impurities are not in equilibrium with the rest of the system, but should be instead considered as fixed in a given sample, the averaging over the disorder being done (unlike the thermal averaging) over different samples.

The character of the disorder gives rise to a complicated averaging problem, which can be solved if one introduces a set of different copies (replicas) of the system, a mathematical trick first used by Mézard and Parisi in the context of our problem [4]. The method is complemented by the substitution of the original problem by a simpler one which can be solved (i.e. we have used a mean-field approach) and which works as our approximation. The precise form of the new model is chosen so as to resemble the original one as closely as possible.

In order to solve the new problem, we used the so-called ‘replica symmetry breaking ansatz’, whose physical interpretation is that there are quantities in our system whose measurement in different samples would yield different results, a consequence of the loss of spatial homogeneity, due to the presence of impurities (i.e. these quantities are not ‘self-averaging’).

Finally, we have obtained a set of self-consistent equations whose solution has allowed us to compute the roughening exponent of the domain wall, which provides a measure of the deviation of the domain wall from the straight line configuration. The value obtained was 1/3. This value can be shown to be exactly 1 in the absence of dipolar interactions, which shows that the long-range character of the dipolar interactions ‘smoothens’ the domain-wall, as is to be expected from intuition.

[1] J. E. Santos, E. Frey and F. Schwabl, Phys. Rev. B **63**, 054439 (2001).
[2] J. E. Santos, E. Frey and F. Schwabl, Phys. Rev. E **65**, 031608 (2002).
[3] R. P. Feynman, Phys. Rev. **97**, 660 (1955).
[4] M. Mézard and G. Parisi J. Phys. A **23**, L1229 (1990); J. Phys. I **1**, 809 (1991).

J. E. Santos

No noise – no wave – Intracellular *Ca*$^{2+}$-dynamics as a stochastic medium

Theoretical studies on the control of Ca^{2+} *concentration in living cells:*

The cell organelles like the nucleus, mitochondria or the endoplasmic reticulum (ER) in living cells are embedded in the cytosol. The endoplasmic reticulum and the mitochondria are used among other functions as Ca^{2+} stores. Living cells control the concentration of Ca^{2+} in the cytosol by release and uptake of Ca^{2+} by these intracellular storage compartments and by Ca^{2+} binding proteins, so called buffers.

The exchange of Ca^{2+} between the ER and the cytosol is controlled by channels and pumps. Upon opening of a channel, Ca^{2+} is released into the cytosol. Pumps transport Ca^{2+} against the concentration gradient back into the ER. The opening of the channels depends on the calcium concentration: the calcium release itself is calcium induced.

Intracellular calcium concentrations oscillate in many cells. The information transmitted by the second messenger calcium is encoded in the form and frequency of these oscillations. Calcium induced calcium release is at the core of the oscillations and models are constructed with oscillatory dynamics in mind. The crucial question is, whether oscillations are caused by the dynamics of calcium induced calcium release alone or are due to higher control processes. The answer will determine the targets of research to come.

Our research focuses on the role of stochastic fluctuations in intracellular Ca^{2+} dynamics. Fluctuations are important, if they change system behavior qualitatively. The random events relevant for the dynamics of waves and oscillations are binding and dissociation of molecules controlling the opening probability of Ca^{2+} channels. We could show for the system in that both waves and oscillations are caused by fluctuations. All spatial and temporal structures are lost in the deterministic limit [1,2]. The reason for this behavior in theoretical terms is that fluctuations are larger than the thresholds separating different attractors in phase space.

The emerging picture of intracellular Ca^{2+} dynamics implies that oscillations in the oocytes *of the Xenopus* frog as examples of large cells are due to repetitive random nucleation of waves. That implies that the average wave frequency depends on the characteristics of spatial coupling and system size. Periods become independent of spatial characteristics at large opening probabilities.

Trade mark of oscillations due to stochastic nucleation is a distribution of periods instead of a single sharp value as in deterministic periodic processes. Many small cells exhibit very precisely timed oscillations. That points towards higher processes setting the period. This will be the subject of future investigations.

From a physicist's point of view, the results published in [1, 2] imply that intracellular calcium dynamics is the realization of a stochastic medium. That will allow us to study fundamental questions of nonlinear structure formation from the elemental event all through to global phenomena.

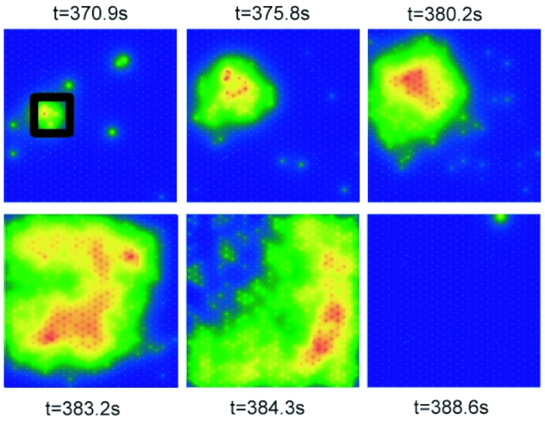

Nucleation of a calcium wave. Time is indicated at the panels. Blue means low calcium concentration, green, yellow and red mark increasing concentration values [1].

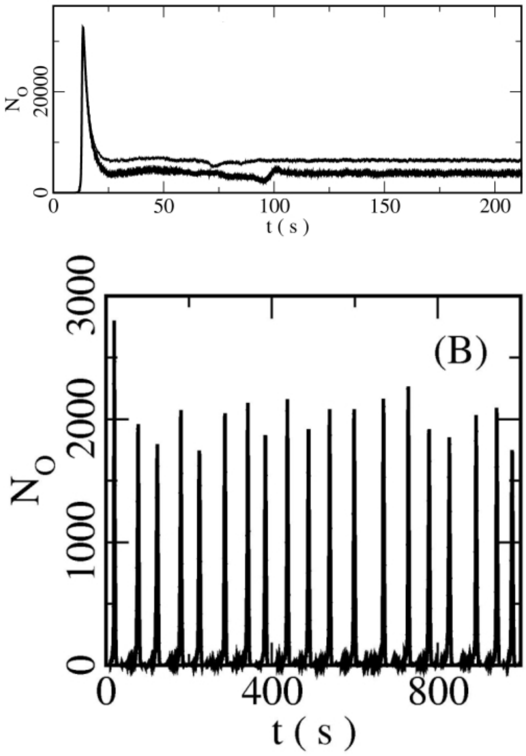

Comparison of the deterministic limit (upper panel, large channel numbers) and stochastic limit (lower panel, small channel numbers) of a model of intracellular calcium dynamics [1]. N_O *is the number of open channels.*

[1] Falcke M. (2003) *Biophys. J.* **84**, 42-56
[2] Falcke M. (2003a) *Biophys. J.* **84**, 28-41

M. Falcke

Biological macromolecules: kinetics & structure

Theoretical studies of single biological macromolecules at different length and time scales, aimed at describing their kinetics and their structural properties, focused on motor proteins.

In recent years, instrumentation development has opened the possibility of investigating properties of proteins, nucleic acids and protein complexes at the single molecule level. This represents a complete change of perspective for a field that had dealt only with quantities averaged over large (and not directly controllable) ensembles. Therefore, new theoretical models are needed to analyze, interpret and possibly explain the huge amount of data that are being constantly collected. Our research aims at developing such models in the clear framework provided by statistical physics and stochastic processes.

In particular, we have focused on the problems posed by the application of an external load to molecules moving in a viscous environment. This problem is extremely relevant for motor proteins, huge proteins that are able to transform chemical energy stored in the ATP molecule into mechanical work.

Using the framework of a master equation approach and its continuous counterpart, the Fokker-Planck equation, we have developed a coarse graining procedure to obtain a sensible force dependence for single transition rates. This framework has been used for the interpretation of kinetic data (velocity, reaction rates and diffusion coefficients) from experiments on the motor protein kinesin [1], leading to a remarkable agreement with the experimental results (see Fig. 1) and significantly reducing the number of parameters needed to perform such data analysis. We have also discussed the effect of a positive force (i.e. a force along the direction of motion) on the kinetics of these proteins, in a parameter region that awaits a careful experimental investigation. The model is not limited to the field of motor proteins and can be easily generalized to other mechano-chemical systems of biological relevance.

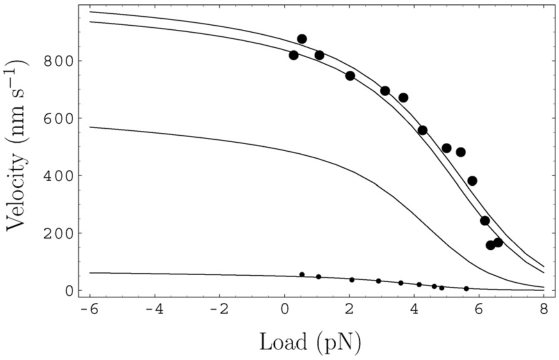

Fig. 1: Comparison of model predictions (continuous curves) and experimental data (points) for the velocity of the motor protein kinesin under load. The different curves refer to different concentrations of ATP, the chemical fuel of kinesin.

A considerable amount of work has also been dedicated to the analysis of protein structures obtained from X-ray diffraction and NMR experiments. The focus has been constantly on motor proteins, but the methods have been developed and/or investigated under most general conditions, with application on the widest set of available protein structures. In this spirit, we have applied the Gaussian Network Model (GNM) to a set of protein structures and compared model predictions with data from experiments. The GNM model has been extended so as to include the effect of a fictitious temperature, whose role is to drive the protein structure out of its native conformation [2]. This improvement of the model opens the possibility of investigating the dynamics of proteins on long time scales at extremely low computational costs. This is extremely important, since currently available Molecular Dynamics simulations at the atomic level are able to describe biological systems only on time scales up to *10 ns* (*10^{-8} s*), while most biological processes occur on the *ms* (*10^{-3} s*) time scale.

The comparison with random networks and more compact three-dimensional structures has shown that secondary motifs (helices and pleated sheets) play a key role in endowing proteins with the elastic properties they need to perform their biological function. We are currently working on the development of the model and its application to obtain information on the conformational dynamics of proteins and their interaction with ligands, following a preliminary application of GNM to the analysis of the kinesin motor domain and the kinesin dimer (Fig. 2).

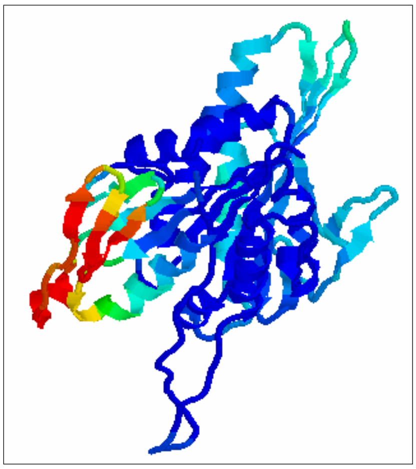

Fig. 2: Kinesin motor domain, analyzed through GNM (2nd slowest eigenmode): in red the parts that undergo large fluctuations around their equilibrium position. These parts are thought to be responsible for the biological function of the protein.

[1] G. Lattanzi and A. Maritan, J. Chem. Phys. 117 (2002), 10339.

[2] C. Micheletti, G. Lattanzi and A. Maritan, J. Mol. Biol. 321 (2002), 909.

G. Lattanzi

Traffic jam on molecular highways

A theoretical study of non-equilibrium and collective phenomena inspired by motor protein transport.

The transport of inner components in cells (organelles) is a fundamental topic of cellular biology, with interesting implications in fundamental and applied physics (from the foundations of Statistical Mechanics up to studies on the dynamics of urban traffic of pedestrians, cars and trucks).Intracellular transport of organelles in eukariotic cells is a complex and intrinsically non-equilibrium phenomenon driven by ATP powered enzymes called motor proteins.

Enzymes like kinesins and dyneins hydrolyse ATP and move uni-directionally along cytoskeletal filaments such as microtubules. Kinesins are usually involved in anterograde transport (from the nucleus to the cell periphery), while dyneins move in the opposite direction (retrograde transport). Occasionally, motors bound to the filament can detach and diffuse through the cytoplasm or vice-versa, see Fig.1.

Bound to one or a collection of motors, organelles can move uni-directionally along a filament array for distances comparable to the cell size (~10 µm, much larger than the typical motor size, ~10 nm!) or even more. Directed motion, compared to pure diffusion, allows organelles to move efficiently and faster in a complex and dense environment like the cytoplasm.

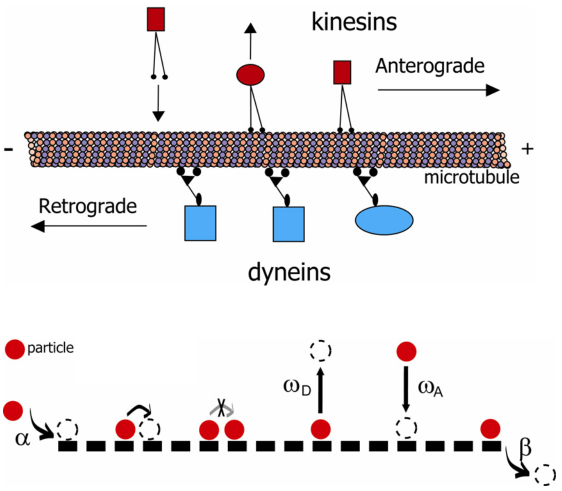

Fig. 1: Scheme of organelle transport on a microtubule driven by kinesins and dyneins and related theoretical one-dimensional "lattice gas" model for one class of motor.

Our research focuses on the study of the non-equilibrium properties of the flow of a collection of motors (*particles*) in a system composed by a single filament (*lattice*), in contact with the cytoplasm (*particle reservoir*) [1]. Over the lattice, particles move with microscopic dynamical rules inspired by the essential features of motor protein motion: 1) unidirectional and stochastic stepping of fixed length at a given rate, 2) binding and unbinding dynamics from the filament to the reservoir with given fixed rates. Particles are also in mutual interaction: a step is forbidden if the next site is occupied ("*hard sphere interaction"*), see Fig. 1. This allows the general features of motor protein collective transport to be mathematically reformulated in terms of a *lattice gas model*.

The study of the non-equilibrium dynamics of a gas of interacting and stochastic particles is a topic of fundamental interest in Statistical Mechanics. Particularly, if one wants to understand phenomena like non-equilibrium phase transitions which have no equivalent in thermodynamic equilibrium.

In our case, the lattice gas we considered [1] is a generalisation of a model called "Totally Asymmetric Exclusion Process" (TASEP), extensively studied in recent years because of its richness in genuine non-equilibrium phenomena like formation of (moving) domain walls (i.e. phase separation of the lattice in domains of low and high densities of particles) and continuous or discontinuous phase transitions in the stationary state.

The fundamental difference in our model compared to the TASEP is the inclusion of the particle binding / unbinding dynamics in the lattice bulk.
Directly inspired by motor protein dynamics, this property breaks the particle current conservation in the bulk. As a consequence, new phenomena appear. In particular, contrary to TASEP, we find *stable* domain walls (when the fluxes of particles at the boundaries are comparable with those due to the attachment or detachment of particles in the bulk). The presence of such domain walls is a novel and unexpected phenomenon. Indeed, the microscopic underlining dynamics does not involve any spatial inhomogeneity that could explain the domain wall localisation.

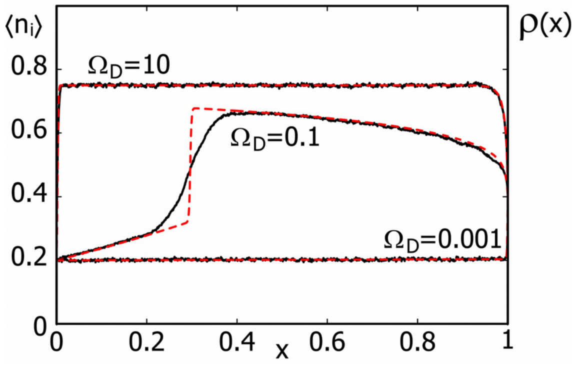

Fig. 2: Simulation (black) and numerical (red) results of possible particle density profiles.

Our results may be also biologically interesting. A jammed phase represents a situation in which the mutual interaction among motors can reduce the effective flow of organelles along the filament. Anomalies in the organelle flow have, indeed, important physiological consequences for cellular processes.

[1] A. Parmeggiani, T. Franosch and E. Frey, Phys. Rev. Lett. **90**, 086601-1-4 (2003).

A. Parmeggiani

Metalloprotein mapping in histological tissue sections by Micro-SRXRF

Most of the trace elements present in the mammalian organisms are bound to proteins where they play a central role as structural or catalytic components. The investigation of these “metalloproteins” will provide valuable information with regard to the functions and tasks of metals and metalloids in health and disease.

In these studies biochemical procedures for tissue fractionation and protein separation have been combined with various trace analytical methods to measure the element contents in the different fractions and in this way identify the metalloproteins and determine their cellular and subcellular distribution.

In addition to the investigations by means of these combined methods, microprobe-synchrotron radiation X-ray fluorescence (micro-SRXRF) was applied to obtain direct information on the distribution of elements within a tissue.

With micro-SRXRF we scan plane histological tissue sections with a focused X-ray beam and measure the intensities of characteristic X-rays emitted from the trace elements distributed among the different compartments. Beam focusing is based on the principle of radiation transmission through glass capillaries by means of total reflection. Depending on the focus of the X-ray optic the spatial resolution ranges from 15 to 5 µm.

In studies carried out at HASYLAB, micro-SRXRF has been optimized with regard to its use in trace element mapping in histological tissue sections. Due to various improvements, especially in sample–detector configuration and detector shielding, the time needed for measuring an X-ray spectrum could be drastically reduced from 900 sec to only 3 sec.

The applicability of micro-SRXRF in this field was shown in an investigation of the metalloprotein distribution in human brain sections affected by Alzheimer’s disease. Morbus Alzheimer is among the most frequent neurodegenerative diseases. Changes caused by oxidative stress are thought to be important factors in its pathogenesis, and in these processes several metals seem to play crucial roles. Metals are known to be involved in the production of free radicals and peroxides, but also in the protective systems against these oxidants.

A specific characteristic of brain tissue in Alzheimer’s disease are the plaques as shown in Fig. 1.

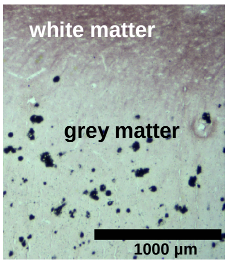

Fig. 1: Histological section of a human brain affected by Morbus Alzheimer showing parts of the grey and white matter. Senile plaques consisting mainly of deposits of the amyloid protein Aß have been made visible by staining.

The first results of the micro-SRXRF measurements of a Morbus Alzheimer brain sample are shown in Fig. 2. Here a 16 µm thin brain section supported by an 0.8 µm polyethylene foil was used. An area of 1000 µm x 400 µm was scanned by measuring 1350 X-ray spectra for 3 sec each by means of a microbeam focused by a polycapillary. An X-ray spectrum obtained in the area with the highest iron concentration is presented as an example in Fig. 2, together with the distribution maps for some elements. The distribution patterns of the mineral elements P, S and K were found to be similar and to reflect differences in white and grey matter fractions, with higher values in the white matter. Zn was distributed quite homogeneously, with only a single enriched spot where the Zn signal intensity was doubled. In the case of Fe some broader patches of about twice the signal intensity of the surrounding were observed.

The results of this study have shown that with the use of a polycapillary and improvements in the beam-sample-detector configuration, micro-SRXRF is suited to the determination of the element distribution in the different compartments of biological tissues without prior fractionation. The method, especially in combination with synchrotron radiation-based Fourier transform infrared (SRFTIR) spectromicroscopy which provides information on the chemical composition of the sections of interest, can therefore become a valuable tool in the research on the role of metalloproteins in health and disease.

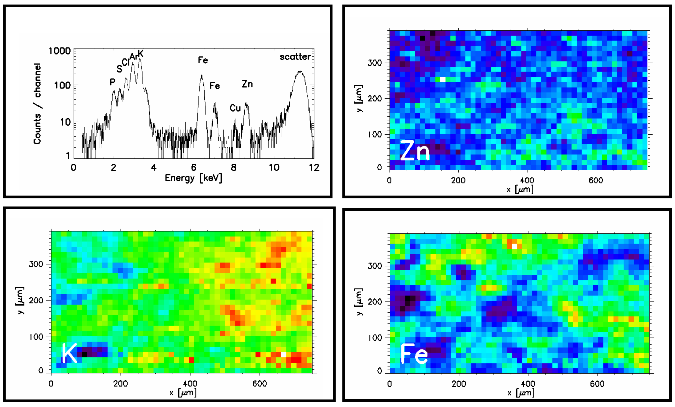

Fig. 2: Element scan on a section of human brain affected by Morbus Alzheimer, with a single spot X-ray fluorescence spectrum and color-coded distribution maps of K, Zn and Fe (increase in fluorescence line intensity from blue to red) shown as examples. Excitation conditions: pink beam (NiC multilayer) at 11.5 keV excitation energy; beam focusing by means of a polycapillary; measuring time per pixel: 3 sec; pixel size: 15 µm x 15 µm.

D. Behne, D. Alber, A. Richarz, G. Weseloh, M. Kühbacher

Selenium and selenoproteins in the central nervous system

Previous investigations have shown that the essentiality of selenium (Se) in the mammalian organism is above all due to the functions of redox-active selenoenzymes which have key tasks in various life-maintaining processes. With its high oxygen supply and its large concentrations of polyunsaturated fatty acids which are susceptible to peroxidation, the brain is especially vulnerable to oxidative stress. As Se in the form of several selenoenzymes is a pivotal component of the antioxidative defense system in various tissues, it could be assumed that it plays an important role in this organ, too. It is therefore of great interest to identify the selenoproteins present in the CNS and to obtain information on their functions. By combining radioanalytical procedures with biochemical methods, several experiments have been carried out to achieve these goals.

The determination of Se in the tissues of the rat by neutron activation analysis revealed a more or less even distribution of the element among the different brain regions (Fig. 1). The brain Se concentration of about 0.5 mg Se/kg dry mass was relatively low as compared with the highest values of 6.0, 5.3 and 2.7 mg Se/kg found in the testis, kidney and liver, respectively. In severely Se-depleted rats, however, where the Se concentration in the main pools such as the liver dropped below 1 % of the normal value, the brain still retained about 60 % (Table 1). This is achieved by preferential supply from the small amounts of Se taken up with the deficient diet and redistribution of the element from the other tissues.

Table 1: Changes in the Se content of high and low priority target tissues of rats fed Se-deficient diet for 6 generations

Organ	Se content (µg/kg dry mass)[1]		Se-/Se+
	Se+	Se-	(%)
Brain	480 ± 90	280 ± 50	**58**
Liver	2660 ± 270	17 ± 3	**0,6**

[1] Mean±SD of 3 rats; Se+: 300 µg Se/kg diet; Se-: 5 µgSe /kg diet

The fact that in periods of insufficient Se intake the brain is the target organ with the highest priority for Se supply, is an indication of the importance of the element for the CNS.

The Se-containing proteins present in the brain cells were detected by labeling rats and neuronal cell lines with ^{75}Se, separation of the proteins in the sample homogenates by two-dimensional electrophoresis and determination of the labeled Se-containing proteins by autoradiography. As here the proteins are separated according to differences in two of their characteristics, isoelectric point and molecular mass, a very high power of resolution is achieved. By labeling Se-depleted rats and cells with ^{75}Se with a very high specific activity, produced from enriched stable ^{74}Se by long-term neutron activation, the labeling techniques were optimized and the limit of detection improved to such an extent that even the Se compounds present in the cells at very low concentrations could be detected. Fig. 1 shows as an example the Se-containing proteins in the cytosolic fraction of the neuronal cell line HT22. Most of the Se-containing proteins present in other tissues were also found in the brain cells. They include several members of the families of redox-active selenoenzymes such as the glutathione peroxidases, the deiodinases and the thioredoxin reductases, and a larger number of Se-containing proteins not yet identified. Of special interest was the presence of a novel 15 kDa selenoprotein which was enriched in the brain and in the neuronal cell lines and was shown to be different from the previously detected 15 kDa selenoprotein which is mainly located in the prostate gland.

In this way, for the first time, information was obtained on the complete pattern of the Se-containing proteins present in the mammalian brain. These findings provide basic data which may be of great help in the future research on the roles of Se and selenoproteins in the CNS in health and disease.

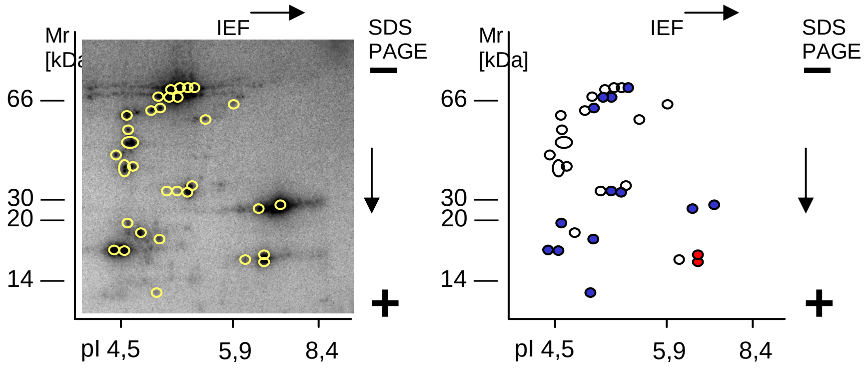

Fig. 1: Se-containing proteins in the neuronal cell line HT22 detected by labeling the cells with ^{75}Se, protein separation by two-dimensional electrophoresis and autoradiography of the labeled proteins: **o** Se-containing proteins; **o** identified selenoproteins; **o** novel 15 kDa selenoprotein

A. Kyriakopoulos, D. Behne, H. Bertelsmann, B. Hoppe, K. Bukalis, L. Dalla Puppa

Selenium and brain functions: Discovery of a novel role of selenium in neuroprotection

The brain is highly susceptible to damages by oxidants such as free radicals and peroxides, and oxidative stress is among the main pathogenic factors in neurological disorders. One of the mechanisms of cell destruction, necessary in the elimination of overproduced or unhealthy brain cells, is a process called excitotoxicity which is initiated by the release of large amounts of the amino acid glutamate. Glutamate normally acts as an excitatory chemical transmitter in the central nervous system. However, when too much glutamate is present, a suicide cascade is generated which leads to the production of free radicals and peroxides and results in the death of healthy cells nearby. It is this excitotoxic response that is rapidly triggered by damaged neurons in stroke, epileptic seizures or traumatic head injury to produce a destructive secondary injury, often killing more brain tissue than the initial insult. There is also evidence that the excitotoxic reaction can occur over a longer period of time, thus causing deterioration and death of the brain cells in Alzheimer’s disease, Parkinson’s disease and other neurodegenerative disorders.

As selenium (Se) is the essential component of several enzymes with antioxidant functions, we started a series of investigations in which we studied possible protective effects of this element in brain cells exposed to excitotoxic conditions. In these experiments on rats and cell cultures, which have been carried out in close collaboration with Prof. R. Nitsch and his coworkers from the Institute of Anatomy of the Humboldt University Medical School Charité, nuclear reactor-based methods such as neutron activation analysis and radiotracer techniques have been combined with various biochemical and histological procedures.

For the investigation of the neuroprotective effects of Se in vivo an animal model was used. Neuronal destruction was triggered in Se-depleted (Se-) and Se-adequate (Se+) rats by injection of the seizure-inducing excitotoxin kainate. Although, due to the hierarchy in the Se distribution, the brain Se level in the deficient group was reduced by only 10 %, the decrease was sufficient enough to result in a remarkably higher seizure rate after kainate treatment when compared with the Se-adequate control group (Fig. 1). Moreover, we found a strongly increased loss of neuronal cells in the hippocampus, a brain section with important functions in the memory system. After repletion of the Se-deficient animals by feeding the Se-adequate diet, both seizure rate and percentage of cell loss decreased to the values found after kainate treatment in the control animals.

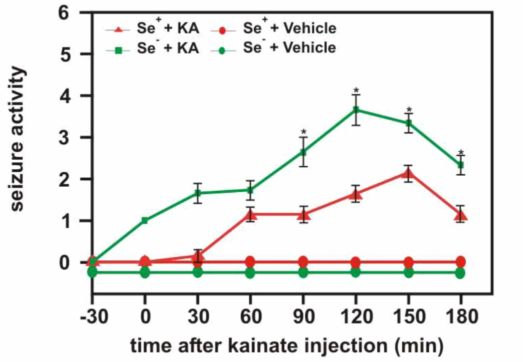

Fig. 1: Selenium deficiency increased seizure activity. Seizure activity in rats after injection of the seizure-inducing excitotoxin kainate (KA) or saline (vehicle) into Se-deficient (Se-) or Se-adequate (Se+) animals

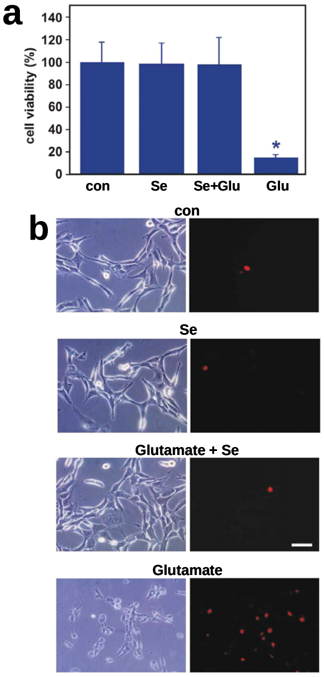

Fig. 2: Neuroprotective effect of selenium in glutamate-induced oxidative stress. Cell cultures of the hippocampal neuronal cell line HT22 were treated with 100 nM sodium selenite (Se) and/or 10 mM glutamate (Glu) for 24 h: a) Cell viability of controls (Con) (100 %) and treated cells; b) bright-field (left) and rhodamine-fluorescence (right) micrographs of the cell cultures, red cells indicate cell death

Further information on the mechanisms of the Se-mediated neuroprotection was obtained in cell culture experiments. Here the hippocampal neuronal cell line HT22 was grown in a cell medium with a relatively low Se concentration, and excitotoxic conditions were induced by adding an excessive amount of glutamate. This treatment was found to reduce cell survival by more than 80 % (Fig. 2a and b). However, the glutamate-induced cell death could be prevented by adding sodium selenite to the cell medium. The protective effect of the element was shown to be due to the incorporation of Se into selenoproteins. Interestingly, the glutamate-induced cell death could also be prevented in rescue experiments in which selenite was added hours after the glutamate insult.

In these studies an important novel role of Se was discovered. Our data indicate that Se in the form of selenoproteins protects the brain cells against destruction by oxidative stress as induced by excitotoxic reactions in disorders such as stroke, traumatic head injury and epileptic seizures and can even be effective early after the initial insult. Se supplementation may therefore be used as both a preventive and therapeutic measure to counteract the detrimental effects of excitotoxicity in patients with brain cell damage and neurodegenerative diseases.

D. Behne, A. Kyriakopoulos, H. Bertelsmann, A. Richarz

Measurement of the charge dependence of energy losses in thin media

The description of the stopping power of swift heavy ions in matter with the traditional semi-empirical formulas or the common tables turned out to be insufficient in recent times. Scientists from different working fields are asking for better accuracy, especially for energy losses in thin layers and for straggling effects. It turned out that a more microscopic description is needed, including charge state dependent stopping powers S(q) and the evolution of the charge state distribution in dependence on the layer thickness. Therefore, we are measuring at ISL, Berlin, the charge state evolution F(q,x) of ions penetrating carbon foils of varying thickness, as well as the charge state dependent energy losses $\Delta E(q)$ of ions for all relevant incoming and outgoing charge states q. As the measured energy losses in these very thin carbon foils are in the range of about 1 % of the ion energy or even less, we have to use the magnetic spectrograph Q3D with its excellent energy resolution of $\delta E/E=5\times10^{-4}$. The experimental method has been described in earlier annual reports and in Refs. [1,2]. We measure for increasing foil thickness the charge state distributions and energy losses and obtain as a result experimental information, how the charge state distribution evolves from the single charge state of the beam and how the energy loss depends on this with increasing layer thickness. These measurements are performed for different incoming charge states. From the evolution of the charge state distributions we can deduce all relevant cross sections of charge transfer reactions by solving the rate equations for all relevant processes, including electron capture, ionization, excitation and radiative and Auger decay. Using these cross sections and the measured energy losses in Monte-Carlo simulations, the charge state dependent stopping powers S(q) of the projectile ion can be extracted.

In 2002 we investigated the energy loss and the charge state distributions of ^{40}Ar-ions in carbon foils. Fig. 1 shows the charge state distributions for the incoming charge state $q_i = 18^+$ in the upper graph and for $q_i = 14^+$ in the lower one. The x-axis, indicating the carbon foil thickness, is interrupted at 40 µg/cm^2 and thereafter the charge state equilibrium distribution measured with a 231 µg/cm^2 thick carbon foil, is plotted. This equilibrium distribution agrees well with theoretical predictions of a mean charge state of 16.1.

The analysis of the stopping power is still in progress. Fig. 2 shows preliminary data of the measured energy losses for three different charge states with $q_i = q_f$. The solid line indicates the energy loss for charge equilibrium conditions calculated with the method of Biersack and Ziegler. There are deviations up to 15% between, e.g., the energy loss for $q_i = 18^+$ and the theoretical prediction. As expected, the equilibrium energy loss is close to that one of $q = 16^+$.

In the frame of our collaboration with the GSI, Darmstadt, these data will be used for the description of the energy loss and the charge state distributions of argon ions interacting with a laser generated carbon plasma.

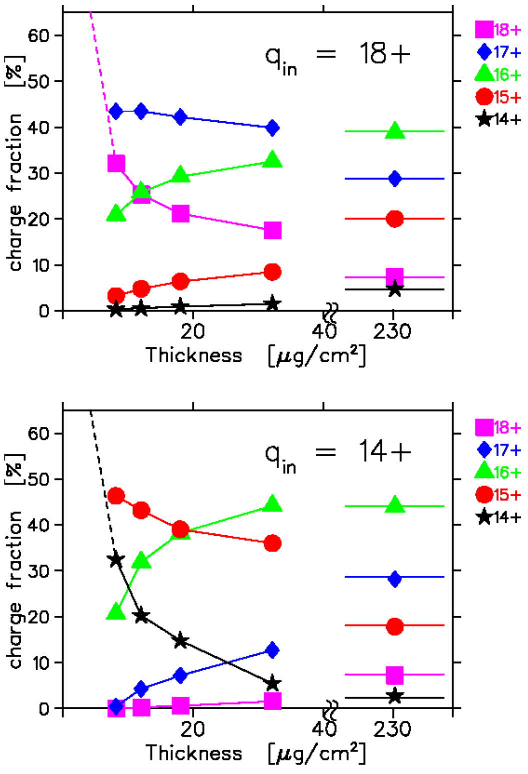

Fig. 1: Experimental charge state distributions evolving from incident Ar^{14+} ions in thin layers of carbon with thicknesses from 8 µg/cm^2 to 231 µg/cm^2.

Further calculations were performed on the dependence of the stopping power to the electron configuration of the projectile. The CASP code of Schiwietz [3] allows the calculation of the stopping power for a given potential. For the case of oxygen projectiles we calculated with the Hartree-Fock code of Cowan [4] potentials of different electron configurations and investigated their influence on the stopping power. As shown in Fig. 3 (upper panel) for O^{7+}, the stopping power differs drastically in dependence of the shell of the single electron due to the decreasing screening of the nucleus with increasing shell number. By dividing these calculated stopping powers by the stopping power of the bare nucleus (O^{8+}, blue filled circle in Fig. 3) a set of scaling factors for each shell (SF_i) is obtained. The same calculations were done for the two electron system (O^{6+}), as shown in Fig. 3, lower panel, (red filled diamonds). The green diamonds show the stopping powers calculated by multiplying S(O^{8+}) with the scaling factors of the corresponding shells of the electrons:

$$S = S(O^{8+}) \cdot \Pi_i (SF)_i^{n_i} \qquad (1)$$

i= 1s, 2s, 2p, 3s, 3p, 3d,
n_i number of electrons in the shell i.

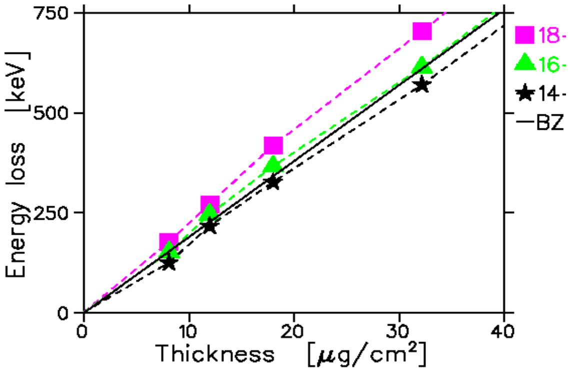

Fig. 2: The charge state dependent energy loss of Ar ions in carbon for the charge states 14$^+$, 16$^+$, 18$^+$. The solid line shows the energy loss according to the method of Biersack and Ziegler.

The agreement of this simple scaling with the calculated stopping powers is surprisingly good, and it turns out to be an effective and easy procedure to calculate the stopping powers, e.g., in the Monte-Carlo simulation, where the electron configuration of the projectile is known. Further investigations on the systematic behavior of the scaling factors for different projectiles or energies will be continued.

References:
[1] A. Blazevic, H.G. Bohlen and W. von Oertzen, Phys. Rev. A**61** (2000) 032901
[2] A. Blazevic, H.G. Bohlen and W. von Oertzen, Nucl. Instr. Meth. Phys. Res. B**190** (2002) 64-68
[3] G. Schiwietz and P.L. Grande, Nucl. Instr. Meth. Phys. Res. B**153** (1999) 1
[4] R.D. Cowan, *The Theory of Atomic Structure and Spectra*, University of California Press (1981)

A. Blazevic*, H.G. Bohlen, W. von Oertzen,
P. Pirzadeh*,
*) TU Darmstadt

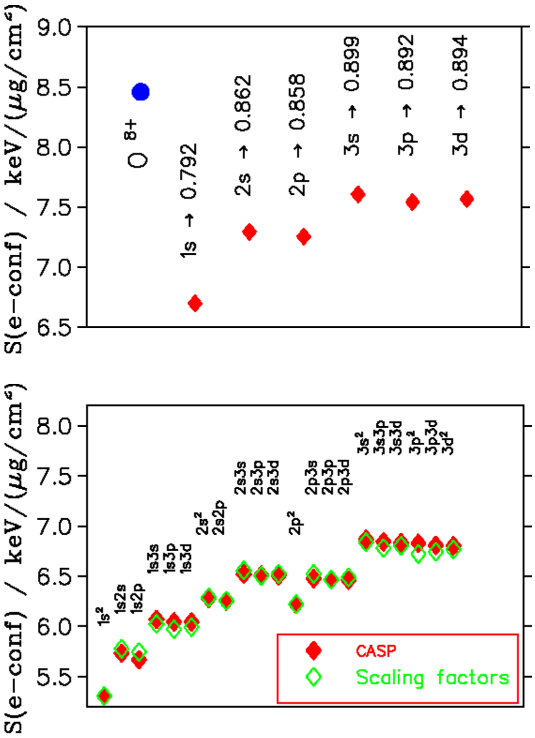

Fig 3: Upper panel: Stopping power S of $^{16}O^{7+}$ ions (one-electron system) at 2 MeV/nucleon in dependence on the occupied electron configuration calculated with the code CASP [3]. The filled circle shows the value for the fully stripped ion $^{16}O^{8+}$. Lower panel: Same as upper panel, but for the two-electron system $^{16}O^{6+}$. The CASP calculation is compared with values obtained by the scaling of the one-electron values according to eq. (1).

Structure investigations on ^{16}C and ^{14}C

Neutron-rich carbon isotopes can be built on a basic structure of three α–particles plus the excess neutrons. In fact, the nucleo-synthesis of ^{12}C occurs in a 3α-collision through a 0^+ resonance in ^{12}C just 195 keV above the 3α-threshold. This resonance decays by the emission of two γ-quanta to the ^{12}C ground state, and it represents therefore the only doorway to the formation of carbon isotopes and the *heavier elements*. The α-cluster structure of the ^{12}C ground state manifests itself in a strong oblate shape. The above mentioned 0^+ resonance is also oblate and has even a shape of 3 touching α-particles.

In ^{16}C (and ^{14}C) a linear chain configuration of 3 α-particles may exist, with a covalent bond between each α-pair via two neutrons (one neutron): α-2n-α-2n-α, as pointed out by von Oertzen [1]. A signature of this structure would be the observation of rotational bands with a correspondingly large moment-of-inertia and hyperdeformation. These structures are expected above 18 MeV excitation energy (the ^{6}He-α-^{6}He threshold is located at 23.92 MeV) and the structure of ^{6}He-^{10}Be above 13 MeV (threshold: 16.51 MeV).

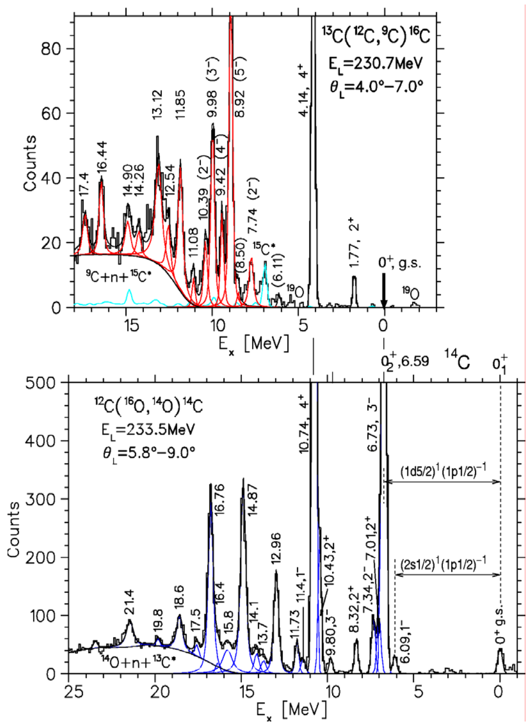

Fig. 1: Spectra of ^{16}C (upper panel) and ^{14}C (lower panel) obtained in three-neutron and two-neutron transfer reactions, respectively. The states shown in red were previously unknown.

Until now little is known about ^{16}C, e. g., excited states only up to 6 MeV. To investigate the different structures in ^{16}C (including also particle-hole (ph) structures), we measured the three-neutron transfer reaction ^{13}C(^{12}C,^{9}C)^{16}C at 230.7 MeV incident energy using the Q3D magnetic spectrograph at ISL. The spectrum (see Fig. 1, upper panel) shows 14 previously unknown states up to 17.4 MeV excitation energy. The low-lying 2^+ and 4^+ states at 1.77 MeV and 4.14 MeV, respectively, have a well known neutron (sd)^2 configuration [2]. In the region of 8.9-10.4 MeV we find a group of 4 states, which belongs to the neutron ph-configuration $(1d5/2)^3 \otimes (1p1/2)^{-1}$. The largest cross section is expected for the stretched configuration 5^-; this spin is assigned to the strongest state of this group at 8.92 MeV. This behavior is well known for direct reactions with large negative Q-values (here Q_0=-39.48 MeV). The strong population of the 4^+ state at 4.14 MeV, which has a stretched $(1d5/2)^2$ configuration, illustrates this effect. The other three states of this group at 9.42, 9.98, and 10.39 MeV are assigned as 4^-, 3^-, 2^-, respectively, according to a coupled channel analysis of angular distributions. The assignments are also consistent with the dublet structure (5^-, 4^-), (3^-, 2^-) generated by the parallel and anti-parallel coupling of the 1p1/2-hole to the $9/2^+$ and $5/2^+$ particle configurations.

The states above 11 MeV excitation energy up to 17.4 MeV are not yet assigned because different possible structures are present in this region: (i) ph-configurations including the 1d3/2 and 1f7/2 shells for particles, and the 1p3/2 shell for holes, (ii) collective modes (i. e., 3^-, 2^-) including proton excitations, and (iii) possible low-lying α-cluster structures. The latter should be investigated in a larger excitation energy range by decay studies. At present, we obtained for the high-lying new resonances valuable information about excitation energies and widths.

The ^{14}C isotope has a closed neutron shell in its ground state, which is therefore spherical. The lowest lying excited states have a 1p1h and 2p2h character: the excitation of a neutron from the 1p1/2 to the 2s1/2 or 1d5/2 shells leads to the 1p1h-dublets (1^-, 0^-) and (3^-, 2^-), respectively, which are found between 6.09 MeV and 7.34 MeV (see Fig. 1, lower panel). But also states with the (sd)^2 configurations, which are present in the ^{16}C spectrum, appear in the ^{14}C spectrum, here as $(sd)^2 \otimes (1p1/2)^{-2}$ configurations. In Fig. 1 the corresponding 4^+ states in ^{16}C and ^{14}C in the upper and lower panels are aligned to the same position by a shift of 6.59 MeV; in this case the corresponding 2^+ and 0^+ states are also simultanously aligned. The structure of ^{14}C states up to about 11 MeV is well known from many investigations. Definite spin assignments for the higher-lying states exist, however, only in a few cases and their structure is scarcely known for most states.

We have studied these states in a systematic way using 2n-stripping reactions on ^{12}C, 2p-pickup reactions on ^{16}O and the ^{9}Be(^{7}Li,d)^{14}C reaction to populate neutron-particle, proton-hole and α-cluster states, respectively. Our new data and all data in the literature on ^{14}C [4] will be reviewed for a consistent interpretation of the structure and spin-parity as-

assignments. In this complete spectroscopy, the levels are ordered into bands of different structure [5].

We measured the ^{9}Be(^{7}Li,d)^{14}C reaction at the Q3D magnetic spectrograph in Munich. The reaction mechanism is very different as compared to the two-neutron transfer in the population of ^{14}C states. The (^{7}Li,d) reaction corresponds to an “α+n“ transfer, which favors the formation of α-cluster structures in ^{14}C, but this reaction has also strong compound nuclear contributions. Due to the excellent experimental resolution (40 keV), we observe in the spectrum (Fig. 2) all known states of ^{14}C up to 21.4 MeV and 7 additional states between 15.8 and 21 MeV, which were unknown before. There are different background contributions resulting from the (^{7}Li,d) reaction on contaminations in the target: (i) ^{16}O (dark blue dashed line, Fig. 2) and (ii) ^{12}C (pink line, peaks are also marked by “ ^{17}O* “); furthermore, there are (iii) three-body (dark blue continuous line) and (iv) four-body phase space distributions (light blue line). The analysis of the spectrum is not yet completed, the spin assignments shown in Fig. 2 are taken from the literature [4].

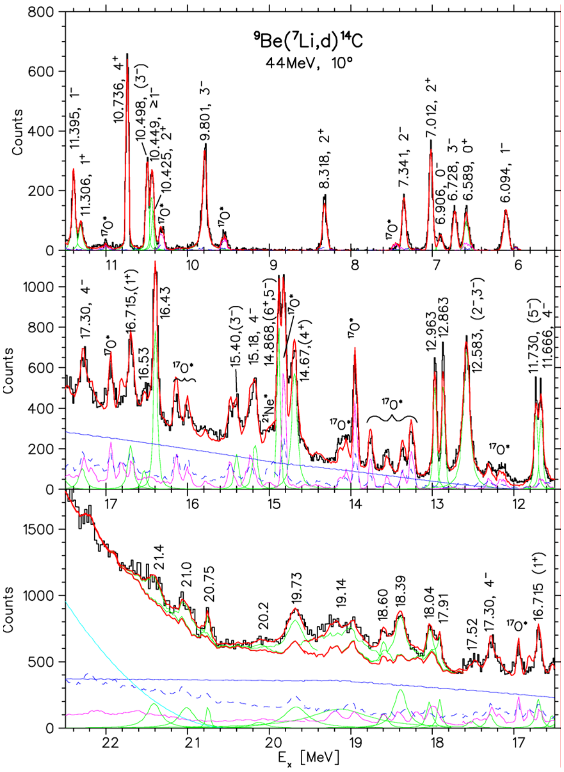

Fig. 2: Spectrum of the ^{9}Be(^{7}Li,d)^{14}C reaction measured at 44 MeV incident energy and at 10°. The red line (in the lower panel: the upper red line) corresponds the sum of all contributions.

In the two-proton pick-up reaction on ^{16}O we expect to populate proton-hole states in ^{14}C. We observe in the spectrum of the ^{16}O(^{15}N,^{17}F)^{14}C reaction, which was measured at the Q3D magnetic spectrograph in Berlin, mainly 2^{+} states: the strongest ones are the states at 7.01 MeV and 8.32 MeV: Both states are also observed in the two-neutron transfer reaction (Fig. 1). Their wave function is composed of the $(1p1/2\otimes1p3/2)_{2+}$ and $(1p3/2)^{2}_{2+}$ configurations for protons. For neutrons, the former configuration is coupled to $(2s1/2)^{2}_{0+}$ and $(1d5/2)^{2}_{0+}$, but also the 2p2h configurations $(2s1/2\otimes(1d5/2)_{2+}\otimes(1p1/2)^{-2}_{0+}$ and $(1d5/2)^{2}_{2+}\otimes(1p1/2)^{-2}_{0+}$ contribute. Odd-parity states like the 3^{-} level at 9.80 MeV can be excited in this reaction, when the wave function contains a proton 1p1h-component, e. g., $\pi(1d5/2\otimes1p1/2)^{-1}$. In the spectrum, no states are populated above 15.9 MeV, whereas we observe states up to 21.4 MeV in the two-neutron transfer and (^{7}Li,d) reactions. This can be understood from the number of proton-hole configurations, which is rather limited for ^{14}C, even for second order contributions in combination with neutron excitations. The absence of states above 16 MeV in the 2p-pick-up supports the interpretation that most of the higher-lying states observed in the (^{7}Li,d) reaction have cluster structures.

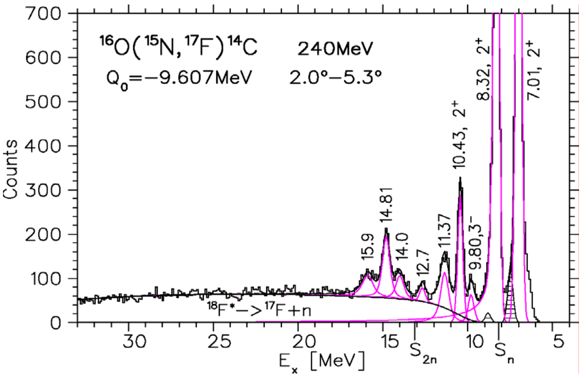

Fig. 3: Spectrum of the two-proton pick-up reaction ^{16}O(^{15}N,^{17}F)^{14}C to states of ^{14}C. States below 7 MeV excitation energy are not in the focal plane.

[1] W. von Oertzen, Z. Phys. A **357**, 355 (1997)
[2] H.G. Bohlen et al., submitted to Phys. Lett. B
[3] H.T. Fortune et al., Phys. Lett. B **70**, 408 (1977)
[4] F. Ajzenberg-Selove, Nucl. Phys. A**523**, 1 (1991)
[5] W. von Oertzen, H.G. Bohlen et al., to be published in Eur. Phys. J. (2003)

H.G. Bohlen, W. von Oertzen, R. Kalpakchieva[1], S. Thummerer, Y. Eisermann[2], Th. Faestermann[3], G. Graw[2], R. Hertenberger[2], T. Kokalova, H.J. Maier[2], T.N. Massey[4], M. Milin, Ch. Schulz, H.F. Wirth[2], A. Tumino.

[1] FLNR, JINR, Dubna, Russia, and Bulgarian Acad. of Science, Sofia, Bulgaria;
[2] LMU München,
[3] TU München,
[4] Ohio University, Athens, USA

Parity Doublets as Indications of Cluster Structure in Nuclei

Recently molecular structures have been identified in light nuclei. Intrinsically asymmetric binary systems, which occur in atomic or nuclear molecules, will give rise to rotational bands with a double structure called parity inversion doublets [see ref. 1]. Intrinsically asymmetric nuclear structures consisting of an α-particle and a larger core cluster giving rise to a parity doublet are well known in ^{20}Ne (with α + ^{16}O). We have studied the system (α + n + ^{20}Ne), which has spin different from zero, and for which a molecular picture predicts parity doublets with K=3/2 and K=1/2 as discussed in ref.1.

The other case, ^{40} Ca, (consisting of α + ^{36} Ar) was aimed on the establishment of parity doublets in a nucleus with spin = 0; in this case rotational bands with states with the alternating even spins for plus parity must appear. Both experiments have been performed with the GASP-γ-detector and the ISIS-charged particle ball at the Laboratori Nationali di Legnaro (LNL). For the study of ^{21}Ne the reaction ^{7}Li + ^{16}O -> ^{21}Ne + (p, n) has been used.

The most important result of this experiment is the observation of the E1 interband transitions connecting states of the negative parity band (K=3/2) to the states of positive parity in the K=3/2$^{\pm}$ bands. The results cast into a decay scheme are shown in fig.1. Remarkably, no intra band transitions are not observed for the negative parity states (these would be of M1 or E2-character), the inter band transitions are E1-transitions as determined from directional correlation measurements of the γ-arrays, (DCO-values), as shown in more detail in ref.2.

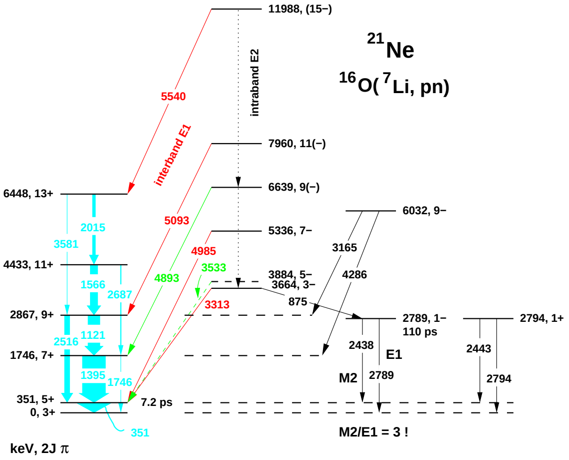

Fig.1 Gamma transitions observed in ^{21}Ne in the ^{16}O(^{7}Li,pn) reaction as observed with the GASP spectrometer. The E1-transitions connect between the negative and positive parities of members of rotational bands of the inversion parity-doublet with K=3/2.

Further, we have studied the rotational bands in ^{40}Ca with excited states which imply a structure with the excitation of 4particles – leaving 4holes in the core (4p-4h). This corresponds to alpha-particle clustering, for which also the existence of a parity doublet has been predicted.

From the non-observed E2 intraband transitions and assuming the same quadrupole moment in ^{21}Ne as for ^{20}Ne we obtain from the E1 transitions an estimate of the dipole strength and the intrinsic dipole moment of ^{21}Ne. We obtain a large intrinsic dipole moment of D_o > 0.1 e fm; this result shows that the octupole deformation of ^{20}Ne prevails in ^{21}Ne, and that in fact a structure (^{16}O + α + n) dominates in ^{21}Ne, which is in close analogy to a covalently bound asymmetric nuclear molecule.

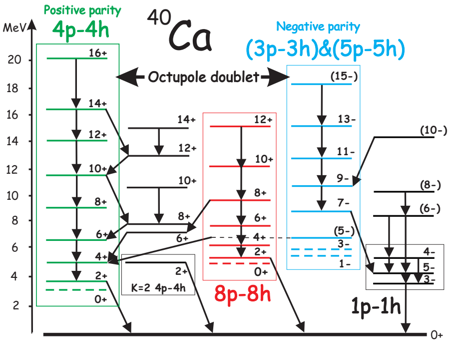

Fig.2 Band structure of ^{40}Ca, as observed in the ^{24}Mg (^{32}S, 3α) ^{40}Ca reaction using the GASP-ISIS-Spectrometer. The 4p-4h and 5p-5h bands are partners of a parity inversion doublet.

In our study of the ^{24}Mg + ^{32}S reaction at high energy, we were able to complete the spectroscopy of ^{40}Ca, by analysing the 3α channel. In this reaction under appropriate conditions of high incident energy the 3 α-particles populate the highest states of the rational bands, without intermediate low energy statistical γ-decays. Therefore, only natural parity states (0^+, 2^+,4, and 5^-, 7^-… etc.) are populated. Therefore, we were able to identify a negative parity band, which appears as the doublet partner to the previously observed (at Gammasphere) 4p – 4h band. The total decay scheme of the observed band structure is shown in Fig. 2. We are also able to confirm the existence of the 8p – 8h band, which has a large deformation parameter of $\beta_2 \approx 0.6$.

The observation of the present negative parity band is unique, and different from the corresponding band predicted in a potential model. However, in a description with an octupole deformation, as proposed by Jolos et al. (3), the energy splitting of the two bands is very well predicted. In addition, the observed vanishing of the energy splitting with increasing angular momentum is well described by the theory. This result establishes for the first time the unique structure of the excited states of ^{40}Ca as deformed bands based on cluster structure.

[1] W. von Oertzen, Eur. Phys. J. A11 (2001) 403
[2] S. Thummerer, W. von Oertzen, Tz. ,Kokalova et al. J. Phys. G. 29 (2003) 509
[3] R. V. Jolos, P. von Brentano, Phys. Rev. C49 (1994) R 2301 and private communications

S.Thummerer, Tz. Kokalova, S.Torilov, W. von Oertzen, H. G. Bohlen, G. de Angelis et al

Cluster Emission in Compound Nuclear Reactions

Normally the expected compound nuclei decay by the evaporation of nucleons and α-particles. We have studied several systems where the compound nucleus decay at higher excitation energy gives rise to emission of several α-particles or simultaneously to the emission of unstable fragments with excited states just above the α-particle emission thresholds. The observation of ^{8}Be (0_1^+, unbound by 92 KeV) and ^{12}C*(0_2^+) becomes possible in a ΔE-E telescope if the geometric angular opening is larger than the opening angle of the emission cone of the α-particles, which are typically emitted (in their center of mass system) with energies below 100 KeV. The experiments cited below have been performed with the γ-detector ball GASP and the silicon-detector ball ISIS (40 ΔE-E telescopes, each telescope extending over an angular range of ca 27°). The width of the emission cones for the α-particles from the emitted ^{8}Be and ^{12}C*(0_2^+)-fragments are typically 7° – 12°.

The reaction discussed here is ^{28}Si + ^{24}Mg at E_L= 139 MeV, yielding a high probability for 2α and 3α emission. The ΔE-E spectra are shown in fig.1.

The γ-spectra in GASP in these experiments can be gated for example on 3α-particles or on ^{12}C*(0_2^+), the latter appearing as a prompt pile-up of 3α-particles (see fig.1). The probability of a multi-hit event to contribute to this event line is below 1%. For the ^{8}Be the probability of a chance double hit is in the range of 10% - 15%, depending on laboratory angle. The simultaneously expected emission of ^{7}Li (and ^{6}Li) in the same region ΔE-E values is suppressed due to negative Q-values (and the absorber foils inside of ISIS).

In Fig. 2 we show the γ-spectra obtained with two charged particle triggers representing the emission of 3α's. The most visible difference between the γ-ray-spectra gated on 3α-particles and those gated with the ^{12}C* (0_2^+)-cluster, is the appearance and dominance of the γ-transitions of lighter masses than ^{40}Ca; these are the nuclei ^{39}K and ^{36}Ar, indicating that the residual nucleus has been left at higher excitation energy with the emission of ^{12}C, and a subsequent emission of another charged particle (proton or α-particle) becomes rather probable. The explanation of this effect is that the ^{12}C* - fragment is emitted into the phase space of the final nucleus in one step, whereas for the emission of the three α-particles the emission phase space occurs in three consecutive steps, producing a larger probability, and a larger total amount of kinetic energy is carried away. This effect is also reflected in the energy spectra of the sum of the three α-particles (taken from three different telescopes) as compared to the energy spectrum of ^{12}C* fragments; the latter reach only to a fraction of the energy carried by the three α-particles.

This is the first time that the emission of unbound multiple α-clusters has been observed in the decay of compound nuclei with N=Z.

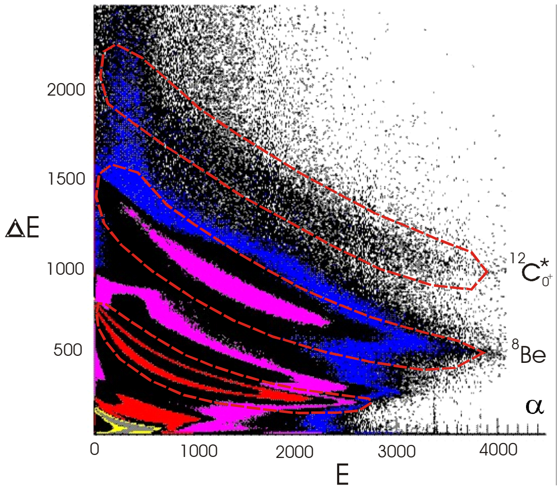

Fig. 1: Plot of Energy-Loss and Energy signals from the ΔE-E telescopes of the ISIS-GASP detector system Note the observation of ^{8}Be and ^{12}C(0+,2) emission.*

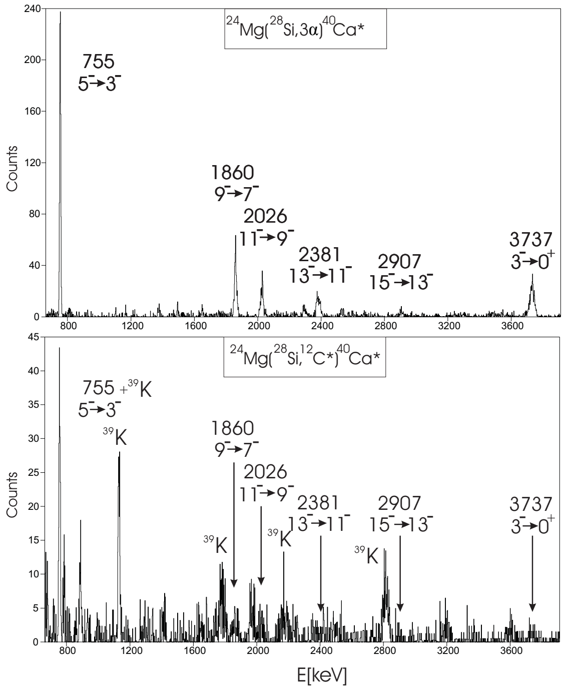

Fig. 2: γ-spectra gated with 3α-particles or with ^{12}C$_O^+$ (7,56 MeV) respectively. The residual nucleus for 3α-particles is ^{40}Ca. Transitions in ^{39}K and ^{36}Ar are due to subsequent particle decay of highly excited ^{40}Ca.*

S. Thummerer, Tz. Kokalova, S. Torilov, W. von Oertzen, H. G. Bohlen, G. de Angelis et al.

Development of high-rate and high-resolution thermal neutron imaging detectors

The development of high-rate and high-resolution thermal neutron detectors [1] with two-dimensional position- and time-of-flight (TOF) resolution, which are based on a thin composite ^{157}Gd/CsI converter foil sandwiched between two low-pressure micro-strip gas chambers (MSGC) with MSGC plates in 4.5 mm distance either side of the converter, was continued. Utilizing the extraordinarily high thermal neutron capture cross section of ^{157}Gd of 255,000 barn, resulting in 67% capture in a 3µm thick ^{157}Gd layer, the converters for cold to thermal neutron detection are fabricated by sputter-deposition of 0.5-1.5µm thick layers of ^{157}Gd either side of a 6µm thick stretched ARAMID (Kevlar) support foil. After thermal neutron capture in 3 µm ^{157}Gd, at least one fast conversion electron of 29-182 keV is emitted with 60% efficiency from one of the converter sides. A detectable cluster of low-energy (eV) secondary electrons is obtained if both sides of the converter are over-coated by ~1µm thick CsI layers with pyramidal or columnar surface morphology. These electrons are then amplified in a two-stage avalanche amplification mode, which is possible at the high reduced field strengths E/p achievable at the low operation pressure p~20mbar in isobutane: In the first stage the electron avalanche is amplified in parallel-plate mode at constant E/p, extending from the converter surfaces (on negative potential) up 0.5 mm above the MSGC plates, and in the second stage further in micro-strip mode in strongly rising E/p when the avalanche is approaching the anode strips on the MSGC plate. This two-stage amplification mode gives safe operation at high gains >10^5 and very fast pulses of 4-5 ns FWHM, which lend themselves e.g. to delay line readout.

In the present detector version an improved delay line readout with capacitive interpolation between adjacent strips, impedance matching amplifiers on each readout node, fourfold electrical sub-division per detection plane and evaluation of double-hit events is used for position resolutions ≤0.3mm and counting rates ≤2 MHz per MSGC plate. In addition, TOF resolutions <10 ns can be achieved. Thus, large-area modular detector arrays can be set up economically. For readout a powerful PCI data acquisition (DAQ) board has been developed comprising four dead-time free 8-channel multihit TDC chips of the F1 type with 120 ps LSB (i.e. time bin size), 256 Mbytes histogram memory and a 1 GFLOP digital signal processor (DSP) [2]. In addition, pulse height can be measured in the TDCs with fixed shaping time via the pulse length by means of time-over-threshold discriminators. Since the intrinsic resolution and counting rate capacity of the low-pressure MSGC detectors is even higher, in the next EU frame program FP6 a detector version with single-strip readout and a new self-triggering ASIC shall be developed allowing for ~0.1mm position resolution and counting rates of ~10^8/s/plate, for applications like time-resolved tomography or quasi-Laue diffraction at next generation spallation neutron sources [3]. On the other hand, as spin-off of the project for ^{3}He filled multi-wire chambers (MWPC) of BENSC a simpler board has been developed last year, too, comprising only one 8-channel TDC chip, 256 Mbytes histogram memory, a 0.9 GFLOP DSP and in addition a 40 MHz flash ADC for digitization of amplitude signals, thus allowing for pulse height corrections per software. With this board so far counting rates up to 1.5 MHz have been detected.

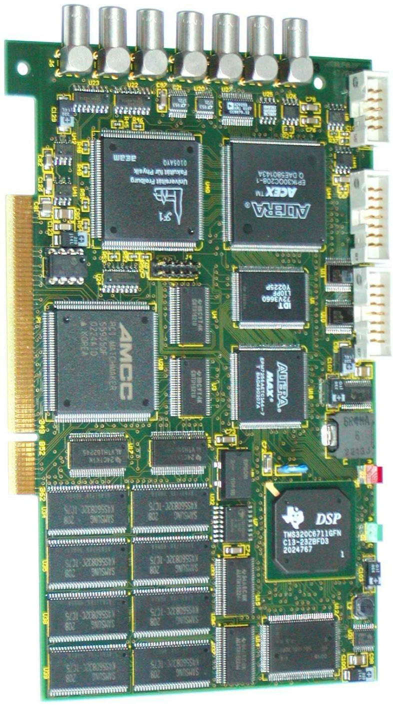

Fig. 1: Photograph of the MWPC DAQ board. The main components are a F1 TDC chip with control CPLD and FIFO buffer, a 40 MHz flash ADC, a 0.9 GFLOP DSP, 256 Mbytes histogram memory with its control CPLD and a PCI interface.

[1] B. Gebauer et al., Hahn-Meitner-Institut Berlin, Ann. Rep. 2001, pp. 90-91; Nucl. Instr. and Meth. A 409 (1998) 56-62

[2] B. Gebauer et al., Nucl. Instr. and Meth. A 471 (2001) 249-253; Ch. Schulz et al., in “Advances in Neutron Scattering Instrumentation, I.S. Anderson, B. Guerard, editors, Proc. SPIE Vol. 4785 (2002) 203-213

[3] B. Gebauer, in “Advances in Neutron Scattering Instrumentation”, loc. cit., (2002) 182-196

Work supported by the European Commission under contract no. HPRI-CT-1999-50005

B. Gebauer, Ch. Schulz, G. Richter, F.V. Levchanovski, A. Nikiforov, et al.

Division

SE Solar Energy Research

The solar energy division of the HMI concentrates its research activities on the exploration of the potential of highly productive thin-film technologies for solar cells of „tomorrow“ and „beyond“. The main objective is to realize systems which lead to substantial cost reduction at high conversion efficiency. This requires research for improvements of materials and systems which are already at the edge of being industrialized but also research for new materials and innovative solar cell structures. Therefore, the activities reach from basic material research to the development of technologies for solar cells and minimodules on the laboratory scale.

The work is supported by the broad range of analytical methods available in both sections of the HMI, particularly in the field of surface and interface physics, defect spectroscopy, ion-beam techniques and structural characterization, solid states physics, as well as conventional material and device analysis.

The groups collaborate in numerous projects and networks with national and international partners. The division Solar Energy Research comprises 5 scientific departments:

SE1 Silicon Photovoltaics
SE2 Heterogeneous Material Systems
SE3 Technology
SE4 Dynamics and Interfacial Reactions
SE5 Solar Energetics

and the group

SE6 Electronic Structure of Semiconductor Interfaces

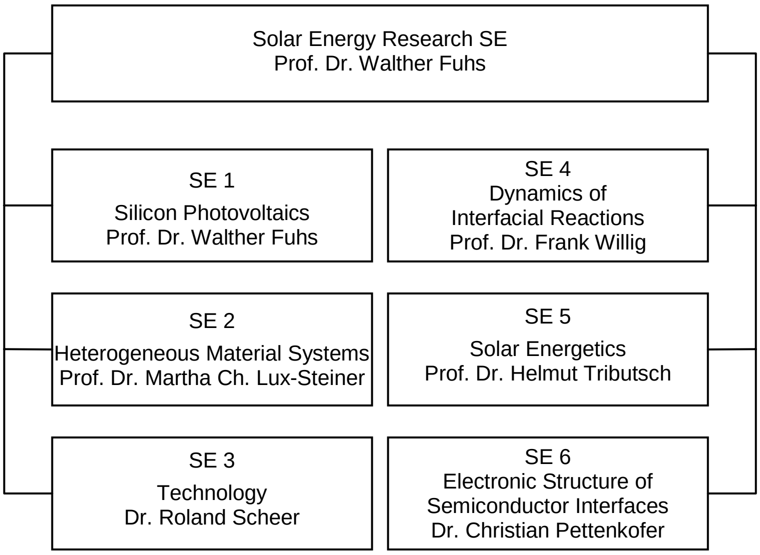

Aluminium-induced layer exchange – Influence of the oxide layer

A future generation of silicon thin-film solar cells could well be based on polycrystalline silicon (poly-Si) on foreign substrates with grain sizes larger than the thickness of the active Si layers. A promising approach for such a development is the formation of a thin large-grained poly-Si seed layer on a glass substrate and a subsequent homoepitaxial thickening of this seed layer by a low-temperature deposition process ($T \leq 600°C$). A very attractive process for seed layer formation is the aluminium-induced layer exchange (ALILE) which makes use of aluminium-induced crystallisation of amorphous silicon (a-Si). In this process an initial film sequence glass/Al/a-Si is transformed into a glass/poly-Si/Al+Si film stack. The transformation takes place during an annealing step at temperatures well below the eutectic temperature of the Al/Si system (T_{eu} = 577°C). The process starts with the local formation of Si nuclei within the Al layer. These Si nuclei grow in lateral direction until adjacent Si grains touch each other and finally form a continuous poly-Si film on the glass substrate [1,2].

So far the mechanism of crystallisation in the ALILE process is only poorly understood. It has been speculated that a thin oxide layer is essential for the process between the initial Al and the initial a-Si layer which may be formed by oxidation of the initial Al layer during the vacuum break prior to the a-Si layer deposition. We have addressed this question using energy-filtered TEM and electron energy loss spectroscopy to analyse the distribution of Al, O and Si at the Al/a-Si interface. These studies proved convincingly that an Al-oxide layer had formed during the vacuum break. For a more quantitative understanding we studied the growth of the poly-Si films for samples where an oxide layer had been grown deliberately by exposing the Al film for different oxidation times t_{OX} to an atmosphere with a partial pressure of oxygen of $6.5 \cdot 10^{-3}$ mbar. The poly-Si film growth can be observed during the annealing process by placing the sample in a heat stage of an optical microscope and observing the reflection from the initial glass/Al interface through the glass substrate.

Fig. 1 shows the crystallised fraction (ratio of poly-Si area to total area) as a function of the annealing time at a temperature of 420 °C for different oxidation times. The thinner the oxide layer, the faster is the layer exchange. However, this enhancement of crystallisation for thin oxide layers is connected with a strong increase of the number of Si grains (Fig. 2, blue curve) which results in a reduction of the average grain size. The average area of a single grain equals the total area under investigation divided by the number of grains. Assuming a square shape for the grains, we calculated the edge length of the squares and defined this as the estimated grain size. With increasing thickness of the oxide the number of nuclei decreases and the average grain size increases correspondingly (Fig.2).

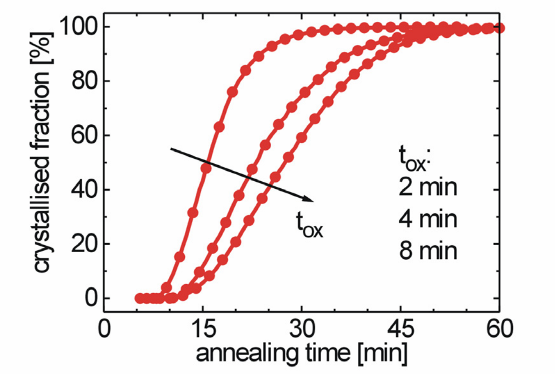

Fig. 1: Crystallised fraction versus annealing time for different oxidation times t_{ox}.

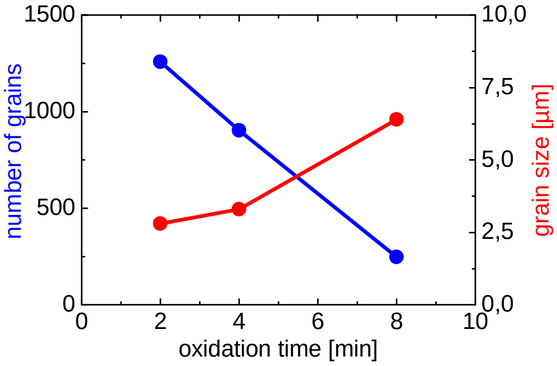

Fig. 2: Number of grains (blue curve) within the area under investigation (A = 100µm x 100µm) and the resulting estimated grain size (red curve) versus oxidation time.

These results underline the important role of the oxide layer for nucleation and growth of the poly-Si film. The working hypothesis is that the oxide layer acts as a barrier for the diffusion of Si (Al) into the initial Al layer (a-Si layer). The thicker the oxide layer, the lower is the number of grains and the longer is the process time to complete the layer exchange process. In this view nucleation is related inhomogeneities or defects in the thin oxide layer. This experience opens new process paths for actively controlling the nucleation rate.

[1] S. Gall, J. Schneider, M. Muske, I. Sieber, O. Nast, W. Fuhs, Proceedings of PV in Europe (2002), in press.
[2] I. Sieber, R. Schneider, I. Doerfel, P. Schubert-Bischoff, S. Gall, W. Fuhs, Thin Solid Films (2003), in press

---

S. Gall, J. Schneider, M. Muske, I. Sieber, W. Fuhs

Amorphous/crystalline-silicon heterojunction solar cells

Heterojunctions between hydrogenated amorphous silicon, a-Si:H, and crystalline silicon, c-Si, can be made at low process temperatures of typically 150-200 ^{o}C and therefore offer a low-temperature and low-cost alternative to the traditional silicon wafer technology. The so far best results have been obtained by Sanyo Corporation. Using textured n-type silicon wafers Sanyo reached an efficiency of 20.7 % for a laboratory cell where for both the emitter and the back contact a-Si:H technology was employed. The focus of our work is to develop this low-temperature technology for application in case of temperature sensitive silicon absorbers such as poly-Si films but also multicrystalline or band-grown Si-material. Since these absorbers are in general p-type we so far have worked with heterojunctions on p-type Si wafers only. The best result which we obtained in close collaboration with the FU Hagen in the frame of a networking project (BMBF) is illustrated in Fig.1.

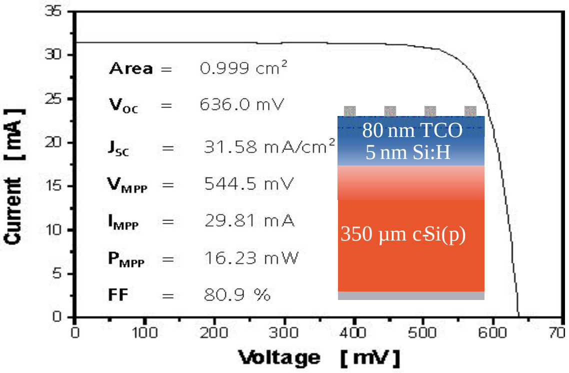

Fig.1 I-U characteristics of an a-Si:H(n)/c-Si(p) solar cell (certified by ISE-Freiburg). Inset shows a schematic sketch of the structure.

The structure is TCO/a-Si:H(n^{+})/c-Si(p) with back surface field (BSF). The transparent conducting oxide, TCO, was indium tin oxide (ITO) but similar results have also been obtained using ZnO:Al as window material. This solar cell with an area of 1 cm^{2} has a certified efficiency of 16.23 %. This is to our knowledge the best result so far published for this inverse structure on a p-type flat Si wafer.

The most critical part in this cell structure is the preparation and optimization of the a-Si:H emitter. In order to develop a deeper understanding of the physics of this device we carefully analysed bulk and interface properties of such amorphous layers and studyied the cell parameters as a function of the thickness d. The result is that the optimum emitter thickness is close to d = 5 nm. At higher values of d the optical absorption in the emitter becomes a limiting factor and at lower values there is a detrimental influence of the TCO work function and of emitter shorts on the a-Si:H/c-Si heterojunction. It turned out that the properties of the above solar cells were not limited by the quality of the hetero-interface. This results from the fact that the active heterointerface is perfectly passivated by an optimized wafer precleaning and an a-Si:H(n) layer deposition process. For this purpose special analytical tools including such for getting information on an atomic depth scale were developed.

The amorphous films were deposited by plasma enhanced chemical vapor deposition (PECVD) from gas mixtures of silane SiH_4 and phosphine PH_3 at a substrate temperature of 170 ^{o}C. UV-excited constant final state yield spectroscopy (CFSYS) is used to study the density of states distribution in such films. Comparison with results from photoyield measurements proved that this method has advantages as compared with UPS and gives the most reliable results.

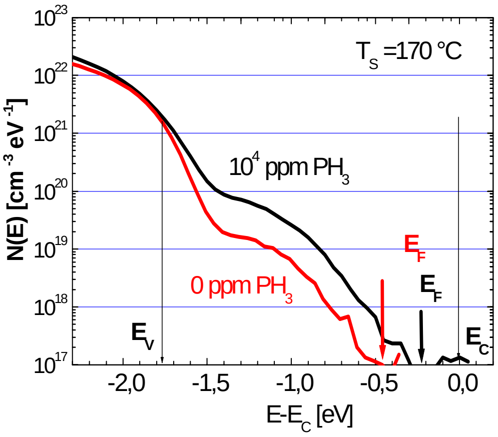

Fig.2 Density of state distribution resulting from CFSYS measurements of a doped (10000 ppm PH_3 /SiH_4) and a non doped ultrathin a-Si:H(n) films on crystalline silicon. Deposition temperature was 170 C.

Fig. 2 compares the gap state distributions and Fermi level positions of undoped and phosphorus doped films. Doping clearly leads to a shift of the Fermi level towards the conduction band from E_C – E = 0.5 eV to 0.25 eV. This is connected with a pronounced increase of the concentration of deep gap states and a flattening out of the band tail at the valence band. Qualitatively these observations are similar as in case of thick amorphous films. However, there are pronounced quantitative differences in particular in case of undoped a-Si:H which for thick films would have much lower N(E) values.

Fig. 3 shows that the doping effect saturates at a gas phase doping level of about 10^{4} ppm. For the performance of the solar cell the Fermi level position in the thin film is a crucial parameter. The Fermi level position determines the minimal emitter layer thickness which allows to screen the field penetration from the TCO-a-Si:H(n) contact and thus the reachable band bending in the absorber. The Fermi level position here amounts to about E_C-E_F = 0.25 eV. Of course this value strongly depends on the deposition and posttreatment conditions. This is the first investigation of the behavior of ultra thin a-Si:H emitter films on c-Si substrates by CFSYS.

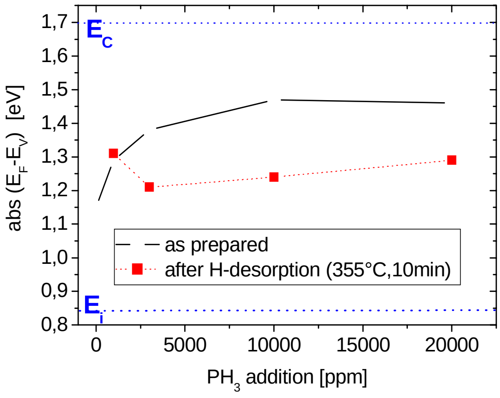

Fig. 3 Position of the Fermi level in a-Si:H films with different doping levels before and after H-desorption.

The dependence of the cell parameters on the thickness d of the emitter layer is presented in Fig. 4. These results reflect the opposing influence of two effects which leads to optimum performance at a value of around 5 nm. The short circuit current j_{SC} decreases continuously with increasing d due to the increase of optical absorption in the a-Si:H(n^+) layer and their extreme low contribution to the photocurrent if the a-Si:H emitter layer becomes thicker (dead layer). The second opposing influence consists in the decrease of the open circuit voltage V_{OC}. Two explanations may be given to this behavior. The break down of V_{OC} may be the result of imperfections (shunts) in the ultra-thin a-Si:H film. However, measurements of surface photovoltage (SPV) suggest as an alternative explanation that the band bending in the Si-wafer is reduced at very low thicknesses. The TCO-layer may form a Schottky contact with the a-Si:H(n^+) the field of which penetrates into the c-Si space charge region thus reducing V_{OC}. Such results suggest that the TCO is not just acting as a window material but also influences the electronic structure of the heterojunction. Therefore the complete contact system TCO/a-Si:H/c-Si has to be analysed and considered in a process of optimisation.

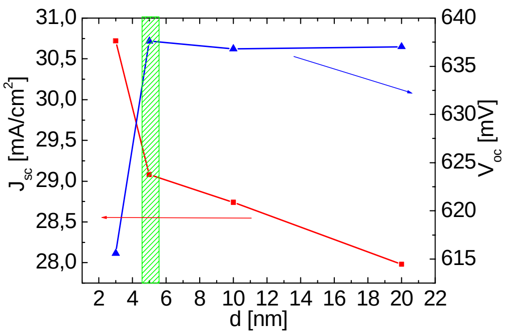

Fig. 4. Experimental determined parameters J_{sc} and V_{oc} of the TCO/a-Si:H(n) /c-Si(p) solar cell in dependence on the a-Si:H(n) emitter thickness.

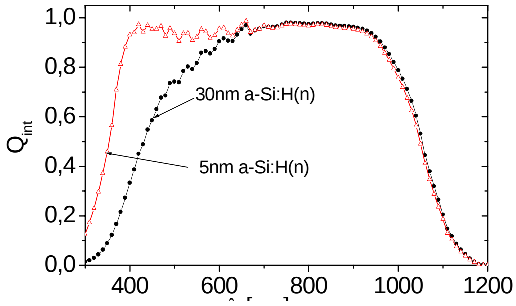

Fig. 5.Internal Quantum efficiency of a-Si:H(n)/c-Si(p) solar cell with 5 nm and 30 nm emitter, respectively.

Fig. 5 shows that in fact the internal quantum efficiency in the short wavelength region is strongly enhanced when the thickness descreases from 30 nm to 5 nm. The blue response in the case of a 5 nm thick emitter layer is limited by the TCO absorption edge.

Thes results make evident that the whole TCO/a-Si:H/c-Si system has to be analyzed and considered for an optimization of the solar cell device.

A detailed analysis of the temperature dependence of V_{OC} and the dark saturation current of the hetero solarcell presented in Fig. 1 and Fig. 5 shows that the cell efficiency is not limited by the a-Si:H(n)/c-Si(p) interface, but by the quality of the absorber and the rear contact. Therefore further improvements are possible by an optimisation of the back contact and the absorber. In addition the use of light trapping structures will increase J_{SC} and will not reduce V_{OC} as long as the interface of the heterojunction is well passivated.
Results are published in Ref.1-4

[1] M.L.D. Scherff, A. Froitzheim, A. Uljaschin, M. Schmidt, W.R. Fahrner, W. Fuhs, Proceedings of PV in Europe (Rome, Oct. 2002), in press
[2] M. Schmidt, A. Froitzheim, R. Stangl, L. Elstner, K. Kliefoth, W. Fuhs, Proc. of 17th Europ. Photovoltaic Solar Energy Conf. (2001), 1383
[3] M.Schmidt, O. Milch, Th.Lußky, A.Schöpke, Mat. Res. Soc. Symp. Proc. (San Francisco, 2003), accepted.
[4] A.Froitzheim, R.Stangl, L.Elstner, W.Fuhs, 29th IEEE Photovoltaic Solar Energy Conf. (New Orleans, Mai 2002).

A. Froitzheim, R. Stangl, H. Angermann, L. Elstner, W. Fuhs, K. Kliefoth, A. Laades, A. Schöpke, M. Schmidt

Laser crystallisation of amorphous silicon: texture-formation on metals

Excimer laser crystallization of hydrogenated amorphous silicon (*a*-Si:H) is a well-established method to produce polycrystalline silicon (poly-Si) with a grain size of up to 5µm. The goal is to use laser-crystallized poly-Si as a seed layer for an epitactically grown absorber. Due to the short absorption depth of poly-Si, a back contact and a reflector are necessary for solar cell applications. In addition to the electrical back-contact, a thin metal layer on the glass substrate can be utilized as the reflector. For this purpose, we developed for the first time a reliable process for laser-crystallization of *a*-Si:H on molybdenum (Mo) coated glass.

Undoped *a*-Si:H films were deposited at 230 °C by plasma-enhanced chemical vapor deposition (PECVD) on Mo coated glass substrates to a thickness of ≈ 80 nm. The thickness of the Mo layer varied between 100 and 200 nm. The *a*-Si:H films were crystallized using a XeCl excimer laser (wavelength 308 nm, pulse duration ≈ 20 ns). To prevent explosive out-diffusion of hydrogen the specimens were crystallized using a step-by-step crystallization procedure. In Fig. 1 the average grain size, $<x>$, of the laser-crystallized poly-Si determined from SEM images is plotted as a function of the final laser fluence, E_L, for a Mo layer thickness of 100 and 200 nm. The samples containing a 100 nm thick Mo layer show the same crystallization regimes that are well known from the crystallization of poly-Si on glass and quartz substrates. At small laser fluences ($E_L \leq 450$ mJ/cm^2) the *a*-Si:H layer is partially molten which results in the formation of small grained poly-Si ($<x> \approx 100$ nm). At $E_L \geq 530$ mJ/cm^2 the *a*-Si:H film is completely molten which also results in the formation of small grained poly-Si since epitaxial re-growth from the substrate cannot occur. In between these two melting regimes a laser-fluence window exists where $<x>$ increases to about 450 nm. This regime is called the super lateral growth (SLG). The dependence of the average grain size on E_L is similar to samples that do not contain a metal layer between substrate and poly-Si (open diamonds in Fig.1). However, the presence of the thin metal layer causes a significant reduction of $<x>$ by about a factor of 4 compared to the crystallization of an a-Si:H layer with identical thickness on quartz. Additionally, E_{SLG} depends critically on the Mo layer thickness. A 200 nm thick Mo layer results in an increase of E_{SLG} to about 770 mJ/cm^2. The shift of E_{SLG} to 770 mJ/cm^2 is accompanied by a pronounced increase of the maximum average grain size to 900 nm. This might be due to a change of the heat diffusion through the metal-substrate structure [1].

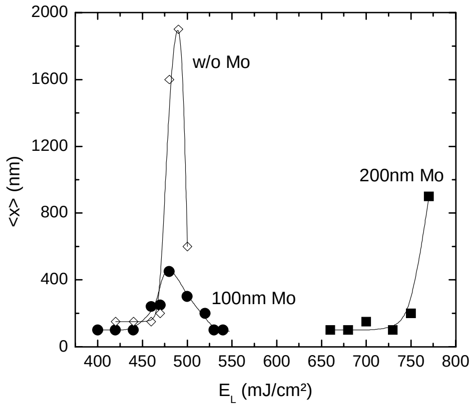

Fig. 1: Average grain size, $<x>$, of poly-Si as a function of the laser fluence, E_L, for Mo layers with a thickness of 100 nm (circles), 200 nm (squares) and without a Mo layer (open diamonds). The thickness of the *a*-Si:H layer is 80 nm. The lines are guides to the eye.

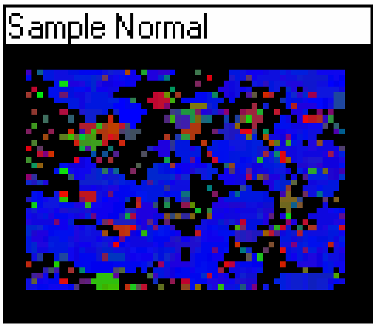

Fig.2: Orientation mapping from electron backscattering diffraction measurements. Red, green, and blue represent (100), (110), and (111) oriented grains.

The results shown above reveal that the crystallization process is not influenced by a thin Mo layer. This is further corroborated by the fact that on Mo coated glass a preferential {111} orientation in the direction of the surface normal is observed for specimens crystallized in the SLG regime. Recently, the same observation was reported for poly-Si on quartz. Fig. 2 shows results of grain orientation measurements from electron backscattering diffraction. The specimens exhibit a pronounced preferential {111} orientation of the silicon grains. Other metals investigated such as Al resulted in significant damage of the silicon layer during laser crystallization [2].

K. Brendel, N. H. Nickel, P. Lengsfeld, W. Fuhs

[1] K. Brendel, P. Lengsfeld, I. Sieber, A. Schöpke, M. Nerding, H. P. Strunk, N. H. Nickel, and W. Fuhs, J. Appl. Phys. **91**, 2969 (2002).

[2] K. Brendel, P. Lengsfeld, I. Sieber, A. Schöpke, M. Nerding, H. P. Strunk, N. H. Nickel, and W. Fuhs, Thin solid films, at press (2003)

Recombination in Cu(In, Ga)S_2 thin-film solar cells

As we have shown in our previous work, recombination via interface states at the $CuInS_2$/CdS interface dominates the transport of charge carriers in $CuInS_2$ solar cells. This explains the open circuit voltages of about 750 mV which is a moderate value in view of the absorber band gap E_g of 1.5 eV. In this study we investigate the influence of the incorporation of Ga into the chalcopyrite absorber on the dominating transport mechanism. Recom-bination losses are analyzed by measuring *j(V)* curves as a function of temperature and illumination.

The activation energy of the dominating recombination is determined from the slope of an Arrhenius plot of the saturation current density which is corrected for the temperature dependence of the diode quality factor. As shown in Fig. 1, the $CuInS_2$ cells show activation energies below the absorber band gap, due to the dominating recombination at the interface over a barrier which is reduced by the unfavourable band line-up or Fermi-level pinning at the $CuInS_2$/CdS interface. In contrast, the investigated Cu(In,Ga)S_2 cell shows an activation energy equivalent to the absorber band gap, indicating that recombination in the space charge region dominates the current transport.

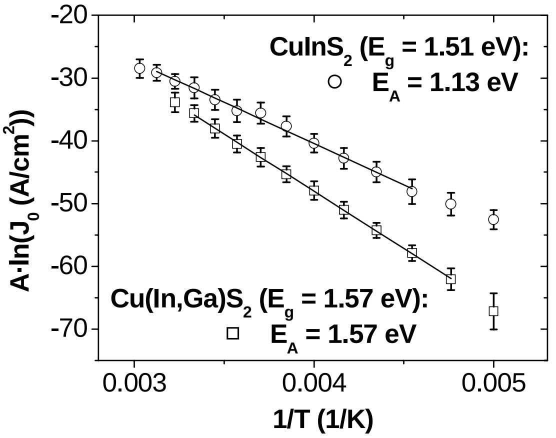

Fig. 1: Corrected saturation currents for Cu(In,Ga)S_2 cells depending on absorber composition

Proportional to the increase of the activation energy one could theoretically expect an increase of the open circuit voltage. But so far, the highest observed open circuit voltages correspond only to an increase of about 40 mV beyond the increase in the band gap. We can explain this behavior by the stronger influence of tunneling assistance to the recombination which we observe for the cells with higher activation energies. Therefore the increase in activation energy due to shifting the dominating recombination from the interface into the absorber cannot yet be fully converted into an increase of the open circuit voltage. To this aim the tunneling has to be reduced by proper device design.

To explain the described changes in the recombination mechanism we presume that positive interface charge determines the band bending towards the absorber/buffer interface as well as towards absorber grain boundaries. In this we follow the assumption that intergrain interfaces in the polycrystalline absorber layer have interface states of the same type as the $CuInS_2$/CdS interface states, as it was postulated to explain the oxygenation and air annealing effects on the electronic properties of Cu(In,Ga)Se_2 devices [1].

In case of dominating interface recombination the activation energy of the saturation current is a measure of the band bending towards the interface. The band bending towards the grain boundaries can be deduced from the temperature dependence of the series resistance. The temperature dependence of the series resistance of cells with a typical non-oriented grains structure is shown in Fig. 2. The series resistance increases with decreasing temperature with an activation energy which we can ascribe to the height of the potential barriers at the grain boundaries in the absorber. For comparison, the temperature dependence of the series resistance is shown for a cell with a columnar grain structure. Due to the lack of grain boundaries in the transport direction of the diode current, these particular cells don't show increasing but decreasing series resistance with decreasing temperature.

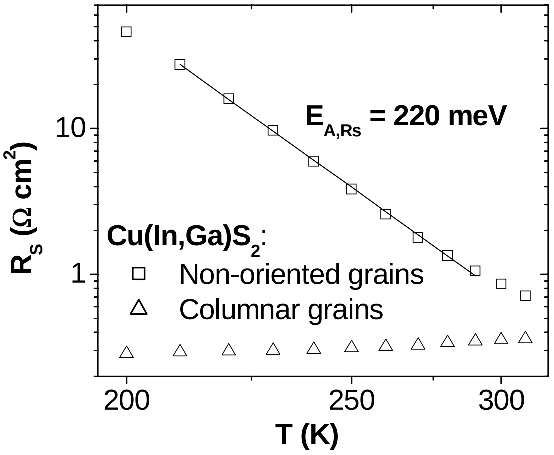

Fig. 2: Temperature dependence of the series resistance for Cu(In,Ga)S_2 cells depending on absorber grain structure

Analysis of a large number of cells reveals that the activation energy of the series resistance as well as the activation energy of the saturation current are varying with absorber composition and illumination. There are, however, strongly correlated. While there are a number of mechanisms which could in principle shift the dominant recombination away from the heterointerface, this correlation confirms the original assumption. Hence, it has to be concluded that the incorporation of Ga increases interface charges, thereby increasing the band bending to a value that prevents excessive recombination at the absorber heterointerface.

Reference
[1] U. Rau, J. Appl. Phys. 86 (1999) 497

J. Reiß, S. Bakehe, R. Klenk, M.C. Lux-Steiner

Chalcopyrite Thin Film Tandem Cell with V_{OC} = 1.2V

A stacked tandem cell based on a $Cu(In,Ga)Se_2$ bottom and a $CuGaSe_2$ top cell is prepared. The efficiency of the complete cell is 7.4% with an open circuit voltage of 1.18V.

One main objective to investigate and develop wide gap chalcopyrite solar cells is the ultimate goal of a thin film tandem solar cell, using the well developed $Cu(In,Ga)Se_2$ absorber for the bottom cell, utilizing the "red" part of the solar spectrum, and a wide gap chalcopyrite, e.g. $CuGaSe_2$ for the top cell, to harvest the "blue" light. Taking the solar spectrum into account one can estimate a factor of 1.5 improvement for the efficiency compared to a pure $Cu(In,Ga)Se_2$ cell. Therefore a cell with 30% efficiency seems feasible, combining high efficiency with the economic advantages of thin film solar cells. Before a commercial tandem cell will be within reach a number of problems are still to be solved. The ultimate goal is a monolithic tandem cell with the top cell prepared directly on top of the bottom cell, but as an intermediate step we develop stacked tandem cells with separate $Cu(In,Ga)Se_2$ and $CuGaSe_2$ cells on their individual substrate glasses. The four terminal device is wired in series (as would be a monolithic tandem cell).

The bottom cell is a standard $Cu(In,Ga)Se_2$ cell with an absorber from the Shell Solar pilot line, and the CdS-buffer, ZnO window and NiAl grid prepared by the HMI base line. The top cell is a transparent $CuGaSe_2$ cell based on ITO as a transparent back contact with a $CuGaSe_2$ absorber layer prepared in our standard two stage process, CdS buffer, ZnO window and NiAl grid. A thin Au-wire is soldered to the front grid of the $Cu(In,Ga)Se_2$ solar cell and to the ITO back contact of the $CuGaSe_2$ top cell to connect the two cells in series. IV curves are measured in our solar simulator. Optical transmission is measured in a UV-VIS spectrometer.

I - V curves in the dark and under illumination of the $CuGaSe_2$ cell show no indication of a counter diode at the back contact. This counter diode would be expected taking the band alignment and the doping of the $CuGaSe_2$ and the ITO into account. Currently we have no understanding why this contact behaves ohmic. But this phenomenon has been observed by others too, therefore the ITO back contact appears as a feasible way to prepare transparent top cell. Fig. 1 shows the IV curves under illumination of the individual cells and the tandem cell. The $Cu(In,Ga)Se_2$ cell is measured as illuminated through the transparent $CuGaSe_2$ cell. As becomes clear the current is limited by the current through the bottom cell which naturally shows a reduced current compared to illumination by the full solar spectrum. Still, this current is much less than one would expect from the solar spectrum transmitted through $CuGaSe_2$ with a band gap of 1.7 eV.

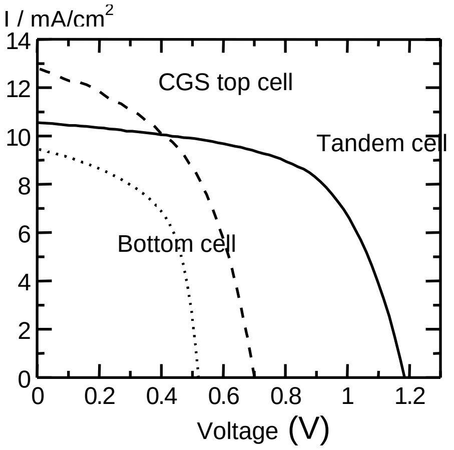

Fig. 1: J-V characteristics of the individual cells and the tandem cell

Therefore transmittance measurements have been performed on untreated ITO films, $CuGaSe_2$ on glass and on the $CuGaSe_2$ on ITO solar cell. The results show clearly that the ITO lost transparency due to the $CuGaSe_2$ deposition process. It is likely that a reaction with Se at the high deposition temperatures leads to the reduced transparency of the ITO. Future work will focus on the reason for the transparency loss and on ways to keep the ITO transparent throughout the deposition process.

Nevertheless a tandem cell with the parameters given in table I has been obtained. Certainly the efficiency is not remarkable especially since it is lower than the efficiency of the original $Cu(In,Ga)Se_2$ solar cell when illuminated with the full solar spectrum. But the open circuit voltage of almost 1.2V is remarkable and the work shows that a first step towards stacked tandem cells has been taken.

Table I: PV parameters of the tandem cell

V_{OC}/V	1.18
j/mA/cm^2	10.6
FF/%	60
η/%	7.4

Reference

[1] S. Nishiwaki, S. Siebentritt, P. Walk, M. C. Lux-Steiner, Prog. in Photovoltaics 11 (2003) 1-6

S. Siebentritt, S. Nishiwaki, P. Walk

$CuGaSe_2$ thin films prepared by a novel Chemical Close-Spaced Vapor Transport (CCSVT) technique for photovoltaic application

The novel CCSVT-technique

Sustaining excellent photovoltaic material properties at reduced deposition temperature and high deposition rates represents an unique challenge for further process development.

Very recently, a halogen-supported chemical vapor transport technique (CCSVT) has been highly successfully implemented allowing fast and large-area deposition of high quality semiconducting chalcopyrite thin films for photovoltaics. A schematic drawing of the system is shown in Fig. 1 (for details see Ref. 1).

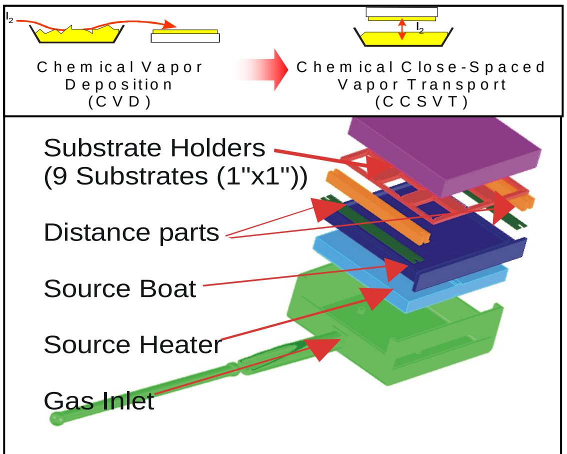

Fig. 1: Schematic drawing of the novel CCSVT-deposition reactor [1].

First results

Thin metallic Cu films deposited on clean and Mo-coated soda lime glass (SLG) substrates are thermally and chemically treated under gaseous $GaCl_x/H_2Se$ atmosphere in the CCSVT cell. The Ga_2Se_3 employed as source material is stoichiometrically volatilized by a controlled amount of HCl/H_2 agent at a certain pressure. The thin film deposition of Ga_2Se_3 binary source material was performed under varying conditions of the source temperature (T_{source}), the substrate temperature ($T_{substrat}$), the distance between source material and substrate holder ($D_{source\text{-}substrate}$), the reactor pressure ($p_{reactor}$) and the gaseous HCl content within H_2 carrier gas (Q_{HCl}/Q_{H2})

Single phase $CuGaSe_2$ layers are prepared with a growth rate of 230-240 nm/min by using a single stage process. A two stage process is applied for the fine tuning of the $CuGaSe_2$ composition and electronic properties appropriate for the solar cells preparation. Particularly, the Ga-to-Cu ratio is controlled within an error of 3.0% of the as-prepared films. The CCSVT-process parameters have been summarized and compared with conventional used evaporation process parameters in the table.

Parameters	CCSVT	evaporation
T(source) [°C]	520 - 580	1200–1400 (Cu/Ga) 300 (Se)
T(growth) [°C]	450 - 520	> 600
Growth rates [nm/min]	240	< 200
materials use [%]	50 - 60	5– 50 (Cu/Ga) ≤ 10 (Se)

Film characterization including X-ray diffraction (XRD) measurements, scanning electron microscopy (SEM) observations, transmission electron microscopy (TEM) studies, X-ray fluorescence analysis (XRF) and elastic recoil detection analysis (ERDA) has been carried out (see Fig.2). By means of the ERDA method, high depth homogeneity of the deposited $CuGaSe_2$ layers was observed. The detected Na distribution in the depth profile favors a back side field.

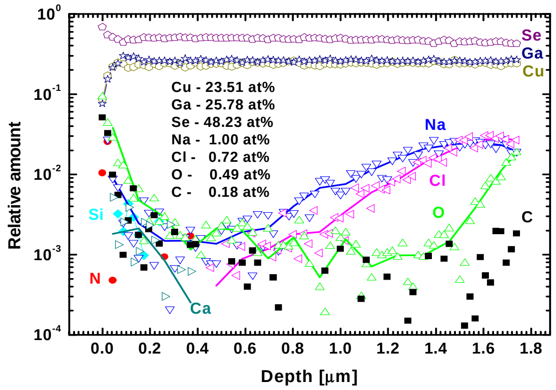

Fig. 2: Chemical composition of thin $CuGaSe_2$ film detected by elastic recoil detection analysis (ERDA).

The solar cell devices consisting of Mo/CGSe/CdS/ZnO heterostructures show under AM1.5 conditions a total area efficiency of maximal 7.0% with V_{oc} = 788 mV and J_{sc} = 15.19 mA/cm^2.

Reference

[1] Verfahren und Anordnung zum Abscheiden von Material aus einem Vorrat, DE 102 08 911.6
AT: 27.02.2002.

M. Rusu, S. Wiesner, S.M. Babu, D. Fuertes Marrón, K. Höhn, A. Jäger-Waldau, S. Lindner, A. Meeder, T. Münchenberg, A. Rumberg, Th. Schedel-Niedrig, R. Würz and M. Ch. Lux-Steiner
W. Bohne, W. Fritsch

ILGAR-ZnO/CIGSSe solar cells – effects of damp/heat exposure

The main goal of the project is the further progress in chemical low-cost methods for the deposition of semiconductor thin layers, mainly the ILGAR process (Ion Layer Gas Reaction, patents by HMI). The classical ILGAR is limited to a layer thickness of 100 nm due to the limited growth rate of involved dip steps. In order to deposit µm-layers an ILGAR spray process has been developed. Thin film solar cells with so-prepared CIGS ($Cu(In,Ga)S_2$) absorbers have already reached an efficiency of 3.5%.

Effects of damp/heat (DH) exposure on ZnO-WEL/CIGSSe solar cells (WEL=Window Extension Layer, CIGSSe=$Cu(In,Ga)(S,Se)_2$)

ZnO WELs (i.e., buffer layers of the same material as the sputtered window, but deposited by a mild process) were optimized such that record efficiencies up to η=15% could be reached (reference with CBD-CdS buffer η=14.1%). In the new WEL concept without sputtered i-ZnO cells with η=14.6% (reference CdS η=14.8%) and mini modules with 10.9% (reference CdS η=12.9%) were already obtained (Fig.1).

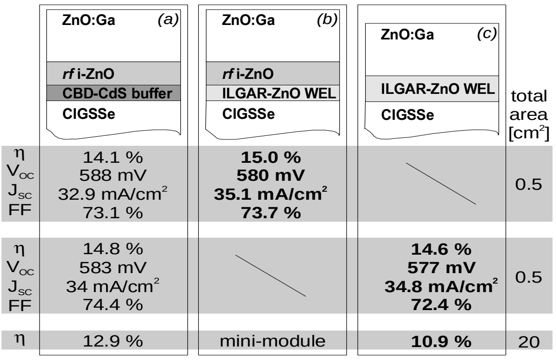

	(a)	(b)	(c)	total area [cm²]
η	14.1 %	**15.0 %**		0.5
V_{OC}	588 mV	**580 mV**		
J_{SC}	32.9 mA/cm²	**35.1 mA/cm²**		
FF	73.1 %	**73.7 %**		
η	14.8 %		**14.6 %**	0.5
V_{OC}	583 mV		**577 mV**	
J_{SC}	34 mA/cm²		**34.8 mA/cm²**	
FF	74.4 %		**72.4 %**	
η	12.9 %	mini-module	**10.9 %**	20

Fig. 1: Different structures of solar cells (upper part) and photovoltaic parameters of corresponding devices (lower part).

A broad, 100 h DH stability study of cells with CIGSSe absorbers from Shell Solar and buffer layers deposited at the HMI by various wet and dry processes revealed that ILGAR-ZnO and CBD-ZnS equally belong to the best Cd-free candidates with a relative decrease in efficiency of approx. 40%. Because this is still poorer than the CBD-CdS reference (20%), we investigated the reasons for the DH-degradation in ZnO-WEL cells.

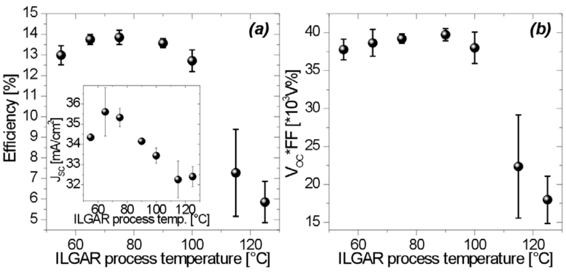

Fig. 2: Photovoltaic parameters of devices with ILGAR WELs prepared at different temperatures.

ILGAR-ZnO layers are obtained by repeating the following cycle: Dipping the substrate in $Zn(ClO_4)_2$ solution and converting the dry solid Zn^{2+}- precursor by gaseous NH_3/H_2O into the hydroxide, followed by dehydration to the oxide. Above 100°C the cell parameters strongly decrease, indicating absorber damage under the process conditions (Fig. 2). However, 100h DH tests show a better stability for 100°C than for 75°C and 55°C process temperatures (Fig.3).

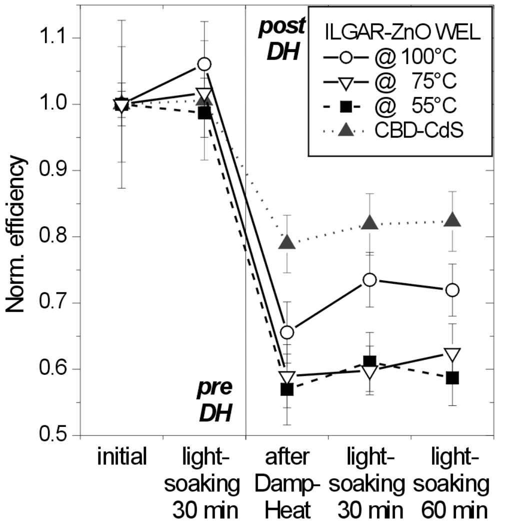

Fig. 3: Stability of the power conversion efficiency of solar cells with differently prepared WELs before (pre DH) and after (post DH) DH-test as well as after lightsoaking cycles compared to CBD-CdS buffered references.

FTIR measurements (IWF Dresden) of ILGAR-ZnO deposited at these three temperatures show a decreasing content of hydroxide from 50°C until 100°C (not detectable). As derived from XPS measurements, $Zn(OH)_2$ is converted into ZnO during DH exposure. Therefore, we conclude that the water thereby formed deteriorates the highly sensitive WEL interfaces. (Most likely this is also a reason for the degradation of CBD-ZnS having $Zn(OH)_2$ as a by-product). Consequently, for stable cells, the hydroxide content should be kept as low as possible, e.g., by high ILGAR process temperatures, but without damaging the absorber.

Ch.-H. Fischer, M. Bär, H.-J. Muffler, T. Kropp, J. Reichardt, M.C. Lux-Steiner

C. Kelch, M. Kirsch

M. Giersig, U. Bloeck

B. Leupoldt (Fraunhofer Institut Werkstoff- und Strahltechnik, Dresden);

T. P. Niesen, F. Karg (Shell Solar GmbH, München)

Preparation of wide band gap materials by structure conformal conversion

In thin-film photovoltaics, transparent semiconductors like doped SnO_2 or ZnO are used as transparent front contacts. Further demands for these materials appear in extremely-thin-absorber solar cells (eta cells). This cell concept is based on very thin but highly folded absorbers. This reduces the required degree of purity. But the absorber needs to be deposited on a transparent conductor with a highly „folded“ surface. Here, new surface structures of known materials have been accessed by materials conversion.

Starting from electrodeposited columnar ZnO, which can itself be prepared in different morphologies, columnar or tubular ZnS was obtained by anion exchange in the gas phase, and further metal sulfides with the same surface structure by subsequent cation exchange in solution [1, 2]. In this step, the outer quality of the reproduced morphology depends on the interaction of the involved processes, namely dissolution, precipitation and exchange inside the solid. This was further examined by a series of Ag_2S films from increasingly higher diluted solutions, until the rate of initial precipitation no more overexceeded the overall rate of the following internal conversion [3].

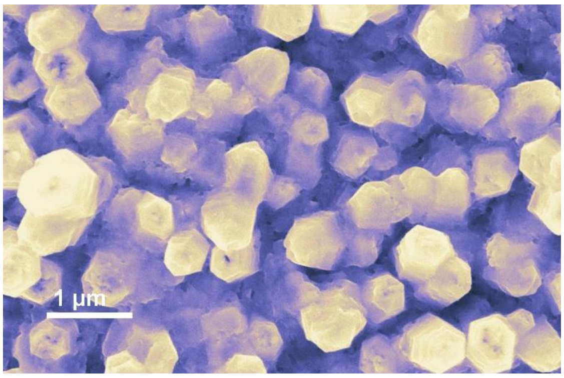

Fig. 1: columns of Ag_2S from columnar ZnS reacted with highly diluted $AgNO_3$ solution.

However, most transparent semiconductors are n-type. Only few p-type are known, e.g. CuSCN, CuI or p-conducting polymers. All those are of questionable long-term stability. Oxidic compounds have a general better stability, but only for the mixed oxide $CuAlO_2$ p-conducting behaviour has been found (on low level), and is ascribed to its exceptional layered structure (Delafossite structure, Fig 2) [4]. But this crystal phase is not the favored, most stable reaction product. Reacting the components at high temperature (around 1000°C), as well as all large-area film deposition methods, yield mainly spinel-type $CuAl_2O_4$ and Cu oxides instead.

Here, it was possible to achieve the synthesis by the structure conformal conversion of the isostructural compound α-$LiAlO_2$. Making use of the high mobility of the Cu^+ and also of Li^+ ion, a crystal structure conformal conversion of this commercially available starting material could be performed already at temperatures as low as 400°C. This scalable synthesis yields $CuAlO_2$ powder free of $CuAl_2O_4$ and Cu oxides, and allows to include dopants.

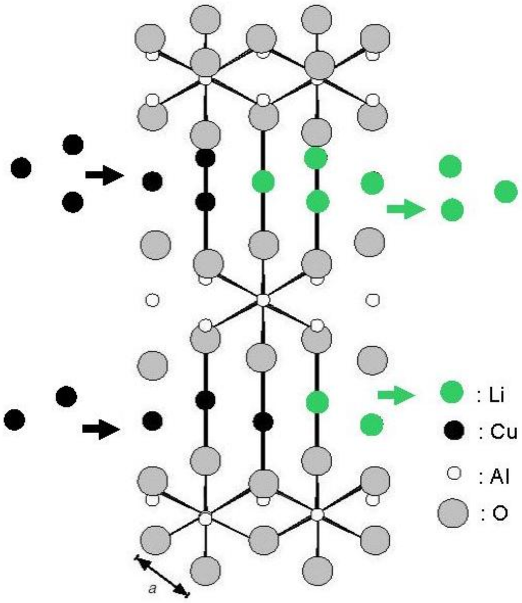

Fig 2: „Delafossite“ crystal structure of $CuAlO_2$ and $LiAlO_2$, and their conversion by ion exchange in the lattice (adapted from [4])

[1] L. Dloczik, R. Engelhardt, K. Ernst, M. C. Lux-Steiner, R. Könenkamp, Sens. Act. B 84 (2002) 33
[2] L. Dloczik, M. C. Lux-Steiner, R. Könenkamp, E-MRS, Strasbourg 2002
[3] L. Dloczik, R. Könenkamp, 53th meeting of the International Society of Electrochemistry, Düsseldorf 2002
[4] H. Kawazoe, M. Yasukawa, H. Hyodo, M. Kurita, H. Yanagi, H. Hosono, Nature 389 (1997) 393

Th. Dittrich, L. Dloczik, J. Chen, R. Bayon, A. Belaidi

Phthalocyanine/C_{60} organic solar cells

We study a new type of solar cell consisting of the organics phthalocyanine and C_{60} [1] as well as buffer layers on the electrodes. The basic principle of this new type of photovoltaic devices is that of a donor-acceptor cell. Phthalocyanine plays the role of a hole-conducting donor. On the other hand C_{60} has a strong electron affinity and is under certain conditions a good electron conductor [2]. Both materials exhibit a remarkable thermal stability. This allows the processing and study of vapor deposited well-defined thin films suitable for the fabrication of organic solar cells.

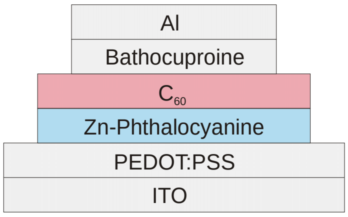

Fig. 1: Schematic cell structure. PEDOT:PSS is spin coated onto an ITO substrate. All other layers are thermally vapor deposited under high vacuum.

We fabricated this kind of photovoltaic devices in order to study charge carrier transport and electron-hole recombination at interfaces. We paid careful attention to the use of poly-3,4-ethylene dioxythiophene:polystyrene sulfonate (PEDOT:PSS) as hole-conducting and bathocuproine (BCP) as electron conducting buffer. (Fig. 1).

As front electrode we employed ITO float glass, spin coated with PEDOT:PSS from aqueous solution. The substrates were introduced into a high vacuum chamber and coated by thermal vapor deposition with Zn-phthalocyanine, C_{60}, bathocuproine and aluminum. In order to protect the cell from atmospheric oxygen it was covered on the backside with a thick C_{60} layer and then encapsulated under inert gas.

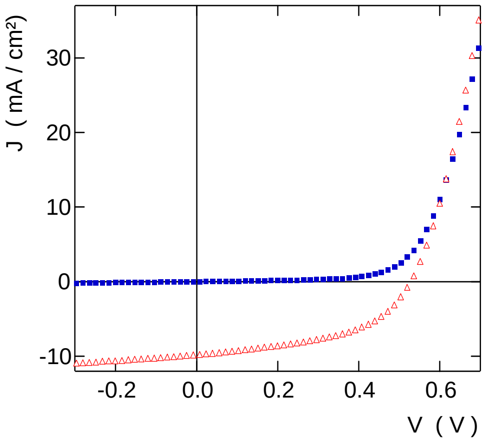

Fig. 2: I-V curve of our most efficient solar cell Triangles mark the illuminated, squares the dark measurement. Power conversion efficiency: 2.5 %.

I-V characteristics were studied under one sun AM1.5 illumination of a solar simulator. Our best devices yielded external power conversion efficiencies of up to 2.5% depending on the quality of the PEDOT:PSS layer (Fig. 2). In the case of Fig. 2 the appendant cell parameters were: J_{sc} = -9.8 mA/cm^2, V_{oc} = 0.53 V, fill factor = 0.49. The photoactive area is 3.2 mm^2. Photocurrent contribution of the active layers is shown in the external spectral quantum efficiency (ESQE, Fig. 3). ZnPc generates most charge carriers at wavelengths between 550 and 750 nm. A weaker absorption caused by C_{60} is located in the short wave part of the visible spectrum (350-520 nm). In order to study the evolution in time of ESQE, the cell was first measured immediately after the fabrication (Fig. 3, blue), then the solar cell's power conversion efficiency was determined (1.4%) under the solar simulator. After 30 minutes in the dark the second ESQE measurement (red) was recorded.

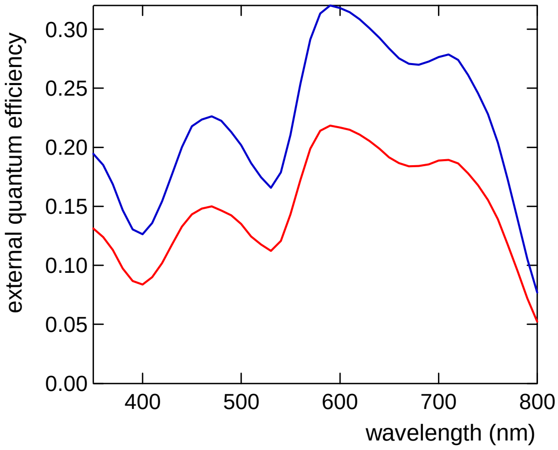

Fig. 3: After the cell's fabrication the ESQE was recorded (blue) then the power conversion efficiency was determined (1.4%). After 30 minutes another ESQE measurement (red) was recorded.

We observed an uniform decrease of the photocurrent over the whole spectrum by one third. Since the conductivity of C_{60} is strongly influenced by oxygen impurities in the film [2], we suspect that the degradation is due to oxygen, which soaks through C_{60} during the measurement in the solar simulator and to a minor degree in the dark.

[1] P. Peumans and S.R. Forrest, Appl. Phys. Lett. 79 (2001) 126
[2] R. Könenkamp, G. Priebe, and B. Pietzak, Phys. Rev. B 60 (1999) 11804-11808

K. Fostiropoulos, M. Vogel, B. Johnev, B. Mertesacker, A. Weidinger

Kelvin Probe Force Microscopy: Direct observation of electronic grain boundary properties

Kelvin probe force microscopy (KPFM) in ultra-high vacuum allows to simultaneously obtain structural as well as electronic information (work function Φ) of a sample's surface with an extremely high lateral (~ 20 nm) and energy resolution (~ 5 meV).

The application of the KPFM to a solar cell absorber material was demonstrated using CuGaSe$_2$ (E$_g$=1.68 eV) deposited on Mo covered glass by physical vapor deposition. In Fig. 1 (a) we present the topography image as measured with the KPFM. Clearly the various grains can be seen, with the grain size varying between 200 and 700 nm. In Fig. 1 (b) we present the simultaneously measured work function image for dark conditions. It is observed that the various grains show different absolute values of the work function. This effect was previously observed and explained by different electron affinities depending on the crystallographic orientation of the surface. Additionally, the work function is seen to decrease at the grain boundaries, as observed by the dark "rings" around the various grains.

In Fig. 2, we show the work function along the line in Fig. 1 (b). The work function is seen to drop at the grain boundaries by ~100 meV and ~170 meV, with an average of (110 ± 24) meV, when many grain boundaries are evaluated. The upper curve shows the work function along the same line for the sample measured under illumination (20 mW, λ = 685 nm). The absolute value of the work function is increased by ~ 110 meV, which can be explained by a reduced band bending at the surface. It is also apparent that the work function decrease at the grain boundaries is reduced. Averaging over many grain boundaries, the drop at the grain boundaries under illumination is found to be (76 ± 30) meV. Besides the size of the potential drop at grain boundaries, we can also extract information about the width of the space charge region (SCR) that develops at the grain boundaries. Averaging over many grain boundaries we find a SCR width of (42 ± 9) nm in dark conditions, and (56 ± 10) nm under illumination.

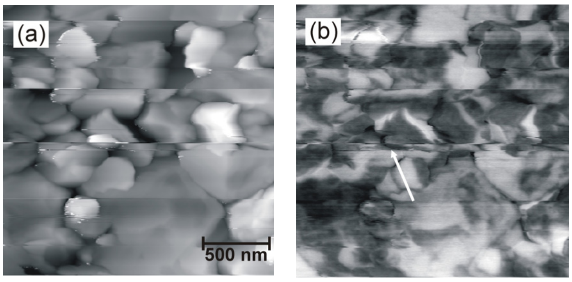

Fig. 1: KPFM measurement on CuGaSe$_2$. The topography (a) shows the grains of the polycrystalline thin film (grey scale = 360 nm). The simultaneously measured work function (b) shows a downward band bending at the grain boundaries (Φ = 4.23 – 4.39 eV). The white line gives the position of the linescan in Fig. 2.

We consider the relative changes in the work function as determined at the grain boundaries to reflect the electronic properties of the absorber material. By assuming that the grain boundary corresponds to a surface with a surface charge we determine the net doping P_{net} of the absorber material from the size of the band bending $\Delta\Phi_{gb}$ and the SCR width w, finding $P_{net} \approx 9\cdot10^{16}$ cm^{-3}. By the fact that the SCR width at the grain boundaries does not extend to the center of the grains, we can estimate the density of charged trap states $p_{gb} \approx 8\cdot10^{11}$ cm^{-2}.

We can compare these results to recent transport measurements on samples originating from the same growth process. Schuler *et al.* found $P_{net} \approx 1$ - $5\cdot10^{17}$ cm^{-3} for the net doping concentration, $\Delta\Phi_{gb}$ = 60 – 135 meV for the band bending at the grain boundaries and concluded the charged defect density at the grain boundary to be $p_{gb} \approx 1\cdot10^{12}$ cm^{2}. Whereas we analyzed a number of individual grain boundaries from our KPFM images, Schuler *et al.* investigated an "average lowest" grain boundary barrier, determined by the average barrier of the percolation path through the material. Nevertheless, the results of this study and the present KPFM study are in good agreement. The origin of the defect states at the grain boundaries can be manifold, for example dangling bonds, oxygen contamination due to air exposure, Na contamination from the glass substrate, etc.

Similar studies were also performed on the absorber material Cu(In, Ga)S$_2$ (E$_g$=1.55 eV). We do not observe a significant difference in the electronic properties at the grain boundaries between the selenide material CuGaSe$_2$ and the sulfide material Cu(In, Ga)S$_2$.

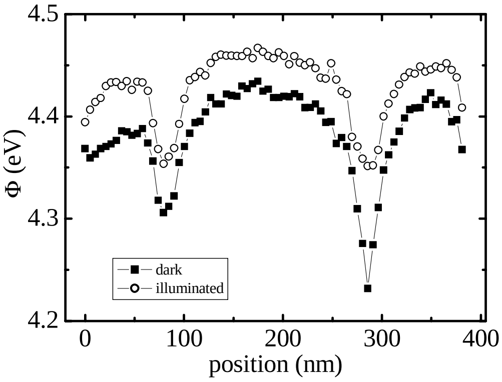

Fig. 2: Linescan along the white line in Fig. 1 (b) showing the drop in the work function at the grain boundaries. Closed symbols are for dark condition and open symbols represent the work function along the same line under illumination (20 mW, λ = 685 nm).

S. Sadewasser, Th. Glatzel, M.Ch. Lux-Steiner

Analysis of buried interfaces in Cu(In,Ga)(S,Se)$_2$ thin film solar cells by X-ray emission and photoelectron spectroscopy in the CISSY apparatus

The general aim of the CISSY project is the investigation of buried interfaces and surfaces in Cu(In,Ga)(S,Se)$_2$ ("CIGSSe") thin film solar devices. The CISSY endstation (Fig.1), completed in 2002, combines several relevant in-system preparation tools for thin layer deposition (sputter chamber, glove box for wet chemical processes) and the spectroscopic equipment for x-ray emission (XES, Scienta Gammadata) and photoelectron spectroscopy (PES, VG CLAM 4) and a variety of laboratory techniques. The analytical concept of CISSY is based on information from XES and PES on the electronic properties and the chemical composition from different information depths (XES: several 100 nm; PES: surface) for the study of buried interfaces in layer systems.

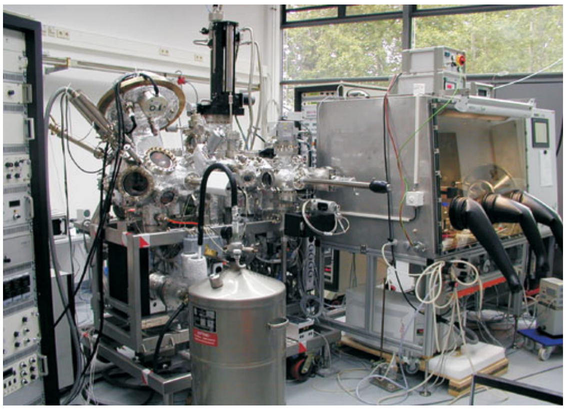

Fig.1: CISSY endstation with attached glovebox.

All CIGSSe absorbers stem from the pilot line of Shell Solar, and subsequent depositions of buffer layers (CdS, ZnS, ZnSe, ZnO) were performed either in the attached glovebox of the CISSY apparatus or in several labs at the HMI. Several preparation procedures were employed, including chemical bath deposition, absorber surface pre-treatments, and, in particular, the sequential cyclic ILGAR process (Ion Layer Gas Reaction) consisting of dipping and solid/gas reaction steps.

A broad study was dedicated to the stability of the CIGSSe solar cells during so-called "damp-heat tests" ("DH", 85°C/85% rel. humidity, 100 h for unencapsulated samples), a fundamental issue for the photovoltaic industry. We started with the systems ILGAR-ZnO/CIGSSe and sputtered-i-ZnO/CIGSSe, each with Cd^{2+}/NH$_3$ treatment of the CIGSSe absorber. In order to localize and understand the observed effects, variations of preparation conditions as well as measurements before and after damp-heat exposure were From the S L$_{2,3}$ XES spectra in Fig. 2 we learn that ILGAR-ZnO deposited on CIGSSe under air contains sulfate, the signal of which disappears after damp-heat treatment (Fig.2, left), whereas in sputter-i-ZnO on CIGSSe sulfate is observed only after damp-heat exposure (Fig.2, right). Apparently, the chemical composition and hence the electronic behavior of ZnO depends on the preparation method. One has to keep in mind

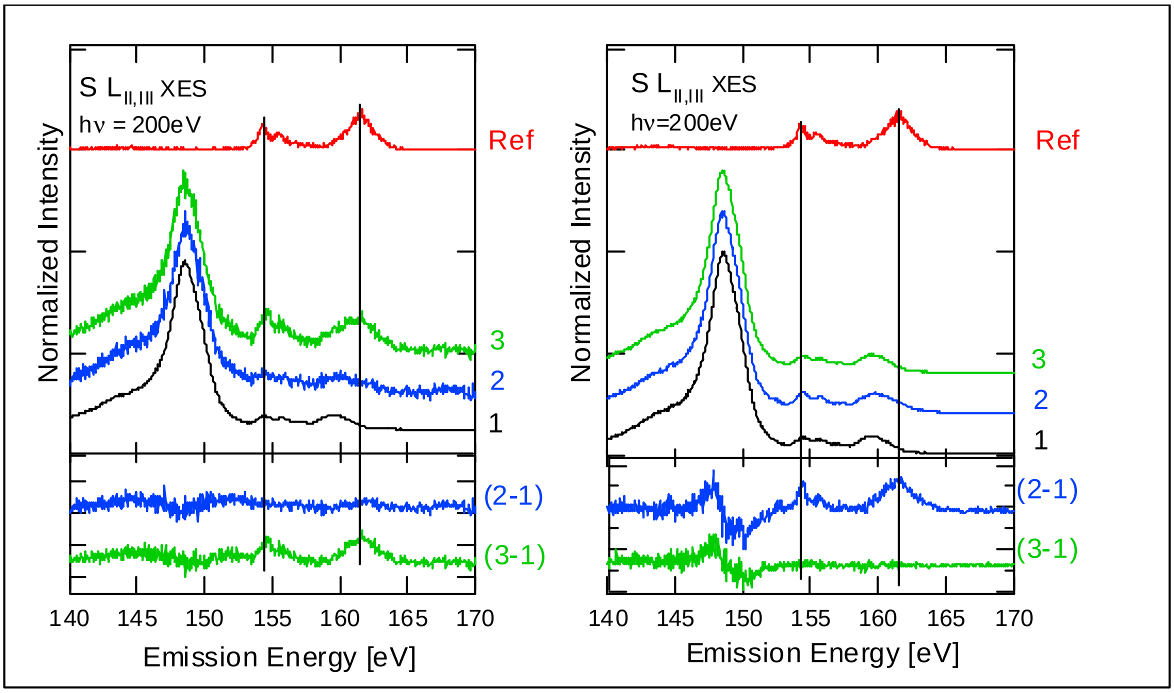

Fig.2: SL$_{2,3}$ XES spectra of 25nm ILGAR ZnO (left) and of 30nm sputter i-ZnO (right), both on Cd^{2+} treated CIGSSe as well as difference spectra and spectrum of a sulphate reference. 1: Cd-treated Absorber, 2: before damp heat test, 3: after damp heat test, Ref: CdSO$_4$.

that the sulfate represents only a small fraction of the volume analyzed by XES, i.e., that the sulfate contribution to the resulting spectrum is very small. For a better visualization of the sulfate signals, the spectra of the absorber *before* damp-heat treatment and *before* i-ZnO deposition, respectively, are subtracted from those taken *after* the respective treatments, in order to account for the large number of S atoms within a CIGSSe environment. For comparison a sulfate reference spectrum is also shown.

Complementarily, the PES spectra of the as deposited ILGAR sample give no evidence of sulfate at the ZnO surface. Therefore, the sulfate must be localized at (or near) the ZnO/CIGSSe interface.

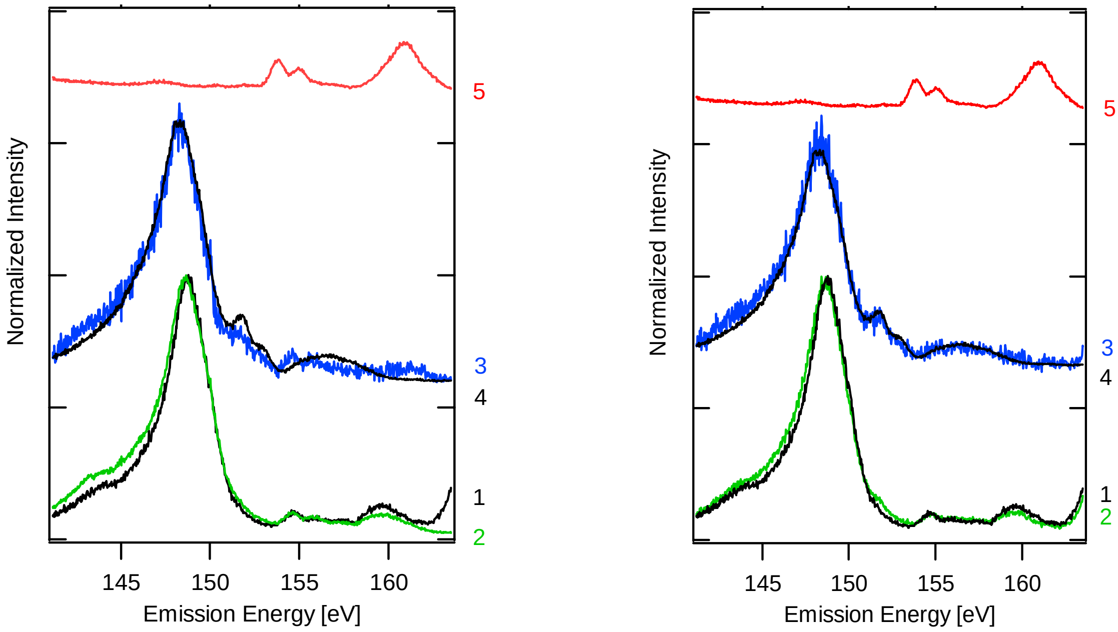

Fig. 3: S $L_{2,3}$ XES spectra of CBD-ZnS/CIGSSe, CIGSSe, and difference spectra for excitation energies of 200 eV (left) and 165 eV (right), showing the effect of deliberate excitation below the sulfate absorption edge. 1: bare CIGSSe-absorber, 2: CBD-ZnS on CIGSSe, 3: difference spectrum (2-1), 4: ZnS-reference, 5: sulfate-reference.

PES spectra of the same sample after DH show peaks corresponding to the absorber elements, indicating that the ZnO coverage is no longer complete, in agreement with scanning electron micrographs.

The unique CISSY feature of in-system preparation allows a preparation by wet chemical processes in the attached glovebox under N_2 atmosphere and therefore a direct comparison to products of standard preparation in air. When ILGAR-ZnO is deposited on CIGSSe in the glovebox, S $L_{2,3}$ XES spectra clearly show a reduced sulfate signal indicating that oxygen and/or humidity from the ambient environment is involved in the sulfate formation process. These results can be very important for better solar cell efficiency and stability and will be fed back directly into the solar cell production process.

Alternative ZnS buffer layers prepared by chemical bath deposition ("CBD", A. Ennaoui, HMI) have resulted in high cell efficiencies. The presence of S-Zn bonds could be confirmed by XES (Fig. 3), in spite of the small amount of material (thickness of no more than a few nm). The difference of the spectra "after minus before deposition" obtained with an excitation energy of 200 eV points to the presence of ZnS and $ZnSO_4$. However, ZnS becomes more evident by XES with deliberate excitation below the sulfate absorption edge (165 eV). Therefore, in addition to the advantage of high flux excitation, undulator-based synchrotron radiation also offers the possibility to "switch-off" a certain chemical core hole species, allowing a significantly enhanced spectral interpretation.

The present results, taken during the two inaugural beamtimes of the CISSY apparatus at the U41-PGM and the UE46-PGM beamline, give a first perspective of the multitude of information which can be obtained when combining different spectroscopic methods with in-system and, in a later stage, in-situ thin film preparation.

Ch.-H. Fischer, M. Bär, A. Grimm, I. Kötschau, I. Lauermann, J. Reichardt, S. Sokoll, and M.C. Lux-Steiner

L. Weinhardt, O. Fuchs, C. Heske, *Experimentelle Physik II, Universität Würzburg*
C. Jung and W. Gudat, *BESSY GmbH, Berlin*
T. P. Niesen and F. Karg, *Shell Solar GmbH, München*

$CuInS_2$ mini-modules - preparation and testing

Thin film solar modules of $CuInS_2$ which are prepared in an industrial relevant process are currently under development in a joint effort with the department SE2. These solar devices have the advantage over crystalline silicon devices that series connection of single solar cells to a complete module can be achieved right during processing. This integrated series connection requires the deposited layers to be cut at three different levels. According to the large area of commercial modules totally more than 100 m scribe length per level has to be performed on a single module. Thus the technology chosen for cutting the different layers not only has to be highly reliable but also fast enough to meet the production time pattern.

The first layer to be cut is the molybdenum backside metallization. A suitable procedure is laser scribing. In 2002 we have put into operation a specially designed machine consisting of a laser to cut the molybdenum layer and a stylus to mechanically cut the other two layers. The requirement of fast and reliable cuts implies the proper setting of a variety of parameters. Important parameters are laser power, laser pulse frequency and cutting speed. They all are not independent but influence one another. Complete electrical isolation can be achieved with a set of parameters in the high power regime as well as with moderate laser power. The latter has benefits in terms of the thermal strain to the molybdenum layer close to the scribeline. Fig. 1 shows a laser scribeline less than 20 microns wide in a 1 micron thick molybdenum layer.

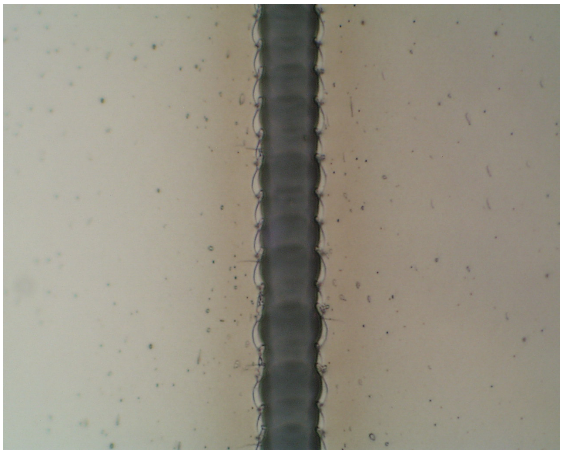

Fig. 1: Molybdenum layer of 1 micron thickness with a laser cut less than 20 micron wide.

A scribing speed of close to 1 m s^{-1} has been realised at a isolation resistance of $>10^6$ Ω. First mini-modules including laser-cut molybdenum have been fabricated. However, fine adjustment of the parameters is still ongoing.

In collaboration with SE2, the routine preparation of mini-modules in a so-called baseline has been strongly intensified. The ultimate goal is to test the baseline at a throughput of 20 mini-modules per months. Module efficiencies up to 9.7 % could be achieved on 5x5 cm^2 glass substrates (aperture area efficiency, independent measurement by FhG-ISE, Freiburg). Up to now, not all of the modules reach top efficiencies, there are also devices that show poorer performance. In order to discover the reasons for unsatisfactory performance these modules have been analysed in order to reveal defect mechanisms. By application of our infrared camera system shunts could be revealed as a major loss mechanism. Electrical current is passed through the solar device which leads to Joule heating of every cell of the module. As shunts tend to focus this current, local heating will occur which can be detected by the camera. Using lock-in technique this infrared camera is able to discriminate lateral temperature differences on a sample in the sub-mK range.

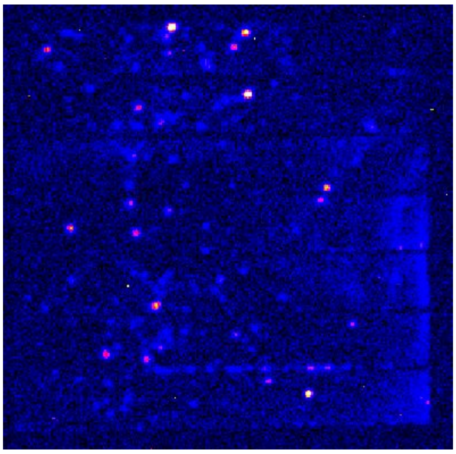

Fig. 2: Thermography image of a mini-module with 9.7 % efficiency and 66.6 % fill factor. The brighter the colour, the higher the local temperature.

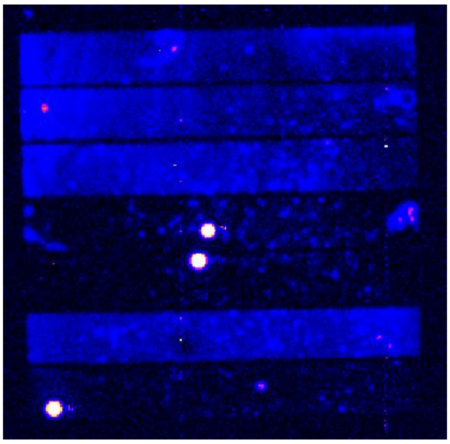

Fig. 3: Thermography image of a mini-module with 8.6 % efficiency and 59.2 % fill factor. Three hot spots are due to small local shunts. As in a series connected module the current through all cells must be the same the shunted cells show darker because part of the current in these cells is concentrated at the shunt paths.

Fig. 2 and 3 show thermography images taken of two modules of unequal performance. While the module in Fig. 2 with 9.7 % efficiency and 66.6 % fill factor shows almost homogeneous temperature distribution over the entire module area, the infrared image of the less efficient module reveals three hot spots, which are caused by small local shunts. Delamination of the absorber layer in the vicinity of the scribe line has been identified as a major cause for shunts. This problem could be reduced by changing the dimensions of the interconnect pattern. The infrared camera system has thus turned out to be a powerful tool for quality control and failure analysis.

Solar modules for outdoor application have to be protected against environmental influences. To this end, the devices are often encapsulated by laminating a second glass plate onto the thin film layer structure. This procedure has been performed using a ethyl-vinyl-acetate (EVA) foil. Attention has to be paid to the lamination temperature: on one hand to fulfil the requirements of sufficient polymerisation, on the other hand not to degrade the device. Other important parameters are lamination pressure and time. The critical regions of the modules are the edges since there is only a small rim to seal glass on glass and where humidity can penetrate into the layers. This small rim is necessary in order to obtain as much active device area as possible.

Alternative procedures have been considered in order to facilitate the encapsulation process. A very simple method has been developed by the department SE5 and has been evaluated in co-operation. An organic wax of natural provenience is deposited by dipping the module into a solution of the wax. These wax sealed modules are tested without an additional cover by a second glass plate.

Fig. 4: $CuInS_2$ mini-modules at the test array on the HMI campus (near the guesthouse) exposed to the Berlin weather.

The encapsulated modules have been exposed to several stress tests to examine their stability and to evaluate the reasons of possible degradation. Modules have been exposed to Berlin weather since October 2002 at a new experimental test array close to the guesthouse. This test array which has a capacity of up to 20 modules of different sizes has been developed together with SE2. During 3 months of field exposure, the laminated modules exhibited a degradation of only 5% in efficiency. The wax sealed modules did not show a stronger degradation than the glass laminated ones.

A standardised method for time-accelerated tests for solar modules is the so-called ISPRA-test (IEC 1215). Under this test, modules are stressed for 1000 hours at 85 °C and 85 % relative humidity (damp-heat). In order to provide this widely used standard test procedure, a new climate exposure test cabinet was put into operation in December 2002. Fig. 5 depicts the relative efficiency of 3 modules as a function of exposure time to the damp-heat test. The module (a) in Fig. 5 has been exposed without any protective cover and serves as a reference. Within 200 h, the efficiency of this device deteriorated to 20% of its initial value. It should be noted that degradation in 85°C dry atmosphere on the contrary is negligible. Thus, the strong degradation of the uncovered module emphasizes the importance of sealing against humidity. The physical mechanism of degradation is not known so far. Both encapsulated modules (b) and (c) in Fig. 5 exhibit a decreased degradation with respect to the non-excapsulated one. Again the wax sealed modules behaved similar to the glass encapsulated ones. Nevertheless, the degradation is still much larger than required in order to pass the ISPRA test. Further work has to concentrate on 2 aspects of this type of stability: (i) improved inherent stability of the solar cells to humidity and improved encapsulation and/or sealing.

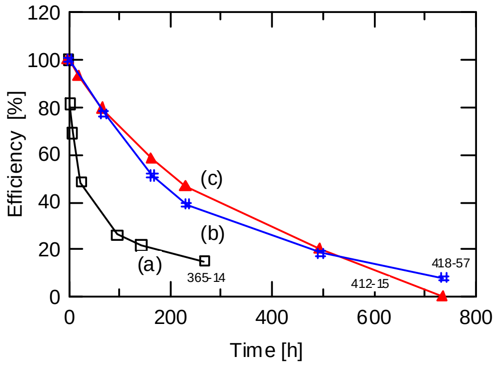

Fig. 5: Degradation of the efficiency of a non-encapsulated (a), a glass-encapsulated (b), and a wax covered (c) module under climatic test at 85 °C and 85 % relative humidity.

J. Klaer, I. Luck, A. Boden, A. Werner, I. Gavilanes-Perez, R. Klenk, R. Scheer

$CuInS_2$ quality assessment by Raman spectroscopy

It is well known that Raman scattering can qualify the perfectness of materials such as thin films. The goal of this work is to develop Raman scattering as a quality control for $CuInS_2$ solar cell production. Our group, in collaboration with the university of Barcelona, previously investigated Raman spectroscopy for $CuInS_2$ thin films (see HMI Annual Report 2001 SE3.01b). Samples with different structural quality, as it results from Cu-poor compared to Cu-rich preparation, has been studied. It was found that films of Cu-poor stoichiometry or those formed at significant too low substrate temperature exhibit a defect ordering, the so-called CuAu ordering. Absorbers prepared in our baseline grow under Cu-rich conditions and show only a small or even no content of that CuAu ordering. In-situ Raman spectroscopy performed during the growth of the films, however, revealed that the CuAu ordering marks an intermediate state of crystallisation.

In order to investigate the baseline $CuInS_2$ films by Raman scattering and to derive further relations between spectroscopic features and photovoltaic performance, a large number of samples has been investigated. They were prepared under different conditions, e.g. variation in process temperature, Cu/In-ratio and absorber thickness, and completed to working solar cells. All samples have in common that a dominant Raman mode (A_1-mode) can be observed which is caused by the vibration of the anion sublattice. As already known from other materials the FWHM (full width at half maximum) of a Raman peak is an indicator for crystal quality, i.e. the density of localised and extended defects, of a material. Therefore, the aim of the current work is to find a correlation between the signature of the A_1-mode and the solar cell parameters.

Fig.1 shows Raman spectra of three representative samples together with the fit results. As can be seen, the dominant Raman mode appears at approximately 292 cm^{-1} corresponding to the A_1-phonon mode of $CuInS_2$. No contribution of the CuAu related mode at 305 cm^{-1} could have been detected.

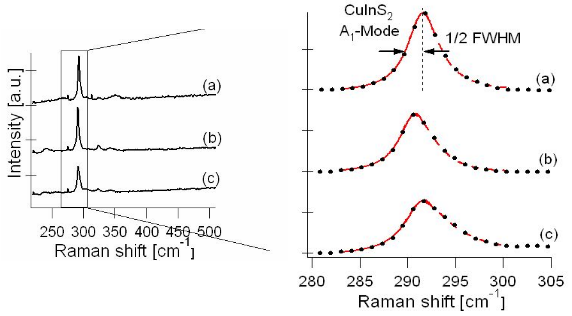

Fig. 1: Raman scattering intensities versus wavenumbers for different Glass/Mo/$CuInS_2$/CdS/ZnO samples. Primary and scattered light of the Raman experiment were passing the window layer of ZnO/CdS. The dots represent the measured data, the full line the symmetric fit. Open circuit voltage : (a) 726 mV, (b) 651 mV and (c) 194 mV

The spectra shown are characterised by different spectroscopic broadening (FWHM values), where the large FWHM of spectrum (c) can be appreciated by the naked eye. This sample has been measured with a V_{oc} (open circuit voltage) of below 200 mV. As already implied by Fig.1, a decrease in V_{oc} values (from samples (a) to (c)) is correlated with an increase in FWHM of the A_1-mode.

In Fig.2 the solar cell parameter V_{oc} of numerous solar cells is plotted as a function of the determined values for FWHM of the dominant Raman mode. Up to a FWHM of 3.5 cm^{-1}, values for V_{oc} of 0.7 V or above have been found. In the range of 3.5 to 4.0 cm^{-1} the data of V_{oc} show a scattered behaviour (between 0.7 and 0.54 V) which seems to have a slightly decreasing tendency. But below 4.0 cm^{-1} a significant decline in the values for V_{oc} can be stated. Thus we interpret the data as suggested by the dashed line in Fig.2. According to the experimental relation between V_{oc} and Raman line width, a quality condition of FWHM < 3.5 cm^{-1} can be formulated. This condition now qualifies the absorber material as such before testing it in a complete solar cell.

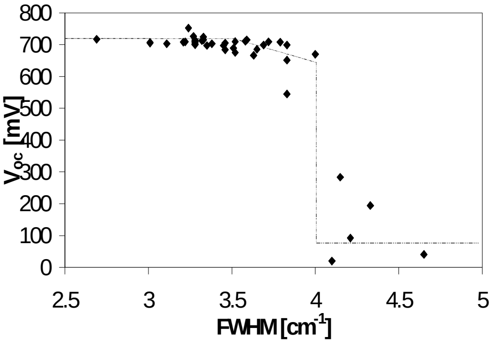

Fig. 2: Open circuit voltages of solar cells versus the FWHM of the A1 mode.

Raman peak broadening can be explained by high defect densities in the lattice. Although little is known about the specific type of defects in our films, we assume the same relationship to explain our results. The decreasing V_{oc} can be interpreted as a result of higher defect densities: The V_{oc} of a solar cell depends logarithmically on the saturation current j_0. If we assume that for $CuInS_2$-based solar cells the main recombination path appears in the space charge region, a direct correlation exists between the density of the recombination sites N_t and j_0. Therefore, V_{oc} is expected to be reciprocal to $\ln(N_t)$. This indeed has been found by admittance spectroscopy. Thus, crystal defects seem to be the limiting factor for the V_{oc} for FWHM values larger than 3.5 cm^{-1}. But as indicated by the saturation behaviour of V_{oc} for low FWHM values, crystal defects cannot be the only limiting factor. Obviously there are other limitations which reduce the V_{oc} below the predicted theoretical value of 1V.

E. Rudigier, I. Luck, R. Scheer

A new application of NOPA: Generation of sub-20 femtosecond laser pulses in the visible and near infrared at 100 kHz repetition rate

A novel 100 kHz Nonlinear Parametric Optical Amplifier (NOPA) for the generation of sub-20 femtosecond laser pulses was developed and successfully installed. The new apparatus provides shorter and better tunable laser pulses than commercially available NOPAs that run at only 1 kHz. Femtosecond Transient Absorption and Two Photon Photoemission measurements at semiconductors require low level laser excitation keeping signal detection in an acceptable linear range. This is achieved here via the high repetition rate of 100 kHz. The new device represents thus a significant improvement towards time-resolving the dynamics of hot charge carriers at the surface and in the bulk of III-V materials and verifying theoretical models. In addition the still lasting controversy regarding electron injection times in dye sensitized solar cells can now be solved making use of the better time resolution and tunability. The new device was planned and designed in collaboration with the group of Prof. E. Riedle at the LMU in Munich. So far NOPAs have only been used with 1 kHz Ti:sapphire pump systems and pump energies above 100 µJ [1]. The low energy pump (5 nJ) required a careful optimization of the setup. The NOPA is adjustable from 460 nm to well beyond 1 µm (Fig. 1). At the maximum of the tuning curve a pulse energy of 750 nJ was obtained corresponding to a quantum efficiency of more than 30 % from the blue and an overall energy conversion efficiency (800 nm to green) of about 10 %. The average power of 75 mW is considerably higher than that obtained from comparable commercially available 1 kHz systems with sub-20 fs pulse length.

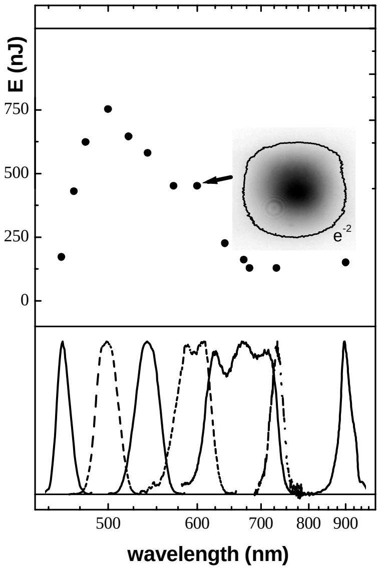

Fig.1: Pulse energies and spectral performance of the NOPA. The inset shows the beam profile at the output at around 600nm.

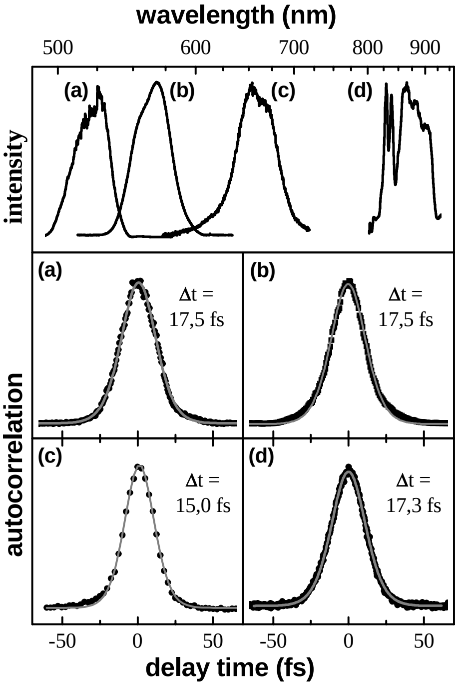

Fig.2: Autocorrealation traces and sech^2 fits with corresponding spectral bandwidths

Fig. 2 shows the laser pulse width measured in an autocorrelation setup with a SiC diode as two-photon mixing device. Similar results were obtained when a thin BBO crystal was used for mixing. The pulses were recompressed in a quartz prism compressor assembly. The spectral bandwidths should allow for even shorter pulses in more sophisticated compression setups.

Reference

[1] E. Riedle, M. Beutter, S. Lochbrunner, J. Piel, S. Schenkl, S. Spörlein, W. Zinth, Appl. Phys. B **71** (2000) 457.

R. Eichberger, L. Gundlach, R. Ernstorfer,
C. Zimmermann, F. Willig

Experimental proof of electron injection with finite lifetime from the excited perylene chromophore anchored on TiO_2 with a carboxyl group

Ultra-fast photo-induced electron transfer from large molecular adsorbates into semiconductors is firstly an interesting fundamental case study [1] and secondly of considerable importance for some application-oriented devices, e.g. unconventional dye sensitized solar cells [2]. The dynamics of electron transfer from a photo-excited molecular donor state into the conduction band of a nano-structured film of TiO_2 anatase was studied with transient absorption spectroscopy.

It is important to distinguish between two border cases of ultra-fast heterogeneous electron transfer, i.e. a direct optical transition or a transition from the first optically excited state (finite lifetime) of the adsorbed dye molecule. The different oscillator strengths involved require a different amount of adsorbed dye necessary for absorption saturation and hence also influence the recombination time constant via the thickness of the light absorbing layer.

The strength of electronic coupling is reflected in the degree of mixing between excited molecular states and unoccupied electronic levels of the semiconductor. In the first case of strong coupling, which is given for small molecules directly bound to a semiconductor surface, the corresponding electron transfer times can be faster than 3 fs [3] with an energy uncertainty above 0.5 eV. The effect of vibrational excitation of the molecular donor is nearly washed out, and new states may arise in this strong coupling case. Photo-excitation of such so-called charge transfer states results in a direct optical transition from a localized molecular to a delocalized bulk state [3]. In the second case of weak to moderate electronic coupling typical electron transfer times are several ten to a few hundred femtoseconds.

The influence of vibrational wavepackets on heterogeneous electron transfer dynamics has been studied in such systems with laser pulses of e.g. 20 fs duration [4].

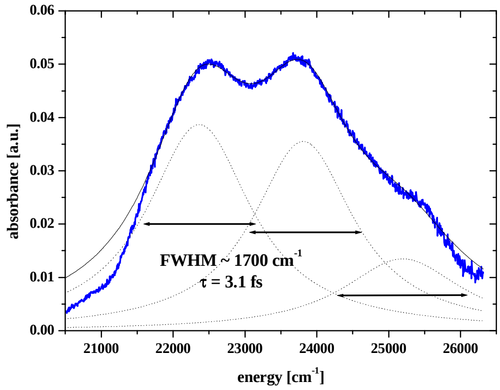

Fig.1: Absorption spectrum of Pe'-COOH adsorbed on colloidal TiO_2 anatase.

We have varied the electronic coupling between a chromophore, i.e. perylene, and the surface of TiO_2 in a systematic fashion by inserting different molecular spacer groups with saturated bonds [5]. Fig.1 shows the absorption spectrum of 2,5-Di-tert.butyl-9-perylenyl-carbonic acid (Pe'-COOH), the perylene derivative with the strongest coupling, attached to colloidal TiO_2 anatase. The vibrational signature of the non-adsorbed chromophore is conserved, indicating the absence of very strong coupling that is often attributed to a direct opticalcharge transfer transition to bulk states. From the maximum linewidth compatible with the spectrum one can determine a minimum injection time longer than 3 fs.

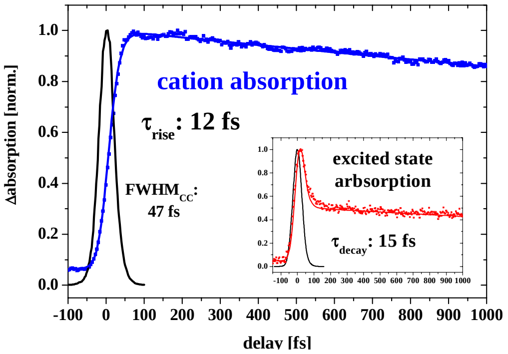

Fig.2: Transient absorption of Pe'-COOH on TiO_2 after photo-excitation with a 30 fs laser pulse: The rise of the cation signal (blue) and the decay of the excited state absorption (inset) indicate an injection time constant of 12 fs and 15 fs, respectively.

A direct measurement of the transfer dynamics is shown in Fig.2. The rise of the molecular product state, i.e. the perylene cation, was monitored at 570 nm after excitation with a 430 nm pump pulse (FWHM of the cross-correlation: 47 fs). The solid line shows the fit of the mono-exponential rise with a time constant of 12 fs. The inset shows the decay of the photo-excited singlet state (probe wavelength: 710 nm), which contains equivalent information. Excited state and cation dynamics agree well within the experimental uncertainty and give a proof of the finite injection time in the strong coupling case that is realized by attaching perylene via a carboxyl group onto TiO_2.

References

[1] S. Ramakrishna, F. Willig, V. May, Phys. Rev. B 62 (2000) R16330.

[2] B. O'Regan and M. Grätzel, Nature 353 (1991) 737.

[3] J. Schnadt, B.A. Brühwiler, L.Patthey, J.N. O'Shea, S. Södergren, M. Odelius, R. Ahuja, O. Karis, M. Bässler, P. Persson, H. Siegbahn, S. Lunell, N. Martensson, Nature 418 (2002), 620.

[4] C. Zimmermann, F. Willig. S. Ramakrishna, B. Burfeindt, B. Pettinger, R. Eichberger, W. Storck, J. Phys. Chem. B 105 (2001), 9245.

[5] R. Ernstorfer, S. Felber, L. Gundlach, C. Zimmermann, R. Eichberger, F. Willig, in preparation.

R. Ernstorfer, W. Storck, S. Felber, L. Gundlach, S. Ramakrishna, C. Zimmermann, R. Eichberger, S. Kubala, L.Töben, F. Willig

In-situ Control of MOCVD grown GaSb(100)

GaSb is a low bandgap semiconductor that is of great interest for novel solar cell devices, i.e. firstly for thermo- photovoltaic cells and secondly for high efficiency multi-junction solar cells. It is well known that the growth of GaSb is more complicated and puts more restrictions on the growth parameters (gas pressures, temperature) than other III-V materials like GaAs and InP. In-situ monitoring of MOCVD (metalorganic chemical vapor deposition) growth is a key issue since it can lead to a better control over the growth of the semiconductor layer. Reflectance difference/anisotropy spectroscopy (RDS/RAS) is a powerful tool for performing this in-situ monitoring of III-V-semiconductor growth in an MOCVD reactor. This technique delivers optical spectra that show unique spectral features for different materials, surface properties and even can give information on dopant concentration. Once the relation between the RDS signals and the material properties is known, these 'fingerprint' signals can be used to monitor and optimize the growth process. RDS is a reflectance technique that probes the anisotropy arising from the different atomic structure on the surface compared to an isotropic bulk. It measures the difference in the normal-incidence reflectance $\mathbf{r}_{[-110]}$ and $\mathbf{r}_{[110]}$ of linear polarized light that impinges at normal incidence onto the sample. This difference is normalized to the total reflectance <r> (Fig.1). The RDS signal arises due to a reduction in symmetry on the reconstructed surface. RDS signals can originate also from anisotropic atomic steps, terraces, and 3D structures of micrometer dimensions.

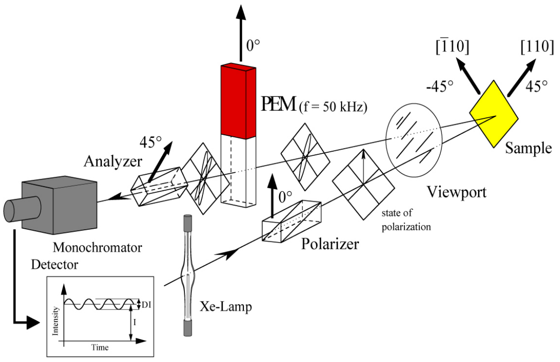

Fig.1 Experimental set-up for RDS/RAS measurements according to [1]: The difference in reflectance is measured employing the lock-In technique. Diagram from J. Rumberg, TU Berlin (1995)

Epitaxial GaSb(100)-semiconductor films were prepared in an AIXTRON AIX-200™ reactor using triethylantimony (TESb) and triethylgallium (TEGa) as precursors. Sample growth was monitored in the MOCVD reactor with RDS. Fig. 2a shows the RDS spectra of a successfully grown GaSb sample. It is also the first published application [2] of the recently introduced RAS apparatus that allows for measurements in the near IR spectral range (0.8 eV to 5.0 eV).

With unfavorable parameters (high flow rates or unsuitable Sb/Ga-ratios) the growth of anisotropic 3D islands of micrometer dimensions was promoted (Fig. 2b). The occurrence of the latter led to a strong RDS signal. Compared to a flat surface these islands led to an increase in the RDS signal by more than one order of magnitude. The growth of such 3D islands was avoided by the choice of appropriate growth parameters (Fig.2a). State of the art GaSb films were grown with residual charge carrier concentrations $N_p < 3 \times 10^{16}$ cm^{-3} under appropriate growth conditions (V/III-ratio=1.55, $p_{TEGa} < 7 \times 10^{-4}$ mbar, growth rate=1.6 µm/h, T=550°C).

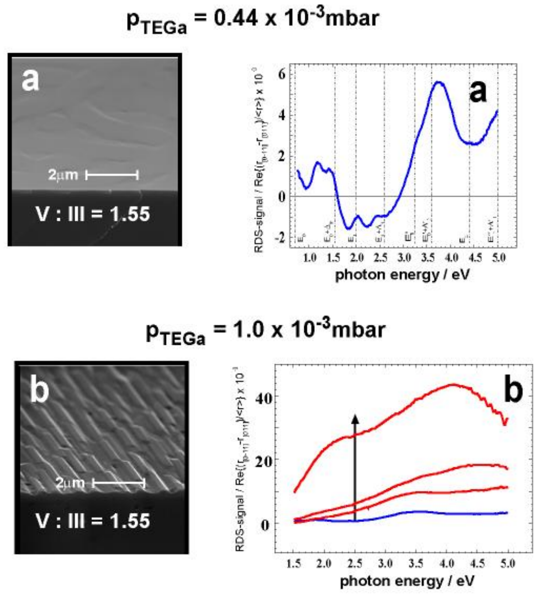
p_{TEGa} = 0.44 x 10^{-3}mbar

p_{TEGa} = 1.0 x 10^{-3}mbar

Fig.2 a) RDS signal of GaSb(100) and electron microscope image of the surface for proper growth conditions. b) GaSb(100) grown with unfavorable growth parameters: The extremely strong RDS signal originated at 3D structures that were oriented parallel to the [-110]-axis.

Reference

[1] D.E. Aspnes, J.P. Harbison, A.A. Studna, L.T. Florez, and M.K. Kelly J. Vac. Sci. Technol. A6 (1988) 1327

[2] K. Möller, Z. Kollonitsch, Ch. Giesen, M. Heuken, F. Willig, T. Hannappel J. Crystal Growth 248 (2003) 244

K. Möller, Z. Kollonitsch, H.-J. Schimper,
T. Hannappel, F. Willig

Energies of unoccupied and occupied electronic surface states on In-rich (2x4)-reconstructed InP(100) measured with femtosecond 2PPE

The pioneering work of Bokor and Haight [2] has established that time-resolved two-photon-photoemission (2PPE) is a powerful tool for elucidating the existence and energetic positions of unoccupied electronic surface states or interface states in the band gap, and also of surface and interface resonances, where the latter are isoenergetic with bulk states in the conduction band. It is at hand to employ this powerful tool for investigating materials of technological relevance, in particular III-V semiconductors for solar energy conversion grown via MOCVD (metalorganic chemical vapor deposition). It is meaningful to test these sometimes complicated 2PPE signals first at a well-defined surface where valuable supporting information concerning the atomic structure on the surface can be collected by applying many different tools of surface science. In addition it is helpful when experimental results can be compared with theoretical predictions. All these criteria are met by the (2x4)-reconstructed In-rich surface of InP(100). Electrons lifted by a laser pulse to an unoccupied electronic state are not stable at this energy level and will scatter with other charge carriers and phonons thereby reaching unoccupied electronic levels at lower energies. Such processes occur in femtosecond time windows. Thus, measurements of meaningful 2PPE spectra require laser pulses of femtosecond duration. Photons in the probe laser pulse must have sufficient energy to lift the electrons from the unoccupied electronic states in the solid into vacuum where they are recorded and analyzed for their kinetic energy and angular distribution.

Fig. 1 shows the 2PPE spectrum (solid curve) of the clean ordered (2x4)-reconstructed In-rich surface of InP(100) measured with 4.66 eV photons and pulse widths below 50fs (FWHM) [2]. The origin of the peaks was elucidated in additional measurements where e.g. the photon energy and polarization of the pump pulse was varied. It was found that i_4 stems from occupied surface states located close to the upper edge of the valence band as had been seen also with UPS. Peak i_3 stems from a bulk state, and i_2, i_1 originate at unoccupied surface resonances. The rise in the signal at kinetic energies corresponding to photoemission from the band gap, i.e. below the conduction band minimum (CBM in Fig.1), was attributed to defects that are inhomogeneously distributed over the surface, probably tiny cluster of Indium. Preparation of the ordered (2x4)-reconstructed In-rich surface involved temperatures above 360°C, where phosphorus is preferentially desorbed from the crystal lattice. It is well known that a large concentration of Indium droplets can easily be formed on this surface at elevated temperatures. In agreement with this scenario this part of the signal was not observed on the ordered (2x1/2x2)-reconstructed P-rich surface of InP(100). The uppermost layer of the latter is made up of only phosphorus atoms. It is highly unlikely that Indium clusters or droplets can be formed on this surface.

The peaks ascribed to the surface states were strongly diminished (Fig.1) after the surface had been exposed to hydrogen. The two unoccupied surface states i_1 and i_2 are located 0.2 eV and 0.85 eV above the conduction band minimum, respectively. Our experimental findings are in excellent agreement with theoretical predictions by Schmidt et al. for this surface reconstruction of InP(100) [3]. The obvious next task will be time-resolving the dynamics of hot electrons on this surface, i.e. measuring in real time electron scattering between surface resonances and bulk states in the conduction band.

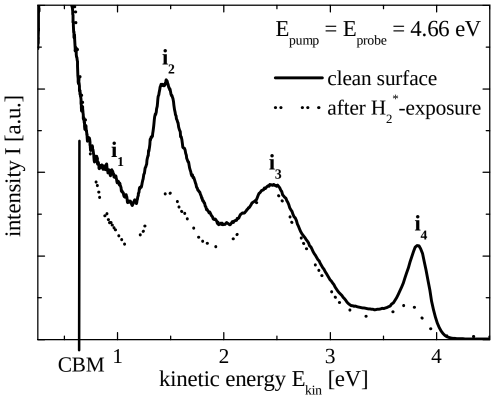

Fig.1: 2PPE-spectrum (4.66 eV photons) of the ordered (2x4)-reconstructed In-rich surface of InP(100) before (solid curve) and after (dotted curve) exposure to excited hydrogen.

References

[1] R. Haight, Surface Science Reports 20 (1994) 276

[2] L.Töben et al., J. Cryst. Growth 248C (2003) 206

[3] W.-G.Schmidt et al., Phys. Rev. B 61 (2000) R16335

L. Töben, R. Eichberger, L. Gundlach,
T. Hannappel, R. Ernstorfer, F. Willig

Electrochemical Surface Conditioning

Electrochemical methods are increasingly used because of their high specificity allowing potential, current and charge control. For semiconductor surface modification of photovoltaic absorbers, changes can be made from the submonolayer range up to several micrometers as will be shown below. The initial stages of roughening of float-zone n-Si(111) could be investigated according to Fig. 1 where a photocurrent-voltage and the current behaviour with time are shown schematically; interruption of the conditioning procedures are marked by labels (A) and (a) – (c). After sample emersion from the electrolyte at potential (A), the surface was analysed by synchrotron radiation photoelectron spectroscopy (SRPES)(Fig. 2). The conditions (a) – (c) were investigated by atomic force microscopy (AFM) (Fig. 3).

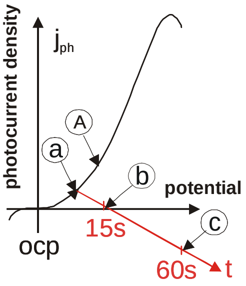

Fig. 1: Schematic photocurrent-voltage and photocurrent-time behaviour of n-Si(111) in 0.1 M NH_4F including emersion times amd potentials (see text).

Fig. 2: Si 2p line including deconvolution obtained after sample emersion at position (A) in Fig. 1.

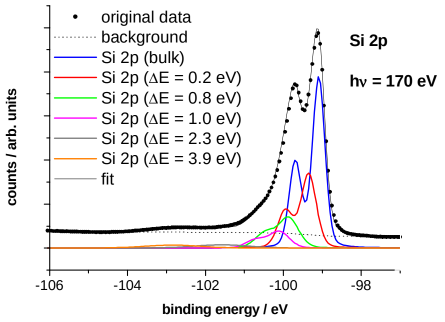

Fig. 2 shows the Si 2p core level line after emersion (see (A) in Fig. 1) only slightly positive of the rest potential (ocp) in the NH_4F solution. The original data have been fitted by mainly 5 contributions which exhibit shifts in binding energy E_b with respect to the so-called bulk line at E_b = -99.2 eV and are characterised by different areas. From comparison with density functional theory calculations made for expected reaction intermediates at the surface, the following assignments can be made; H-termination (ΔE=0.2 eV), =Si-H-OH (ΔE=0.8 eV) and =Si-H-F (ΔE=1.0 eV) species and a precipitate (ΔE=2.3 eV).

The AFM images show the onset of the dissolution process at step edges of atomic terraces (Fig. 3a) with formation of nanometer-sized pits. The images demonstrate that the initial progress in pit growth (Fig. 3b) occurs rather in lateral than in vertical direction. For increased dissolution charge, rather regular features (Fig. 3c) develop which exhibit large flat mesa-type islands.

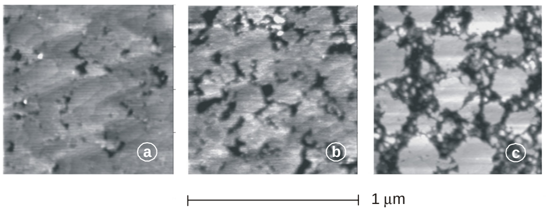

Fig. 3: AFM micrographs of n-Si(111) obtained after emersion at potential and times labelled (a)-(c) in Fig. 1. Dissolution charge: 0.28 mCcm^{-2} (a), 0.69 mCcm^{-2} (b), 4.5 mCcm^{-2} (c).

In 0.2 M solution, the dissolution current is considerably higher (AFM images not shown) and the analysis of the 3-dimensional roughness shows a hitherto unknown exponential relationship with the charge passed upon dissolution. The understanding of the selective roughening serves as a prerequisite for directed nanostructure formation for light coupling and photonic devices.

The elctrochemical conditioning of $CuInS_2$ solar cell absorbers covered with a deleterious CuS phase has been partly successful as shown in Fig. 4. After a treatment at cathodic potential (reduction of CuS) the photocurrent-voltage characteristic in a photoelectrochemical (PEC) solar cell with $V^{2+/3+}$ redox electrolyte is compared to the one obtained after the poisonous KCN etch. The lower performance of the electrochemically treated sample is attributed to Cu_2S remnants acting as shunts as evidenced by recent X-ray emission spectroscopy measurements at BESSY II. New conditioning procedures are currently tested.

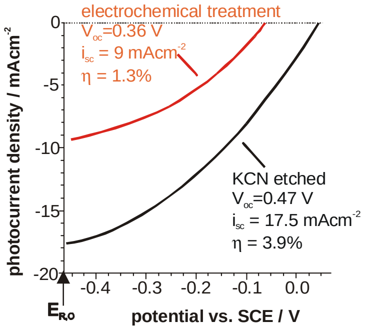

Fig. 4: PEC solar cell characteristics of electrochemically (red) and KCN etched (black) $CuInS_2$

H.J. Lewerenz, H. Jungblut, M. Aggour, J. Jakubowicz, C. Murrell, M. Kanis, M. Gaul

Charge carrier kinetics in the space charge region

The interface Si_3N_4/Si is of large practical and theoretical importance. On the practical side the application in MOSFETs, as energy converting interface, anti-reflection system [1] in solar cells and as electronic passivated Si surfaces in Si devices [1] can be mentioned. On the theoretical side the Si_3N_4/Si interface can be considered as one of the most simple forms of a hetero junction and so it can be used as a model system for the study of the behaviour of hetero junctions.

The Si_3N_4/Si interface is characterized by a high fixed, positive charge density (about $2x10^{12}$ cm^{-2}) in the Si_3N_4 part compensated mainly by free electrons in the Si part of the junction . So at the Si_3N_4/p Si heterojunction an inversion layer is built up. It is reported that the mobility of minority carriers (i.e. electrons) in the inversion layer is strongly reduced down to 250 $cm^2V^{-1}s^{-1}$[2]. Excess charge carrier kinetics in silicon wafers is described by recombination and trapping of excess charge carriers in the volume and at the surface. Generally surface processes are taken into account by defining an effective surface recombination velocity at the edge of the surface space charge region. Volume recombination is mostly represented by a simple volume recombination time although trapping may occur. However, also the separation and storage of excess charge carriers in the space charge region must be taken into account .

In this work the influence of the pSi/Si_3N_4 interface on excess charge carrier kinetics in the pSi substrate has been studied by contactless transient photoconductivity measurements. Substrate wafers of different resistivities have been investigated. Furthermore, the difference between samples at one face and at both faces coated with a Si_3N_4 film has been studied.

Contactless and non-invasive transient photoconductivity measurements in the microwave frequency range were performed at 10GHz with the Time Resolved Microwave Conductivity (TRMC) method in an equipment as described previously [3]. The TRMC signal, i.e. the relative change of the microwave power reflected from the sample upon illumination, $\Delta P(t)/P$, is proportional to the photoconductance $\Delta S(t)$ [3]:

$$\Delta P(t)/P = A\,\Delta S(t) = A\,(\Delta n(t)\mu_n e + \Delta p(t)\,\mu_p e) \qquad (1)$$

where A is a proportionality constant, depending on dark conductivity, thickness etc., and $\Delta n(t)$ ($\Delta p(t)$) is the excess number in cm^{-2} and μ_n (μ_p) is the mobility of electrons (holes). TRMC signals are displayed in arbitrary units (a.u.).

TRMC signals were excited by 10ns (FWHM) pulses at 1064nm, leading to an approximately uniform generation of charge carriers.

Silicon nitride (Si_3N_4) films (70nm thick) were deposited in a commercial parallel-plate plasma deposition reactor (Plasma Technology). These films were deposited on high quality single crystalline p-type (Boron doped) silicon wafers (0.53 mm thick) mostly on both sides. For the sample covered at only one side with Si_3N_4 it was controlled by TRMC measurements induced by 532nm light at the uncovered face of the wafer that this face can be considered as an infinite sink for excess charge carriers [3]. Measurements of the conductance of the samples before and after the deposition of Si_3N_4 by microwave reflection measurements [3] lead to essentially the same results as reported previously: a conductance increase $2x10^{-4}$ Ω^{-1} is observed after deposition of a Si_3N_4 film at one Si surface [2].

TRMC measurements of several pSi wafers with different resistivities yield essentially the same results:
The maximum TRMC signal height (the TRMC amplitude) is proportional to the excitation density in the range covered. A fast initial decay is followed by a slower decay, where the signal shape does not change in the low excitation density range (lower than $3x10^{-8}$ Jcm^{-2}) but the initial decay becomes considerably slower at high excitation densities. The shape of the TRMC signal does not even depend on the resistivity of the wafer in the low excitation density as it can be seen in Fig.1, where as an example the normalized TRMC signals of the three wafers are displayed for excitation by 1064nm light ($30nJcm^{-2}$):

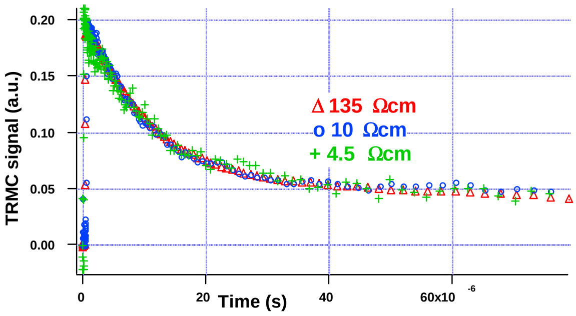

Fig. 1: Normalized TRMC transients induced by 1064 nm light pulses (excitation density 30 nJcm^{-2}) in 3 pSi wafers (0.53 mm) with resistivities 140 Ωcm, 10 Ωcm and 4.5 Ωcm (as indicated in the figure) covered at both sides with Si_3N_4 films in a linear representation

It can be concluded from the experiments that the decay behaviour of the TRMC signal (cf. Fig.1) cannot be due to some volume decay channel but must be due to a process at the Si/Si_3N_4 interface. Furthermore, this decay channel saturates at higher excitation densities .

Further evidence for the attribution of the decay to a junction process comes from experiments on two samples of the same wafer, where one is coated by Si_3N_4 films at both faces and the other one is covered only at one side by a Si_3N_4 film, whereas the other side can be considered as an in infinite sink for excess charge carriers. The shape of the TRMC signal is approximately the same but the slower decaying part of the signal is clearly larger in the sample covered at both sides. Obviously, surface recombination at the uncoated surface competes with the junction process.

Only one process can be related to the initial decay process: the decrease of the minority carrier (electron) mobility in shifting position from the bulk to the Si/Si_3N_4 interface.

The following model seems appropriate:
Excess charge carriers (uniformily generated by 1064nm) diffuse to the junction where electrons are

swept to the interface by the space charge field and holes stay at the edge of the space charge region. The contribution of the holes to the TRMC signal does not change but the contribution of electrons decreases drastically due to the decrease of their mobility. Also a recombination process in the space charge region must be taken into account to explain the long time slower decay. This yields three parameters for the description of excess charge carrier kinetics:

- A rate parameter k_{tr} describing the transport of the generated excess charge carriers to the space charge region.
-The reduced electron mobility μ_n* at the surface.
-The rate parameter k_{rec} describing recombination in the space charge region.

It seems sound to assume that excess charge carrier pairs arriving at the edge of the space charge region are instantaneously separated as long as the space charge field is still considerable. This is evidently only valid at low excitation densities. Then the transport of the excess charge carriers to the space charge regions will be diffusion controlled and k_{tr} is given by [3]:

$$k_{tr} = \frac{D_{amb}\pi^2}{l^2} \qquad (2)$$

where D_{amb} is the ambipolar diffusion constant, given in the low injection range by the minority (electron) diffusion constant. In principle Eq. 2 is not instantaneously valid as first the principal mode must be established [3]. However, application of Eq. 2 in the comparable case of Si wafers with abrased surfaces has learned that a few microseconds after excitation the decay is described by Eq.2 for 1064nm excitation. As a further simplification it will be assumed that the recombination process characterized by k_{rec} is exponential. Under these conditions $\Delta S(t)$ is described by a two exponential equation with only two varying parameters μ_n* and k_{rec}, whereas k_{tr} is given by Eq. 2 and μ_n and μ_p are known.

All experimental data could be fitted within the experimental accuracy by the two exponential equation in the low excitation density range. As an example, experimental data and the best fits are shown for a 400Ωcm pSi wafer (l= 0.53 mm) at both sides covered by a Si_3N_4 film in Fig.2. It can be seen that up to a limiting number of excess carriers Δn_0^{lim}=1x10^{11} cm^{-2} the experimental signals are satisfactorily described by the simple two exponential model.

In Table I the values of k_{rec} and μ_n* found by fitting the experimental data are displayed. The values are obtained by averaging the values obtained for all excitation densities up to a number of generated excess charge carriers Δn_0^{lim} (in cm^{-2}), corresponding to the highest excitation density yielding TRMC signals agreeing with the model. μ_n* is independent of the excitation density, but for k_{rec} the results of some samples suggest a weak increase with Δn_0 . It must be noted that the error in the parameters is relatively large, in particular because the experimental data is rather sensitive to combinations of k_{rec} and μ_n*

Particularly convincing is the agreement between the parameters found for a wafer covered at one side and at two sides with Si_3N_4: within the accuracy of the measurements the same values for k_{rec} and μ_n* are found.

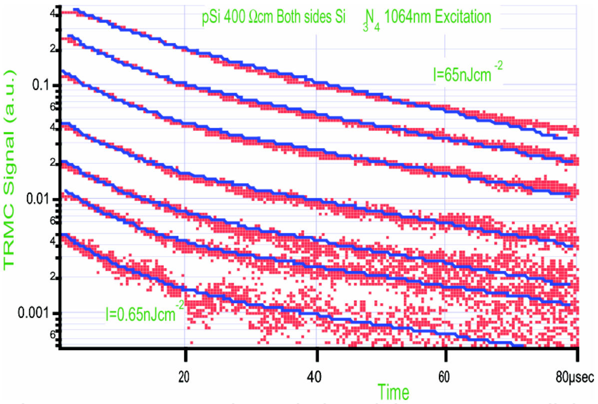

Fig. 2: TRMC transients induced by 1064 nm light pulses (excitation densities from 0.65 - 65 nJcm^{-2}) in a pSi wafer (400 Ωcm, 0.53 mm) covered at both sides with Si_3N_4 films in a semi-logarithmic representation. The (blue) lines drawn represent the best fits of the experimental data to the two exponential model with parameters given in Table I.

Resistivity (Ωcm)	Coated	Δn_0^{lim} (cm^{-2})	μ_n* (cm^{2}V^{-1}s^{-1})	k_{rec} (s-1)
400	both sides	1x10^{11}	230	2x10^4
400	one side	1x10^{11}	280	2x10^4
140	both sides	1x10^{11}	230	1x10^4
10	both sides	4x10^{11}	200	8x10^3
4.5	both sides	8x10^{11}	200	1x10^4

Table I: The parameters obtained for the best fit of the experimental data to the two exponential model for five samples.

This points to the adequacy of the model for the description of the experimental data. For all samples a value for μ_n* between 200-300 cm^{2}V^{-1}s^{-1} is found. This indicates that μ_n* can be considered as constant within the accuracy of the experiments. The value for μ_n* agrees satisfactorily with the value μ_n* = 250(-+20%) cm^{2}V^{-1}s^{-1}determined by different measurements [2]. The parameter k_{rec} depends on the deposition conditions and the wafer pretreatment.

The present work shows that excess charge carriers in the space charge region detected by photovoltage measurements are also accessible to (contactless) transient photoconductivity measurements, although with another weight factor

References

[1] M. Kunst, O. Abdallah and F. Wünsch, Thin Solid Films 383, 61 (2001).
[2] J.R. Elmiger and M. Kunst, Appl. Phys. Lett. 69, 517 (1996).
[3] C. Swiatkowski, A. Sanders, K.-D. Buhre and M. Kunst, J. Appl. Phys. 78, 7741 (1995).

S. von Aichberger, G. Citarella, F. Wünsch, M. Kunst

Growth monitoring of reactively sputtered MoS_x and WS_x thin films

The aim of this project is to prepare van-der-Waals-layer type semiconductors MX_2 (M = Mo, W; X = S, Se) which have been proposed as absorber materials for thin film solar cells [1]. Studies have shown that the texture of thin films of these materials is an important factor for their photoactivity (e.g. [2]). The (001) texture, where the van-der-Waals planes are parallel to the substrate surface, is favoured for the application in solar cells because such films have less surface states which can act as charge carrier recombination centres. Since reactive magnetron sputtering from metallic targets in mixtures of argon and a reactive gas (e.g. O_2, H_2, H_2S) is a well established technique for thin film deposition of oxides and sulfides we investigated this method for the deposition of MoS_x and WS_x films. In order to understand the growth mechanisms *in situ* experiments with energy dispersive x-ray diffraction (EDXRD) during the sputtering process were performed at the synchrotron radiation source HASYLAB at DESY, Hamburg.

Analysing the stoichiometry of the films using elastic recoil detection analysis (ERDA) and Rutherford backscattering (RBS) revealed sulphur-to-metal ratios of $x \leq 2.3$, dependent on the amount of H_2S in the H_2S / Ar sputtering gas mixture. Stoichiometric MS_2 is however only formed at substrate temperatures below 200°C, at which the films are practically x-ray amorphous. It was possible to prepare well crystallised films at substrate temperatures of 450°C and above with a suphur/metal ratio of approximately x = 1.7 - 1.8.

In situ-energy dispersive x-ray diffraction (EDXRD)

The setup of the experiment is shown in fig. 1a. At a fixed diffraction angle θ *in situ*-EDXRD spectra were measured by a high purity Ge detector with a time resolution of 20 – 30 s. Fig. 1b depicts a series of spectra which were collected during the deposition of a highly (001) textured WS_x thin film. From the spectra series structural properties of the films were obtained in dependence on the deposition parameters H_2S partial pressure, sputtering power, sputtering pressure ($5 - 90 \cdot 10^{-3}$ mbar), substrate temperature (190 - 620°C) and film thickness. Low deposition rates led to the formation of a strong (001) texture, in which the van-der-Waals planes were parallel to the substrate, which is a prerequisite for high photoactivity of MS_x films ($c_\perp$ orientation of the crystallites). In fig. 2 this is demonstrated for eight experiments where MoS_x films were deposited at increasing sputtering pressure, i.e. decreasing deposition rate. In the diagram the (002) diffraction peak area of the hexagonal MoS_2 phase is plotted against the atomic areal density of the deposited Mo, which represents a normalized film thickness and was calculated from the peak area of the MoK_α fluorescence line. The appearence of the fluorescence lines is due to the use of polychromatic ("white") x-rays and is one advantage of the EDXRD method because it allows a film thickness monitoring additionally to the obtained diffraction pattern. The peak area of the (002) reflection shows a characteristic behaviour during the deposition. A steep increase is followed by a saturation effect. The saturation value of the peak area depends on the sputtering pressure. With increasing pressure this value also increases, indicating that an increasing volume of coherently scattering crystallites, which have their c-axes perpendicular to the substrate ($c_\perp$), is obtained with decreasing deposition rates.

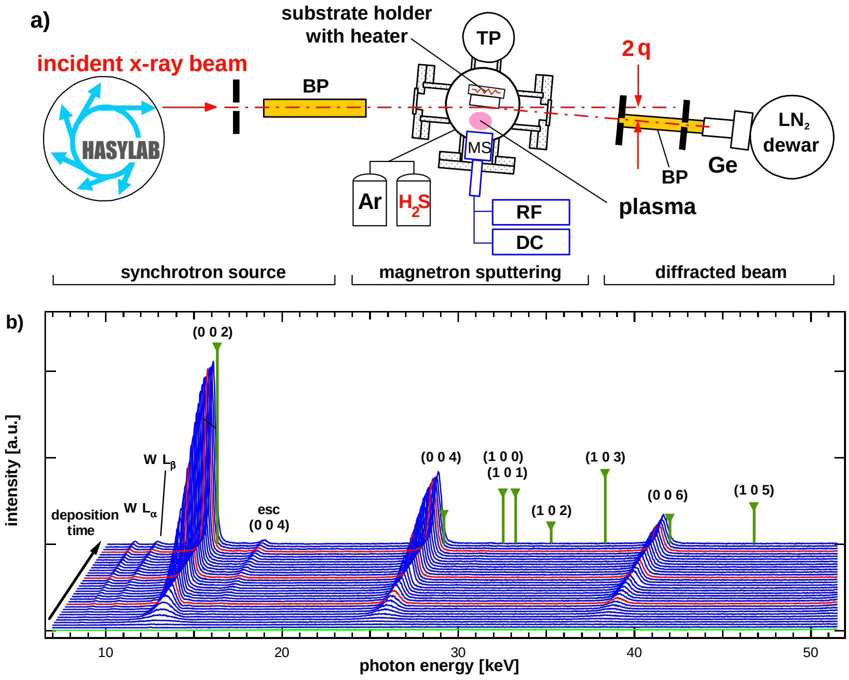

Fig. 1: a) Setup of in situ sputtering chamber for EDXRD experiments at HASYLAB (BP: He-filled beam pipe; TP: turbo pump; MS: magnetron sputtering source; RF, DC: power supplies for the magnetron; Ge: high-purity germanium detector. b) Series of in situ-EDXRD spectra during magnetron sputtering of a WS_x thin film. The green bars with the triangles mark the positions and the intensities of the powder diffraction spectrum of 2H-WS_2 (JCPDS 8-237), esc is an escape peak due to the detection system. Deposition conditions: RF (27.12 MHz) sputtering power 50 W; T_{sub} = 450°C; p_{total} = 0.02 mbar; gas flow ratio F_{H2S} / (F_{H2S}+ F_{Ar}) = 0.75; total deposition time 16 min; diffraction angle θ = 4.474°.

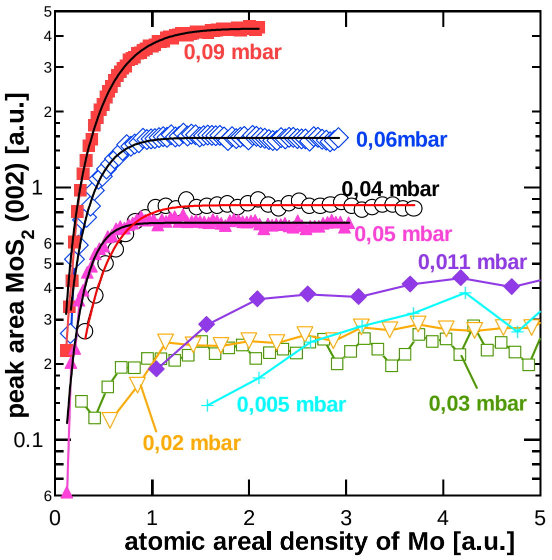

Fig. 2: Development of the peak area of the (002) EDXRD signal during reactive sputtering of MoS$_x$ thin films on oxidized silicon substrates. Eight depositions with varying sputtering pressure are shown. The normalized film thickness is given as atomic areal density of the deposited Mo and was calculated from the MoK$_\alpha$ fluorescence line. Deposition conditions: DC sputtering power 50 W; substrate temperature 450°C; gas flow ratio $F_{H_2S} / (F_{H_2S} + F_{Ar}) = 0.75$; floating substrate potential.

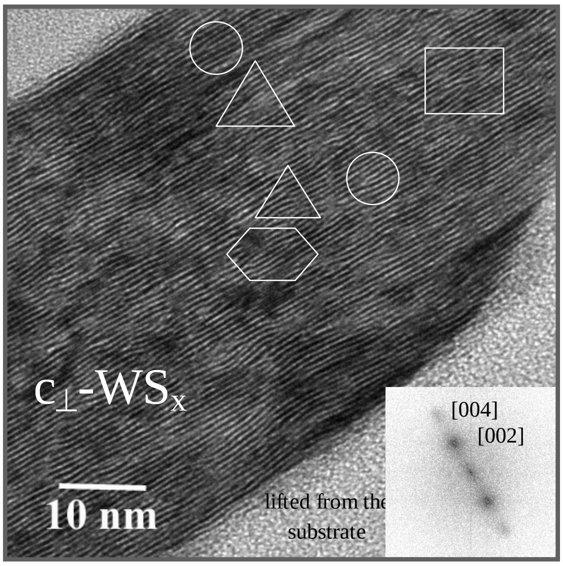

Fig. 3: Cross-sectional TEM picture of a reactively sputtered WS$_x$ thin film on an oxidized silicon substrate. Each black line represents one S-W-S stack, several stacking faults can be observed (marked). The inset is a Fourier transformation of the micrograph showing the diffraction spots of the (002) and (004) lattice planes. Deposition conditions: See fig. 2, substrate temperature 620°C; total sputtering pressure $4 \cdot 10^{-2}$ mbar.

At high deposition rates, the initial (001) preferential orientation of the crystallites turns into a (100) texture. It is proposed that the texture cross-over can be interpreted on the basis of the model of competing contributions of surface energy and microstrain energy to the total energy of the crystallites. The saturation of the (002) peak area shows that the texture crossover is irreversible what can be explained by different growth velocities in the different crystallite directions. Once the (100) orientation occurs it will dominate the subsequent film growth because the crystallites grow 60 - 500 times faster in this direction than in the [001] direction. This value was obtained as approximation by comparing the size of single crystals of these materials in both directions.

Lattice strain and stacking faults

The development of the lattice strain ε of the c-axis relative to the lattice parameter of the powder material could be derived during sputtering from the energetic position of the (002) diffraction peak. It was observed from SEM and TEM images that the (001)-oriented basal layer had a thickness of about 20 nm to a maximum of 100 nm. The strain ε of the c-axis of the unit cell of MoS$_2$ and WS$_2$ exhibited a characteristic evolution with increasing film thickness which was proved not to result from mechanical stress in the films. A steep increase in the strain up to a maximum value was observed at the beginning of the deposition followed by a relaxation towards a slightly smaller saturation value. The maximum value of ε was up to 4% depending on the deposition rate [3].

It is assumed that crystal defects such as dislocations, self intercalated metal atoms or by analogy to graphite, turbostratic growth, i.e. a random stacking deviation from the perfectly parallel stacking order of the 2H or 3R polytypes, are responsible for the c lattice strain and grain sizes below 70 nm. This is plausible because of the weak bonds between the S-M-S stacks. The very small grains can be explained by a high defect density, which was confirmed by high resolution cross-sectional TEM analysis of the sputtered films. Fig. 3 shows a detail of a WS$_x$ film in which different stacking faults can be identified. From the micrographs dislocation densities of up to $3 \cdot 10^{12}$ cm^{-2} were estimated. In combination with the metal surplus of many films in comparison to stoichiometric MS$_2$ the strain of the crystallographic unit cell can also be explained by the intercalation of additional metal atoms between the van-der-Waals planes.

Further *in situ*-EDXRD experiments during reactive sputtering of MoS$_x$ and WS$_x$ thin films are planned to find out wether the variation of the plasma excitation mode (DC and/or RF) and the radio frequency can shift the texture further towards the (001) orientation.

References

[1] H. Tributsch, Z. Naturforsch. 32a, 972 (1977).
[2] E. A. Ponomarev, R. Tenne, A. Katty and C. Levy-Clement, Sol. Energ. Mat. Sol. C. 52, 125 (1998).
[3] V. Weiß, R. Mientus, K. Ellmer, Mat. Res. Soc. Symp. Proc. 721, 131 (2002).

V. Weiß, R. Mientus (Optotransmitter-Umweltschutz-Technologie e.V.), U. Bloeck, K. Ellmer